NOTICE

The quality of this microform is heavily dependent upon the quality of the original thesis submitted for microfilming. Every effort has been made to ensure the highest quality of reproduction possible.

If pages are missing, contact the university which granted the degree.

Some pages may have indistinct print especially if the original pages were typed with a poor typewriter ribbon or if the university sent us an inferior photocopy.

Reproduction in full or in part of this microform is governed by the Canadian Copyright Act, R.S.C. 1970, c. C-30, and subsequent amendments.

AVIS

La qualité de cette microforme dépend grandement de la qualité de la thèse soumise au microfilmage. Nous avons tout fait pour assurer une qualité supérieure de reproduction.

S'il manque des pages, veuillez communiquer avec l'université qui a conféré le grade.

La qualité d'impression de certaines pages peut laisser à désirer, surtout si les pages originales ont été dactylographiées à l'aide d'un ruban usé ou si l'université nous a fait parvenir une photocopie de qualité inférieure.

La reproduction, même partielle, de cette microforme est soumise à la Loi canadienne sur le droit d'auteur, SRC 1970, c. C-30, et ses amendements subséquents.

A COMPARATIVE STUDY OF SOME MN- AND FE-BASED CHALCOPYRITE SEMICONDUCTOR ALLOYS: BASIC PROPERTIES AND THE EFFECTS OF ORDERING

by

Riccardo Brun del Re

Submitted to the School of Graduate Studies
in partial fulfillment of the requirements
for the degree of Ph.D. in Physics

Ottawa Carleton Institute for Physics
University of Ottawa
Ottawa, Canada

ISBN 0-315-75051-0

Canada

UNIVERSITÉ D'OTTAWA
UNIVERSITY OF OTTAWA

Acknowledgments

The completion of this project involves the merits of many people to whom I wish to express my gratitude.

First and foremost, I wish to profoundly thank and acknowledge my parents, Teresa and Lino for creating this opportunity for me. Their continued support, moral, spiritual and financial, has contributed to me in ways that I cannot begin to describe here.

Secondly I wish to thank Carla and Roberto Brun del Re, and Diana Stukel for taking care of me during the most difficult stages of the work, and making my life so much more enjoyable, and fulfilling. I also thank Renato Brun del Re for his wonderful influence as an older brother and as a scientist during my earlier years.

I am deeply grateful to my supervisor, Professor John C. Woolley for being so patient during my long incubation period and then for being a constant scource of inspiration, guidance and creativity throught the project. This thesis would not have been possible without him, and he remains for me, an inspiring model scientist in the most complimentary sense. His financial support is also gratefully acknowledged.

I wish to thank Professor Gilles Lamarche for his excellent guidance, constant partnership and for his financial assistance. His scientific influence runs deeply in my work, and he was a joy to work with, even at 2:00 a.m.

Thanks to Dr. Denis . Rancourt for providing his facilities, knowledge, financial assistance and inspiration.

His influence has added a much appreciated 'edge' to my work.

Thanks to professor Richard Hodgson for his assistance with the computer analysis, and more importantly for catalyzing my personal transition into the computer age.

Thanks to Anne-Marie Lamarche for being a scource of aid, inspiration and good cheer, and to Bei-Wah Chan, and Joan Curry for the ESR measurements and for their partnership.

Thanks to Dr. Peter Piercy for the workspace, to the late professor Manoogian for his guidance with the ESR measurements and for his wonderful presence, and to Ron Hartree for his assistance with the x-ray diffractometer and databases.

Thanks to my friends Shahragim, Ardavan, and Moneca Tajbakhsh, Paul Touzin, Karen and Michel Dion, Marc-Ande and Alysone Greg and Judy, John and Tamara Shonfield, Gillian Reid, for the support, and for being so patient during my long periods in hiding.

Finally I wish to thank the many friends at Ottawa University for the comic relief, and good vibes over the years; Mike Jackson, Mike Murphy, Lorraine Gravelle, Charlie Sauriol, Line Robitaille, Michel Royer, Pierre Cote, Claude Plante, Chang Gang Zhang, Pamela Tume, Art Buser, Len Paiment, Dave Leblanc, Rob Parent, Bob Hart, Ron Lavigeur, Herve Beaudoin, Brian Logan, Cyril Benson, Roger Chagnon, Russ Chalifoux, Simon Fafard, Paula Heron, Kevin Gibb and others.

Abstract

Dilute magnetic semiconductor alloys based on I-III-VI_2 chalcopyrite structure compounds and containing either iron or manganese as the magnetic component, were investigated in the context of a comparative study. The implications and effects of crystallographic ordering were of particular interest to this research.

Polycrystalline samples of $CuIn_{1-x}Fe_xS_2$, and $(AB)_{1-z}Mn_{2z}Te_2$, (with A=Ag or Cu, B=In or Ga) were fabricated by the melt and anneal technique. X-ray and neutron diffraction, optical absorption, and differential thermal analysis were utilized to characterize the materials. As a result of these experimental investigations, the phase diagram of the $CuIn_{1-x}Fe_xS_2$ system was proposed, and certain modifications to the previously accepted phase diagrams of the systems containing manganese were given. The magnetic properties of the materials were then investigated using ESR, magnetic susceptibility, and Mössbauer spectroscopy.

It was found that while some of the properties of the materials could be predicted on the basis of simple atomic physics considerations, other important properties of the materials deviated from initial expectations. For the iron containing system, the magnetic behaviour was interpreted in terms of a Curie-Weiss law, and the applicability of ligand field theory was investigated as a theoretical basis for understanding the results so obtained. It was determined that a transition similar to the $^6A_1$-$^4T_1$ crossover of crystal field

theory may occur as a function of iron concentration in this material.

Although the experimental data relating to crystallographic ordering was found to be consistent with the random substitution of Fe^{3+} on the chalcopyrite indium sublattice, the presence of Fe^{2+} was also detected. Through the results of various experiments, the Fe^{2+} was interpreted to be due to substitutional-defect iron sites.

Various computer fits and simulations were carried out in order to analyze the diffraction, and magnetic susceptibility measurements made on the alloys containing manganese. Besides displaying the usual non-magnetic-ion type of cationic ordering as in the transition from zincblende to chalcopyrite structure, these systems have been shown to exhibit behaviour characteristic of magnetic- ion crystallographic ordering (Mn-ordering). These ordering properties have been shown to be highly sensitive to sample heat treatment.

The diffraction techniques were found to be insensitive to the types of Mn- ordering suspected to occur, however these alloys yielded direct evidence for the Mn-ordering in the form of their static, low field magnetic susceptibility behaviour. Indeed most of the previously reported types of magnetic behaviour associated with Mn-ordering were found to be reproducible. In addition, some previously unreported types of magnetic behaviour for these systems were discovered. Of particular interest, some of the low temperature annealed, high concentration magnetic ion materials were found not to

display the low temperature spin-glass cusp characteristic of the rapidly cooled samples, and this was interpreted to be the clearest signature of the Mn-ordering.

In an attempt to explain all the results on these materials, a model based on the stannite-like ordering of the manganese within the I-III-VI_2 chalcopyrite lattice was postulated. This model, which incorporated randomly distributed manganese planes, was designed to be consistent with the previously reported results on the systems, and found to be generalizable to the newly discovered properties brought to light in the course of this research.

In contrast to the concentration dependent ionic magnetic moment found in the iron alloy, the interpretation of the magnetism of the manganese alloys was facilitated by the highly stable Mn^{2+} $^6A_1$ (S=5/2) state. The interpretation of the measurements made on the Mn-containing systems was however complicated by the discovery, through the neutron diffraction analysis, that the manganese systems may deviate from the chalcopyrite structure in the low temperature region of the phase diagram. Indeed the presence of some octahedrally coordinated cation sites, (which do not occur in the strictly zincblende- or wurtzite-based ordered structures) has been proposed in order to explain the diffraction data. The magnetic behaviour of these alloys was shown to be consistent with a long-range exchange, mean-field analysis of the planar ordering model. However the possible presence of some octahedral coordination suggested that the assumptions made in the earlier work on these alloys should be carefully reviewed.

TABLE OF CONTENTS

ACKNOWLEDGMENTS.....2

ABSTRACT.....4

TABLE OF CONTENTS.....7

LIST OF FIGURES AND TABLES.....10

LIST OF ABBREVIATIONS.....14

CHAPTER 1

1.0 Introduction.....1

1.1.1 Semiconducting Materials and DMS.....2

1.1.2 Fe- and Mn-Containing Chalcopyrite Semiconductors.....5

1.2 Preliminary Observations on Mn and Fe Ions.....8

CHAPTER 2

2.0 Experimental Techniques.....12

2.1 Diffraction Techniques.....15

2.1.1 X-ray Diffraction.....16

2.1.2 Neutron Diffraction.....22

2.2 Differential Thermal Analysis.....28

2.3 Spectroscopic Techniques.....31

2.3.1 Optical Energy Gap Measurement.....31

2.3.2 Electron Spin Resonance.....34

2.3.3 Mössbauer Effect Spectroscopy.....41

2.4 Magnetic Susceptibility.....48

CHAPTER 3

3.0 Iron Containing Chalcopyrite DMS.....57

3.1 Prelimimary Results on Iron and Chromium Alloys.....59

3.2 The $CuIn_{1-x}Fe_xS_2$ System.....62

3.2.1 Sample Preparation.....62

3.2.2 Differential Thermal Analysis.....64

3.2.3 Phase Diagram.....65

3.2.4 X-ray Crystallography and Phase Data.....70

3.3 Mossbauer Spectroscopy of $CuIn_{1-x}Fe_xS_2$.....77

3.4 Magnetic Measurements.....91

3.4.2 ESR.....96

3.4.3 Crystal (Ligand) Field Approach.....99

CHAPTER 4

4.1 Ordering in the Mn-Containing Chalcopyrites.....107

4.1.1 Magnetic Susceptibility.....107

4.1.2 Optical Energy Gap.....112

4.1.3 ESR.....114

4.1.4 X-ray Diffraction.....116

4.2 Proposed Ordered Structure.....117

4.2.1 The Stannite-Like Ordering.....120

4.3 Search For Signatures of Stannite Ordering.....122

4.3.1 X-ray Signatures.....122

4.3.2 Magnetic Susceptibility Signatures.....126

4.3.3 ESR Signatures.....138

4.3.4 Optical Energy Gap.....142

4.3.5 Summary.....143

4.4 Neutron Diffraction.....145

4.4.1 Experimental Results.....148

4.4.2 Preliminary Analysis of Results.....159

4.4.3 Diffraction Data Fitting.....163

4.4.4 Summary.....169

4.5 Magnetic Susceptibility Data Analysis.....171

4.5.1 Analysis of Susceptibility Data on LTA $(AgGa)_{1-z}Mn_{2z}Te_2$ Samples.....171

4.5.2 Assumptions.....175

4.5.3 Results.....179

4.5.4 Simulations.....183

4.5.7 Summary.....187

4.6.1 Mean-Field Analysis of Mn-Planes.....189

4.7 Summary and Conclusions.....198

5.0 Summary and Synopsis.....200

Appendix 1 (Comparison of Atomic Parameters).....209

Appendix 2 (Fe-S systems).....210

REFERENCES.....211

List of Figures and Tables

1.1 The Chalcopyrite Structure.....3b

2.1.1 Neutron Diffraction Apparatus.....25b

2.2.1 Differential Thermal Analysis Apparatus.....28b

2.3.1 Optical Absorption Apparatus.....31b

2.3.2 Optical Absorption of $(AgGa)_{0.75}Mn_{0.5}Te_2$.....32b

2.3.3a Schematic Diagram of The ESR Apparatus.....35b
2.3.3b ESR Transitions in Fe-doped $CuGaS_2$.....35c

2.3.4 Mössbauer Spectroscopy Apparatus.....42b

2.3.5 Nuclear (Mössbauer) Transition Diagram.....43b

T2.3.1 Table of Mössbauer Parameters.....47b

2.4.1 $[C(T-\theta)^{-1}+D]^{-1}$ vs. Temperature.....55b

3.2.1a DTA of $CuIn_{0.85}Fe_{0.15}S_2$.....64b
3.2.1b DTA of $CuIn_{0.85}Fe_{0.15}S_2$.....64c

3.2.2 Phase Diagram of the $CuIn_{1-x}Fe_xS_2$ System.....65b

3.2.3 The ISS Field of the Cu-Fe-S System at 600°C.....66b

3.2.4 Lattice Parameter (a) of $CuIn_{1-x}Fe_xS_2$.....72b

3.2.5 c/a vs. Composition $CuIn_{1-x}Fe_xS_2$.....73b

3.2.6 LTA Samples in Relation in to the Phase Diagram.....75b

3.2.7 Diffractometer Trace of LTA $CuIn_{0.7}Fe_{0.3}S_2$.....75c

3.3.1 Some Important Mossbauer Spectra
3.3.1a $CuFeS_2$ (Synthetic).....77b
3.3.1b FeS_2.....77c
3.3.1c $CuFeS_2$ (natural).....77c
T3.1.1 Table of Experimental Mössbauer Parameters.....77d

3.3.2a $CuIn_{1-x}Fe_xS_2$ x=0.1 LTA.....78b
3.3.2b $CuIn_{1-x}Fe_xS_2$ x=0.15 LTA.....78c
3.3.2c $CuIn_{1-x}Fe_xS_2$ x=0.2 LTA.....78c

3.3.3a $CuIn_{1-x}Fe_xS_2$ x=0.4 LTA.....79b
3.3.3b $CuIn_{1-x}Fe_xS_2$ x=0.6 LTA.....79c
3.3.3c $CuIn_{1-x}Fe_xS_2$ x=0.85 LTA.....79c

3.3.4a $CuIn_{1-x}Fe_xS_2$ x=0.1 HTQ.....80b
3.3.4b $CuIn_{1-x}Fe_xS_2$ x=0.2 HTQ.....80b
3.3.4c $CuIn_{1-x}Fe_xS_2$ x=0.4 HTQ.....80c
3.3.4d $CuIn_{1-x}Fe_xS_2$ x=0.6 HTQ.....80c

3.3.5 Fe^{2+} Defect Sites in the Chalcopyrite Lattice.....81b

3.3.6 Observed Width of Mössbauer α Doublet.....82b

3.3.7a Mössbauer Isomer Shift of α Doublet.....85b
3.3.7b Mössbauer Isomer Shift of β Doublet.....85c

3.3.8 Mössbauer Quadrupole Splitting Parameters.....87b

3.4.1 Susceptibility vs. Temperature for $CuIn_{1-x}Fe_xS_2$
3.4.1a $CuIn_{1-x}Fe_xS_2$ x=0.04 LTA.....91b
3.4.1b $CuIn_{1-x}Fe_xS_2$ x=0.06 LTA.....91c
3.4.1c $CuIn_{1-x}Fe_xS_2$ x=0.1 LTA.....91c
3.4.1d $CuIn_{1-x}Fe_xS_2$ x=0.15 LTA.....91d
3.4.1e $CuIn_{1-x}Fe_xS_2$ x=0.3 HTQ.....91d
3.4.1f $CuIn_{1-x}Fe_xS_2$ x=0.1 Polyphase Sample.....91e

3.4.2 Inverse Susceptibility vs. Temperature for $CuIn_{1-x}Fe_xS_2$
3.4.2a $CuIn_{1-x}Fe_xS_2$ x=0.04 LTA.....91f
3.4.2b $CuIn_{1-x}Fe_xS_2$ x=0.06 LTA.....91g
3.4.2c $CuIn_{1-x}Fe_xS_2$ x=0.1 LTA.....91g
3.4.2d $CuIn_{1-x}Fe_xS_2$ x=0.15 LTA.....91h
3.4.2e $CuIn_{1-x}Fe_xS_2$ x=0.3 HTQ.....91h
3.4.2f $CuIn_{1-x}Fe_xS_2$ x=0.6 HTQ.....91i
3.4.2g $CuIn_{1-x}Fe_xS_2$ x=0.4 HTQ.....91i

3.4.3 Curie-Weiss Temperature vs. Composition.....92b

3.4.4 Magnetic Transition Temperatures vs. Composition....94b

3.4.5a, b, p_{eff} vs Concentation for $CuIn_{1-x}Fe_xS_2$.....96b

3.4.6a Low Temperature ESR Spectra for $CuIn_{1-x}Fe_xS_2$ x=0.2..97b
3.4.6b Estimated ESR Linewidth vs. Temperature.....97b

3.4.7 Correlation Diagram for d^5 in T_d Symmetry.....101b

4.1.1 Susuceptibility Cusp Temperatures vs. Composition..108b

4.1.2a, b, Curie-Weiss θ vs z in $(AgIn)_{1-z}Mn_{2z}Te_2$.....110b

4.1.3 Curie-Weiss θ vs Temperature in $Cd_xZn_yMn_zTe$.....111b

4.1.4 Curie Constant (C) vs. z in $(AgIn)_{1-z}Mn_{2z}Te_2$.....111b

4.1.5 Optical Aiming Points in $Cd_{2x}(CuIn)_yMn_{2z}Te_2$.....113b

4.1.6a, b, Double Quantum ESR Transition.....115b

4.2.1a Planes in the Chalcopyrite Structure.....118b
4.2.1b The Stannite Structure.....118b

4.2.2a, b, Possible Stannite-Like Ordered Structures.....120b

T4.3.2 Important Parameters of MnTe and $MnTe_2$.....124b

4.3.1 Correction to $(AgGa)_{1-z}Mn_{2z}Te_2$ Phase Diagram.....126b

4.3.2 Susceptibility of $(AgGa)_{1-z}Mn_{2z}Te_2$ z=0.40.....127b

4.3.3 Susceptibility of $(CuIn)_{1-z}Mn_{2z}Te_2$ Samples

4.3.3a, b, $(CuIn)_{1-z}Mn_{2z}Te_2$ z=0.50 Q400.....129b
4.3.3c, d, $(CuIn)_{1-z}Mn_{2z}Te_2$ z=0.50 LTA150.....132b
4.3.3e, f, $(CuIn)_{1-z}Mn_{2z}Te_2$ z=0.50 LTA100.....132c

4.3.3 Susceptibility of $(AgIn)_{1-z}Mn_{2z}Te_2$ Samples

4.3.4a, b, $(AgIn)_{1-z}Mn_{2z}Te_2$ z=0.33 Slowly Cooled.....134b
4.3.4c, d, $(AgIn)_{1-z}Mn_{2z}Te_2$ z=0.40 Slowly Cooled.....134c
4.3.4e, f, $(AgIn)_{1-z}Mn_{2z}Te_2$ z=0.50 Slowly Cooled.....134d

T4.3.1 Table of Expected Ordering Line Intensities.....135b

4.3.5 ESR of $(CuIn)_{1-z}Mn_{2z}Te_2$ z=0.50 Samples.....138b

4.3.6a, b, Temperature Dependent ESR of $(CuIn)_{1-z}Mn_{2z}Te_2$..139b

4.3.7a, b, Temperature Dependant ESR of $(AgIn)_{1-z}Mn_{2z}Te_2$..141b

4.3.8a, b, Temperature Dependant ESR of $(AgGa)_{1-z}Mn_{2z}Te_2$..141c

4.4.1 X-ray and Neutron Structure Factors vs. z.....146b

4.4.2 Neutron Diffraction Pattern for $(AgGa)_{1-z}Mn_{2z}Te_2$...148b

4.4.3 X-ray Diffraction Pattern for $(AgGa)_{1-z}Mn_{2z}Te_2$.....148c

4.4.4a, b, Neutron and X-ray Patterns $(AgGa)_{1-z}Mn_{2z}Te_2$....148d

4.4.5a, b, Fit to $(AgGa)_{1-z}Mn_{2z}Te_2$ z=0.25 Diffraction.....156b

4.4.6a, b, Fit to $(AgGa)_{1-z}Mn_{2z}Te_2$ z=0.33 Diffraction.....156c

4.4.7a, b, Fit to $(AgGa)_{1-z}Mn_{2z}Te_2$ z=0.40 Diffraction.....156d

4.4.8 Difference Plot for $(AgGa)_{1-z}Mn_{2z}Te_2$ z=0.25 Fit....158b

4.4.9 Anionic Displacement Model.....163b

4.4.10a, b, Fit to Displacement Model.....164b

4.4.11 Eskebornite Structure.....166b

4.4.12 Fit to Octahedral Site Model.....167b

4.5.1a, b, Susceptibility of $(AgIn)_{1-z}Mn_{2z}Te_2$ z=0.50.....171b

T4.5.1 Table of Susuceptibility Fitting Parameters.....174b

4.5.2 Fit to Static Susceptibility of $(AgGa)_{1-z}Mn_{2z}Te_2$

4.5.2a, b, Fit to Susceptibility $(AgGa)_{1-z}Mn_{2z}Te_2$ z=0.25..183b

4.5.2c, Fit to Susceptibility $(AgGa)_{1-z}Mn_{2z}Te_2$ z=0.33.....183c

4.5.3d, Fit to Susceptibility $(AgGa)_{1-z}Mn_{2z}Te_2$ z=0.40.....183d

4.5.3 Magnetic Response Function.....184b

4.5.4 Field Cooled and Zero-Field-Cooled Susuceptibility.184c

4.5.5 Susceptibility Simulations $(AgGa)_{1-z}Mn_{2z}Te_2$

4.5.5a, b, Suscept. Simulation $(AgGa)_{1-z}Mn_{2z}Te_2$ z=0.25....185b

4.5.5c, d, Suscept. Simulation $(AgGa)_{1-z}Mn_{2z}Te_2$ z=0.33....185c

4.5.5e, f, Suscept. Simulation $(AgGa)_{1-z}Mn_{2z}Te_2$ z=0.40....185d

4.5.5g, h, Suscept. Simulation $(AgGa)_{1-z}Mn_{2z}Te_2$ z=0.40....185e

4.5.6 Fit to Field-Cooled Susceptibility.....186b

4.6.1 Mn-Planes Used in MFT Calculation.....193b

T4.6.1 Table of MFT Parameters.....194b

Table of Abbreviations
(in order in which they first appear).

DMS·····Dilute Magnetic Semiconductor
LTA·····Low Temperature Annealed
HTQ·····High Temperature Quenched

Q^2·····experimental quantity from diffraction experiment $=4\sin^2\theta/\lambda^2$

nd·····neutron diffraction

F^2·····scattering structure factor
FWHM·····Full Width at Half Maximum
HWHM·····Half Width at Half Maximum

ch·····chalcopyrite
DTA·····Differential Thermal Analysis
$\alpha,\beta,\gamma,\delta,\varepsilon$·····phase field labels
E_g·····electron crystalline energy gap

ESR·····Electron Spin Resonance
μ_B·····Bohr magneton
g·····spectroscopic splitting factor
ΔH_{pp}·····peak to peak width of derivative ESR line

h_{pp}·····peak to peak height of derivative ESR line

MES·····Mössbauer Effect Spectroscopy
δ·····Mössbauer center shift (chemical isomer shift)
Δ·····Mössbauer quadrupole splitting
EFG·····Electric Field Gradient

χ·····static magnetic susceptibility ($\chi(0)$)
SQUID·····Superconducting Quantum Interference Device
T_c·····magnetic transition temperature
T_n·····antiferromagnetic transition temperature
C·····Curie constant
θ·····Curie-Weiss temperature
D·····temperature independant susceptibility
fc·····field-cooled susceptibility
zfc·····zero-field-cooled susceptibilty

T_d·····group of symmetry operations of the tetrahedron
O_h·····group of symmetry operations of the octahedron

AgGa·····$(AgGa)_{1-z}Mn_{2z}Te_2$
AgIn, CuIn·····$(AgIn)_{1-z}Mn_{2z}Te_2$, $(CuIn)_{1-z}Mn_{2z}Te_2$

t_2·····the 3 d orbitals which belong to the same irreducible representation of T_d as the p orbitals (d_{xy}, d_{yz}, d_{xz})

e·····the 2 non-t_2 d orbitals (d_{z^2}, $d_{x^2-y^2}$)

$^6A_1$, $^4T_1$·····crystal symmetry labels of electronic states (see below).

10Dq·····crystal field splitting of the d orbitals

The energy units cm^{-1} are related to eV through the relation $E=hc/\lambda$ i.e. $E(cm^{-1})=8,065*E(eV)$.
Typically 10Dq = 10,000 cm^{-1}= 1.23 eV.

The nomenclature for the group theoretical considerations is as follows. In a symbol such as $^6A_1$, the superscript gives the spin multiplicity, and the letter indicates the dimensionality of the irreducible representation of the symmetry group of the tetrahedron to which the state belongs. 'A' signifies uni-dimensionality whereas levels bearing a 'T' belong to three-dimensional irreducible representations. The subscripts indicate the character that the representation posseses in the class of the principal rotation axis. A subscript of 1 indicates the character to be +1 a subscript 2 indicates a character of -1.

1.0) Introduction

This thesis consists of a study of the materials science and physical chemistry of a specific class of diluted magnetic semiconductor (DMS) alloys which are based on chalcopyrite structure compounds. The underlying approach is one of comparison between the manganese and iron containing systems in the context of the possible crystallographic ordering which these systems can support.

Chapter 1 constitutes a very brief summary of semiconducting materials which places DMS in the context of semiconductor physics. Also summarized are some aspects of the chalcopyrite structure semiconducting compounds and DMS materials. A brief discussion of the important differences between the manganese and iron ions themselves, as well as postulated properties of the materials to be studied in this report is also included.

Chapter 2 briefly introduces the experimental techniques which were utilized in the course of this research. The techniques are presented with an emphasis on their important aspects which are required for the correct interpretation of the experimental results. In some cases, specific details of the measurements are dealt with.

Chapter 3 contains a brief discussion on the observed solid-solutions of chalcopyrite iron containing DMS. Some preliminary results on various chromium and iron-containing systems are given, as well as the detailed results obtained on the $CuIn_{1-x}Fe_xS_2$ system.

Chapter 4 includes a summary of the results on the

manganese-containing chalcopyrite-based alloys pertaining to the possible crystallographic ordering of the manganese ions. The rest of the chapter concerns an in-depth study of selected materials suspected to be manganese-ordered.

Chapter 5 represents an attempt to summarize all the above results in a coherent way, and suggest possible avenues for further research.

In the following text, the liberty is taken of utilizing the chemical abreviations such as Mn and Fe, to represent the elements.

1.1.1) Semiconducting Materials and DMS

The term 'semiconductor' has come to mean virtually any form of condensed matter which exhibits a small gap between its conducting and non-conducting electronic states. Under this definition, many liquids [1] and certain biological materials can be called semiconductors.

Of the conventional crystalline semiconductors, a progression in complexity which closely coincides with the chronological order of the onset of research interest in the materials can be seen. In fact the possibility of semiconductor behaviour in the I-III-VI_2 compounds was first considered in 1954 [2], two years before the awarding of the Nobel prize for the transistor, however research interest in those materials grew at a later time. In the short time since, considerable work has been done and there are already books [3] [4] and review articles [5] written on the subject of the semiconducting ternary and multinary compounds.

The sequence of complexity in the adamantine systems is constrained by the fact that an average of four electrons per site is needed in order to fill the tetrahedral bonds:

Element Group	Example
IV	Ge
III V	GaAs
II IV V_2	$CdGeP_2$
II VI	CdTe
I III VI_2	$AgInTe_2$

The case of the diamond structure elements (Si and Ge) is clear since each atom already has the correct valency of 4. In the cases of the zincblende or wurtzite compounds (II-VI and III-V), the average valency is also 4 and each atom of one group is tetrahedrally bonded to 4 atoms of the other group in which case adjacent atoms can always be paired together into charge balanced units. The next step in complexity from the binary compounds are the I-III-VI_2 and II-IV-V_2 materials. The dominant structure exhibited by these materials is named after the mineral chalcopyrite $CuFeS_2$, and is diagrammed in fig. 1.1. In this structure, charge balanced tetrahedra consisting of equal numbers of each type of cation can be seen to exist.

DMS materials can be exemplified by the solid-solutions of compound semiconductors with magnetic materials such as MnTe, FeS and $CuFeS_2$, as illustrated in the following:

DMS Group	Example
$II_{1-z}Mn_zVI$	$Cd_{1-z}Mn_zTe$
$II_{1-x}Fe_xVI$	$Hg_{1-x}Fe_xSe$

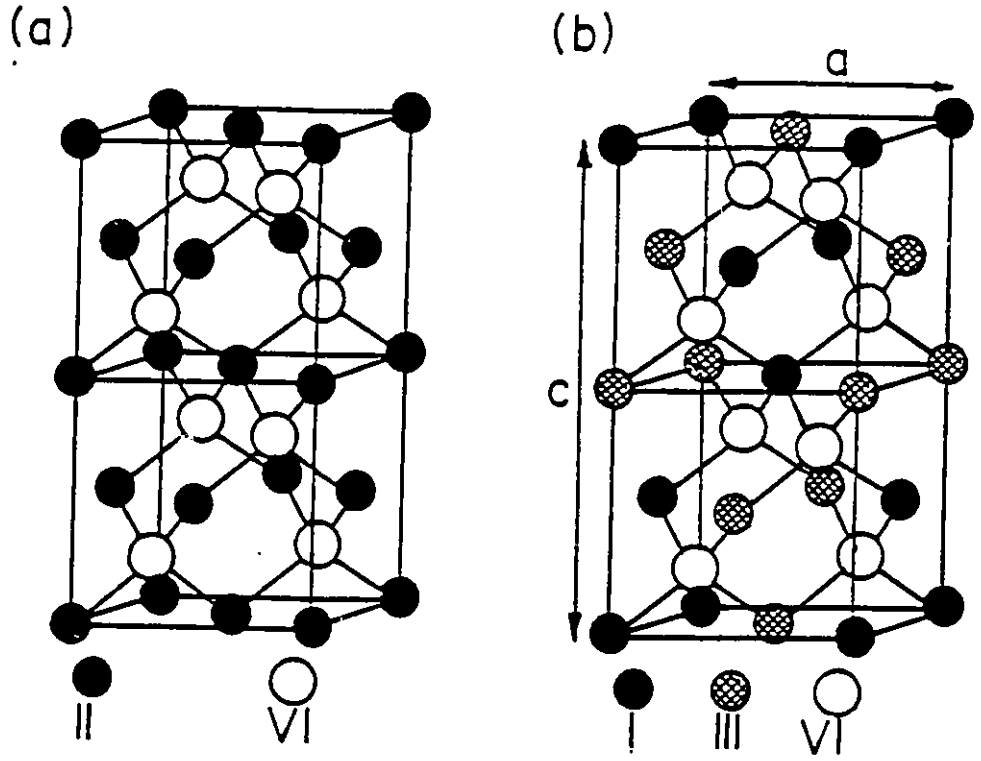

Fig.1.1 The chalcopyrite structure.
The conventional unit cell of the chalcopyrite structure is illustrated in fig. 1.1b. Two zincblende unit cells stacked in the c-direction are given in fig. 1.1a for comparison purposes. The diamond structure occurs if all sites in either of the two figures are occupied by the same type of atom. The tetragonal lattice parameters 'a', and 'c' are shown in 1.1b.

DMS Group	Example
$(I\ III)_{1-z}Mn_{2z}VI_2$	$(AgGa)_{1-z}Mn_{2z}Te_2$
$I\text{-}III_{1-x}Fe_xVI_2$	$CuIn_{1-x}Fe_xS_2$

Most of the work done on DMS to date has involved primarily II-VI compounds alloyed with Mn. Relatively little work has been carried out on Fe-containing DMS. Indeed in a 60-page review article from 1984 [6], Fe is barely mentioned. Part of the reason for this is that in the earliest work it was noticed that even small amounts of Fe spoiled what were commmonly held as "desirable" characteristics of the host semiconductor. For example, 10^{-4} molar Fe makes the otherwise orange crystals of $CuGaS_2$ virtually black [7] thus ruining its optical transmission. Interest in the Fe containing systems is however one of the most recent trends in DMS.

Since DMS systems are solid solutions, they introduce the possibility of band-gap and lattice parameter tailoring by alloy composition, one Mn-DMS has already found application as such in the fabrication of a yellow LED [8]. The general interest in DMS stems however in their magnetic properties. This is because the magnetism affects the optical and transport properties of the materials in novel ways, such as through the sp-d interaction or through localized magnetic ion states which are resonant with the delocalized band states of the solid. The by now classic effect of giant faraday rotation, first obtained in $Cd_{1-z}Mn_zTe$, is one example of the former phenomenon and several review articles [6] and books [9], [10] discuss such properties.

Recent advances have led to a bewildering variety of new

results in the field of DMS. A brief survey of the most recent research would include that of magnetic polarons [11], the magnetic field, or concentration induced metal insulator transition [12] and the effect of the giant spin-splittings on the conductivity and anomalous magnetoresistance of the materials [13]. The role of resonant donor d-levels on the peculiar transport properties of some Fe containing systems has been studied [14], and HgSe:Fe has been shown to be a superconductor [15]. Finally, the predicted existence of a field-induced typeI-typeII superlattice transition has been demonstrated in ZnSe-$Zn_{1-x}Fe_xSe$ [16].

1.1.2) Fe and Mn-Containing Chalcopyrite Semiconductors

The richness of physical behaviour in the currently studied DMS is apparent from the previous section, however the increase in complexity of non-magnetic compound semiconductors is also associated with new effects and potential new applications. Some of the possibilities afforded by the chalcopyrite compound semiconductors (I-III-VI_2 and II-IV-V_2) involve non-linear optical applications, visible and IR light emission and detection, and solar energy conversion [3]. Some of these compounds can be grown p-type which enhances their possible uses in conjunction with heterostructures. Other interesting features of these materials involve the effects on the band structure due to the non cubic symmetry and the mixing of noble-metal d-levels into the energy bands [17].

Although the chalcopyrite compounds have been reasonably well characterized, chalcopyrite-based DMS have been much less

intensively studied. The DMS of predominant interest in this report are based on the I-III-VI_2 stoichiometries and are illustrated in the table of DMS above. As in the case of the previously described DMS, such materials have all of the interesting features of the parent compounds in addition to the many new properties due to the presence of the transition metal ions.

The possibility of crystallographic ordering of the magnetic ions within these materials is one prominent new feature of these DMS which sets them apart from the more conventional materials. Although less has been attempted with Fe-DMS, evidence for Mn ordering has already been seen in the chalcopyrite based systems (see chapter 4). In contradistinction, the zincblende DMS support only random replacements of magnetic ions on the cation sublattice.

One effect which can result from ordering within DMS has recently been suggested by Shapira [18] and by Wolff [19]. This is the possibility that ordered DMS could possess high temperature (77 K) bound magnetic polarons. Polarons are ferromagnetic alignments of the local moments in the lattice, and have been seen only at very low temperatures [20]. The ferromagnetic interaction in bound polarons is mediated via bound impurity electrons. A material exhibiting such structures at high temperature could have very useful magneto-optical properties, particularly a strong enough Faraday effect to be used as an epitaxial (thin-film) optical isolator. The type of ordering required in these cases is one in which the resulting inter-magnetic ion lattice interactions

are weak, only then could the ferromagnetic polaron-forming interaction dominate the strong AF inter-ion exchange. One way to achieve such a configuration is in the case where there are no magnetic nearest neighbour pairs, and could in principle be achieved with magnetic ion concentrations up to and including z=0.25 in our materials. This possibility will be investigated in chapter 3.

The possibility of ferromagnetic behaviour in DMS is also of academic interest because of its rarity. Indeed an application of the Goodenough-Kanamori rules [21] indicates that it is probably impossible to attain ferromagnetic spin structures within the adamantine structure materials via the more direct magnetic ordering processes. This is due to the preponderance of antiferromagnetic superexchange channels in the adamantine (tetrahedral) bonding arrangement. Indeed all the known adamantine DMS have dominant AF inter-moment exchange interactions. In more complicated structures the possibility of ferrimagnetic DMS occur, and this is being investigated by a few groups including Prof. Woolley at Ottawa.

Other aspects of DMS which are of interest will be presented in the context of the chapters in which they appear. In the next section, some simple comparisons between the Mn and Fe-containing I-III-VI_2 systems to be studied in this report will be made on the basis of the magnetic ions themselves.

1.2) Preliminary Observations on Mn and Fe Ions

Mn has a uniquely stable 2+ chemical ionization state and Mn-DMS are characteristic of the Mn^{2+} chemistry and magnetism. Fe-containing DMS include the possibilities afforded by the two ionization states (2+ and 3+) of Fe, however Fe is generally more difficult to incorporate into semiconducting hosts than Mn. In particular although Fe^{2+} has an ionic radius very similar to that of Mn^{2+}, its miscibility in appropriate II-VI DMS is generally an order of magnitude less than that of Mn^{2+} [ref 6, p.4]. Some examples are $Hg_{1-x}Fe_xSe$ and $Hg_{1-x}Fe_xTe$ which exist as single phases only up to x=0.12 and 0.06 respectively [22] [23], while the Mn-containing counterparts have solubility limits above z=0.5 [3]. $Cd_{1-x}Fe_xSe$ has a solubility limit of x=0.15 [24] while $Cd_{1-z}Mn_zSe$ has a limit of 0.6 [25].

In the Mn and Fe derived DMS based on $I\text{-}III\text{-}VI_2$ chalcopyrites, one would expect to be concerned with the Mn^{2+} (a fortiori), and Fe^{3+} states. Some immediate differences between the Fe^{3+} and Mn^{2+} states in such crystals can be hypothesized. Firstly we note that Fe^{3+} has the correct ionization state to substitute the group III element whereas Mn^{2+} must substitute, on average, equal amounts of group I and III elements if it is to maintain the 4 electron per site criterion for adamantine bonding. A proposition of Garbato et al. [26] (see also section 4.2) takes this to its logical extreme by proposing that in order to avoid the formation of donor and acceptor states which lead to an increase in the free energy, not only average but also local electron balance

should be maintained. This will be discussed further in section 4.2.

In the I-III-VI_2 compounds, a predominant amount of sp^3 and/or $s(d\text{-}t_2)^3$ hybridization occurs. The atomic orbitals which are the obvious candidates for forming such hybrid ligands in the solid are the I $3d(t_2)4s4p$, III 5s5p and VI 3s3p. In the most naive picture, one could say that the ionization states I^{1+}, III^{3+}, and VI^{2-} imply a total of 4 shared valence electrons per site which then occupy the sp^3 ligands formed predominantly of a mixture the atomic s and p-like orbitals. The behaviour of Mn and Fe ions in this milieu must be expected to be qualitatively different.

The distribution of atomic electron levels gives an idea why this is so. A half-filled d shell is able to decrease its Coulomb energy via intra-d-orbital exchange by orienting all five electrons spin up. This is the fundamental mechanism behind Hund's rule relating to spin, by which electrons are added to a shell in such a way as to maximize the total spin consistent with the Pauli exclusion principle. In this way the Mn atom has configuration $3d^5 4s^2$ and not $3d^7$, and the Mn^{2+} $3d^5$ state is low in energy. The fact that the hypothetical Mn^{3+} $3d^4$, and Mn^{1+} $3d^6$ states are energetically far removed from the ground state, suggests that the accessable bonding states in the case of Mn within a nearly cubic environment would be predominantly s-like and arise from the empty 4s states of Mn^{2+}.

In the case of atomic Fe, which has one more electron than Mn, the atomic 4p states are higher than the next

available 3d states so that the 'extra' electron must break the intra-d exchange symmetry despite the consequent increase in Coulomb energy. In this way the ground state Fe configuration is $3d^6 4s^2$, and not $3d^5 4s^2 4p^1$. This suggests (pending an analysis or measurement of the crystal field splittings) that we could expect that the energetically accessable electronic bonding states in the vicinity of the Fe^{3+} ion within the I-III-VI_2 crystal, to be s and d-like. The differences between Mn and Fe can be seen from a different perspective in appendix 1, where their Racah (electron repulsion) parameters are compared.

Hence following the above simple thinking, we could expect important differences between the behaviour of Fe^{3+} and Mn^{2+} (S-state) ions imbedded in an adamantine structure. In the particular cases of Mn and Fe in I-III-VI_2 materials, the Fe would be expected to substitute for one particular cation whereas the Mn would not. Also, the Fe d-levels are expected to interact with the bands more than Mn d-levels would. These considerations will have important consequences for the exchange mechanisms, d level delocalization, crystallographic ordering, and magnetic properties of the materials.

In this thesis we will be concerned with the above differences as well as others due to the host lattice itself. It is known that the interactions between the host lattice and the magnetic ions are also needed in order to explain the relative behaviour of the Mn and Fe-based DMS. Indeed the relative differences of 20% in the atomic parameters of Mn and Fe (see app.1) do not, by themselves explain the order of

magnitude differences in the behaviour of some of their respective DMS [27]. Such considerations also depend critically on possible crystallographic ordering in the materials.

Many researches are carried out on DMS materials of very low magnetic-ion concentration. This allows for the easiest production of mono-crystals, and provides access to some of the most interesting physical properties of DMS. Much of the research in this paper concerns the determination of the basic materials science of a few new DMS, and as such largely relates to ascertaining accurate solubility limits and crystallographic data from the polycrystalline samples.

2.0) Experimental Techniques

This chapter is concerned with the description of the experimental techniques applied in the course of this research. These are; sample fabrication, x-ray and neutron diffraction, differential thermal analysis (DTA), optical absorption, electron spin resonance (ESR), Mossbauer effect spectroscopy (MES), and SQUID magnetometry. Since the techniques are well-known and a detailed description of the theory behind their operation can be found in textbooks, only a very brief introduction to the techniques will be presented. The discussion presented in this chapter will elaborate on the important aspects of the measurements which are especially pertinant to the present research.

Each of these techniques individually merit years of study in their own right however only a relatively small amount of time could be spent on any particular measurement technique during the course of this research. For this reason extra care was taken in order not to abuse the data collection or analysis, and the expertise of the various professors who maintain each apparatus and specialize in the measurement technique was instrumental in achieving this goal.

Despite the differences in the measurement techniques many similarities and inter-relations will be seen. For example; experimental lineshape analysis is an important and similar feature of the x-ray and neutron diffraction, Mössbauer, and ESR measurements, and the magnetic susceptibility can be directly related to the ESR line shape data. Also the Debye-Waller factor and presence of recoilless

interactions will be seen to play equally important roles in both the diffraction and the Mössbauer measurements.

Materials used in this report were fabricated in the form of polycrystalline 1 or 2 gram ingots prepared from the elements. The preparation technique was one of 'melt and anneal' whereby stoichiometric amounts of elements, weighed to ±.004 g accuracy were placed into quartz ampules, sealed with an oxy-acetylene torch under vacuum (10^{-4} Torr.) and heated to 1200°C over a period of approximately 2 hours. The samples were kept at 1200°C for various times depending on their composition with a typical time being 30 minutes. The cooling from the melt also depended on the specific sample however typical samples were cooled by switching the furnace power off. Under these circumstances, the samples cool to room temperature over about 6 hours.

The samples are generally not expected to be in equilibrium after the above treatment, and in some cases would not be expected to be homogenous. In order to ensure homogeneity, they were annealed at relatively high temperature in their initial quartz ampules or in new ampules similar to those used in the melting, as the case required. The subsequent heat treatment after this 'homogenizing' step, can have profound effects on the sample. Samples were either brine-quenched, or slowly cooled, or annealed further at low temperature depending on which part of the phase diagram or sample condition was to be investigated. The conditions of the samples have in some cases been found to be highly dependant on the exact details of the heat treatment, for

example some samples which were annealed at low temperature displayed metastability and subsequently would not achieve equilibrium characteristic of the low-temperature phase if they were cooled too rapidly from the initial, high temperature (homogenizing) anneal.

Specific tricks which were required in order to produce the samples are as follows. For the Mn-containing materials, it was found necessary to 'carbonize' [28] the interior of the quartz ampules to prevent the deterioration of the quartz tubing at high temperature. This is due to the fact that the electrolytic Mn used in the sample fabrication is α-phase which is prone to surface oxidation. The Mn-oxide reacts with the quartz at high temperature and is suspected to assimilate carbon from the coated tube into the samples as well [29]. In the case of this research, it was often found upon examining the inside of the quartz tubing (after extracting the sample) that the carbon coating remained as shiny and mirror-like as before the heat treatment, thus the assimilation of carbon is not suspected to be a significant effect in the Mn-containing alloys used in this report.

For the sulfides, a system was sometimes employed to agitate the ampules while at high temperature. This consisted of a furnace top-mounted motor, either vibrating or rotating the samples via an interconecting quartz tube. From the experience gained in making the sulfide samples, it seems that the use of this agitation decreases the chance of blow-ups.

The amount of handling of the finished samples was kept to a minimum in order to decrease the chance of surface

contamination. Samples were often powdered in preparation for measurement by the use of high-quality ceramic mortars and pestles. The various measurements applied to the samples are described in the following sections.

2.1) Diffraction Techniques

X-ray diffraction was proposed by von Laue, and demonstrated by Knipping and Friedrich in 1912. It is undoubtedly the single most powerful measurement technique of materials science. Neutron diffraction from crystals was first demonstrated by Elasser in 1936 but the application of the technique to materials science really started around 1950. Neutron diffraction has proved to be instrumental in the determination of magnetic ordered structures.

There are many relatively recent advances in these fields provided both by new beam sources and new detector instrumentation. For example, synchrotron 'wigglers' and 'undulators' are being used for the production of x-rays and synchrotron pulsed neutron beams are produced through the nuclear spallation process. These have given rise to variations and improvements on the basic diffraction theme. One example of this is 'small angle scattering' (SANS for neutrons and SAXS for x-rays) which provides direct measurement of microstructure.

X-ray and neutron diffraction are the critical techniques which were used in assessing the nature of the materials in the present research. The measurements utilized the standard applications of Bragg diffraction and provide

direct information on the crystal structure of the materials. The factor which links the diffraction to the exact positions of the various atoms in the unit cell is the structure factor and is given by;

$$F_{hkl} = \sum_j \exp\,[if_j(hx_j + ky_j + lz_j)] \qquad (2.1.1)$$

where the summations are taken over all the atoms in the unit cell, h, k, l are the Miller indices of the reflection, x_j, y_j, z_j are the positions of the j^{th} atom and f_j is its scattering factor. The structure factors for the various reflections are actually the Fourier coefficients of the mean potential seen by the diffracting particles when expanded as a series in the reciprocal lattice vectors. The scattering factors (f_j) are known in the terminology of scattering theory as 'scattering lengths' and are related to the scattering cross sections (σ) via:

$$\sigma = 4\pi f^2 \qquad \text{(s-wave scattering)}$$

The intensities of the diffraction maxima are derived from:

$$I = I_o \int d\Omega (d\sigma/d\Omega) \qquad (2.1.2)$$

and are proportional to F^*F [30] (to be abreviated as F^2 in the following).

2.1.1) X-ray Diffraction

Powder x-ray photographs in the Debye-Scherrer geometry were utilized as well as diffractometer patterns. Only a few diffractometer patterns were obtained and these will be described as they are presented in the later chapters. The photographs will be described in this section, since most of

the x-ray data was obtained from them. The x-ray work was carried out under the guidance of Prof. Woolley.

18 cm. Debye-Scherrer photographs were taken predominantly on a Enraf Nonius Delft 'Diffractus 582' machine with additional photographs taken on two older Phillips x-ray apparatus. The films were developed by hand in the laboratory dark room. Powdered samples were mounted on greased, fused quartz filaments which were produced in the laboratory. In the cases where accurate lattice parameter measurements were required, a silicon or germanium standard was mixed with the sample. The absorption correction (similar to the Nelson-Riley function [31]) was then determined empirically by comparison with the known standard lattice parameter and this correction was subsequently applied to the sample. Film measurements were done on a 'Precision Tool and Instruments' vernier measuring bench.

The x-ray wavelength utilized was that of the $Cu_{K\alpha 1}$ transition, equal to 1.543A, while K_β radiation was shielded in the usual way with a Ni filter. This is the standard radiation used in powder photographs, however it has the drawback in the present case of being of a higher energy than the Kα absorption edges of some of the elements used in the samples. In particular Mn, Fe, S, and Cu all have their Kα edges at energies less than or equal to the diffracting radiation energy. This can lead to an increased diffuse background on the x-ray films and thus constrains the optimal exposure time of the samples to a small range between the developer-saturation time of the highly exposed structure

lines and the saturation time of the diffuse background level.

One possible alternative to the Cu Kα radiation is the Cr Kα (2.29A) radiation which would produce less background intensity by virtue of its longer wavelength (lesser energy), however this leads to a decrease in the number of the resulting high intensity reflections. Utilizing Cr radiation thus is not expected to lead to an overall improvement in the x-ray photographs and since a variable anode, or Cr-anode x-ray tube was not available, the use of Cr radiation was not attempted.

For the tetragonal samples two simultaneous equations are required in order to extract the two lattice parameters 'a' and 'c'. The equations are obtained as follows, writing the Bragg condition for the tetragonal case:

$$Q^2 \equiv \frac{4}{\lambda^2}\sin^2\theta = \frac{h^2+k^2}{a^2} + \frac{l^2}{c^2} \qquad (2.1.3)$$

$$Q^2 = N_1 A + N_2 C \qquad (2.1.4)$$

where θ is the measured quantity from the x-ray film, λ is the x-ray wavelength, A and C are the inverses of the squares of the lattice parameters, and the N values are the squares of the Miller indices as seen above, the equations from which the lattice parameters are obtained are defined as;

$$\Sigma Q^2 = A\Sigma N_1 + C\Sigma N_2 \qquad (2.1.5)$$

$$\Sigma Q^2 N_1 = A\Sigma N_1 N_2 + C\Sigma N_2^2$$

where the summations are taken over all data points. These equations are solved simultaneously to give the lattice parameters A and C, provided that the correct Miller indices are input with the experimental data (Q). In order to solve the equations a 'Basic' microcomputer program was written

which carried out the summations and calculated the resulting determinants. Since the c/a ratio of the samples could deviate significantly from 2, it was not generally a straightforward matter to correctly assign Miller indices to the lines. Line misidentification could be seen by the discrepancy between its expected Q as determined from the fit A and C values, and its experimentally measured Q, and verified simply by checking if the output parameters were drastically changed by the omission of the suspect line from the fitting. The correct Miller indices for the line were then found by an iteration of this procedure.

The precision of the resulting lattice parameters is limited by the accuracy of the line position measurement on the x-ray film. On the x-ray film, line broadening is manifested as a 'fuzziness' of the line and this was the most common accuracy-limiting factor in the measurement. Factors which lead to line broadening are generally related to lattice imperfections such as alloy broadening, phase non-equilibrium, or variations in stoichiometry. Other effects which yielded similar measurement limitations were due to the intrinsic c/a splitting of the lines and the $K\alpha_1$-$K\alpha_2$ radiation splitting, both of which sometimes resulted in the overlapping of two or more lines making their precise measurement impossible. Unfortunately, these effects are accentuated in the high angle reflections from which the most accurate lattice parameter information can be derived. A similar accuracy limiting factor intrinsic to the measurement occurs in the intensity envelope of the reflections (see eq.2.1.6). This envelope

function contains the Debye factor and the polarization factor, both of which diminish the overall intensity of the reflections as the diffraction angle increases. This will be seen in detail in chapter 3. The effect of the temperature factor can be important particularly for high angle reflections and since the calculation of this factor requires a knowlege of the average thermal displacement of the atoms, is difficult to account for precisely. A lack of knowlege of this factor can be circumvented by restricting the intensity analysis to the ratios of closely spaced lines, however this leads to the loss of any information imbedded in the absolute line intensities.

The atomic x-ray scattering factors which appear in the structure factor (2.1.1) are functions of the scattering angle [31]. For low angles the scattering factors are simply proportional to the atomic numbers of the elements, the proportionality factor being the classical electron radius r_o, i.e. $f_{x\text{-}ray} = Z \times 2.8178 \times 10^{-13}$cm. The angular dependance of the scattering factors must however be taken into account in any accurate analysis of x-ray intensity data. As will be seen in the following section, no simple relation between atomic number and low-angle scattering factor occurs in the case of neutron scattering, however the neutron scattering factors do not depend on scattering angle, and this leads to an over-all simplification in the neutron intensity analysis. The intensity of an isotropic powder in which the elementary crystals are small enough for extinction to be negligible, is given by [32];

$$I = I_o r_e^2 \frac{(1 + \cos^2 2\Theta)}{2} \frac{1}{16\pi r \sin^2\theta \cos\theta} \lambda^3 F_{hkl}^2 \frac{n}{V_c} D \, dV \qquad (2.1.6)$$

where I is the power in the diffracted cone per unit arc length intersecting a plane perpendicular to its axis, at a distance r from the sample. The terms in the equation are: I_o = intensity per unit area of the beam, r_e the classical electron radius = $7.9*10^{-26} cm^2$, 1+cos2Θ the polarization factor (with Θ the Bragg angle), $(16\pi r \sin^2\Theta \cos\Theta)^{-1}$ the Lorentz geometrical factor, λ the x-ray wavelength, F_{hkl} the structure factor, n the multiplicity of the reflection, V_c the unit cell volume of the crystal, D the Debye factor, and dV the volume of the diffracting powder.

In the diffractometer geometry in cases where absorption is negligible, dV can be taken as dV = S * t where S is the cross section of the incident beam and t is the thickness of the powder target. In cases where the sample is thick and/or absorption is important, an integration over the irradiated volume must be estimated in order to find an effective volume which depends on the absorption coefficient and density of the target.

Other results of interest concern the sources of broadening in the diffraction lines. These are generally related to some kind of randomness in the distribution of the scattering centers and include planar disorder i.e. randomness. Examples of this type of disorder are stacking faults and plane displacements in the normal direction. Such conditions are dealt with in detail in reference [32].

2.1.2) Neutron Diffraction

Neutrons of kinetic energy in the range 10 to 10^{-3} eV have wavelengths corresponding to 0.1 - 10 A. In particular neutrons which have the same temperature as the reactor moderator (300 K) are called 'thermal' neutrons and have energy $kT \approx 26$ meV and wavelength $\lambda \approx 2A$ (their velocity is of the order 2 km/s). Because they have wavelengths of the same order as lattice spacings, thermal neutrons can be used for Bragg diffraction in much the same way that x-rays can.

There are some important differences in these two types of diffraction however that arise from the differences in the interactions between the atoms and the diffracting particles. Neutron scattering can be seen to arise from the nuclear and magnetic scattering interactions associated with each lattice site, whereas x-ray diffraction occurs by way of the electron density there. The scattering factors for these processes are vastly different and result in correspondingly different behaviour. For example the magnitude of neutron scattering factors are not simply related to atomic size as in they are in the case of x-rays. Also, the scattering factors (f_j) utilized in the calculation of F^2 for neutron diffraction are the isotope and nuclear spin orientation averages which yield the coherent scattering cross section σ_c, whereas in x-rays the f_j are uniquely defined by the atomic number.

Two very important features of the thermal neutron isotope averaged scattering factors of the elemental nuclei are as follows; firstly, a few such as those of H, Li, V, Ti and Mn,

are negative. This is due to resonant scattering in which the intermediate state nuclei have energies close to those of a distinct excited nuclear state. The negative sign signifies a change of phase of the final state (scattered) neutron with respect to the initial state neutron. For the Mn-containing alloys under investigation, this leads to important differences in the experimental x-ray and neutron diffraction patterns which are dependant largely on the position of the Mn within the crystal structure, and hence provide important information regarding the Mn-ordering.

The second important aspect of the elemental neutron scattering factors is that some, for example In, Eu, Pa, have a large imaginary part, in particular this is true of ^{115}In, which constitutes 95% of the naturally occurring element. This signifies a high inelastic or absorptive component and makes difficult the nd measurement of several of the DMS alloys of interest. In particular the Cu-In and Ag-In alloy systems were not studied by neutron diffraction for this reason.

This is also true in the case of Cd[1] containing alloys due to the large reactive (capture) cross section of the Cd nucleus.

The magnetic contribution to the scattering of neutrons must be taken into account and results mathematically in much more complex diffraction relationships than occur in the consideration of x-ray scattering [33]. For example, neutrons

[1]other examples of efficient neutron absorbers are Pu, Hg, Ir, Dy, Gd, Pm, Sm.

can be spin-polarized by Bragg reflection from a saturated ferromagnet[2] in which case the spin orientation of the target atoms becomes important. The data analyzed in this paper was obtained for the case of unpolarized neutrons scattering from magnetically disordered materials, (ie materials above their magnetic ordering temperatures). Under these conditions the magnetic, and spin-flip contributions to the scattering affect only the height of the diffuse background and will not be considered further. This is also true of the diffuse or incoherent scattering component due to the random distribution of isotopes in the samples. For our purposes the neutron diffraction provides data which is treated similarly to the x-ray data yet provides complimentary information by virtue of the different scattering factors involved.

The intensity of the neutron diffraction peaks is given by:

$$I = k\, I_o F_{hkl}^2 \quad \frac{n\, D\, dV}{16\pi\, r \sin^2\theta\, \cos\theta} \qquad (2.1.7)$$

The similarity with x-ray line intensities can be seen by comparison with equation 2.1.6. In particular, for lines close together in the diffraction pattern, the structure factor and multiplicity dominate the expression for the ratio of intensities. Due to the fact that we will require a detailed analysis of nd reflection intensities over the full range of scattering angles, the full expression 2.1.7 will also be utilized. As indicated in the previous section, a simplifying feature of the neutron diffraction is that the

[2]Heusler alloy targets are utilized for this purpose.

neutron scattering factors are not functions of the scattering angle, however the temperature (Debye-Waller) factor must be considered. It should be noted that there is a small correction in the intensity relation due to the finite detector size which was purposely omitted in the analysis of chapter 4.

The experimental data collection was carried out at AECL Chalk River, by Dr. T. Holden and Dr. D. Noakes. The E3 diffractometer was utilized and it is described as follows:

The neutrons are thermalised in the reactor core and exit from the radial reactor tubes via the aluminum windows at the outer reactor casing. In order to achieve the required resolution, the beam must be carefully collimated both before and after monochromatization as illustrated. This is due to the fact that even if the polychromatic incident beam was perfectly collimated, a spread in the reflection angles (all satisfying the Bragg condition) would occur. Indeed the ultimate resolution (FWHM) as a function of the Bragg angle in the configuration illustrated (θ) is given by the Caglioti, Paoletti, Ricci formula :

$$FWHM^2 = U\tan^2\theta + V\tan\theta + W \qquad (2.1.8)$$

where U, V, and W are known functions of the angular divergences of the collimators, and monochromator.

Because the detection range is limited by the apparatus geometry to $2\theta \leq 110^{\circ}$, the wavelength must be chosen in such a way as to access the required range of the reciprocal scattering space (Ewald sphere) yet maintain a low enough

background at high angles to resolve the small Bragg peaks there. The wavelength selection is achieved by the monochromator which consists of a silicon prism at the location between the first two collimators. The wavelength is selected by utilizing the appropriate Bragg reflection from the silicon crystal. For the data obtained in this paper, the silicon 331 reflection was utilized to produce monochromatic neutrons of wavelength 1.3436 A. The beam path optimization was carried out on the E3 apparatus at the NRU reactor of Chalk River by Drs. T. Holden and D. Noakes.

A new 30 element detector array was installed on the E3 diffractometer prior to the measurement of our samples. The components of array consist of He^3 detectors and, due to their numbers, speed up the data collection process. At the time of this writing, the new DUALSPEC system was being installed at the NRU reactor, directly adjacent to the E3 setup. The new system will be available for use in the Winter of 1991.

In preparation for the experiment, approximately 12 g. of sample is powdered and placed in an aluminum cylinder which acts similarly to the sample filament in the Debye-Scherrer configuration. Indeed the neutron diffraction setup is basically an enlarged version of the x-ray camera.

The aluminum sample holder for the nd gives rise to a few diffraction lines in the experimental diffraction patterns and these must be excluded from the data. The gaps apparent on the nd patterns (figs 4.4.1) are due to the exclusion of the scattering angles corresponding to the aluminum reflections,

as well as due to an intermittent counter in the 30 element array. Although only a small total arc length of the pattern is lost due to these effects, this gives rise to some inaccuracies in the powder diffraction intensities and hence proved to be a problem in some cases.

2.2) Differential Thermal Analysis

A thorough description of the DTA technique can be found in [34]. The DTA apparatus used in this research (see fig 2.2.1) was built by Dr. M.Quintero and was modified in the course of this investigation by the addition of the amplification step illustrated. The DTA technique incorporates the use of a double-junction thermocouple which has one junction placed in the standard cell, and the other junction in the cell containing the sample to be studied. Both cells are subsequently placed in the furnace which then applies a smooth heating (or cooling) to the samples. Any material that undergoes a phase transition then experiences a change in its temperature by virtue of the associated specific heat anomaly (ex. latent heat) and produces a characteristic temperature difference (and therefore voltage) in the thermocouple. This 'difference' signal is plotted alongside an absolute temperature as measured by another thermocouple positioned near the location of the samples which provides a temperature calibration of the observed transitions. The estimated size of the temperature differences detectable by the Chromel-Alumel thermocouple in conconjunction with the amplifiers utilized in the apparatus is 0.02 C.

The sample cells were fashioned out of quartz tubing, with thermocouple wells created by pressing one heated end of the tube onto a countersunk hole in a graphite block. When properly executed, this procedure produced thin-walled thermocouple wells which provided good thermal contact with the sample which was subsequently sealed under vacuum inside.

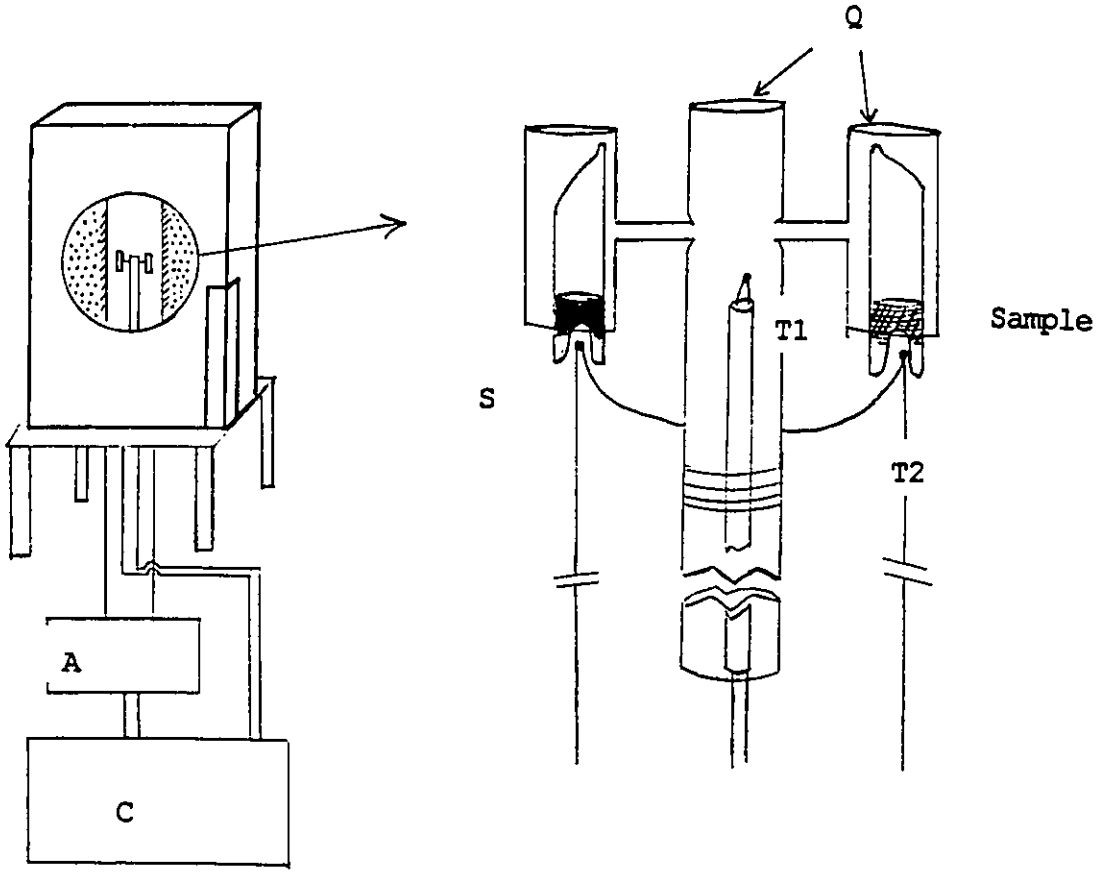

Figure 2.2.1 Differential Thermal Analysis Apparatus.

A diagram of the furnace and support stand is given on the left. The devices labelled A and C are repectively the amplifier and the chart recorder. The cutaway view magnified at right is a detail of the sample chambers (S), quartz support structure (Q), and thermocouples T1 and T2. T1 is the absolute temperature thermocouple and T2 is the double-junction 'difference' thermocouple.

The standard cell material was chosen to be Ag because it has a specific heat comparable to that of the samples and because it has a known (melting) transition temperature outside the range of interest for the samples yet against which the sample transition temperatures could be further calibrated.

Crystallographic, melting and magnetic ordering transitions have all been detected with this apparatus. Indeed a single calibrating DTA heating run of Fe powder was found to exhibit all three types of transitions. It can thus be seen how the information obtained from DTA facilitates the determination of the phase diagrams of the materials when used in conjunction with an appropriate characterization technique.

One important aspect of the DTA in this study is that most relatively low temperature (100 C) transitions were only detectable on heating the samples and were not seen on cooling. Thus samples whose low temperature behaviour was being investigated needed to be in crystallographic equilibrium at low temperature. This is due to the fact that it is easier to optimize and control the heating rate of the furnace rather than the cooling rate, and to the fact that the detection of a phase transition requires at least some of the material in the cell to actually change phase. The latter point is important for low-temperature phases (such as ordered ones), which require long times to form on cooling whereas they can be quickly destroyed by heating, it can thus be understood why many Low-T DTA peaks can only be seen on heating. For similar reasons it was found that an optimal heating rate exists at which the DTA peaks are sharpest. A

slower heating rate allows more material to undergo the phase change at the transition temperature however also allows equilibrium between the sample and standard to be reached thereby decreasing the DTA signal. The optimal heating rate was determined after several trials with the samples. Similar considerations explain why it is difficult to find vertical phase boundaries through DTA. In this case the DTA peak is smeared in temperature as can be seen by considering the phase boundary to be slightly broadened itself.

2.3) Spectroscopic Techniques

The spectroscopic techniques utilized in this research are varied and relate to very different physical processes and properties of the materials.

2.3.1) Optical Energy Gap Measurment

The measurment of the optical energy gap was performed under the guidance of Prof. Woolley, on the apparatus described in fig. 2.3.1. The Spex 1702 spectrometer was calibrated using a He-Ne laser. A 40W tungsten filament lamp was used as the light source for measurment and a 1P28 photomultiplier (PM) tube was used as the detector. Thin samples are required in order for the measurment to give accurate results and the samples for optical measurment were ground in the laboratary using a 1 micron abrasive on a suitable cloth covered grinding table. The thicknesses of the resulting irregular disk shaped samples were measured using a microscope outfitted with a calibrated fine focus and found to be in the range 70-200μm. Since the samples were polycrystalline and hence relatively fragile, it was found difficult to obtain consistently thin samples. The samples were subsequently mounted on the sample holder and any gaps which could allow light to pass directly to the PM were masked.

The theory required for the analysis and interpretation of the optical results is provided in [35]. The important aspects mentioned in that reference involve the form of the expected contributions to the absorption due to

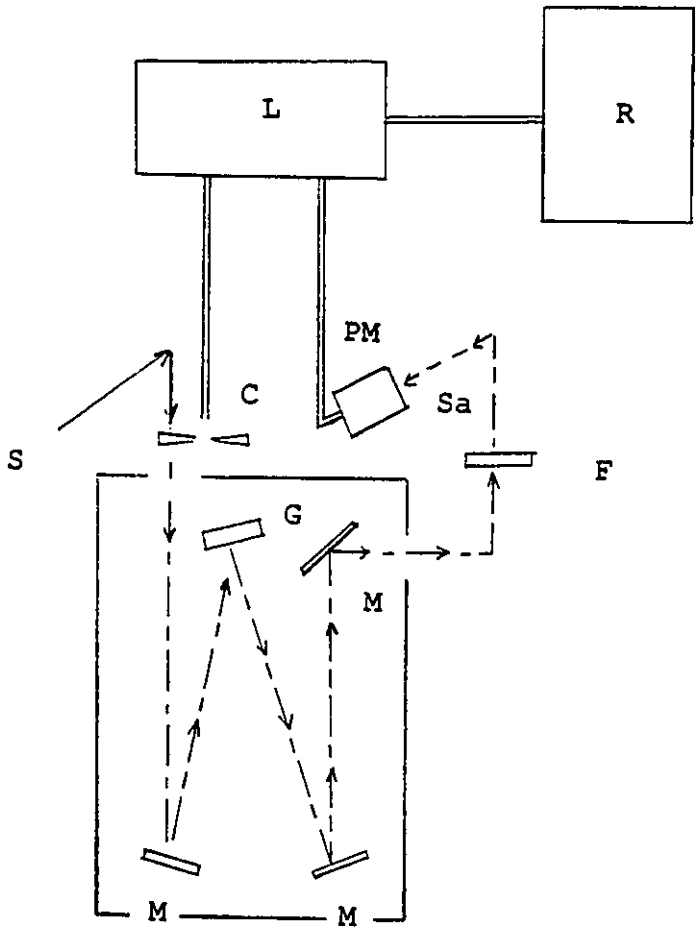

Figure 2.3.1 Optical Absorption Apparatus.

The diagram illustrates the juxtaposition of the light scource (S), mirrors (M), grating (G), chopper (C), sample (Sa), photo- multiplier (PM), phase-sensitive amplifier (L), and chart recorder (R). The filter (F) is required to attenuate higher order reflections from the grating.

polycrystalline effects and impurity scattering. The interband absorption coefficient, as a function of photon frequency is of the form

$$\alpha_b = (h\nu)^{-1}(h\nu - E_g)^n \qquad (2.3.1)$$

with n=1/2 in the case of direct, allowed transitions such as those found in the case of the materials of interest. Impurity scattering gives a contribution to the absorption coefficient of the form

$$\alpha_i = k_1(h\nu)^{-m} \qquad (2.3.2)$$

where m is determined empirically. The raw data consists of the ratio of the measured intensity (through the sample) and the incident intensity I/I_o. In order to extract accurate energy gap values from the absorption data, the impurity scattering contribution must be subtracted. This is accomplished by fitting the low-energy part of the absorption curve to the form (2.3.2) and subsequently subtracting this from the data over the full range of the measurements. This was found to yield graphs such as those of 2.3.2 in which the interband edge occurs at increasing energy and the polycrystalline scattering at decreasing energy. The resulting low-energy portion of the curves was closely linear and its (small) extrapolated value was subtracted form the total signal. Such sub-band enhancement of the absorption has been reported [35] to be due to polycrystalline effects. After this treatement, plots of $(\alpha h\nu)^2$ vs.$(h\nu)$ rendered good straight line portions from which the energy gaps were extracted as the x-axis intercepts. Some band-tailing was seen in the samples as can be seen on fig 2.3.2. This feature

Fig. 2.3.2 $(\alpha h\nu)^2$ vs. hv

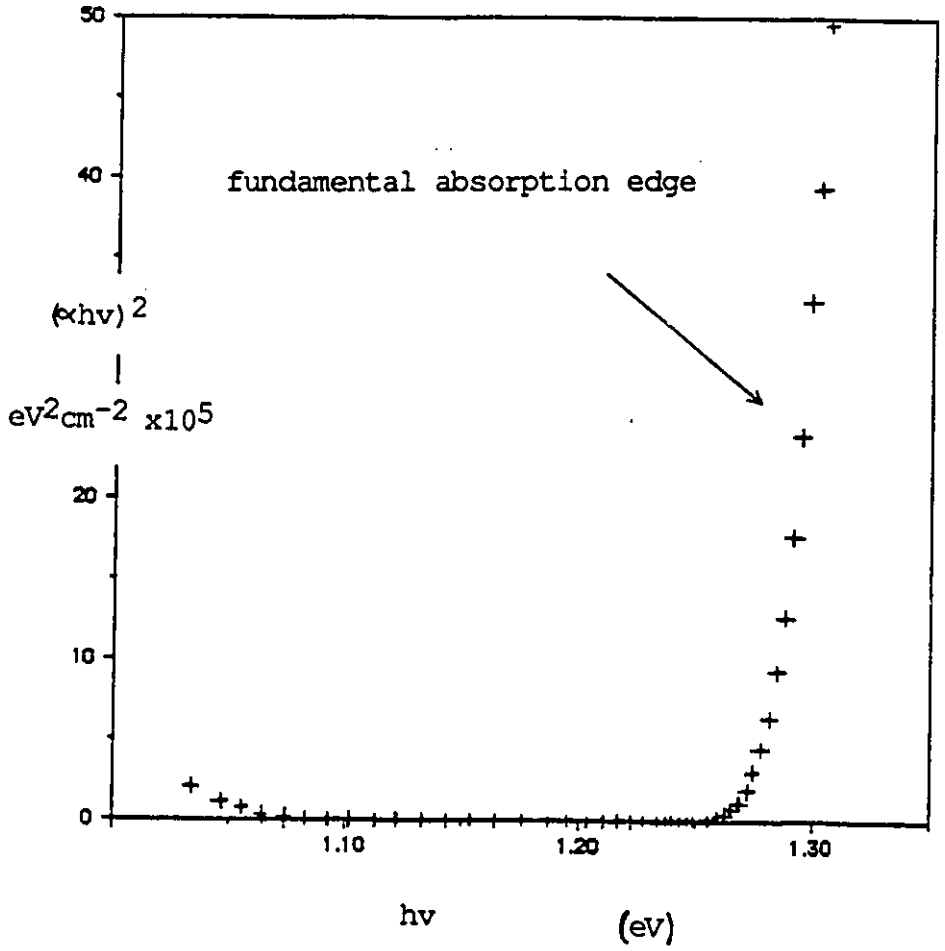

Fig. 2.3.2 Optical Absorption of $(AgGa)_{0.75}Mn_{0.5}Te_2$

The function graphed is $(\alpha h\nu)^2$ vs.hv. The optical energy gap is taken to be the energy axis intercept of the extrapolated straight-line section of the absorption edge. The increased absorption at low energy is due to residual impurity or grain boundary scattering. α is the absorption coefficient and is proportional to the logarithm of the inverse of the transmitted intensity.

of the optical absorption has been reported for many of the ternary and quaternary compounds [36], [37].

Another important aspect of the Mn-containing materials has been elucidated in [38] and is the narrow absorption band due to the Mn^{2+} ^6S $-^4T$ transition. The transition has an energy of 2.2 eV which is close to the E_g of the materials and can mask features of the band structure that would otherwise be seen in the absorption spectrum. This effect will be an important consideration in section 4.3.4.

All the measurments were carried out at room temperature however low-temperature measurements on related materials were made in the course of this investigation in association with Dr.Quintero [39] and will be quoted in this paper. For these measurments a CTI-CRYOGENICS model 21SC CRYODYNE cryocooler was used with a LAKE SHORE CRYOTRONICS drc-80c digital cryogenic thermometer/controller to control the temperature. The system operates by Joule-Thompson expansion of a self-contained He gas circuit.

2.3.2) Electron Spin Resonance

Electron Spin Resonance ESR was initiated around 1946 and was enabled by the wartime research on radar and related instrumentation. Since that time it has become an essential tool in chemistry, biology and condensed matter physics.

The presence of transition metal ions in the alloys allows the use of the ESR technique in their study. ESR provides information on the magnetic ion itself as well as on its crystalline and magnetic environment and so gives valuable information about the material as a whole. The ESR measurements reported in this study were carried out with the aid and guidance of the late Prof. Manoogian. Mdme. Lamarche, Joan Curry, and Bei Wah Chan helped very much by carrying out most of the measurements.

The measurement consists of detecting the fixed-wavelength microwave absorption of the sample as a function of the applied field, thereby sweeping over the resonance condition given by:

$$h\nu_i = g_i \mu_B H_i \qquad (2.3.3)$$

where h is Planck's constant, g_i is the 'spectroscopic g factor', μ_B is the Bohr magneton and H_i is the applied field. Eq. (2.3.3) gives the separations between members of a given multiplet caused by the field along the direction i. The g factor includes the effects of crystal-field splittings electron repulsion, and spin-orbit interaction and is in general obtained from the magnetic moment operator (L+2S). In the case of free ions under Russel-Saunders coupling, this procedure renders the Lande g factor. Such a treatment is

also appropriate to the Mn [40] and sometimes to the Fe ions in the crystal environments of interest:

$$g = 1 + (S(S+1) - L(L+1) + J(J+1))/2J(J+1)$$

For the case of free Mn^{2+} and Fe^{3+} ions, which are d^5 configuration S-state ions having no orbital angular momentum (L=0, J=S), the expected g value can be seen to be equal to 2. Indeed such a g value indicates that the angular momentum from which the magnetic moment is derived, is purely spin in origin. The same is not generally true for Fe^{2+} ions or for those crystalline states which retain angular momentum. This will be dealt with briefly in chapter 3.

In crystal lattices, the g value is a tensor and is defined in the relation between the angular momentum and the magnetic moment:

$$\mu = g\mu_B J \qquad (2.3.4)$$

however in the case of our axially symmetric materials, the 2 independant diagonal tensor components $g_{\parallel}$ and $g_{\perp}$, can be considered separately. Provided there are no internal magnetic fields, the g value of the S-state ions can be measured directly from the position of the -1/2 to +1/2 absorption maximum; $g = 0.7144\ \nu(\text{Ghz})/H_{max}(\text{kOe})$ as derived from (2.3.3). For powdered samples the g value anisotropy leads to asymmetries in the observed ESR lines.

The crystal field splittings of the energy levels in the solid lead to the fine structure transitions. This is shown in fig 2.3.3 which illustrates the ideal S=5/2 condition as well as the actual conditions seen in $CuGaS_2:Fe^{3+}$ [7]. The latter diagram was produced from the crystal field parameters

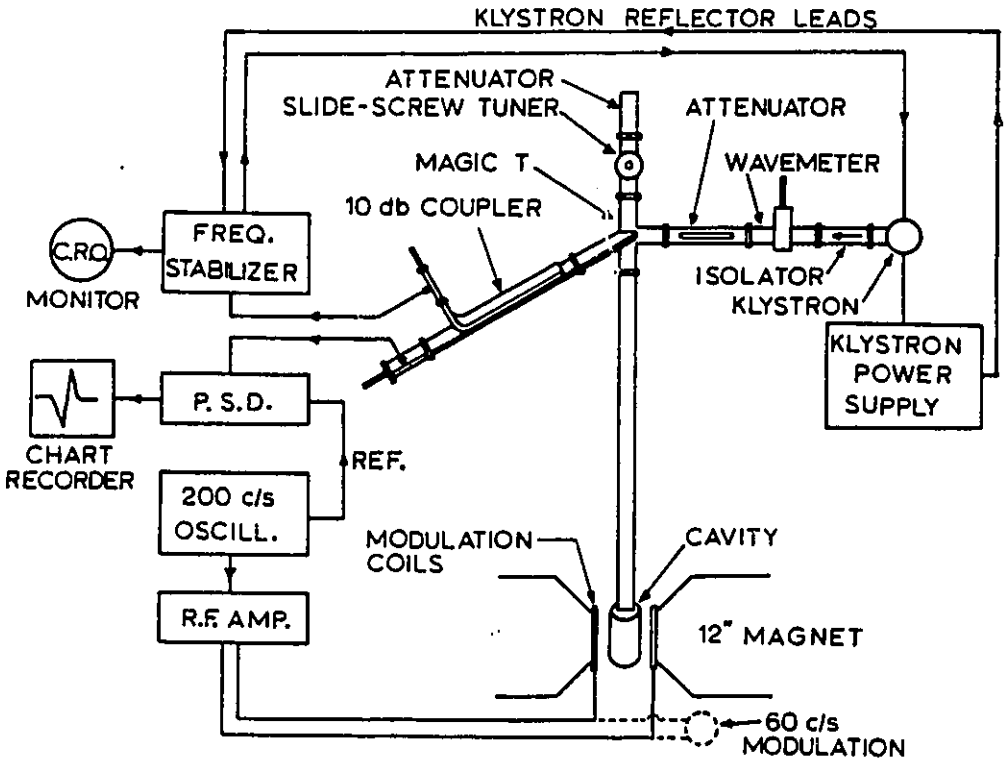

Fig. 2.3.3a Schematic diagram of the ESR settup.
This figure illustrates the basic components of the ESR apparatus utilized in the present research. Not shown on this diagram is the series of components associated with the AFC (Automatic Frequency Control) system which stabilizes the microwave frequency.

Figure 2.3.3b ESR Transitions in Fe-doped $CuGaS_2$.

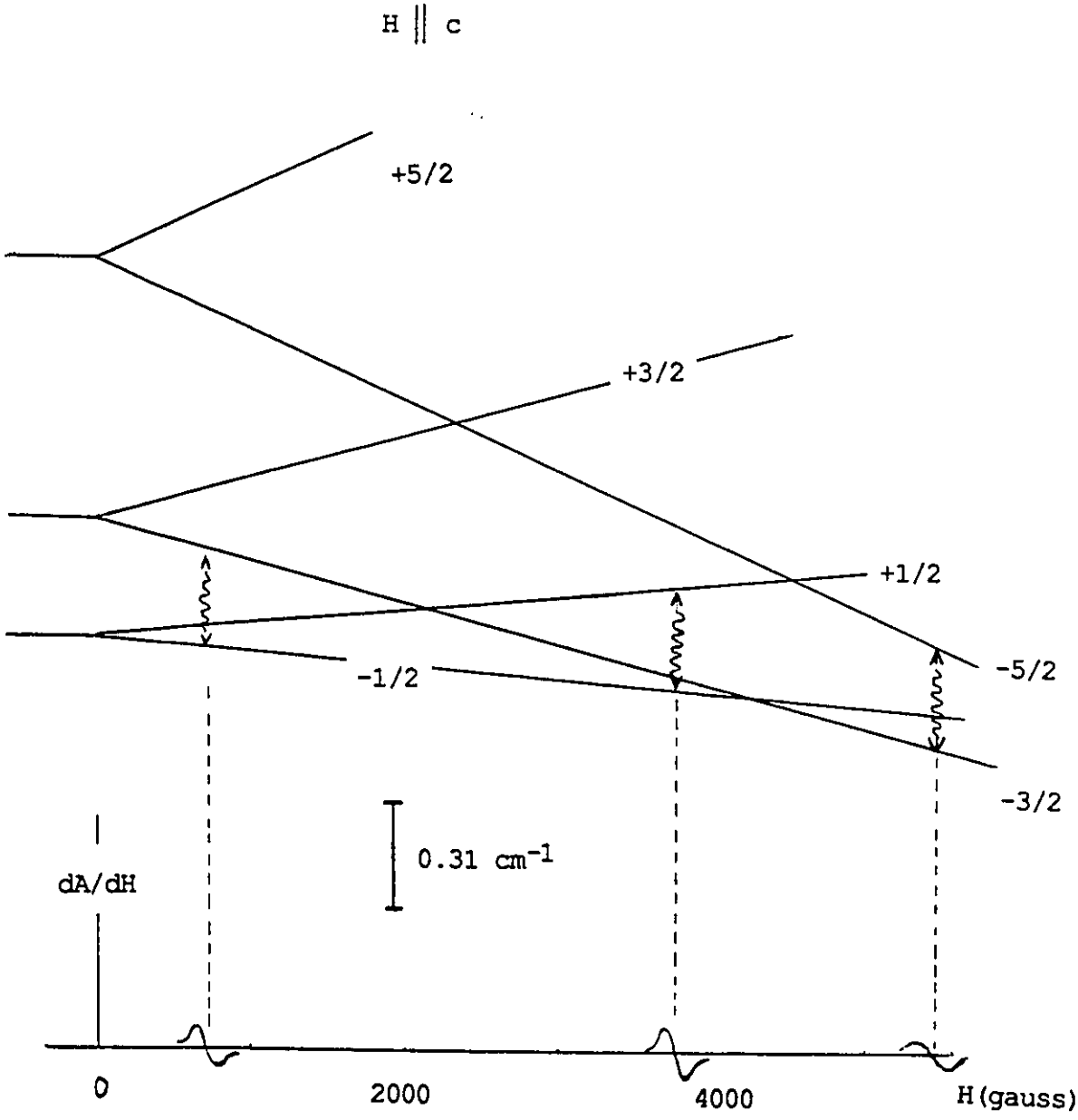

This scale diagram illustrates the ESR transitions and zero-field splittings of Fe^{3+} within the chalcopyrite structure material $CuGaS_2$. The crystal field parameters utilized are those given in [7]. The microwave energy illustrated corresponds to 9.5 GHz. Only the transitions visible over the available field range are shown. The behaviour of Fe^{3+} within the $CuInS_2$ system (see 3.2) is expected to be qualitatively identical to that illustrated.

(derived by ESR) reported in [7], and shows the fine structure transitions which are in principle attainable in our apparatus. It is clear from the slopes of the energy levels on the diagram that the higher m_s transitions are sensitive to random crystal fields, and that the -1/2 to 1/2 transition is totally insensitive to this effect. This can be seen by imagining perturbations in the zero-field splittings which would lead to a 'smearing' of the higher m_s transitions in the materials.

Indeed the ESR line width is an important parameter obtained from the data. Factors which affect the linewidth are of two types; inhomogenous, also known as 'spatial' broadening (such as the random crystal fields) which generally result in Gaussian line profiles, and homogenous or 'dynamic' broadening which can result in Lorentzian lines. In the case of homogenous broadening, the broadening mechanism is faster than the spin transition, in which case certain details of the underlying transitions are lost. This situation has a close analogy in Mössbauer measurements as will be seen in section 3.3.3.

Examples of homogenous broadening are spin-lattice relaxation, and dipole-dipole broadening which includes the critical broadening that occurs with the onset of a magnetic ordering transition. Inhomogenous effects are alloy or strain (random crystal field) broadening, unresolved hyperfine structure and magnetic anisotropy. Hyperfine structure, caused by the interaction of the spin and nuclear moments can be seen in the chalcopyrite Mn-DMS alloys at low ($z \leq 0.01$)

concentration only [41]. At even moderate alloy compositions the hyperfine structure is lost to the inhomogenous broadening effect. In the Fe-containing systems, hyperfine splittings do not occur due to the singlet state of the vast majority of ^{56}Fe nuclei. Particularly important examples of both types of broadening occur in spin-glass materials [42]. In fact the ESR lines of interest in this research are the -1/2 to 1/2 transitions, and even these are generally highly broadened with widths at room temperature ranging from 10^{-2} to 10^{-1} T.

The apparatus consists of a Bruker ER200D-SRC commercial ESR settup with associated ER043 MRD microwave bridge operating in X band (9 Ghz) and is illustrated in fig. 2.3.3a The Bruker field controller was connected to a Newport Instrument magnet and type C155 power supply which produced 0.8 T at a maximum current of 15 Amps. The measurement chamber was one of a rectangular TE 104 (dual chamber) cavity. Samples were powdered, placed in thin-walled quartz ESR tubes and inserted into the active half of the cavity. The system was outfitted with a temperature controller and dewar and the samples could be cooled with N_2 or liquid He to cryogenic temperatures during measurement. Samples were found to be 'lossy' due to their high dielectric constant, however spectra could be obtained easily even without optimal tuning of the cavity.

The ESR absorption is measured by a field modulation which leads to a 1^{st} derivative presentation of the line. The actual absorption lines were found to generally closely approximate Gaussian or Lorentzian character as can be

measured by comparison to tabulated ideal line derivative profiles [43]. Some asymmetrical or non-standard line shapes have however been seen. The asymmetry can usually be understood in the context of g-value anisotropy, and non-standard shapes, such as mixed Lorentzian-Gaussian shapes have been reported elsewhere [44] [45].

The relationship between the ESR, and the magnetic susceptibility data can first be seen in the fact that the ESR line intensity is proportional to the number of paramagnetic spins in the sample. Indeed the sample magnetism is related to the ESR intensity through a Kramers-Kroenig relationship which indicates that for sharp lines, the ESR absorption area is in fact proportional to the static susceptibility [46]:

$$\chi(0) = \frac{g\mu_B}{\pi\hbar\omega_o} \int_0^\infty \chi''(H)\, dH \qquad (2.3.5)$$

In the above expression, ω_o is the frequency of the ESR resonance maximum and χ'' is the imaginary (absorptive) part of the complex susceptibility, usually written as $\chi''(\omega)$. The integral in (2.3.5) thus represents the area under the ESR absorption, however the approximations made in arriving at (2.3.5) are that the linewidth be small relative to the value of the magnetic field at the absorption maximum, a condition not always satisfied in our case. For both Lorentzian and Gaussian lineshapes, the ESR intensity (area) is proportional to the derivative linewidth squared times the derivative peak height [43].

ESR of critical phenomena are of interest in the present research and some resource books [47] and theoretical papers [48] [49] [50] exist on the matter. The measurable parameters

which are affected are the apparent g value, which is the g value obtained through application of 2.3.3, and the linewidth. The apparent g value shifts near transitions due to the stabilization of internal fields (dipole-dipole demagnetization, exchange and anisotropy), while the linewidth generally broadens due to critical behaviour in the relaxation mechanisms. In the case of a para-ferromagnetic transition, the H_{max} (equivalent to 1/g) shift generally follows the form of the magnetization [51] while the linebroadening occurs close to T_c. For an antiferromagnet, the value of $(2H_EH_A)^{1/2}$ where H_E is the exchange field, and H_A is the anisotropy field determines the g-shift, and is often sufficiently large to shift the resonance out of the microwave frequency range. Indeed in general, no ESR signal at paramagnetic energies is observed below T_n. In the antiferro. case the linebroadening and g-shift begin to occur well above T_c (typically at $1.5\text{-}2T_n$, however broadening has been reported as high as $10T_n$ in low-dimensional systems) [51]. The extended range of the broadening often coincides with the range of non-Curie-Weiss behaviour in the susceptibility above T_c. Lower dimensionality systems generally have an enhanced broadening effect [52].

In the case of spin-glasses, large inhomogenously broadened linewidths are observed, and these as well as the centershifts behave similarly to the antiferromagnetic cases. The critical broadenng of the linewidth generally takes the form of a power law in $(T-T_c)$ while well above the T_c, the linewidth follows the magnetic susceptibility. In DMS spin

glasses, resonance lines can be so broadened above the transition temperature that other techniques are used (such as microwave Faraday rotation [53]) to measure their widths.

The ESR measurement can be very sensitive to the presence of paramagnetic impurities, especially when the host signal is broad, however ESR is insensitive to magnetic impurities when the measurement is made below their magnetic ordering temperatures.

2.3.3) Mossbauer Effect Spectroscopy

The Mössbauer effect, whereby nuclear γ-ray photons are emitted and absorbed without recoil or thermal energy transfer, was discovered in 1957. By far most of the work which has lead to the understanding of the effect and its applicability to materials science has been carried out in the last 15 years, and some important fundamental aspects of the technique are still being derived [54].

Approximately 13 elements have isotopes with which the Mössbauer effect can be practically applied. Of the elements making up the alloy systems under investigation, both Fe and Te can in principle support Mössbauer effect spectroscopy (MES) however the easiest and by far most common isotope for MES is ^{57}Fe. Dr. Rancourt at U. of Ottawa has set up an ^{57}Fe MES laboratory and the Fe-containing alloys were studied by this technique under his guidance. Michel Royer, a graduate student in the MES lab was instrumental in the collection of the data and he also assisted in the data analysis.

The Mössbauer technique utilizes the recoilless emission and absorption of γ rays from nuclear transitions. The transitions of interest involve the decay of a ^{57}Co source nucleus to an excited state of ^{57}Fe which can subsequently emit the 14.4 keV γ particle of interest. If the decaying nucleus is imbedded in a crystal lattice, a fraction of the γ rays are emitted without recoil of the nucleus. This recoil-free fraction of γ particles are highly monochromatic and can be precisely Doppler shifted in such a way as to cover the energy range of interest in the reference frame of the

sample. The apparatus which accomplishes this and records the resulting sample absorption spectrum is diagrammed in fig. 2.3.4. The sample (absorber) is placed in between the detector and source such that the resonant absorptions can be seen. The samples consist of powdered material which is spread thinly between two mylar sheets. The sheets were sandwiched together at the edges with two aluminum rings which could be tightened together.

The ^{57}Co source velocity is modulated by a transducer which doppler shifts the emitted γ rays by $(v/c)E_{\gamma}$ where v is the transducer velocity. The transducer is also used to synchronize the detection instrumentation. This allows the absorption data to be sorted into the bin appropriate to its otherwise unmeasurably small Doppler energy shift. As an example of the velocities and energy shifts involved, the fundamental ^{57}Fe MES absorption width, which is equal to twice the Heisenberg resonance width, is $1x10^{-8}$ eV and corresponds to an absorber-source relative velocity of 0.192 mm/s.

The samples, which contain naturally occuring ^{57}Fe (approx. 2% of the total Fe) then absorb the doppler shifted γ of the appropriate energy according to the precise positions of the ^{57}Fe energy levels within their structure. The usefulness of the technique hinges on there being enough recoil-free γ emissions and absorptions to give a strong MES signal. Such recoil free events occur in much the same way that coherent x-ray scattering (which leads to diffraction) occurs. In these cases the recoil energy associated with absorption of the incoming photon is too small to eject the

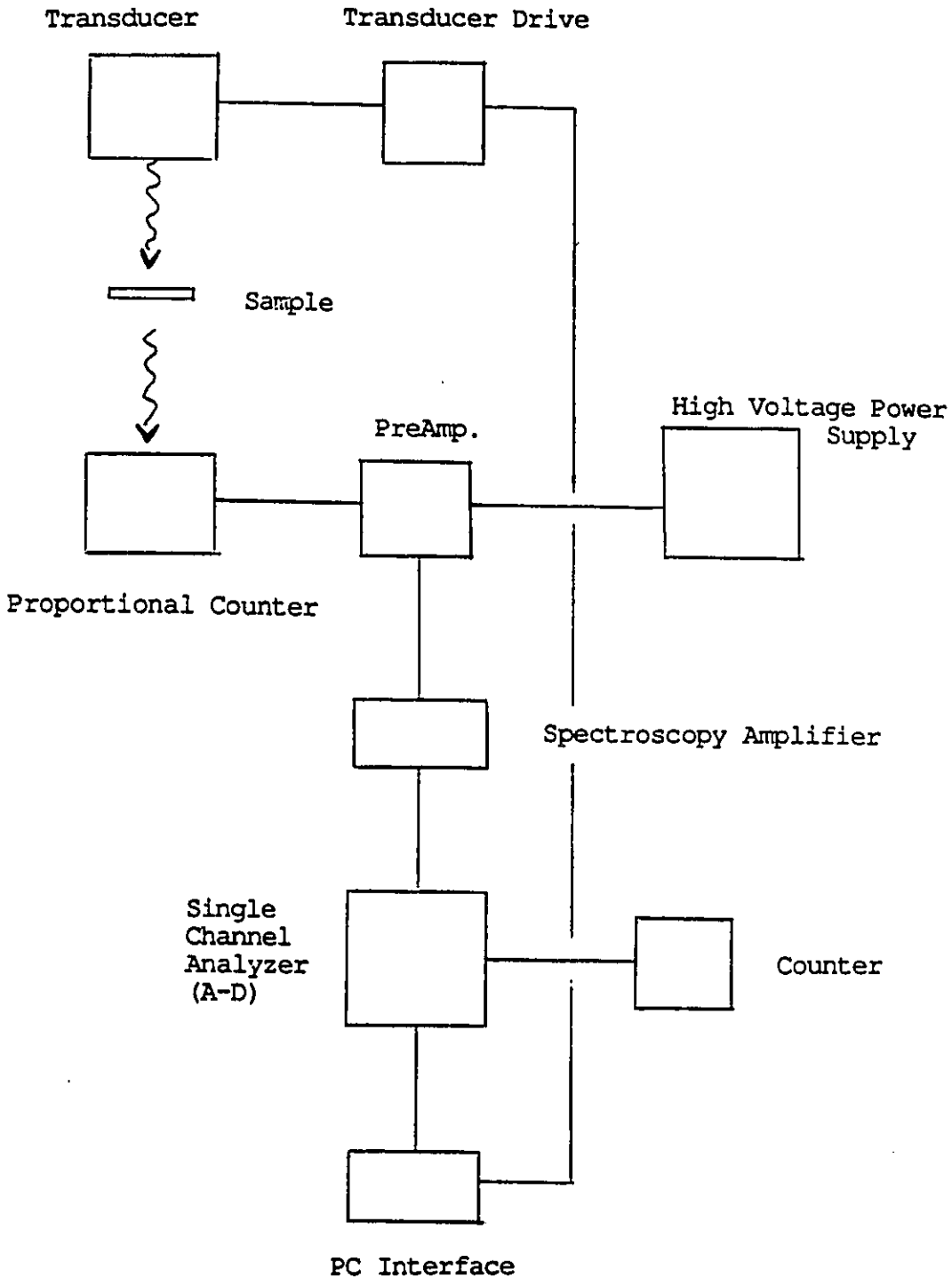

Figure 2.3.4 Mossbauer Spectroscopy Apparatus.

Labelled on the diagram are the components of the Mossbauer apparatus. The gamma rays are depicted as wavy arrows.

atom from the lattice site and is of the appropriate size to excite 0^{th} order thermal modes whereby the whole crystal can take up the recoil momentum, thereby minimizing the net recoil energy loss. For this basic reason, the Debye-Waller factor which relates the fraction of recoil-free events to the lattice vibrations, appears in the expressions for the intensities of both the diffraction and the Mössbauer spectra.

The other crucial aspects of the MES needed in understanding its application are the mechanisms whereby the absorber (sample) nuclear levels are affected by the chemical environment there. As will be seen, in the MES setup the source also acts in many ways as a standard so it is often more precise to speak of these effects as manifesting differences in the source relative to the absorber nuclear ^{57}Fe levels. These effects are characterized by 3 parameters which are described as follows and relate directly to the spectra and energy level diagram illustrated in fig 2.3.5. They are summarized on table 2.3.1:

The chemical isomer shift; δ.

Also called the center shift, indicates the shifting of the centroid of the MES spectrum. This is caused by the difference between the emitter and absorber nuclear s-electron densities (to be abreviated as $\rho_s(0)$), and has its origin in the associated Coulombic interaction energy. The detailed treatement of the δ shift involves a consideration of the nuclear size change associated with the transition. The result is that for ^{57}Fe, a positive δ signifies a decrease in the s electron density at the absorber relative to the

Fe^{57} I=3/2--> 1/2 transitions

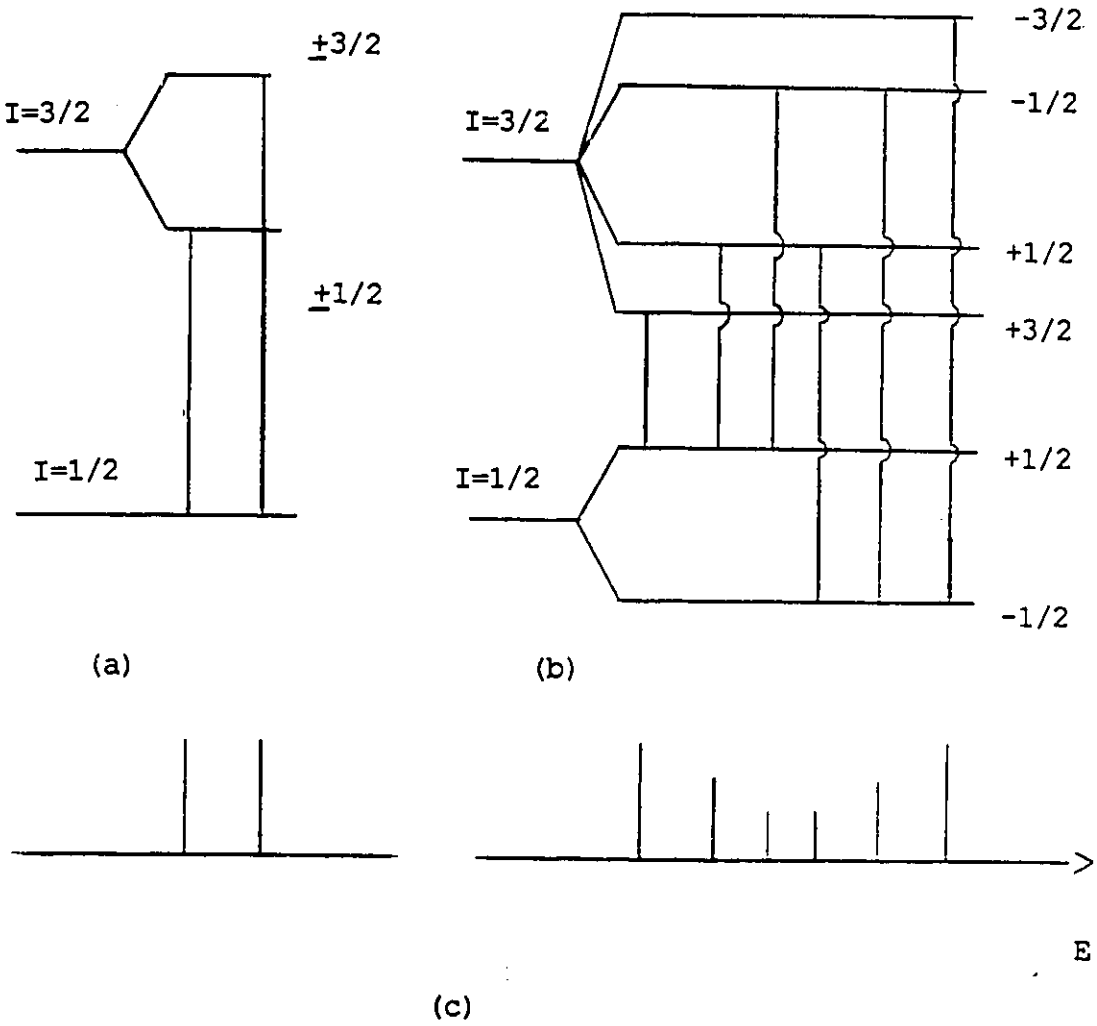

Figure 2.3.5 Nuclear (Mossbauer) Transition Diagram.

Illustrated are the transitions giving rise to (a) the quadrupole doublet and (b) the hyperfine sextet Mössbauer spectra. The singlet transition would arise between the unsplit levels at the far left of (a) (b). Stick diagrams (c) illustrate the appearance of the absorption spectra on an appropriate energy scale.

emitter. Although very small, the associated nuclear energy shift is dependant on the chemical environment of the Fe atom and can be measured through MES. A particularly important example of this is the d-level shielding effect whereby occupied d levels shield the nuclear charge from the outer s electrons and thereby decrease the $\rho_s(0)$. In particular, the $3s^2 3p^6 3d^5$ (Fe^{3+}) state has a lesser δ (relative to a given source) than the $3s^2 3p^6 3d^6$ (Fe^{2+}) state does. This provides one means of distinguishing Fe^{2+} from Fe^{3+}.

The quadrupole splitting; Δ.

Another interaction which affects the nuclear energy levels is that between the nuclear electric quadrupole moment and the electric field gradient (EFG) at the nucleus. The nuclear moment is related to the nuclear shape and is non-zero for any nucleus with a net spin. The electric field gradient results from any non-spherical electronic charge distribution surrounding the nucleus. As such, the electric field gradient can have contributions from the ion itself (valence contribution) as well as from its neighbours, i.e. the crystal field. For example, for a highly symmetric ion such as S-state (high spin) Fe^{3+}, the valence contribution is small and a crystalline tetragonal distortion such as that of the chalcopyrite structure can cause a measurable field gradient [55, p.99]. On the other hand high spin Fe^{2+} (which is D-state) is asymmetric and has a high valence EFG and correspondingly high Δ. As illustrated in fig 2.3.5, the effect of the Δ in the absence of a magnetic hyperfine field, is to split the spectrum into a doublet.

Magnetic hyperfine parameter; H_e.

The nuclear Zeeman effect is characterized by the effective magnetic field H_e. As seen in fig 2.3.5, this results in the ^{57}Fe Mossbauer spectrum being split into a sextet. The effective field is due to magnetic fields and exchange fields. Similarly to the case with the δ parameter, the exchange field affecting the (magnetic) d levels is translated to the nucleus via the s-d interaction. In this case the net s-electron spin density at the nucleus is affected by the spin orientation of the populated outer d levels. In order for the nuclear Zeeman effect to be observed however, H_e must be stable over the Mössbauer measurement time. This measurement time is characterized by the nuclear excited state lifetime and is of the order 10^{-8} sec for ^{57}Fe [48]. In order to provide a comparison, this is a longer time than that characteristic of the x-ray scattering interaction which is of the order 10^{-15} s, and the ESR transition time which is of the order 10^{-10} s. One implication of this is that due to the spin fluctuations, a paramagnetic material displays no Zeeman splitting even though there can be large instantaneous fields at the nucleus. The observation of the MES patterns can similarly be complicated by the spin relaxation dynamics. For example, effects similar to the dynamic broadening of ESR can lead to averaged MES spectra if the characteristic time of the dynamics are comparable to the Mössbauer measurement time.

There are various complications which can arise in the interpretation of the above parameters. For example a

quadrupole splitting in the presence of a magnetic hyperfine splitting complicates the spectrum. Fortunately the experimental spectra obtained from the samples are of the types illustrated above. Even these simple spectra are subject to other more familiar effects such as alloy broadening which can provide further information on the crystalline environment of the absorber ^{57}Fe nuclei. In fact the analysis of the MES lineshapes has some similarity with the ESR case. In both cases, the fundamental lineshape is Lorentzian and can often be observed as such however lines corresponding to Gaussian shape are also commonly seen. Some diffrences between the two techniques are that in the case of MES, Voight line profiles are commonly used in the data fitting whereas this does not occur in ESR, in which however mixed Lorenzian-Gaussian character can be seen. Also in ESR, Dysonian [56] lines occur for conductive samples, a phenomenon without analog in the case of MES.

Fitting of the MES data was accomplished with MINUIT through a computer program setup in the MES lab. Fits utilized in this report are to simple combinations of singlets, doublets and sextets such as those illustrated above. In each sextet case, the angular parameters associated with the relative orientation of the quadrupole moment and the EFG were assumed to be zero.

The intensities of the absorptions were estimated by the simple relation for gaussian lines however this is only an estimate as the effect of the absorption was not taken into account. The absorption tends to equalize all peak heights as

can be seen from considering the limiting case of absolute absorption in which case all peaks intensities are zero. This absorption effect can be seen clearly in the sextet spectra in which the theoretical ratio of peak heights is 3:2:1 as illustrated on fig 2.3.5.

Table 2.3.1

Typical Mössbauer parameters for Fe ions

Fe^{2+} - $3d^6 4s^0$

High Spin 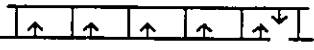 ($^5T_2$)	Low Spin 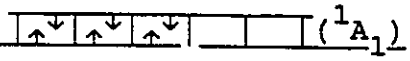 ($^1A_1$)
Δ=2.5 mm/s δ=1.2 mm/s usually found in non-cubic environments, increasing symmetry decreases Δ.	Δ=0 mm/s δ=0 mm/s no intrinsic valence contribution to EFG. Low δ due to occupied 4s orbitals [23].

Fe^{3+} - $3d^5$

High Spin 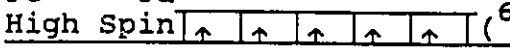 ($^6A_1$)	Low Spin 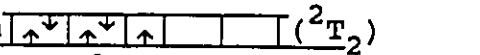 ($^2T_2$)
$\Delta\simeq$0.3 mm/s $\delta\simeq$0.3 - 0.5 mm/s Δ predominantly due to external EFG hence small and temperature dependent provided the d orbitals retain sufficient degeneracy).	$\Delta\simeq$0.5 at 300°K (T dependant) $\delta\simeq 0^-$ - 0.5 mm/s Has strong-field t_{2g}^5 configuration hence the occupied orbitals are suitable for tetrahedral bonding. Δ has temp.dependence due to nearby excited states.

The Mössbauer parameters given are representative values taken from [55]. EFG signifies electric field gradient and indicated is whether the EFG arises from within the Fe ion or from the ligands (only the latter source of EFG is expected to be temperature independent and hence lead to a temperature independent Δ). Along with the box-diagrams of the electronic configurations, are given the ligand-field terms. The high (low)-spin cases correspond to weak (strong) crystal fields. The t_{2g} nomenclature refers to the manifold of d states which possess p-like real wavefunctions.

2.4) Magnetic Susceptibility

The magnetic properties of DMS alloys are one of their most distinguishing features and by virtue of the possible applications outlined in section 1.1, may also be their most useful. Much work has been carried out on the magnetic properties of DMS alloys particularly as they relate to optical behaviour. High-field magnetization studies have been particularly useful in determining the inter-Mn interactions in low concentration random alloys [57] however relatively less work has been carried out on the static[1] susceptibility behaviour of DMS.

Static susceptibility measurements (abbreviated in the following as χ) were carried out on the alloy systems concerned in this report under the guidance of Prof Lamarche. The apparatus has been described in [58] and consists of a reverse dewar setup whereby the niobium SQUID can be kept at 4 K while the movable sample chambers within may be heated to approximately 300 K. For this reason the system is well-suited to measure low temperature χ, however has the drawback of providing limited access to higher temperature behaviour which also can be of interest.

Samples were powdered and weighed while being introduced into the two reusable copper measurement chambers. Typically 40 milligrams (mg) of sample powder was used for measurement. This represents the sample mass that would fill the measuring chamber, and such a sample mass provided signal strengths

[1] Also called the initial or low-field susceptibility.

which were measurable over the full range of temperatures available in the apparatus. At low temperature (and hence relatively high paramagnetic signal strength) the measurements are limited by the saturation of the flux counter, while at high temperature (low signal) they are limited by the weakness of the signal. These sample masses provided signal strengths of the order of 10^2 to 10^3 mV in the flux counter which correspond to 10^3 to 10^4 flux quanta or $\approx 10^{-6}$emu at the SQUID. Measurements of such low fields can be attained by commercial SQUIDS and the performance of the apparatus is comparable to such systems. Signal strengths were generally well above the quantum noise limitation of the SQUID and the measurements generally have high signal to noise ratios. The major source of noise was found to be due to vibration. This attests to the high sensitivity of the SQUID considering that the system is basement wall-mounted and that many precautions assuring mechanical rigidity of the apparatus were implemented by Dr. Lamarche in the design[2].

One advantage of the high sensitivity achieved by the SQUID is that this allows the measurements to be carried out in fields of 10^{-3} to 10^{-2} T. The measurements are thus expected to closely approximate the static susceptibility which is defined as

$$\chi = \lim_{H \to 0} dM/dH \qquad (2.4.1)$$

The most useful data obtained from χ relates to the critical behaviour and to the paramagnetic behaviour of the

[2]One extraordinary case of vibrational noise resulting in the loss of a data point occured during the R 6 earthquake of June/90.

samples. Susceptibility cusps and associated non-equilibrium phenomena- specifically temperature induced hysteresis, give the location of magnetic ordering temperatures (T_C) and can also be used to characterize the materials.

The general expression for the susceptibility [46], [59] supports many types of behaviour of which Curie-Weiss (C-W) paramagnetism is a particular example. Curie-Weiss behaviour is prominent among the Mn-DMS, however certain of the conditions which lead to it are relaxed in the case of most Fe-DMS. The most important of these conditions is the absence of higher energy multiplets within ≈kT of the degenerate ground level. Materials which do not satisfy this condition can exhibit, among other possibilities, the Van Vleck type (temperature in dependent) paramagnetism such as that seen in II-VI(Fe) systems. C-W paramagnetic behaviour yields information regarding inter-spin interactions via the Curie-Weiss (C-W) parameters C and θ which appear in the theoretical susceptibility as;

$$\chi = \frac{C}{T - \theta} \qquad (2.4.2)$$

The Curie constant C is experimentally associated with the slope of the linear inverse susceptibility (χ^{-1}) data and is directly proportional to the number of paramagnetic spins in the sample [59].

$$C = g^2\mu_B^2\frac{J(J+1)}{3k_B} \text{ emu k per magnetic ion} \qquad (2.4.3)$$

For S-state ions, it can be assumed that the J value appearing

in eq. 2.4.3 is given by $J=S=5/2$[3]. In general for DMS, any remaining orbital contribution is considered completely quenched due to the high covalency of the bonding [60] however the validity of this assumption will be questioned in the case of the Fe alloys reported in chapter 3.

The Curie-Weiss temperature θ is indicated as the extrapolated temperature-axis intercept of χ^{-1} and is related to the strength of the inter-spin interactions. The behaviour with respect to alloy composition of the θ's, and the magnetic critical temperatures can constitute direct evidence for ordering, and this will be outlined in chapter 4. Since the C-W parameters are of extreme interest in the following chapters, both the possible sources of measurement error intrinsic to the nature of the measurement as well as to the apparatus will be reviewed.

1) Non-Curie-Weiss behaviour.

It can happen that when susceptibility measurements do not extend over a large range of temperatures, the plots of $1/\chi$ can look reasonably linear (over the measured range) despite the fact that the data is not precisely linear and thus yields incorrect C-W parameters. This concern will be discussed in the case of the Fe alloys, in which case the linear inverse susceptibility (C-W regime) is approached asymptotically from below with increasing temperature. Situations such as these lead to systematic underestimates in the C values. Examples of the opposite effect in which cases

[3]Small orbital contributions to J can however be brought back into the ionic state via spin-orbit coupling.

the low temperature inverse susceptibility is higher than that expected from extrapolating from the C-W regime, and in which cases the linear (C-W) χ^{-1} is approached from above with an increase in temperature have also been seen in high concentration zincblende DMS [39].

For simple systems, high temperature expansions exist which can be used to refine the experimentally obtained C-W parameters [61] [62]. The correction has been calculated for a low concentration DMS by Shapira et. al. [63] who find that for susceptibility measurements extending to 300 K an error of a less than 1% in C, and a few percent in θ occurred by neglecting this effect. In some high concentration DMS, various sources [83] [88] ignore the high temperature expansion correction with good success, and the same procedure will be followed in this paper.

2) Experimental scatter in the measurements.

Experimental scatter leads to inaccurate measurements of the slopes of the inverse susceptibility curves and hence the C-W constants. This is especially important in cases such as ours in which only small amounts of sample (hence small signals) are used in the measurement. Since the magnetic response decreases with increasing temperature, the measurements become relatively less reliable in the high temperature regime due to the existence of noise as discussed above. Indeed some sets of measurements are noticeably more reliable than others due to the lesser amount of scatter in the data points caused by vibrational noise during their

measurement.

3)Sample inhomogeneity, error in sample mass measurement or error in stoichiometry.

Inhomogeneity in non-equilibrium samples or error in mass measurement in sample fabrication can lead to differences between the expected, and the the actual number of spins present in the sample used for measurement, and thus lead to discrepancies in the measured C. Since the amount of material used in the susceptibility measurement is typically 40mg and this is taken from a 1g or 2g ingot, any inhomogeneity would have to be of this scale and therefore represents a flaw in the sample. Some trials to test reproducibility of the results were carried out. These were simply measurements which utilized different 40mg pieces from the same parent ingots. The resulting measurements were usually identical within the margin of error estimated for the known effects listed above indicating that under normal conditions, any sample inhomogeneity occurs on a smaller scale than 40mg. Random errors in sample weight measurements are estimated to be no greater than 5%. Variations in stoichiometry due to inhomogeneity are estimated to be 5%. In the following report, a combined error on the number of spins present in the samples due to the effects of inhomogeneity and mass measurement will be estimated as 7%.

4) Diamagnetic correction.

Due to the fact that the high temperature measurements from which the C-W parameters are derived involve the weakest

susceptibility signal, the relative importance of the temperature-independent diamagnetic correction also increases with temperature. This could in principle, lead to errors in the measured C and θ values.

Care must be taken in calculating this small correction as it applies to our apparatus, since it depends on the sample as well as on the measuring chamber. In fact the empty chamber represent an absence of mass which is seen as anti-diamagnetic to the SQUID and hence yields a positive diamagnetic effect. Careful measurements of the empty chambers carried out during the course of the sample measurements indicate that the effective diamagnetic susceptibility of the chambers is $\chi_{ch(eff)} = +(3.4\pm0.5)\times10^{-7}$ emu/g. Using $\chi_{ch(eff)}$ and the tabulated [64] elemental diamagnetic constants, a reasonable estimate of the total diamagnetic effect in the sample-filled measuring chamber can then be obtained. For example, $(AgGa)_{1-z}Mn_{2z}Te_2$ with z=0.25 has an estimated diamagnetic susceptibility (χ_D) of -2.78×10^{-7} emu/g, while $CuInS_2$ has $\chi_D \simeq -3.87\times10^{-7}$ emu/g, and these susceptibilities (when summed with the anti-diamagnetism of the chamber itself) yield an effective total diamagnetic susceptibility of the order $\chi_{D(eff)} \pm 5\times10^{-8}$ emu/g. Since this is two or three orders of magnitude smaller than the observed paramagnetic susceptibilities of the materials, it can generally be neglected in the analysis of the experimental susceptibility data. The diamagnetic correction $\chi_{D(eff)}$ can however be important in the event that a materials

paramagnetic susceptibility is small, as for example occurs when the observed paramagnetic θ is large.

It is of interest to note what the effect of either the diamagnetism, or any other temperature independant susceptibility would be on a general C-W (paramagnetic) susceptibility, thus letting D represent a general temperature independant susceptibility, consider:

$$\chi = \frac{C}{T-\theta} + D \qquad (2.4.4)$$

$$\text{which yields } \chi^{-1} = \frac{T-\theta}{C + D(T-\theta)} \qquad (2.4.5)$$

In the event that θ is significantly larger than T over the range of temperatures measured, the apparent Curie constant obtained from χ^{-1} becomes approximately equal to C-Dθ instead of C. Examples of this situation are graphed in fig.2.4.2 in which values of the parameters C, θ and D appropriate to the Mn containing materials discussed in chapter 4 are taken.

5)Multi-component response.

The presence of more than one magnetic phase contributing to the χ can yield apparently straight $1/\chi$ plots. A straightforward analysis shows for example that a small pure paramagnetic (θ=0) response (eg. due to isolated spins) added to a large C-W (θ non-zero) signal can yield an apparent C different from that due to the majority of the spins [65]. The size of this effect also depends on the value of θ. The determination of the combinations of parameters with which distinct components to the susceptibility can lead to apparently linear χ^{-1} behavior will be the main subject of section 4.5.

Fig. 2.4.1

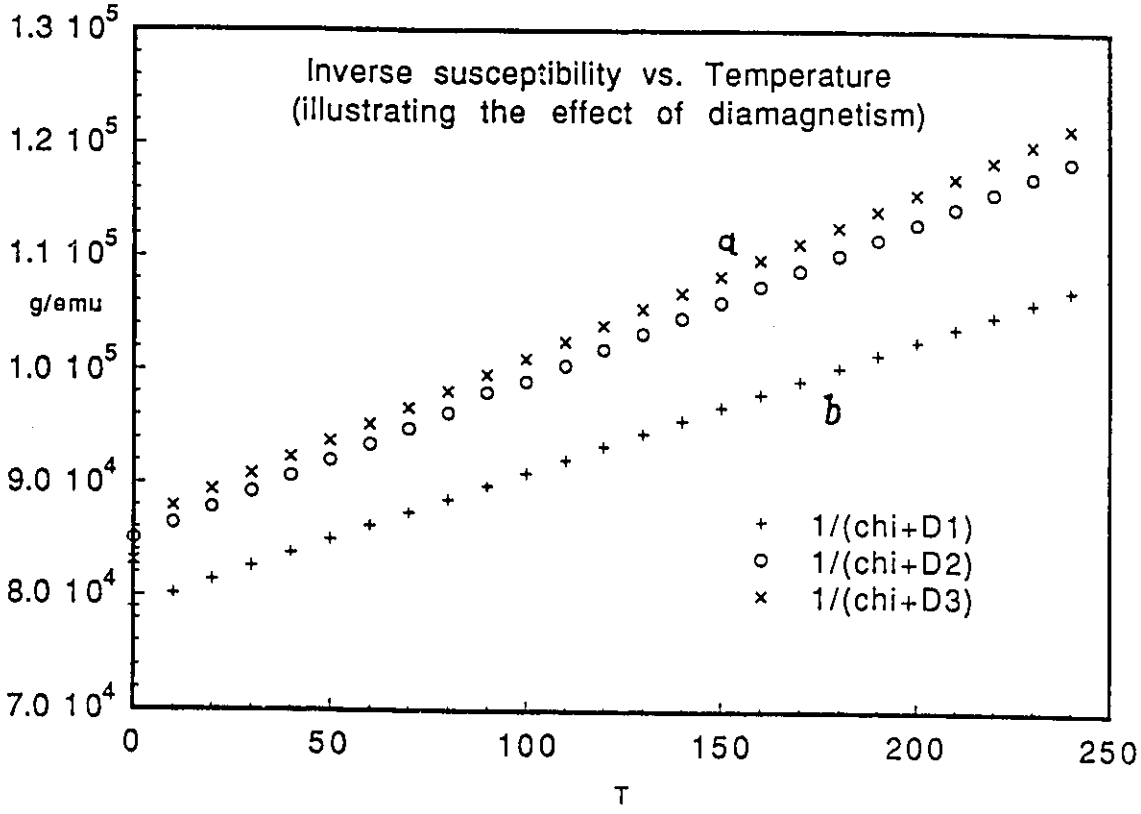

D1= $1x10^{-6}$ emu/g	$C^*=8.52x10^{-3}$ K emu/g	$\theta^*=-673$ K
D2= $1x10^{-7}$ emu/g	$C^*=7.15x10^{-3}$ K emu/g	$\theta^*=-607$ K
D3=$-1x10^{-7}$ emu/g	$C^*=6.96x10^{-3}$ K emu/g	$\theta^*=-594$ K

Figure 2.4.1 $[C(T-\theta)^{-1}+D]^{-1}$ vs Temperature (T). The lines labelled (a) illustrate the effect of the diamagnetic susceptibility, and (b) simulates the presence of a temperature independent paramagnetism. In each case the Curie-Weiss (C-W) susceptibility (chi) has $C=7x10^{-3}$ k emu/g and $\theta=-700$ K and represents values found experimentally for the Mn- containing systems (see 4.4). The values of D are given above, along with the corresponding apparent C-W parameters obtained directly from the slopes of the graphs (C^* and θ^*).

The ratio θ/T_c is an important parameter of magnetic materials particularly in the context of mean field theory, and will play an important role in the analysis of chapter 4. The important aspects of this parameter are summarized in [66] and [67]. In particular the large magnitude of this ratio found for the Mn-containing alloys is of importance. Mean field theory can account for θ/T_n ratios as high as 15 [66] and as will be seen, such ratios do seem to exist in the DMS materials.

3.0) Iron-Containing Chalcopyrite DMS

As mentioned in the introduction, relatively little work has been carried out on Fe-containing DMS's. Among the Fe-containing systems, it can be said that of the two Fe ionization states, relatively less work has been carried out on Fe^{3+} DMS.

Most of the work with Fe^{3+} has been done in chalcopyrite- structure materials in which the ranges of solid solution reported vary considerably depending on the exact system. It has been suggested [ref.4 p.399] that large ranges of Fe solid solution could occur within chalcopyrite-structure materials simply due to the fact that Fe exists in that structure; $CuFeS_2$ is the original chalcopyrite. However the preceding train of thought could lead one to be too optimistic regarding the number of chalcopyrite-based systems which could support Fe as a substitional element. Counterexamples are exemplified by the instability or non-existence of otherwise plausible Fe-rich end members. For example $AgFeTe_2$ and $AgFeSe_2$ are either difficult to make or non-existent [68] [69]. Furthermore although the chalcopyrite structure has been predicted to exist for $CuFeTe_2$ at high temperatures [70], it is beleived to be of another ($P4_{mnm}$) tetragonal structure at room temperature [70b]. Similarly, $CuFeSe_2$ is known to be of eskebornite structure [71], not chalcopyrite structure.

In fact ranges of solution of x=0.16 and 0.3 have been reported for $CuAl_{1-x}Fe_xS_2$ [72] and $CuIn_{1-x}Fe_xTe_2$ [70]

respectively. Also, full solid solution ($0<x<1$) has been reported in $CuGa_{1-x}Fe_xS_2$ [73].

For our purposes, studying an Fe-based DMS opens new avenues through which to study and understand general properties associated with chalcopyrite based DMS, especially as regards crystallographic ordering. Regarding other physical properties, for example exchange mechanisms, the comparison of an Fe-based system to an Mn-based one could give a better understanding of the specific behaviour of both systems. Also, the Fe-containing systems may show new properties which do not exist in the Mn-containing ones.

These investigations are facilitated by the amenability of the Fe-systems to Mössbauer spectroscopy. Fe-containing alloys are one of only a few possible DMS (and are certainly the system of choice) for Mössbauer analysis.

3.1) Preliminary Results on Iron and Chromium Alloys

As mentioned previously a preliminary attempt to fabricate a number of iron and chromium based chalcopyrite systems was undertaken. The systems chosen were: $CuIn_{1-x}Fe_xSe_2$, $CuGa_{1-x}Fe_xS_2$, $AgGa_{1-x}Fe_xS_2$, $AgIn_{1-x}Fe_xS_2$, $CuIn_{1-x}Fe_xS_2$, $CuIn_{1-x}Cr_xSe_2$, $CuGa_{1-x}Cr_xSe_2$. Only the Cu-Ga-Fe system had at the time of this research, been investigated [73].

The procedure carried out in these exploratory cases of alloy systems most of which have not been reported previously was as follows:

1) Bulk materials were prepared according to the melting procedure described in 2.0. They were cooled from the 'melt' and a prelimnary x-ray photograph was taken for reference and occasionally for measurement.

2) Samples were then annealed at high temperature in order to allow for diffusion and hence homogenization, then slowly cooled to room temperature in an attempt to facilitate attaining equilibrium at room temperature.

3) Samples were annealed or sintered at low temperature in order to attain equilibrium at low temperature.

4) A differential thermal analysis (DTA) was perform for the appropriate samples in order to discover phase boundaries.

5) Samples were resealed and annealed within the DTA phase fields in order to attain equilibrium at the chosen temperatures, and quenched from the annealing temperatures as rapidly as possible in order to try to maintain the

equilibrium at that temperature.

Materials were then characterized by x-ray photograph and other methods. At this stage of the analysis, one could usually obtain a good idea of the nature of the phases. In particular, the single-phase fields could often be found and these are the most amenable to further study.

The signature of a single phase field is the existence of a single x-ray diffraction pattern which usually displays a concentration dependent lattice parameter. In the cases where the diffraction pattern is complex or ambiguous or when the lattice parameters do not change with concentration, other measurements can be made to corroborate any suspected single phase field.

All the above systems were prepared with bulk compositions; x=0.0, 0.2, 0.4. The first annealing was done at 600°C for 1 month, except for the Cu and Ag-Fe sulfides which were annealed at 750°C. The samples were cooled from the anneal over a period of approximately 10 hours by switching the annealing furnace off. From the preliminary x-ray photograph, it was found that the most promising systems from the point of view of extent of solid solution (x>.2) were $AgIn_{1-x}Fe_xS_2$ and $CuIn_{1-x}Fe_xS_2$. The Cu system was chosen for further study and this will be dealt with in greater detail after a brief account of the others.

The gallium sulfides blew up in the melting furnace, indeed both compounds (x=0 components) were not formed for this reason regardless of the different heating rates which

were attempted. This feature of the materials has been described previously [5]. $CuGaS_2$ has been successfuly doped and alloyed with Fe by ion transport [7] and by a multi-stage sintering process [73], unfortunately the high sulfur vapour pressure at the reaction temperature makes this system difficult to produce by melt and anneal. Another member of the Ottawa group has since succesfully fabricated samples by closely monitoring the furnace heating rate.

The chromium-based selenides were not considered suitable for further investigation due to the poly-phase nature of the first x-ray result. The Cu-In and Cu-Ga Fe selenides showed no apparent change in lattice parameter and were thus difficult to characterize by x-ray analysis only, however they seem promising systems for further analysis. In fact evidence for limits of solid solution of 45% and 15% in the Cu-Ga and Cu-In cases respectively has recently been found by another group[1].

The Ag-In and Cu-In sulfides were chosen for further analysis due to the presence of small changes in lattice parameters. These could not only facilitate characterisation, but also indicated that a reasonable range of solid solution occurred.

Ingots of the Ag system look shiny and silvery. Detailed x-ray analysis indicated some solid solution, possibly up to x=0.2. However the change in lattice parameter was found to be quite small. The chalcopyrite lines from the

[1]Dr. M. Quintero (private communication)

x=0.2 composition gave values of a and c very close to those of the compound ($AgInS_2$). Thus it is suggested on the basis of a possible slight variation of lattice parameter (along with the absence of lines attributable to other phases at low concentrations) that this system exhibits solid solution and is of interest for further study.

Based on the preliminary pseudo-cubic analysis, the $CuIn_{1-x}Fe_xS_2$ system was the most promising, and chosen for further study. The following is a detailed description of the analysis carried out on this system.

3.2) The $CuIn_{1-z}Fe_zS_2$ System

This system was studied in tandem with the a group based in the laboratory of Dr. M. Quintero at Universidad de Los Andes in Merida, Venezuela. In the following, this group is referred to as the Merida group.

3.2.1) Sample Preparation

Samples were made in Ottawa with bulk compositions; x= .05, 0.1, 0.15, 0.2, 0.3, 0.5, 0.6, 0.7, 1.0. Samples with composition; x=0.85, 0.875, 0.9, 0.925, 0.95, 0.975 were made by the Merida group in order to study the Fe-rich side of the phase diagram. The samples made in Ottawa were melted as in the case of the preliminary samples. The maximum furnace temperature for the melting run was 1200^{0}C and the samples were held above 1190^{0}C for 50 minutes. The vibrating motor setup (described in chapter 2) was used during this time. The samples were cocled to room temperature by cooling the furnace

in stages, over a period of 1 day. In most cases, only two samples were placed in a given melting furnace in order to minimize the risk of losses due to breakage or blow-up.

Inspection of the resulting ingots indicated a porous morphology, the material of the low concentration samples ($x < 0.3$) showing a homogenous black-shiny appearance, while the higher x values were increasingly golden coloured but seemed inhomogenous in the sense that opposite ends of single ingots were different colours.

It often occurs that visual appearance does not indicate the homogeneity of a polycrystalline material. Variation in the surface colouration can be due to small amounts of oxides and does not necessarily indicate variation in the composition of the material underneath. On the other hand, multi-phase samples can often seem homogenous upon visual inspection. It remains true that the materials are not generally expected to be in equilibrium at this stage of the heat treatment, and for this reason the high temperature annealing is used to obtain homogeneity.

Samples were prepared for DTA by annealing at 600^{0}C for a minimum of 2 weeks and subsequently cooling to room temperature by turning the furnaces down in 50^{0} steps over a period of several weeks. This treatment is expected to accurately approximate equilibrium at low temperature and at the very least, to produce some of the low-temperature phase(s) which could be detectable in a DTA study even if absolute equilibrium is not obtainable under these conditions.

The resulting DTA data gave a very good guide to the required further annealing temperatures.

3.2.2) Differential Thermal Analysis

DTA was carried out on these samples using the procedure discussed in chapter 2. Data was collected on both the Ottawa and Merida systems, which agree well with each other. The Merida group obtained data over the whole range of x values but concentrated on the high x end, while the Ottawa system was used to study in detail the low x side of the phase diagram.

As an example of the DTA data, a chart recording of a heating run made on the Ottawa system is shown in fig.3.2.1. As discussed in 2.2, the low temperature peaks are small and only visible on the heating part of the DTA cycle.

The lowest of the two traces (marked 'difference') shown on fig.3.2.1a contains the peaks marked i ii and iii. Peaks iv and v on fig.3.2.1b are on the high temperature extension of the same 'difference' trace. The temperature values of peaks i to iv are shown together on the inset. The errors in these measurements were estimated by the method outlined in chapter 2. On the smallest peaks, a dashed 'background' line was put in by hand in order to facilitate measuring their positions. The large feature to the left of peak iv on fig. 3.2.1b is an artifact due to the immediately preceding change in the furnace power level. The furnace power at high temperature was increased in order to maintain a sufficiently

Fig. 3.2.1a DTA of $CuIn_{0.85}Fe_{0.15}S_2$

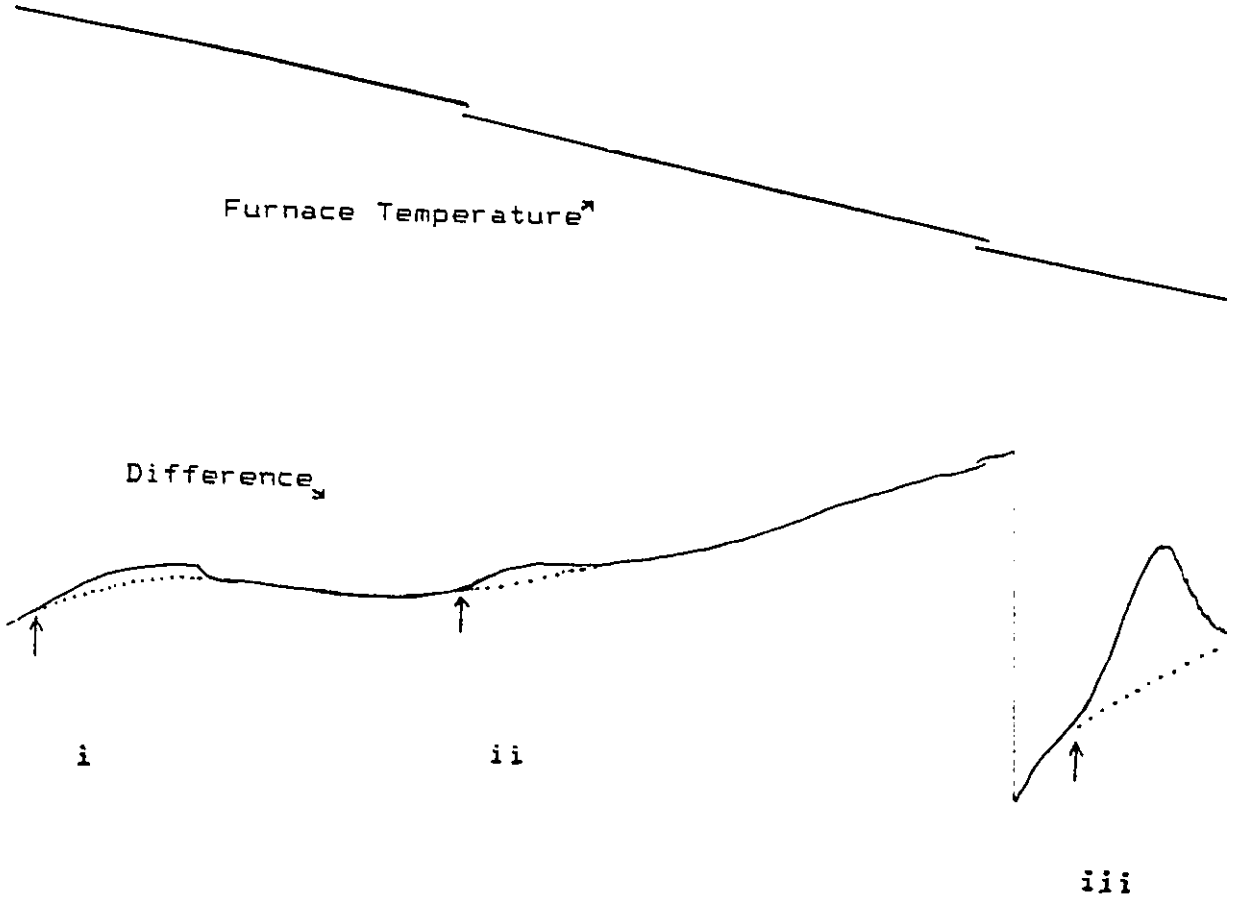

The traces are a photo-reduced reproduction of actual DTA heating curves. Peaks due to the thermodynamic transitions occur on the trace marked 'difference' and are indicated there with arrows. The corresponding transition temperatures are indicated on the phase boundary diagram on the inset to fig. 3.2.1b. The abrupt jump at the location of the peak iii is due to a manual readjustment of the voltage scale.

Fig. 3.2.1b DTA of $CuIn_{0.85}Fe_{0.15}S_2$

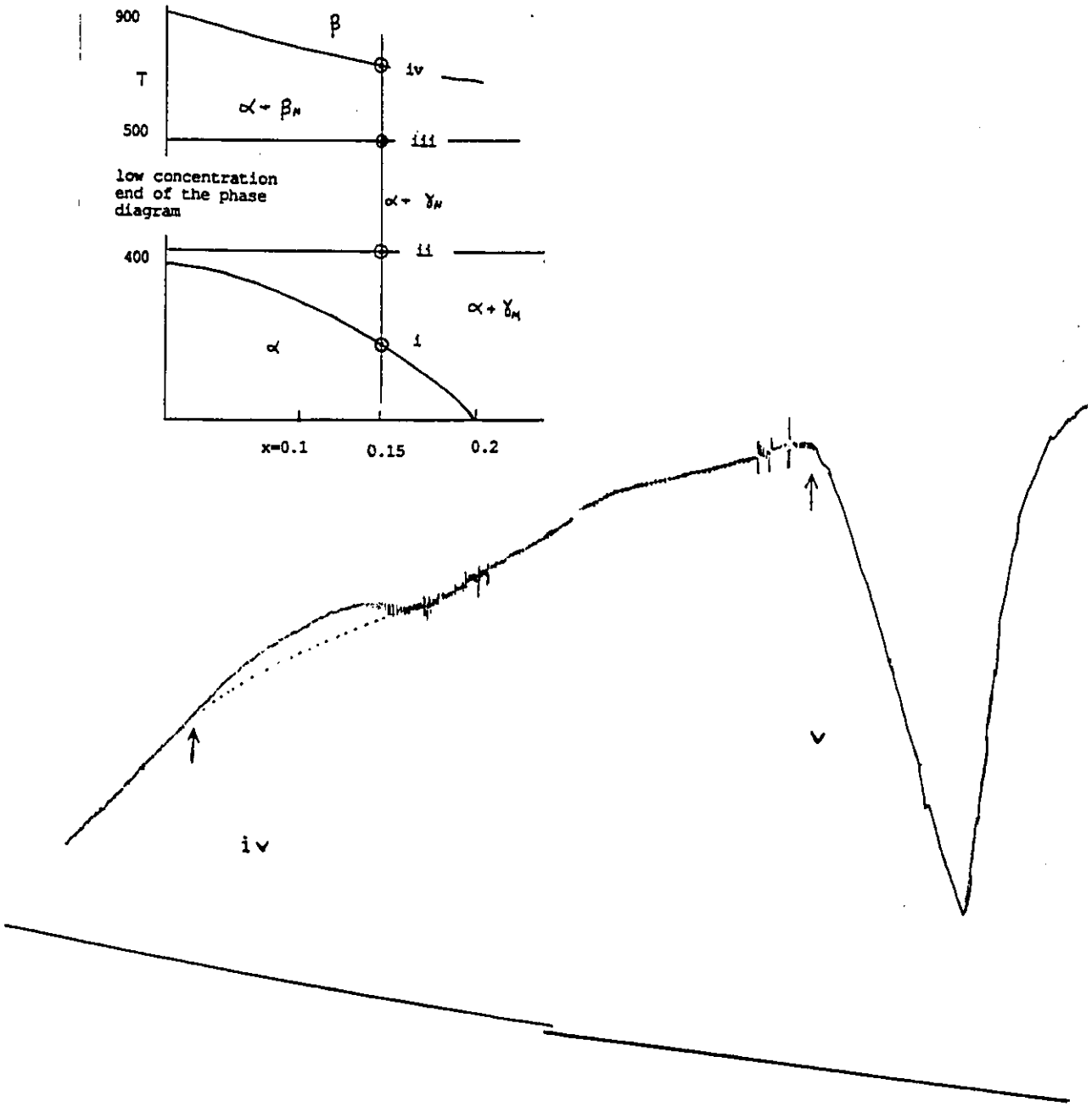

Continuation of fig. 3.2.1a showing sample peak (iv) and the calibration (silver) peak (v). The inset shows the locations of the peaks with repect to the phase diagram.

fast heating rate to resolve the peaks (see ch.2).

Peak v in fig.3.2.1b is the reference Ag melting peak. It deflects the trace in the opposite direction to the sample peaks since the temperature difference between the thermocouple junctions reverses when the Ag undergoes its transition. All the peaks represent endothermic transitions as expected for melting or disordering, i.e. transitions to a higher symmetry.

All the results of the DTA measurments from both the Merida and the Ottawa set-ups are shown in fig.3.2.2. As indicated in chapter 2, the DTA results give the positions of phase-field boundaries, however additional data is required to identify those fields. One useful source of information is a knowledge of the behaviour of the end members (terminal compounds) of the phase diagram.

3.2.3) Phase Diagram

Although it is true [4 pg.13] that the phase transitions of the I-III-IV_2 compounds are often not well known in detail, some data on $CuInS_2$ has been recently made available [70],[71]. These indicate that $CuInS_2$ undergoes three transitions above room temperature. The first, at 980°C demarcates a chalcopyrite to cubic-zincblende transition, the second at 1010°C to an unknown phase (possibly wurtzite), and the third being the liquidus at 1050°C [2]. Thus using the first of these as an example, it is reasonable to propose that

[2] In fact this melting transition was also reported in an earlier reference [4 pg.52]

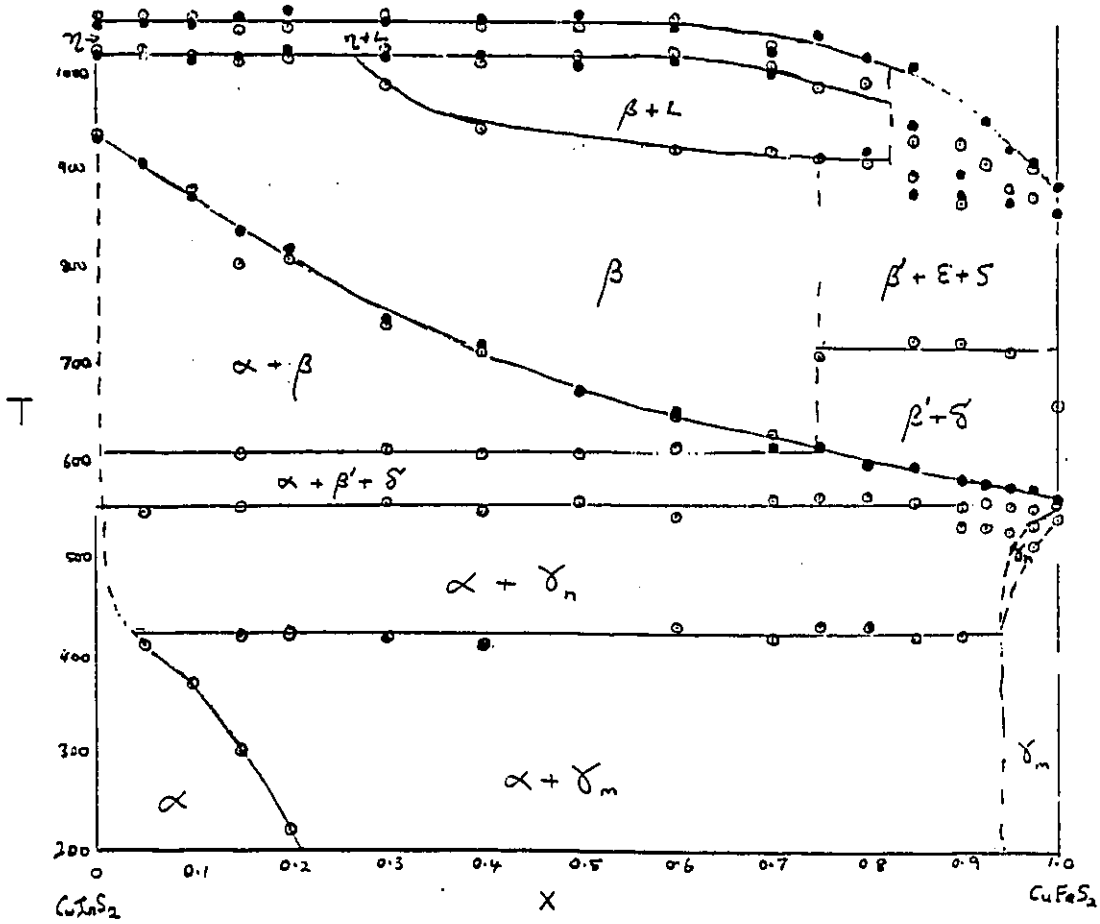

$CuIn_{1-x}Fe_xS_2$

Fig. 3.2.2 The proposed phase diagram of the $CuIn_{1-x}Fe_xS_2$ system. See text for the characteristics of the phase fields.

the field labelled α represents solid solution in the chalcopyrite phase, due to its continuity with the low temperature chalcopyrite phase of $CuInS_2$.

It is known that high temperature zincblende [4 p.28] phases occur within chalcopyrite systems. This is plausible also because of the close relation between the zincblende and chalcopyrite structures. Given the known chalcopyrite to zincblende transition of $CuInS_2$, we propose that the field marked β is such a zincblende field. Care must be taken in verifying this proposal since, as we shall report in the following, materials quenched from the β field show chalcopyrite-like splittings in x-ray diffraction patterns.

At the Fe-rich boundary, the behaviour is much more complex, and confusion in the literature reflects this[3]. Indeed the Fe-S system itself is known for its complexity and for the occurence of regions of metastability and extensive solid solution. Also, high-temperature phases not retainable to room temperature by quenching [74 cs64] are known to exist in the Fe-S system, and this is what we propose also occurs in the case of our high temperature β phase. In order to indicate the range of behaviour possible within the Fe-sulfides, a brief account of these is given in appendix 2.

As can be imagined from the fact that the Fe-S system is complex, the Cu-Fe-S system is also complicated. An important feature of the Cu-Fe-S phase diagram (fig 3.2.3) is the

[3]For example one reference [4] quotes a melting point for $CuFeS_2$ at 875^{0}C while it is now known [74] that $CuFeS_2$ dissociates at 557^{0}C.

Fig 3.2.3 The ISS field of the Cu-Fe-S system at 600°C.

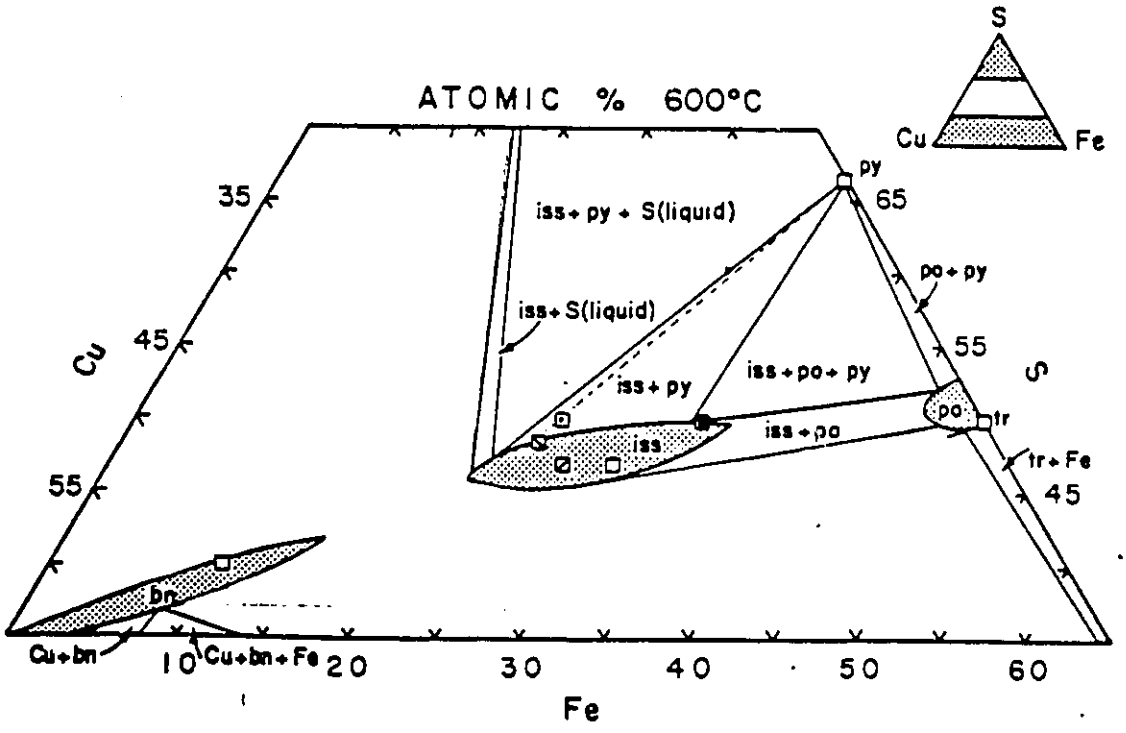

Some of the phase relations in the central portion of the Cu-Fe-S phase diagram are shown (from [17] p. cs-17). The dashed line is the tie line connecting the chalcopyrite composition ⊠ to iss and pyrite. Note that iss is greatly favoured over pyrite. The compositions indicated within the iss field are ▣ talnakhite, ⧄ mooihoekite, □ haycockite and ■ cubanite (see appendix 1).

occurrence of an extensive solubility field which exists over a large range of temperatures in the central portion of that diagram. This field, labeled intermediate solid-solution (iss) in order to maintain consistency with ref [74], will be shown (in the following) to be the analogue of our own β field. The iss field is of zincblende structure with lattice parameters in the vicinity of 5.36 Å.

Something which is not obvious from the diagram, is that there is no temperature at which chalcopyrite (x=1.0) exists in the iss field. Indeed it is known that $CuFeS_2$ deviates little from ideal stoichiometry up to its dissociation temperature of 557°C, at which temperature it becomes iss + pyrite. Pyrite itself undergoes a transition to pyrrhotite plus sulfur at 743°C [74]. Also, from the tie lines in fig.3.2.3 it can be seen that the relative proportion of iss to pyrite greatly favours the iss, with about 5 molar percent pyrite occuring at equilibrium.

As with the α field, we can use the above information to propose the characteristics of our other phase fields. The field marked $\beta' + \delta'$ appears to correlate to the $CuFeS_2$ dissociation to pyrite + iss, with our iss-equivalent β phase containing small amounts of Indium. The field directly above, labelled $\beta' + \eta + \varepsilon$ would then represent the equivalent iss (β') + dissociated pyrite (pyrrhotite + sulfur) phases. The horizontal nature of the upper boundary of the $\beta + \delta$ field would also seem to indicate that little or no Indium is incorporated into the pyrite (δ) phase.

$CuFeS_2$ has a magnetic transition (Neel temperature) at 550^0C [74] and this is the explanation for the first nearly horizontal line which appears above the composition axis of the diagram. Any sample containing γ phase will display a peak at the γ-Neel temperature. This is an example of the situation referred to earlier, in which the magnetic transition of an end-member gives a signature on the phase boundary diagram that could be mistaken for a polyphase-field boundary. The lower temperature of this transition as compared to T_N of chalcopyrite is taken to demonstrate the dilution of the $CuFeS_2$ with Indium, thereby lowering its transition temperature and signifying some solid solution from that end of the diagram.

The field marked γ_m represents a single phase field of magnetically ordered γ phase. The phase labelled γ_n is the non-magnetic (i.e. above the ordering temperature) γ phase. Most of the γ field boundary is invisible to the DTA due to its steepness (see section 2). The boundary shown on fig 3.2.2 has been estimated using a single phase limit of z=0.94 and a corresponding Neel temperature of 420^0C. These figures were arrived at empirically from the structure of the diagram.

The steep boundary on the left-hand side of the $\beta' + \eta + \varepsilon$ field is similarly inferred despite the lack of DTA data, however in this case we have the added knowledge of the small amount of pyrite which is produced in the Cu-Fe-S system indicating that this boundary is probably near the high Fe end of the diagram. In this case the possibility exists that

there is a continuous variation from β to β' over the phase diagram, hence no sharp boundary at all.

The high concentration-high temperature field marked β + L is known to consist of solid + liquid from heating to 950°C and observing the resulting fluid deformation of material. Finally the field labelled η+L coincides with the as yet uncharacterised 1010°C transition of $CuInS_2$ at the x=0 edge of the diagram.

The phase fields labeled α and γ, thus identified as probable chalcopyrite-structure fields, were chosen for an x-ray and Mössbauer study. Samples of composition x=0.05, 0.1, 0.15, 0.2, 0.3, 0.4, 0.5, 0.6, 0.7, 0.8, 0.85, 0.875, 0.9, 0.925, 0.95, 0.975 and 1.0 were re-annealed at 200±20°C for 70 days. They were subsequently air quenched to room temperature. This annealing temperature was chosen in order to intersect as large a portion as possible of the α field while allowing equilibrium to be attainable in a reasonable time, in other words compromising between a desirable higher annealing temperature and concurrent undesirably diminishing range of solid-solution.

That the 200°C anneal does achieve single phase conditions at low concentration was demonstrated by comparison of the x-ray patterns before and after the low-temperature anneal, the latter being single phase chalcopyrite and displaying a full complement of ordering lines, whereas before the annealing there were non-chalcopyrite as well as chalcopyrite lines present.

The success of such a relatively low temperature annealing of these highly covalent materials is attributed in part, to the fast rate of sulfur diffusion due to its low atomic weight, however it is important to remember that the approach to equilibrium also depends on dynamics sensitive to the microstructure[4].

The x-ray patterns of the resulting x=0.05, 0.1, 0.15 samples were characteristic of purely single phase chalcopyrite. A line which corresponds to the $CuFeS_2$ 112 is faintly visible on the x=0.2 composition sample, and 3 lines which correspond to $CuFeS_2$ are visible on the x=0.3 film. This is consistent with the Mössbauer spectra which resolve an increasingly intense $CuFeS_2$-like sextet in these samples (see section 3.3). In these materials, x-rays are about as sensitive as Mössbauer analysis as regards the detection of new phases, at least when the emerging phase is Fe-containing and displays a different Mössbauer multiplicity from the original one. An emerging Fe-containing phase which was above its magnetic transition temperature (i.e. paramagnetic) would not have been so readily detectable, since it would have contributed another singlet or doublet which could have been hard to distinguish from the one already present.

3.2.4) X-Ray Crystallography and Phase Data

It was found essential for obtaining accuracy, to

[4]Marcasite seems metastable relative to pyrite due to its conversion rate being inversely proportional to grain size [74 cs-28].

include a standard Si or Ge in each film and hence to use the technique described in chapter 2 to correct for the systematic errors associated with absorption in the Debye-Scherrer geometry. Ge was best suited to our materials due to the nesting of its pattern into the gaps of the $CuInS_2$-based one.

The variation of lattice parameters over the range of solid solution is approaching the limit of resolution of the x-ray technique. Thus a full compliment of lines, including high angle ones, is necessary in order to obtain precise values. Unfortunately, in these materials the high angle lines are broad and faint. This is presumed to be predominantly an intrinsic feature of these materials as discussed along with the more common broadening mechanisms in chapter 2. The natural c/a≠2 splitting, accompanied at high angles by the $K_{\alpha 1}$-$K_{\alpha 2}$ induced splitting, often resulted in overlapping of the blurred tails (edges) of the lines. This considerably reduced the resolution and hence the accuracy of the measurements based on these lines. Indeed the distortion-induced ($c/a \neq 2$) splitting is small and often comparable to the thicknesses of the individual components. For example, in some cases the relatively low angle doublet 332-316 could not be resolved but rather appeared as a single broad line[5]. For comparison, this same doublet in the x=0.05 sample was well resolved.

A factor which further decreased the resolution of the

5The direct signatures of the splitting in these cases were the lower-angle doublets.

x-ray photographs was the diffuse scattering background, which was noticeably stronger for the Fe-containing materials compared to the Mn alloys, and is due to the Cu, Fe and S incoherent scattering as discussed in section 2.1.

In order to maximize the precision of the lattice parameters, we can use to advantage the fact that the x-ray pattern overdetermines the lattice parameters. Thus even though we may know the exact indices of a given blurred or faint line, we can without a loss of integrity or accuracy, exclude it from the calculation of the lattice parameters because of the large random error it introduces.

A typical best fit for the purposes of obtaining accurate lattice parameters (a and c) was accomplished using 15 or so of the 20-22 lines present. Only well resolved lines were used, and the faint lines and poorly resolved doublets were often excluded from the fit which rendered the quoted lattice parameters.

The errors associated with our a and c values were arrived at by inputing estimated errors on the line positions into the fitting. It is useful to note that a probable error of .003 Å may be expected for typical powder photographs taken on a 12 cm. camera with its chamber at atmospheric pressure. Errors in stoichiometry shown in fig.3.2.4 represent an estimated typical error as found by the Mössbauer results (to be described in the following section).

The variation of lattice parameters (a & c) for the low temperature annealed (LTA) samples is shown on fig 3.2.4. The

Fig. 3.2.4 Lattice Parameter (a) vs. Composition (x)
in CuIn Fe S

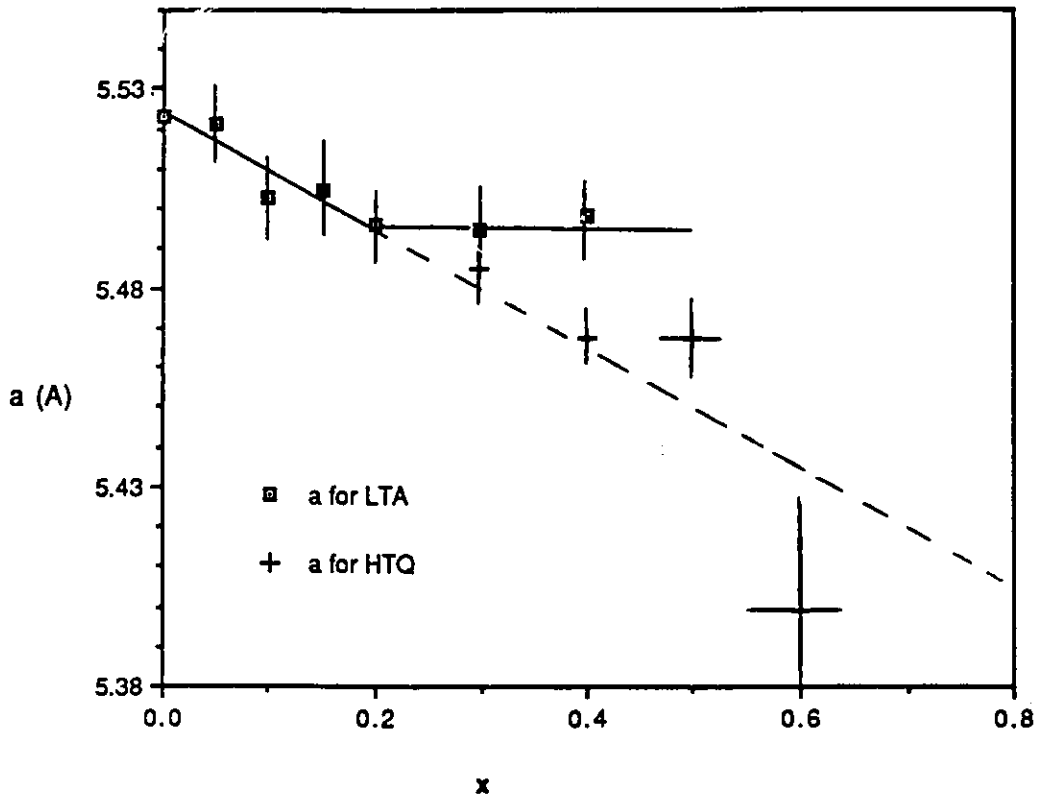

Fig. 3.2.4 illustrates the variation of lattice parameter (a) in the chalcopyrite (∝) phase of $CuIn_{1-x}Fe_xS_2$. The limit of single phase behaviour occurs at the point of intersection of the two lines drawn through the LTA sample data. The dashed line extrapolates the lattice parameter variation to the HTQ sample data. The HTQ samples are believed to be metastable chalcopyrite phase.

parameters were obtained by fitting via the standard least squares technique (see 2.1) to tetragonal structure. Since the experimental scatter of the points on the a vs z graph does not allow a more accurate analysis, straight line fits to the LTA sample points were used. The horizontal line segment illustrates the constant lattice parameter of the ch phase observed in the two phase field, and the intersection of the two lines marks the limit of single phase behaviour at x=0.2±.01.

The value of c/a was found to vary practically linearly with increasing x, from 2.02 to 2.00 as seen on fig 5. This is consistent with the reported value of c/a for $CuInS_2$ [4] and has the correct trend toward the c/a < 2 of $CuFeS_2$.

In an attempt to study the high temperature β field, quenched materials (labeled HTQ for high temperature quench) were prepared. Samples of the appropriate bulk compositions were powdered and sealed as usual. The samples were powdered in order to facilitate inter-grain diffusion and also to increase thermal contact with the sides of the ampoule in which they were sealed in order to facilitate the quenching process. They were quenched as rapidly as possible in cold brine after an annealing time of 2 weeks in the β field. The resulting powder photographs indicated a tetragonal phase discernable from cubic by the splittings 200-004, 220-204, and 312-116. However, due to the large amount of broadening, only low-angle lines for low Fe-concentration samples were clearly resolved.

Fig.3.2.5 Tetragonal Distortion c/a vs. Composition x
in CuIn Fe S

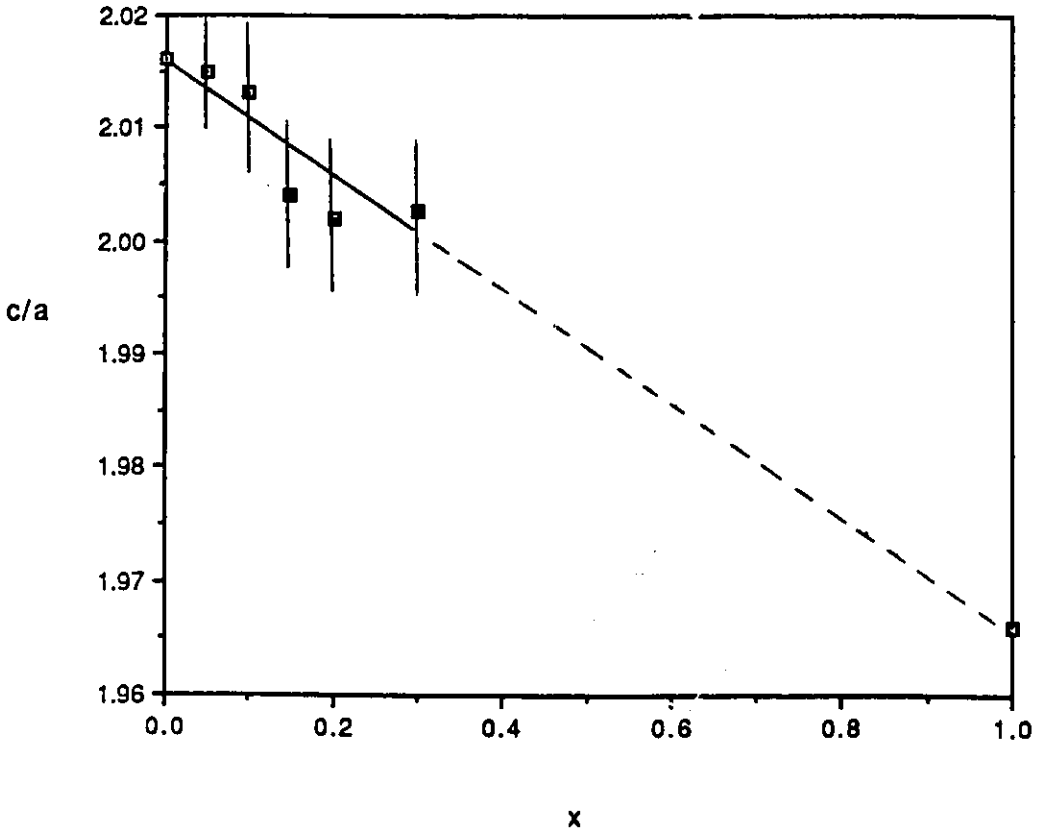

Fig.3.2.5 illustrates the variation of the tetragonal distortion with composition in the $CuIn_{1-x}Fe_xS_2$ system. Two data points above x=0.2 are representative of the HTQ materials, and have large errors due to the broadness of the corresponding diffraction lines. The value at x=1.0 corresponds to that of $CuFeS_2$. The α phase field extends up to x=0.2, however the tendency to form a tetragonal phase with c/a approaching that of $CuFeS_2$ with increasing x, can be seen in all the homogenous materials.

Despite the presence of chalcopyrite-like splittings in these quenched samples, it is proposed that the ß field is actually cubic-zincblende, and that upon quenching a metastable tetragonal phase is formed. This is due to the fact that a ch-like ordering of zincblende material involves only short-range ordering of tetrahedra which can occur quickly. The Fe-sulfides are also known to exhibit metastability and we will give more evidence for the interpretation of metastability in the case of $CuIn_{1-x}Fe_xS_2$ in other parts of this chapter.

The pronounced x-ray line broadening of the high concentration, HTQ samples is probably due to slight variations in composition. This can be understood in the context of the known behaviour of the Cu-Fe-S system. As mentioned in appendix 1, quenching from the iss field in that system has been suspected to produce chalcopyrite-like phases, which are thought to be stable. The possible stoichiometry of these phases is always close to the ideal (chalcopyrite) stoichiometry [74] which indicates that the free-energy surface of the system has many local minima. This feature of the system could manifest itself as slight variations in composition in the quenched materils.

The lattice parameters estimated from the HTQ samples are also graphed in fig 3.2.4. These fit reasonably well to the extrapolation of line beyond the limit of solid solution of the LTA material which occurs at z=0.2. This indicates the close relationship of the HTQ samples to the α phase material.

Samples from the high x end of the phase diagram were also annealed at 200^{0}C in an attempt to find a lattice parameter-variation which could indicate the solubility limit of $CuInS_2$ into $CuFeS_2$. However the x-ray data from these samples did not indicate the composition of the right hand phase boundary since the $CuFeS_2$-like γ phase proved to be indistinguishable from $CuFeS_2$. This together with the absence of an observable DTA phase boundary at the high z end of the diagram indicates that the boundary is nearly vertical (see chapter 2 section on DTA) and situated close to the x=1.0 ($CuFeS_2$) edge. If it were not close to the x=1.0 edge, we would probably discern a shift in the lattice parameter of the Fe-rich samples just as we did for the In-rich end. More importantly the presence of α-phase lines as observed on the x=0.9 film indicates the minimum possible x for the right-hand phase boundary to be in the vicinity of x=0.95.

It is possible to estimate the right hand (high x) boundary by using the lever rule which states;

$$\frac{A_\alpha}{A_\gamma} = \frac{x_r - x_o}{x_o - x_1} \qquad 3.2.1$$

that the molar ratio of amounts of the two phases equals the ratio of lengths of the "levers" connecting the bulk composition x_o to the right (x_r) and left (x_1) phase boundaries (see fig 3.2.6).

In order to carry this out, an estimate of the relative amounts of phases from a sample at equilibrium in the two-phase field is required. Thus a set of samples were

Fig. 3.2.6 Illusration of the low temperature annealed (LTA) samples in relation to the phase diagram.

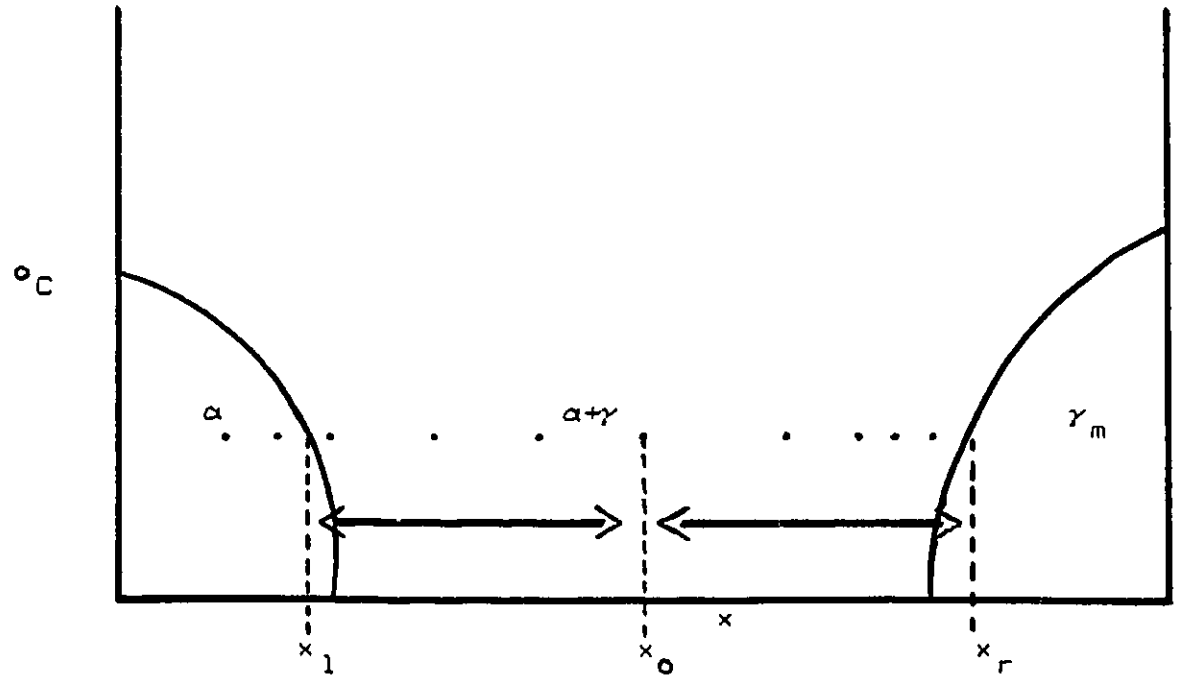

The low temperature portion of the CuInFeS phase diagram is shown schematically. The points represent sample compositions prepared for analysis. Also shown are the 'levers' from the relative amounts of the two phases can be found according to eq. 3.2.

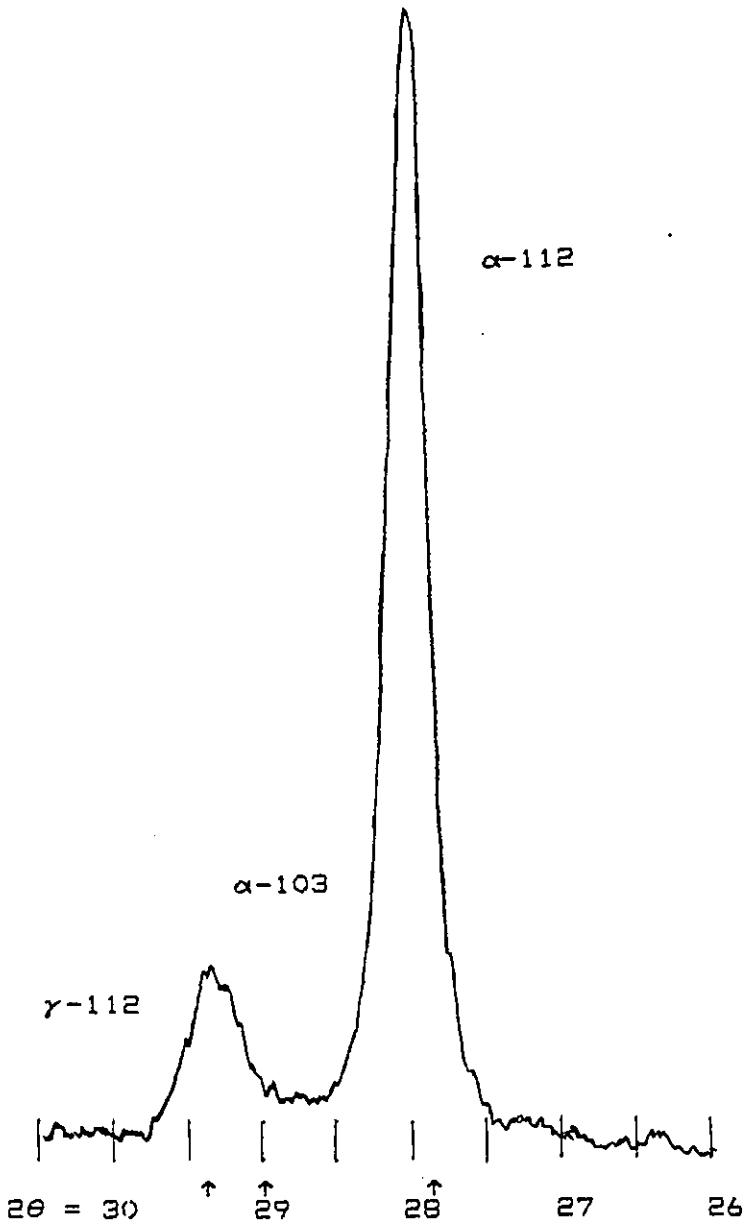

Fig. 3.2.7 Diffractometer trace of $CuIn_{0.7}Fe_{0.3}S_2$ LTA sample. Arrows indicate the positions of the α-112, α-103, and γ-112 reflections. The angles shown are equal to 2θ.

annealed at 200°C (LTA), along the tie-lines illustrated in fig. 3.2.6, and diffractometer traces were obtained for a few select lines of their diffraction patterns in order to get relative intensity measurements. Unfortunately the errors in the experimental intensities were too large to make this analysis useful. One example of a resulting diffractometer trace is given in fig.3.2.7.

3.2.5) Synopsis

The combination of DTA and x-ray analysis of the alloy system chosen for study indicates some important features of its phase diagram. Of particular interest is the existence of a low-temperature chalcopyrite-phase field exhibiting solid solution with the magnetic component.

Further characterization by other techniques could be useful in determining the precise locations of some vertical phase boundaries since the x-ray lever rule analysis proved not to have the desired precision. Also some ambiguities remain in the identification of certain high temperature phases.

3.3) Mossbauer Spectroscopy of $CuIn_{1-x}Fe_xS_2$

Room temperature Mössbauer spectroscopy was carried out on a wide range of alloy compositions. Data collection usually required approximately 48 hours, however for some low-x samples twice as much time was required to attain good statistics. The resulting spectra were analyzed with MINUIT with appropriate subroutines written by M. Royer. The fitting procedure (as described in chapter 2) can be very model-dependent. However it was often found that just the qualitative features of the spectra were sufficient to yield valuable information about the materials.

Lorentzian line fits to the Mössbauer spectra of various samples are illustrated in figs. 3.3.1, 3.3.2, 3.3.3, and 3.3.4. The parameters resulting from these fits are displayed in table3.1.1.

Fig.3.3.1a represents sample x=1.0, the synthetic $CuFeS_2$ obtained from the melt only (i.e. not annealed). A small amount of FeS_2 is also visible, as can be seen by comparison to Fig.3.3.1b. An upper limit to the relative amount of FeS_2 in this sample can be estimated from a naive intensity measurement (see chapter 2) and yields 7% of the Fe in FeS_2. Some residual FeS_2 is expected for samples with $x \geq 0.8$ since these compositions pass through the high temperature FeS_2 containing phase fields upon cooling (see fig. 3.2.2). Fig. 3.3.1b is the spectrum of a commercially obtained FeS_2 (pyrite), the prominant quadrupole doublet is characteristic of this material. Fig.3.3.1c represents a sample of naturally

Table 3.1.1 Experimental Mössbauer Parameters

Sample	Phase	QS(Δ) (mm/s)	CS(δ) (mm/s)	HWHM (mm/s)
x=0.1 LTA	α	0.170	0.297	0.183
	β	2.16	0.601	0.262
x=0.15 LTA	α	0.205	0.293	0.174
	β	2.16	0.601	0.262
x=0.2 LTA	α	0.191	0.311	0.193
x=0.1 HTQ	α	0.104	0.279	0.275
	β	2.16	0.601	0.262
x=0.2 HTQ	α	0.247	0.292	0.301
	β	2.16	0.626	0.269
x=0.3 HTQ	α	0.0	0.314	0.448
	β	2.15	0.640	0.262
x=0.4 HTQ	α	0.348	0.299	0.341
	β	2.16	0.600	0.262f
x=0.6 HTQ	α-β?	0.0	0.309	0.579
x=0.6 LTA	α-β?	0.429	0.330	0.290
x=0.4 LTA	α	0.0	0.292	0.306
x=0.7 LTA	α	0.0	0.289	0.495
FeS_2	δ	0.623	0.312	0.162
$CuFeS_2$ (Synthetic)		0.015	0.246	0.139
$CuFeS_2$ (Natural)		0.052	0.246	0.140

Table 3.1.1 summarizes the observed Mössbauer parameters for the Fe-containing samples. The parameters represent the best fit of the spectra to Lorentzian lines. The α phase refers to the component responsible for the narrow doublet, and the β phase is responsible for the wide doublet which is especially apparent in the quenched (HTQ) samples. QS and CS refer to quadrupole splitting and center shift respectively, while HWHM refers to the width of the spectral lines.

Fig.3.3.1 Some important Mossbauer spectra.

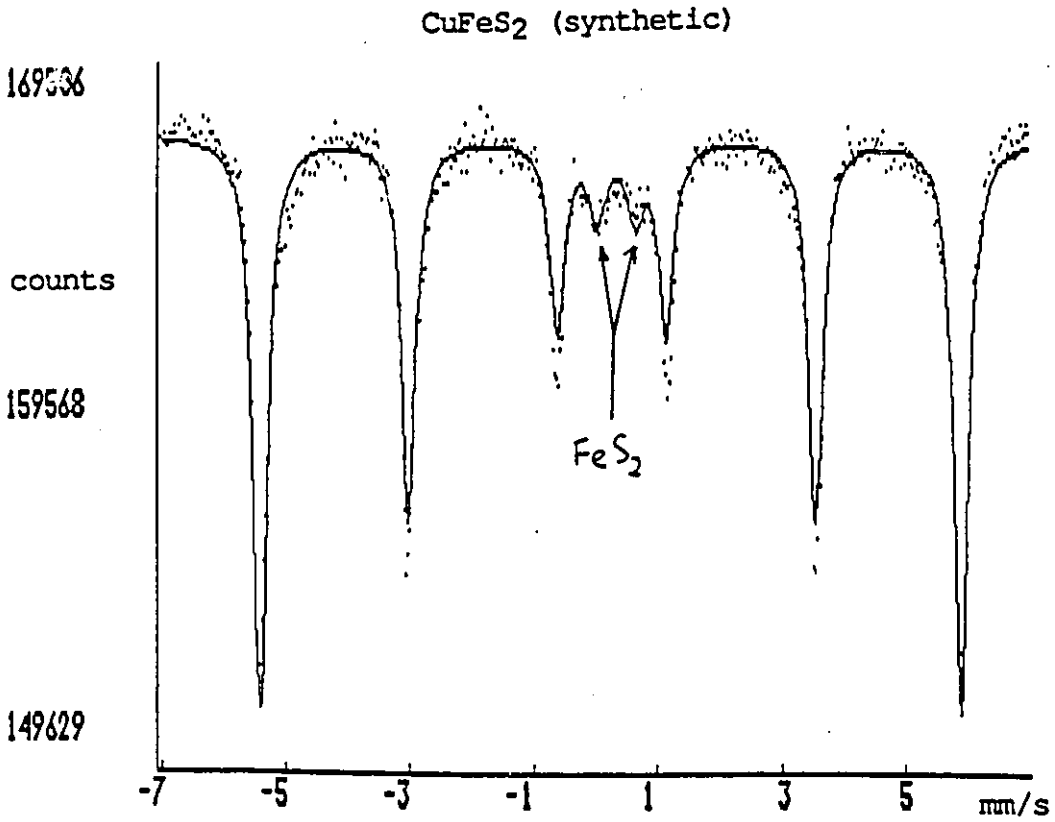

Fig.3.3.1a shown above is the rc m temperature Mössbauer spectrum of the synthetic (x=1.0) $CuFeS_2$ sample. The hyperfine sextet pattern seen is characteristic of the magnetically ordered material. A small amount of FeS_2 contribution can be seen by comparing to the spectrum on fig.3.3.1b on the following page.

Figures 3.3.1b and 3.3.1c (following page). The spectrum shown in fig.3.3.1b is that of FeS_2. The spectrum 3.3.1c is that of the rock 'chalcopyrite' sample. The natural material (3.3.1c) displays a large amount of FeS_2 as well as other impurity contributions.

Fig. 3.3.1b FeS_2

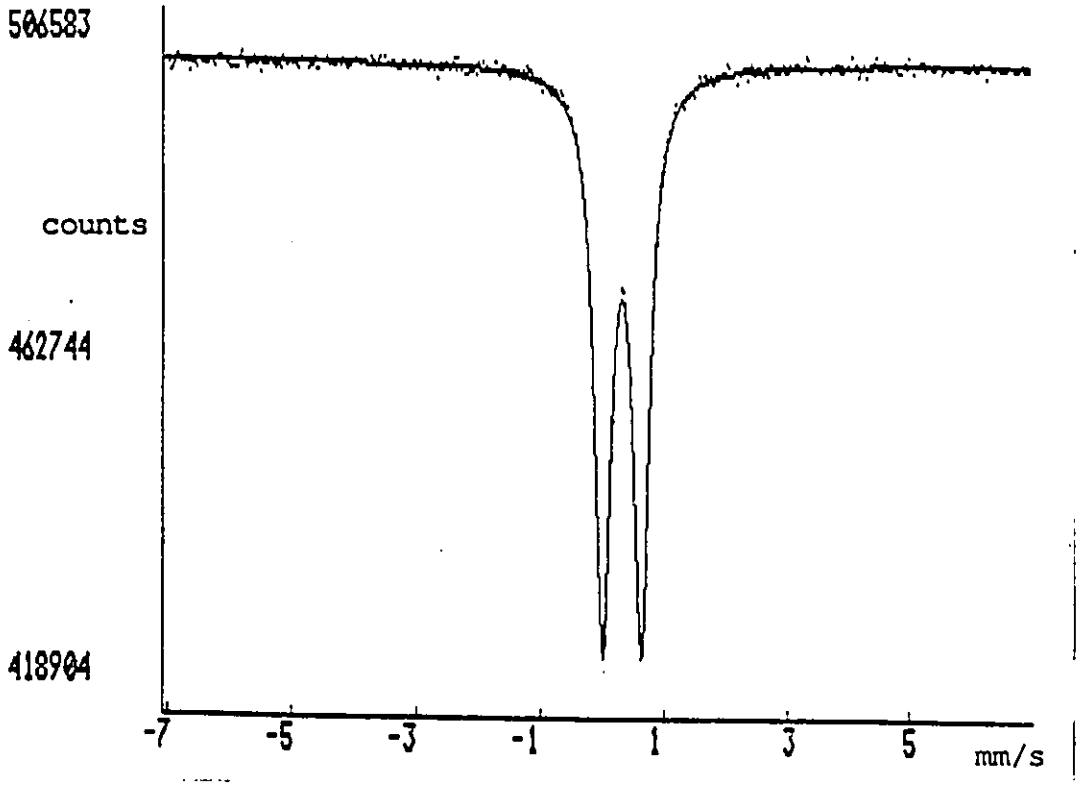

Fig. 3.3.1c $CuFeS_2$ (natural)

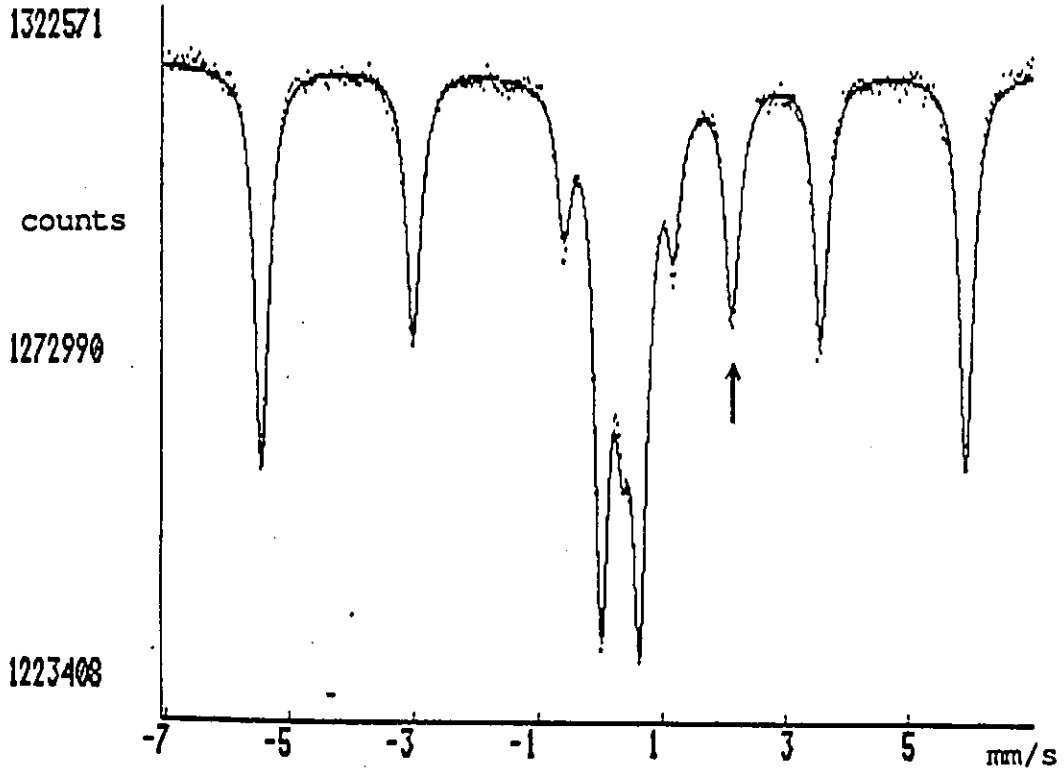

occuring chalcopyrite mineral obtained by Dr. Rancourt from the Geology department. Along with $CuFeS_2$ and FeS_2 seen to be present in this sample, there is also an unidentified doublet, the right hand member of which is marked with an arrow in the figure.

On both the figs. 3.3.1a and 3.3.1c can be seen the discrepancy in the sextet peak heights due to the absorption effect (see chapter 2) This misfit occurs because the absorption tends to equalise peak heights while the fitting program forces the correct 3:2:1 ratio of the peak heights derived from the nuclear transition probabilities.

Figs. 3.3.2 and 3.3.3 show the spectra of the LTA samples as indicated on fig.3.2.6. Figs. 3.3.2a and 3.3.2b obtained from the LTA x=0.1 and x=0.15 samples display an additional doublet which accounts for approximately 15% of the Fe in these samples. This doublet is identical to that found in other present samples and will be discussed in the following. Note that 15% of the Fe represents only 0.75% of the cations present in this sample, hence if the doublet represented another phase in which each Fe was accompanied by a total of 2 or 3 other atoms (Cu, In, or S), that phase would only account for 1% or 2% of the total mass present and could thus remain invisible to the x-ray diffraction. Indeed no extra lines are visible on the x-ray photographs of these samples. The other possibility, which will be discussed presently, is that the doublet is due to the occupation of a second distinct Fe site within the single phase material.

Fig. 3.3.2 Mossbauer spectra of low temperature annealed (LTA) $CuIn_{1-x}Fe_xS_2$.

Fig.3.3.2a $CuIn_{1-x}Fe_xS_2$ x=0.1 LTA

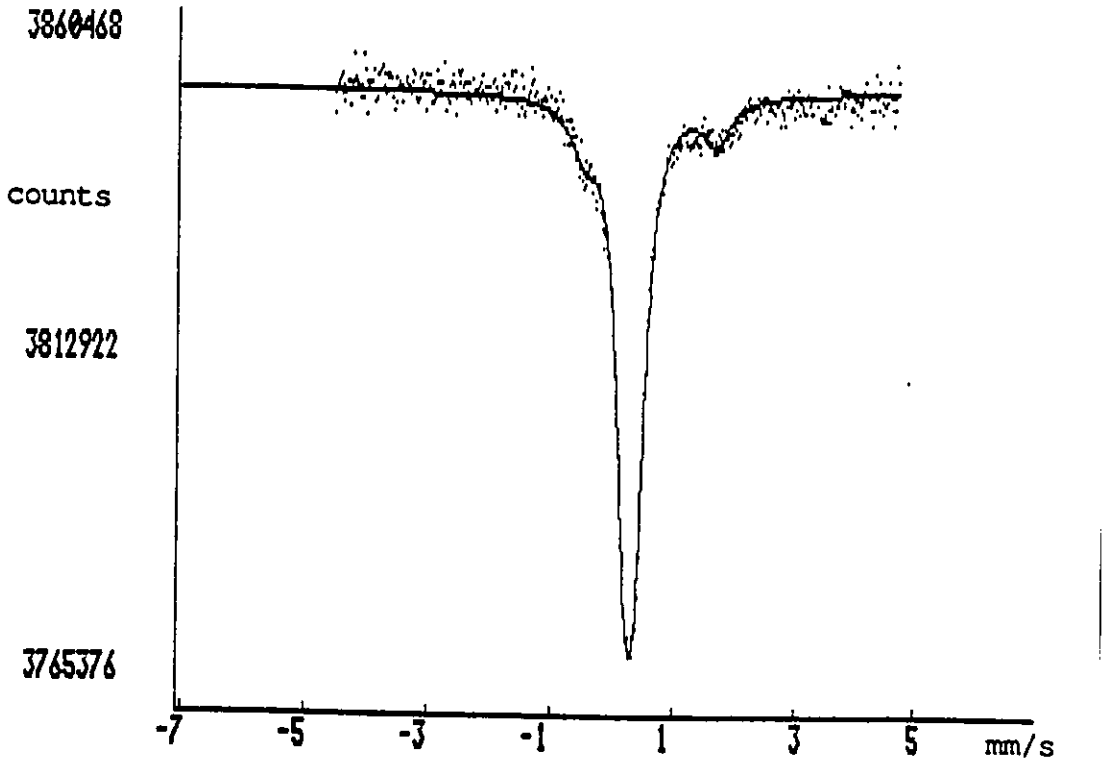

Fig. 3.3.2a is the spectrum of the LTA x=0.1 sample. This, and the following spectra illustrate the 'singlet' and the wide doublet.

Figs. 3.3.2b and 3.3.2c (following page) are the spectra of the LTA x=0.15 and x=0.2 materials. The presence of γ phase can be seen in the x=0.2 sample. The limit of single phase behaviour is characteristic of the 200 °C annealling temperature.

Fig.3.3.2b $CuIn_{1-x}Fe_xS_2$ x=0.15 LTA

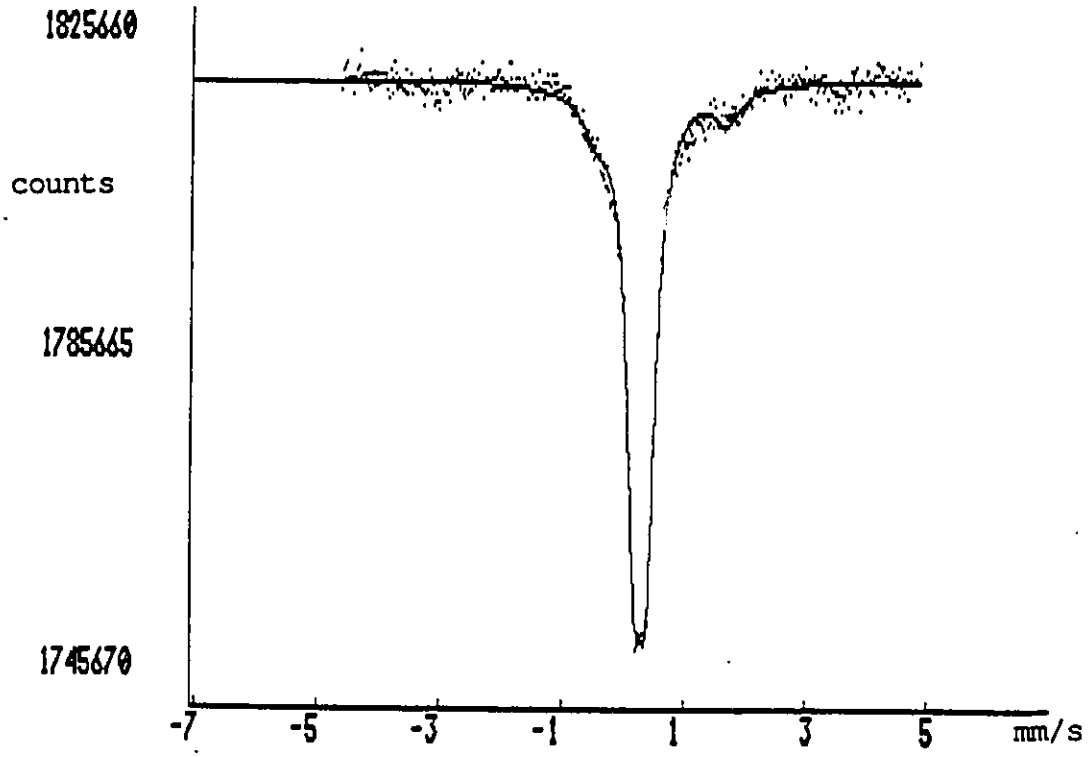

Fig.3.3.2c $CuIn_{1-x}Fe_xS_2$ x=0.2 LTA

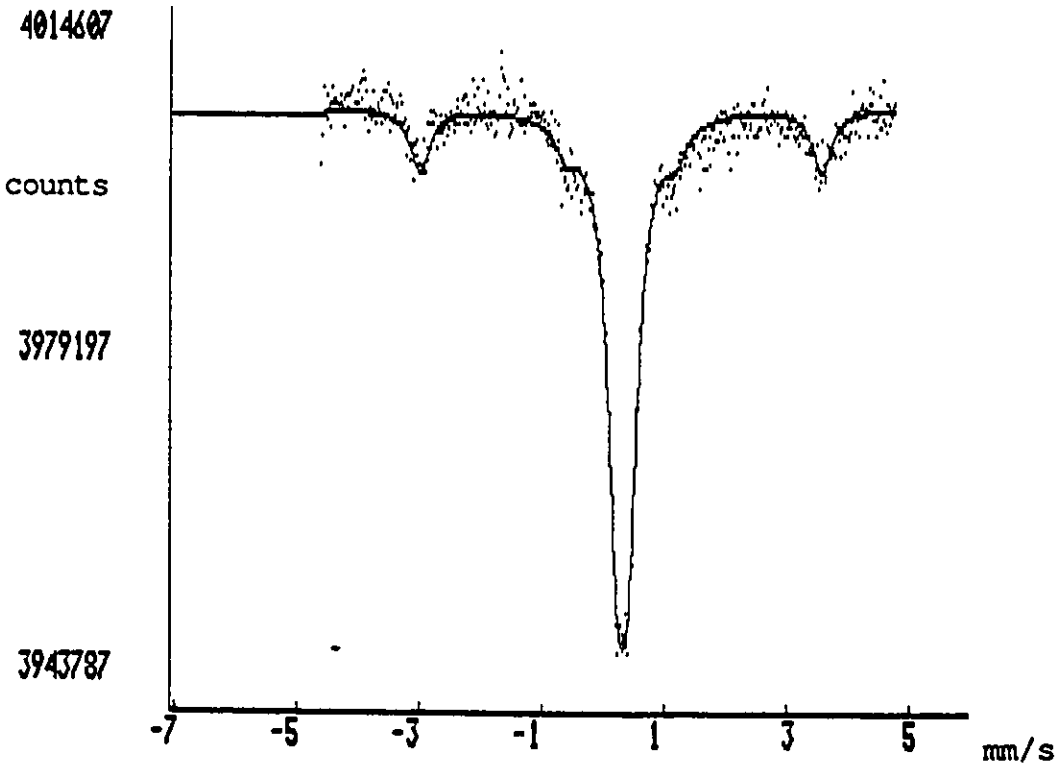

The central broad feature in these, the other LTA and (as will be shown) the HTQ samples is attributed to the α phase. It will be refered to as the 'α doublet'. It fitted reasonably well to a single closely spaced Lorentzian doublet even though in principle it probably has a complex profile composed of a discrete distribution of Lorentzian singlets and doublets. Such a line profile would be expected for a random distribution of Fe on mostly the chalcopyrite Indium sites. Reference 7 gives a geometrical explanation, and the ESR evidence for the existence of two inequivalent magnetic sites in the case of Fe doped $CuGaS_2$ which leads to a splitting of the ESR lines. For the same reasons one could expect a composite Mössbauer spectrum of the alloyed material even from a sample in equilibrium. For our purposes, the Lorentzian fitting is sufficient to extract phenomenological line parameters in a consistent way. The α doublet is qualitatively similar to the absorption peak found in the case of $CuGa_{1-x}Fe_xS_2$ [73].

Fig.3.3.2c shows the emergence of the γ phase in the bulk z=0.2 sample, likewise more γ was produced by annealing at higher temperature (not shown). Figs. 3.3.3a, 3.3.3b show typical spectra obtained from annealing in the $\alpha+\gamma$ field, the increasing amount of γ phase resulting from an increase in the bulk composition is further seen.

Fig.3.3.3c and 3.3.3d show spectra from two high x samples one (x=0.85) of which obtained from the Venezuelan group. As expected from the structure of the phase diagram

Fig. 3.3.3 Mossbauer spectra of low temperature annealed (LTA) $CuIn_{-1x}Fe_xS_2$ samples.

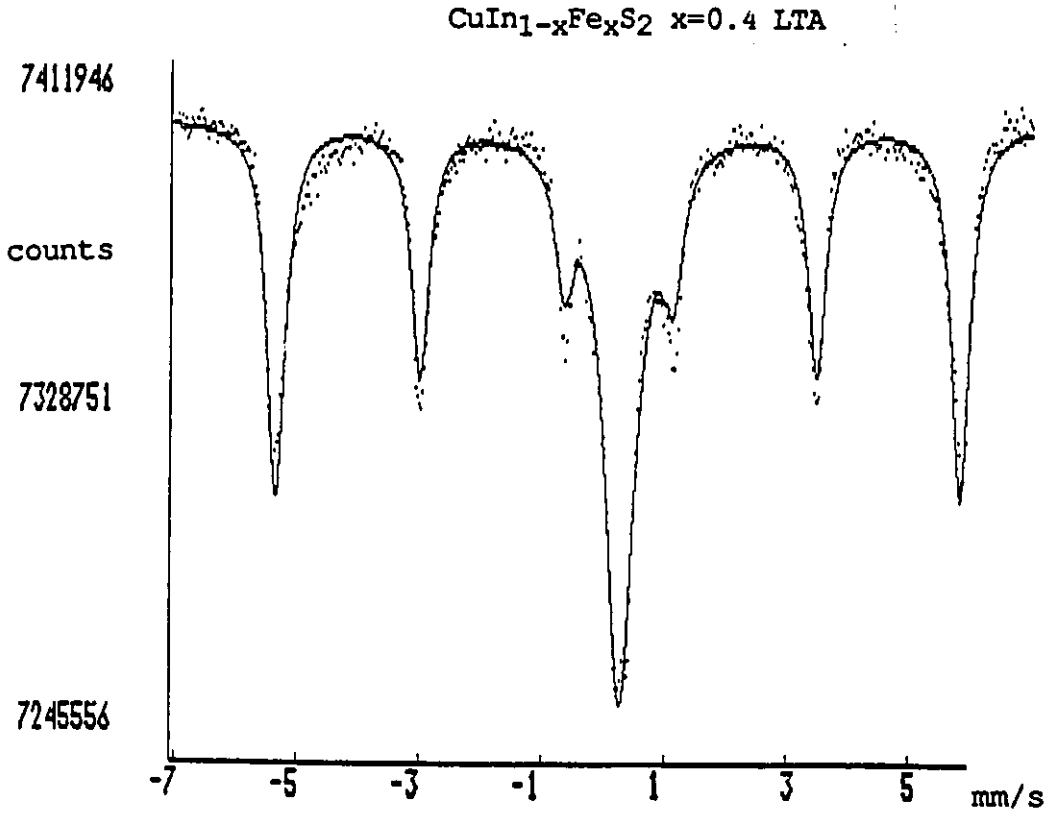

Fig.3.3.3a Mossbauer spectrum of LTA x=0.4 sample. The presence of both α and γ phase can be seen.

Figs. 3.3.3b and 3.3.3c are seen on the following page. 3.3.3b is the spectrum of the x=0.6 LTA sample and can be seen to contain FeS_2. This spectrum is very different from that of the x=0.6 (HTQ) sample of fig.3.3.4d. The x=0.85 sample obtained from the venezuelan group also contains FeS_2 as can be seen in fig.3.3.3c (following page). The relative amounts of FeS_2 was found to vary greatly from sample to sample in the iron rich LTA series.

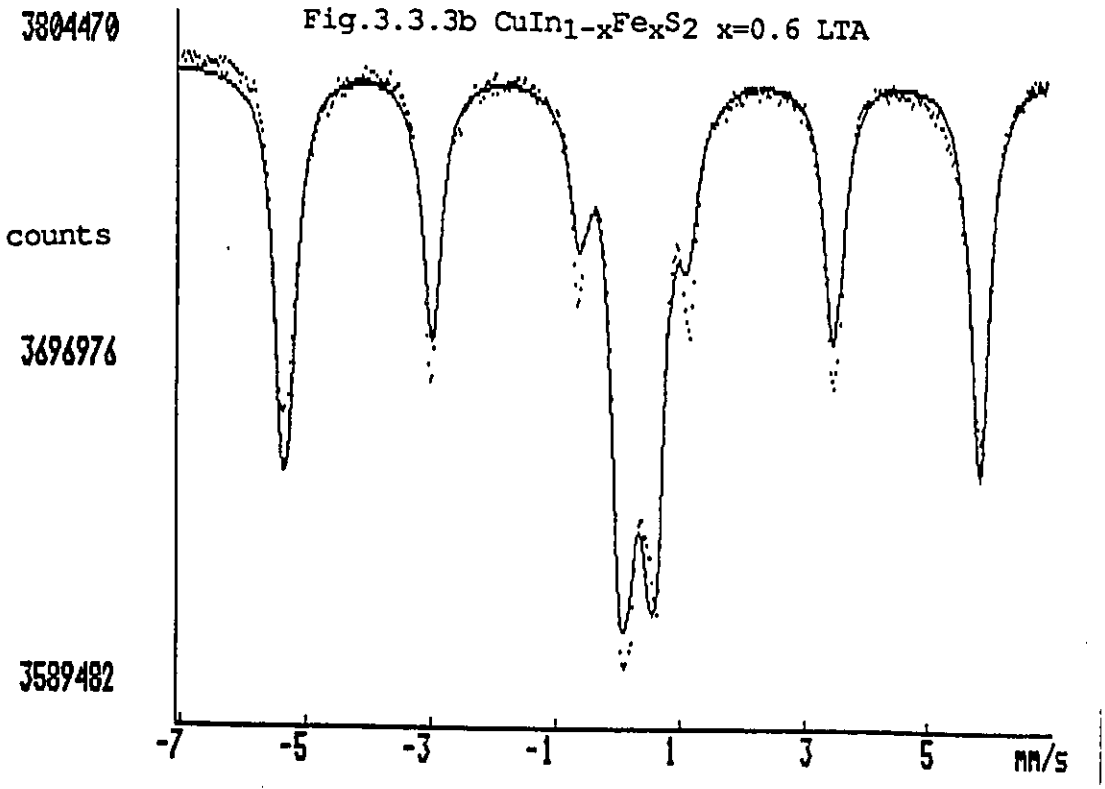

Fig.3.3.3b $CuIn_{1-x}Fe_xS_2$ x=0.6 LTA

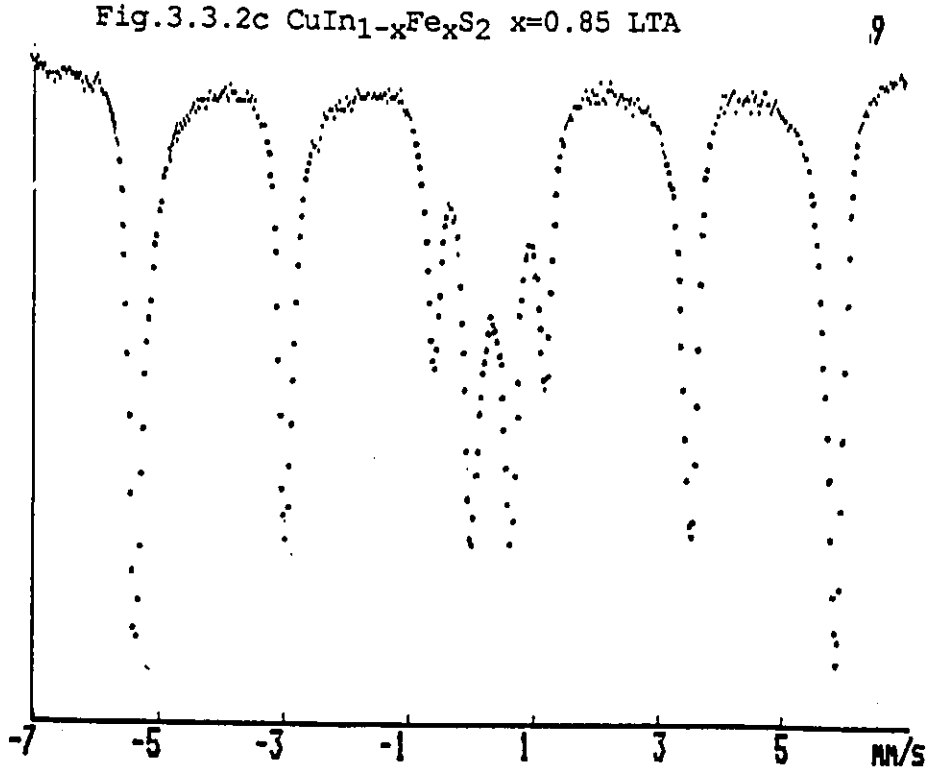

Fig.3.3.2c $CuIn_{1-x}Fe_xS_2$ x=0.85 LTA

Fig.3.3.3b illustrates a fit to the LTA x=0.6 sample. This fit contains 62% , 22% phase and 16% FeS_2. A large amount of FeS_2 is also evident in Fig.3.3.3c which is the unfitted data for the x=0.85 Venezuelan material.

(fig. 3.2.4), these high x samples have considerably more FeS_2 than the lower x samples. It is significant to note however that even after LTA heat treatment, the FeS_2 remains in these samples; FeS_2 is visible in the x-ray films of the x=0.85 and x=0.9 LTA compositions.

The relative amounts of γ to FeS_2 can be roughly estimated from the x-ray films themselves and is consistent with the equilibrium amounts at high temperature in the Cu-In-S phase diagram. As seen previously, the intensities of the x-ray lines can be related to the relative amounts of material if certain plausible assumptions are made. In the case of the Mössbauer spectra, a similar type of analysis can yield upper limits to the amounts of closely related materials but the absorption of these samples precludes any easy estimates of the intensity.

Fig.3.3.4 shows the HTQ sample spectra. The central broad feature, associated with metastable α phase, was fitted to a Lorentzian line shape. The wider doublet has the same characteristics as that found in the LTA samples. Its Mössbauer parameters[1] of large isomer shift; δ=0.6 mm/s and large quadrupole splitting; Δ=2.2 mm/s are indicative of Fe^{2+} although the center shift is rather lower than usually expected for such ions. The wide doublet (to be referred to as the 'β doublet') is especially prominent in the low z samples and is not discernable in the z=0.6 sample whose central α line profile is broad enough to include it.

[1]These parameters are discussed in chapter 2.

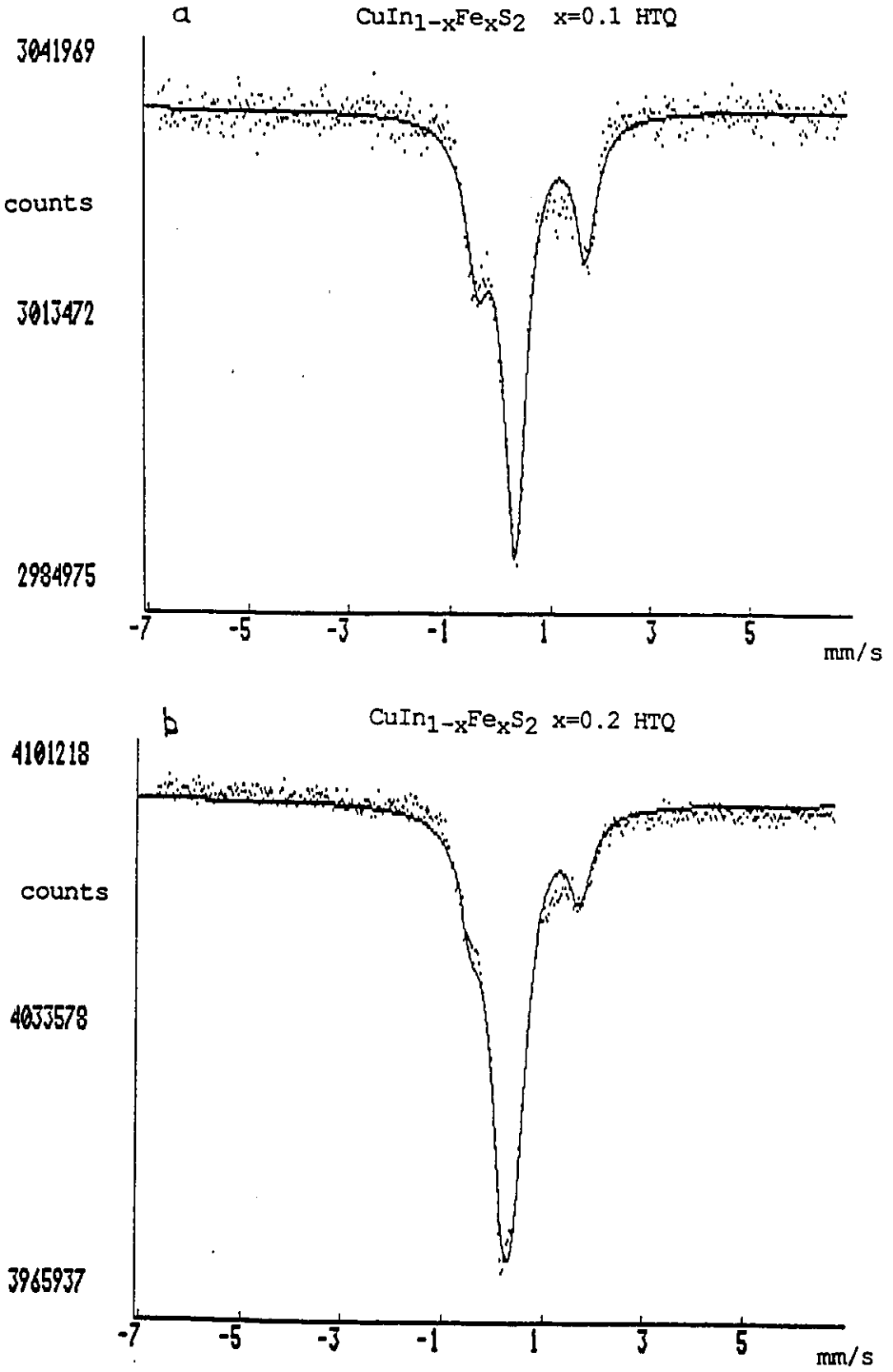

Fig. 3.3.4(a & b) Mossbauer spectra of high temperature quenched (HTQ) $CuIn_{-1x}Fe_xS_2$ samples with x=0.1 (a) and x=0.2 (b) showing enhancement of wide doublet.

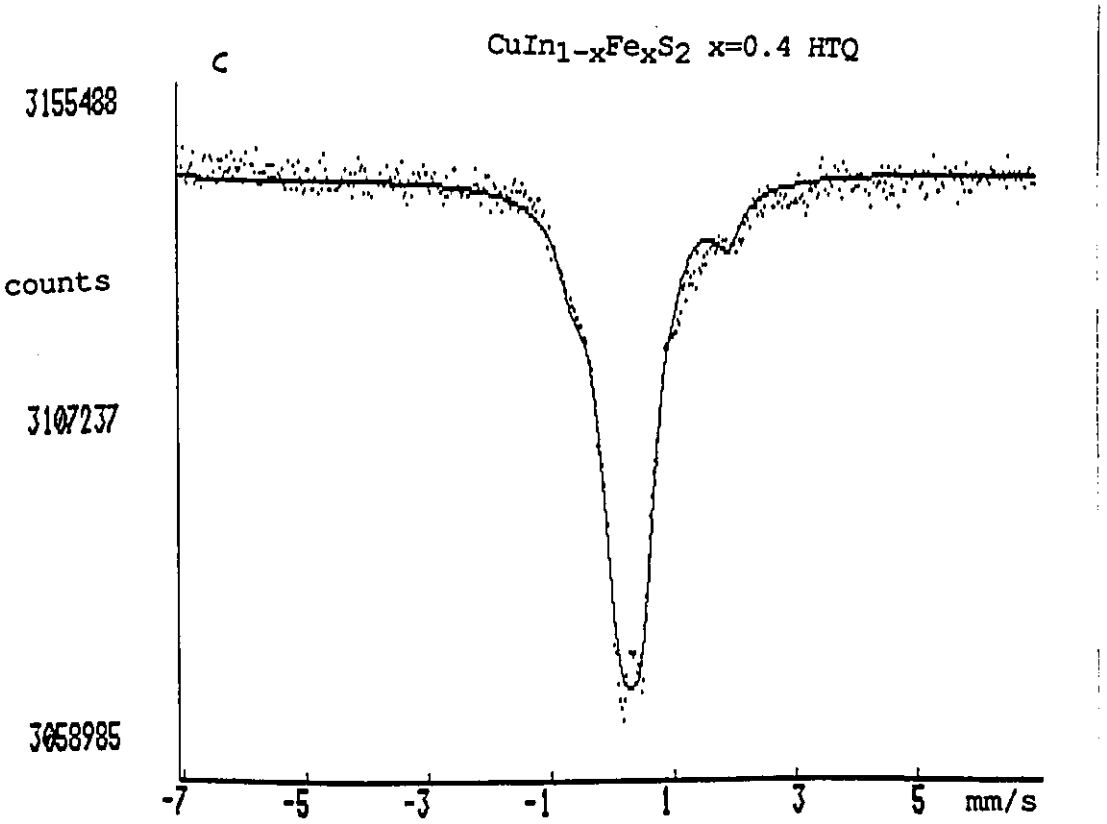

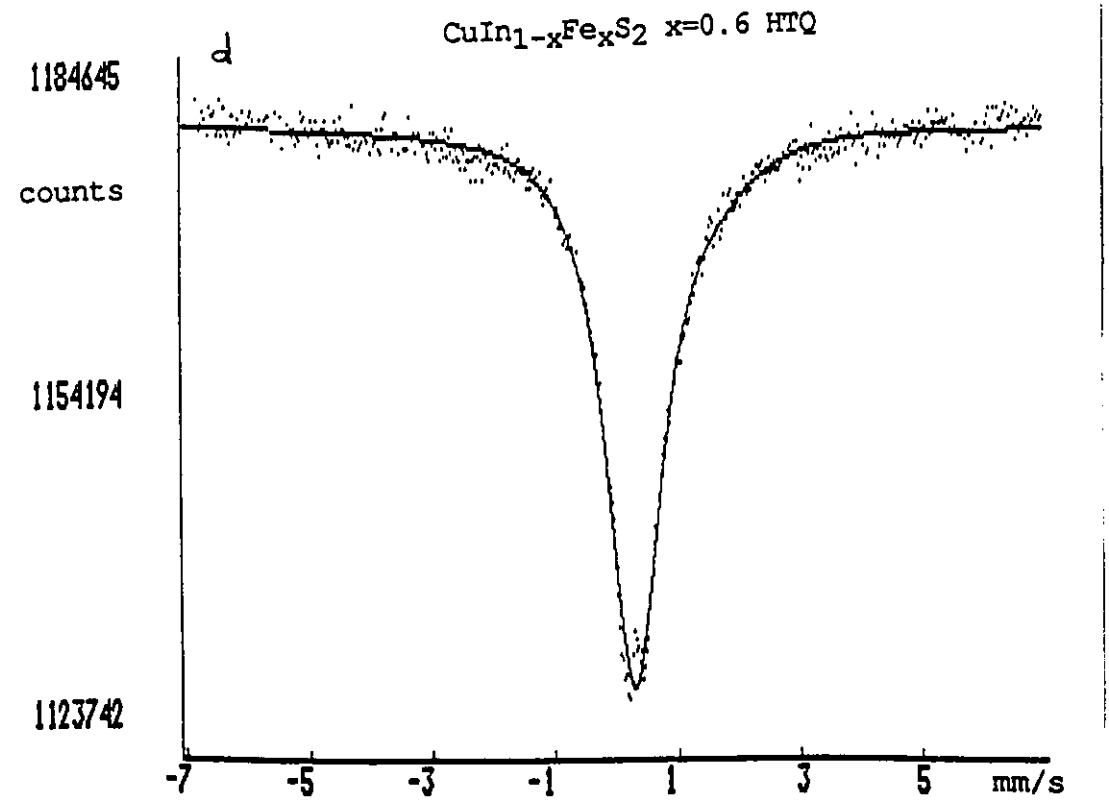

Figs. 3.3.4(c & d)_Mossbauer spectra of high temperature quenched (HTQ) $CuIn_{-1x}Fe_xS_2$ samples with x=0.4 (c) and x=0.6 (d). Note the contrast between the HTQ (fig.3.3.4d) and LTA (fig 3.3.3b) samples with x=0.6.

A plausible explanation for the presence of Fe^{2+} in these samples is based on the supposition that Fe^{2+} occurs as a substitutional defect on Cu sites. Such defects would be expected in the HTQ cases if the quenching process was sufficiently rapid that the Fe could not order fully, and in the LTA cases as smaller equilibrium concentrations of defects. In the cubic β phase the Cu and In randomly occupy the cation sites. Thus even if the Fe atoms stoichiometrically substitute only Indium atoms in the cubic phase, some would be found on sites which would belong to the Cu in the chalco-phase. This means that upon incomplete ordering after quenching, some Fe would be 'frozen' into chalco-Cu sites. Since Fe is not stoichiometrically replacing Cu, each of these Fe-site defects implies a misplaced Cu atom as illustrated in fig. 3.3.5.

If the misplaced Fe were still to behave as 3+ and the misplaced Cu as 1+, this would result in two unbalanced tetrahedra as shown in the figure. These tetrahedra would then act as a double donor and double acceptor respectively. It is possible that a charge transfer between these two tetrahedra could be more energetically favourable than the double-donor double-acceptor configuration. Such charge transfer would introduce Fe^{2+} and Cu^{2+} states in the partially ordered material. In other words, the β doublet in the HTQ and LTA materials could represent Fe on chalcopyrite Cu sites and is especially prominent in the HTQ samples as expected.

This is consistent with there being no extra lines

Fig 3.3.5 Fe^{2+} defect sites in the chalcopyrite lattice.

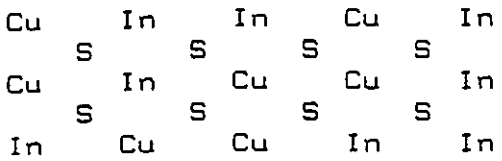

a) Part of the zincblende lattice; β-$CuInS_2$.

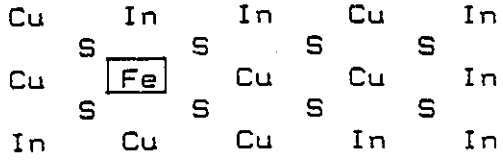

b) The same lattice as (a) with an Fe replacing an In

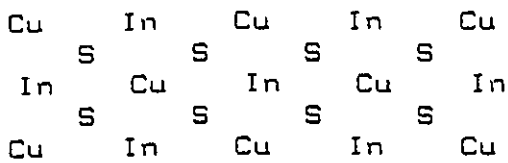

c) The chalcopyrite form of lattice (a); α-$CuInS_2$

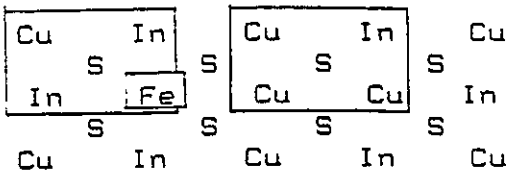

d) Illustration of an Fe frozen into an α Cu site creating electrically imbalanced tetrahedra.

Fig. 3.3.5 illustrates the sequence of events which could lead to the formation of Fe(II) states in the $CuIn_{1-x}Fe_xS_2$ lattice; (a) zincblende structure (the chalcopyrite structure is included in (c) for comparison purposes), (b) substitution of Fe(III) for indium, (d) creation of substitutional defect with subsequent charge transfer (not illustrated).
Local charge balance is approached in (d) if two neighbouring tetrahedra (shown in boxes) transfer a single charge and thereby create Fe(II) and Cu(II) states.

attributable to a new Fe^{2+} containing phase on the x-ray patterns of the materials. This is especially evident in the HTQ x=0.1 sample in which approximately half the Fe (which could imply about 15% by weight of the material) would need to be accounted for in such a phase.

Note that a competing interpretation for the Fe^{2+} is that it is due to non-stoichiometry. Indeed the presence of Fe^{2+} in non-stoichiometric $CuFeS_2$ has been indicated [75], nevertheless it seems unlikely that such large changes in composition as are implied by the amounts of Fe^{2+} in the quenched samples would not affect the x-ray patterns in an easily discernable way. More evidence for the substitutional defect interpretation lies in the Mössbauer quadrupole splitting parameter to be discussed later.

It is interesting to notice that the presence of donor and acceptor states would affect the electrical and optical properties of the materials hence measuring these could elucidate the nature of the proposed defects. Recent studies have examined the properties of some Fe-doped materials [76] [13].

From the relative intensities of the β and α doublets in these materials, it would seem that the amount of Fe^{2+} is roughly constant- independant of the bulk composition.

3.3.1) Interpretation of the Mossbauer Parameters

The observed width (2*HWHM + quadrupole splitting) of the α doublet for all the LTA and HTQ samples is plotted in

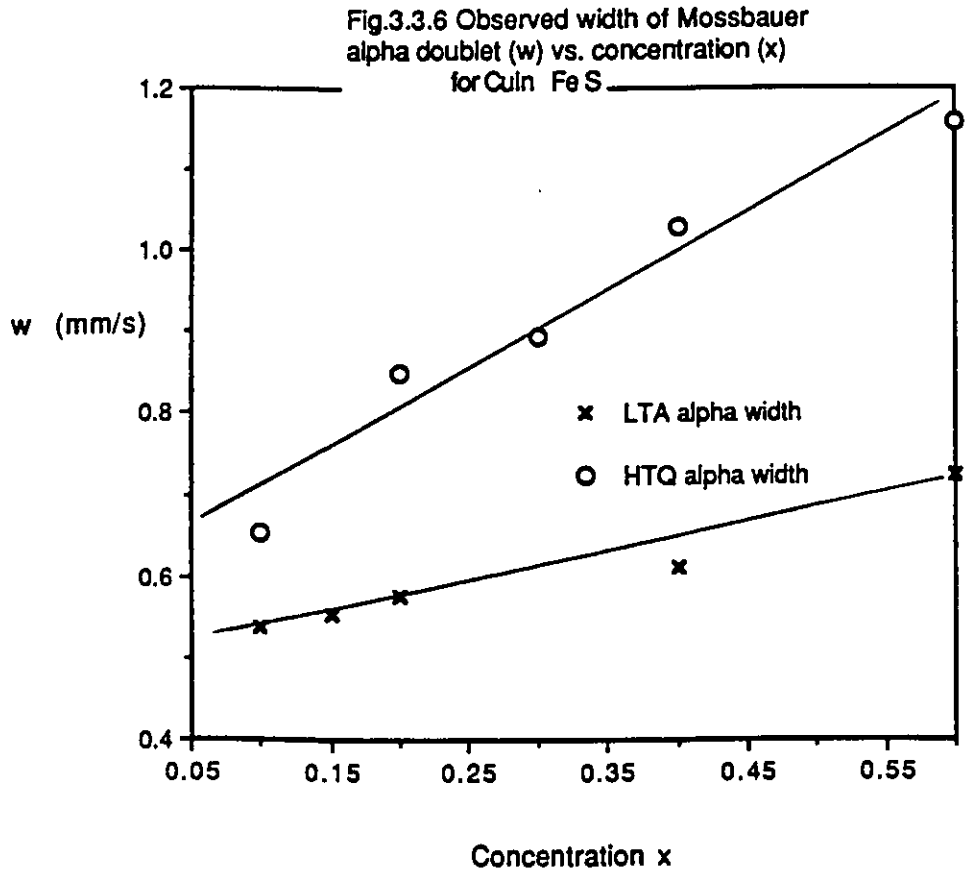

Fig.3.3.6 The observed width of the α doublet for the LTA and HTQ $CuIn_{1-x}Fe_xS_2$ samples. The observed width is taken to be $2*HWHM + \Delta$.

fig. 3.3.6. The trend of increasing width with increasing concentration is evident. The fact that the LTA samples display a monotonic increase in width is taken as evidence of the alloy broadening. It would then be expected that the broadening, for the most part stops at the saturation value, $x \approx 0.2$ of the alloy. The fact that the HTQ materials have slightly higher width which do not saturate, is consistent with those materials being closely related to α phase but displaying an extra broadening effect due to the quenching-in of high temperature lattice defects such as vacancies and substitutional defects as discussed above, and possibly due to other effects to be discussed. Such defects would increase the variety of Fe sites available hence the added broadness of the HTQ α lines. The fact that the width does not saturate in the HTQ case, seems consistent with the β field being single phase.

It is possible that the width of the HTQ spectra is also due to an averaging of Fe^{2+} and Fe^{3+} spectra. This would be caused by rapid charge transfer oscillations between neighbouring Fe^{2+} and Fe^{3+}, and will be discussed in the following.

As shown in the discussion on Mössbauer spectra in chapter 2, that the signature for oscillations between Fe^{3+} and Fe^{2+} which occur at a frequency comparable to the Mössbauer measurement time (10^{-7} sec.), is a single averaged Mössbauer spectrum. The possibility of such behaviour in the alloy system can be seen from the line broadening of the HTQ

sample spectra. The sequence of spectra in fig. 3.3.4 shows an increasing broadening of the HTQ α and β-doublets, the increasingly poor fit of the β-doublet tc a simple Lorentzian profile is especially apparent. The final outcome of this broadening is exemplified in the HTQ x=0.6 sample (fig. 3.3.4d) in which case the two spectra are no longer distinguishable, but what remains has characteristics of both.

Iron charge transfer transitions have been reported from infrared luminescence data of Fe-doped $CuGaS_2$ and $CuAlS_2$, and are attributed to charge transfers leading to a mixed Fe^{3+}- S and Fe^{2+}- S^- state [77]. This suggests that Fe^{2+}-Fe^{3+} oscillations could be mediated through the anions and thus acquire a concentration dependance as the number of Fe^{2+} and Fe^{3+} neighbours varies.

The sextet patterns in the LTA samples fit reasonably well to $CuFeS_2$, the main difference seems to be a systematic increase in HWHM relative to the rock sample. This may be due to the alloy broadening since the γ phase contains some amount of Indium. The fact that the γ phase is otherwise indistinguishable from $CuFeS_2$ is consistent with there being limited solid solution from that end of the diagram. This conclusion, based also on the x-ray data previously described, is consistent (at least at low temperatures) with the prediction of Robbins et.al. [78] that sulfide zincblende and chalcopyrite structures are destabilized by solution with compounds containing large cations. Hence $CuFeS_2$ would be able to accomodate less solution with $CuInS_2$ than vice versa.

This is due to the large size of Indium with respect to iron.

As discussed in chpt.2, the Mössbauer center shift (δ) is a tiny shift in energy caused primarily by the effect of the chemical environment on the total s-electron density at the Fe nucleus. In the case of Fe, a positive shift in δ signifies a decrease in the nuclear s-electron density at the absorber.

Fig.3.3.7 shows graphs of isomer shift vs. concentration. Fig. 3.3.7a indicates that the δ's of the HTQ and LTA α-doublets fall within the expected range for Fe^{3+} while fig.3.3.7b illustrates the previously stated result concerning the Fe^{2+} doublet.

The isomer shift for Fe in $CuFeS_2$ has been reported previously and has been interpreted to signify that the Fe is indeed in the 3+ state [79],[80]. This has some historical significance for Mössbauer spectroscopy which was instrumental in showing contrary to the prediction of Pauling and Brockway [81] (whose argument was based on lattice constant and ionic radii considerations), that there is no resonance between Fe^{2+} and Fe^{3+} occuring in that compound[2]. This is important especially in view of the fact that neutron diffraction measurements [82] indicated the Fe to have a magnetic moment of $3.88\mu_B$ which does not correspond to any of the expected values for Fe^{2+} or Fe^{3+} ions, but which could be interpreted as an average of two spin values.

In the following section (on magnetism), the question of

[2]It is interesting to note that such a resonance has been identified in the case of cubanite $CuFe_2S_3$ [79].

Fig. 3.3.7a Mossbauer isomer shift of alpha doublet (d) vs. concentration (x)

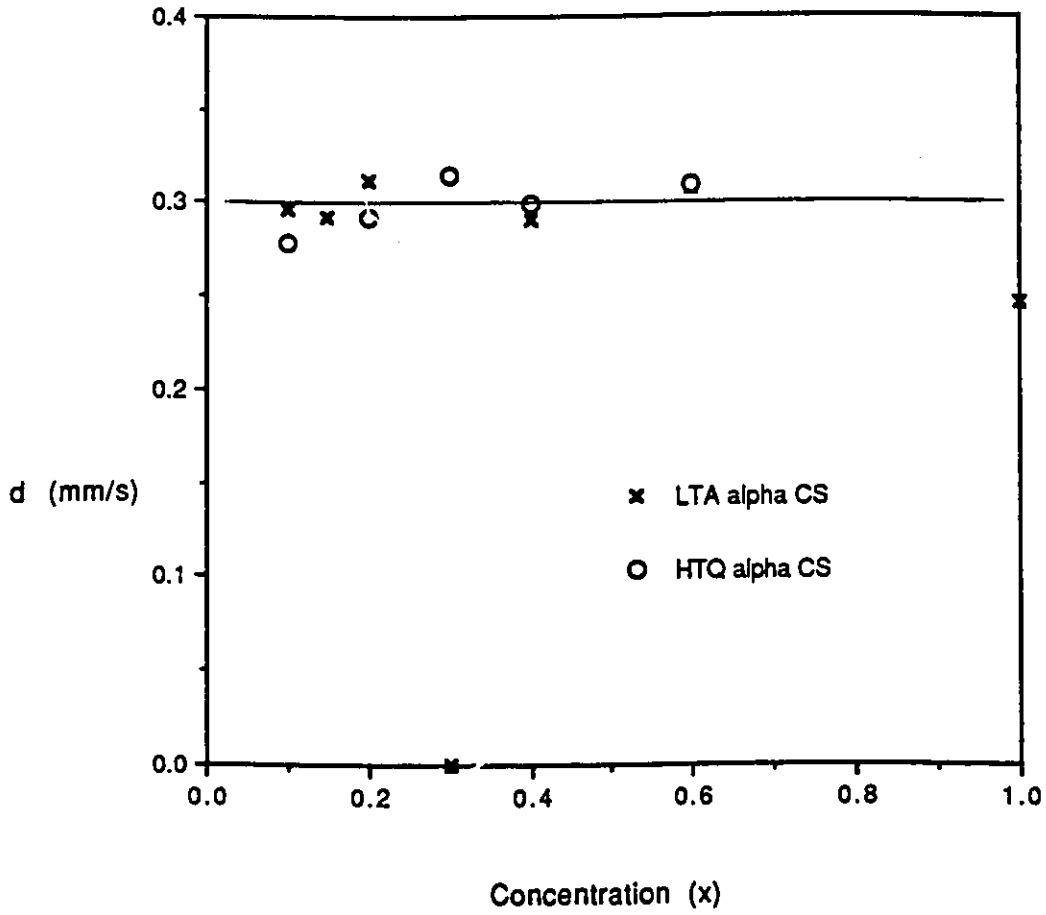

Fig.3.3.7a The shaded region on the figure indicates the range of center shifts observed. The center shift parameter of the α doublet is characteristic of Fe^{3+} as can be seen by comparison to table 2.3.1.

Fig.3.3.7b Mossbauer isomer shift of beta doublet (d) vs concentration (x)

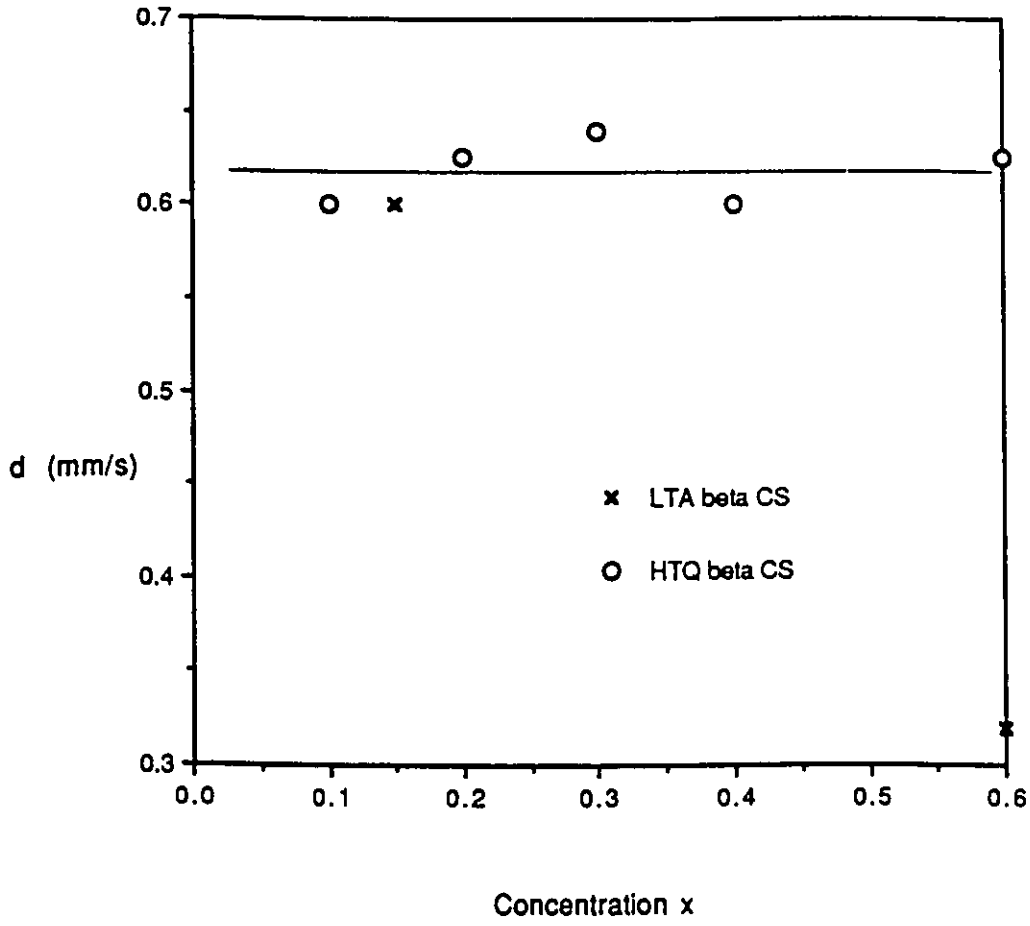

Fig. 3.3.7b Note the change of scale with respect to fig.3.3.7a. The Mossbauer center shift parameter for the doublet can be seen to correspond to that of Fe^{2+}.

whether the Fe in the alloy is in a 3+ low-spin state or a 2+ high-spin state will arise, therefore it is essential to interpret carefully the present results as far as they relate to the Fe oxidation state, and to try to gain as much information from them as possible. The factors which could lead to misinterpretation of the δ values are the effects of covalency (particularly in the case of sulfur ligands) and d-delocalization.

It is known [55] that low-spin complexes show little correlation between oxidation state and isomer shift due to their high degree of covalency. This is partly due also to the circumstance that the difference in δ between low spin Fe^{2+} and Fe^{3+} is considerably smaller than the difference between the high spin Fe^{2+} and Fe^{3+} (see table 2.3.1). Some examples of this in the Fe-sulfides are given in [83] and [55 p-284], and is particularly true for cases involving the highly polarizable sulfur ligands [55] [74 p.pr-21]. The basic physical mechanism is that covalency, through spin pairing, increases the effective number of d-electrons at the Fe site, which in turn increases δ via the shielding mechanism explained earlier (see chapter 2). Concurrently, d-delocalization which can have the reverse effect [55] may not play an important role in our case as any delocalization is accompanied by the formation of a narrow d sub-band which implies little net flow of d electrons away from the Fe sites.

Thus the net effect of the covalency, sulfur polarisability and d-delocalization is expected to tend to

increase δ. These considerations along with the measured low δ values, strongly exclude the existence of high-spin Fe^{2+} in either the α doublet or γ sextet since the measured δ's and quadrupole splitting parameters (Δ) are too small. Indeed the relatively low value of the β-doublet (Fe^{2+}) isomer shift is presumably due to an increase in 4s electron bonding at the defect sites. This would keep the 4s level populated and hence increase the nuclear s-electron density which would in turn decrease the isomer shift [55 p.169]. The presence of low-spin Fe^{2+} in the materials can be excluded by the absence of a singlet at the expected low isomer shift value (0.0) of that state.

An important observation regarding Mössbauer center shifts is that for complexes exhibiting crossover i.e. mixing of spin configurations on a given site, the center shifts are always very close to those for the high-spin complexes. This implies that it could be impossible to distinguish a pure Fe^{3+} high-spin from a mixture of Fe^{3+} low-spin and Fe^{3+} high-spin.

The final Mössbauer parameter which is important in elucidating the chemical state of the Fe, is the quadrupole splitting parameter Δ. This is graphed on figs. 3.3.8a and 3.3.8b for the narrow α (Fe^{3+}) doublet and for the broad (Fe^{2+}) β doublet respectively. The narrow (Fe^{3+}) feature is only crudely fitted and residual sharp doublet peaks in the data can be seen.

The large quadrupole splitting of the wide doublet is evidence enough for the 2+ assignment since it is highly

Fig. 3.3.8 Mossbauer quadrupole splitting parameters for CuIn Fe S

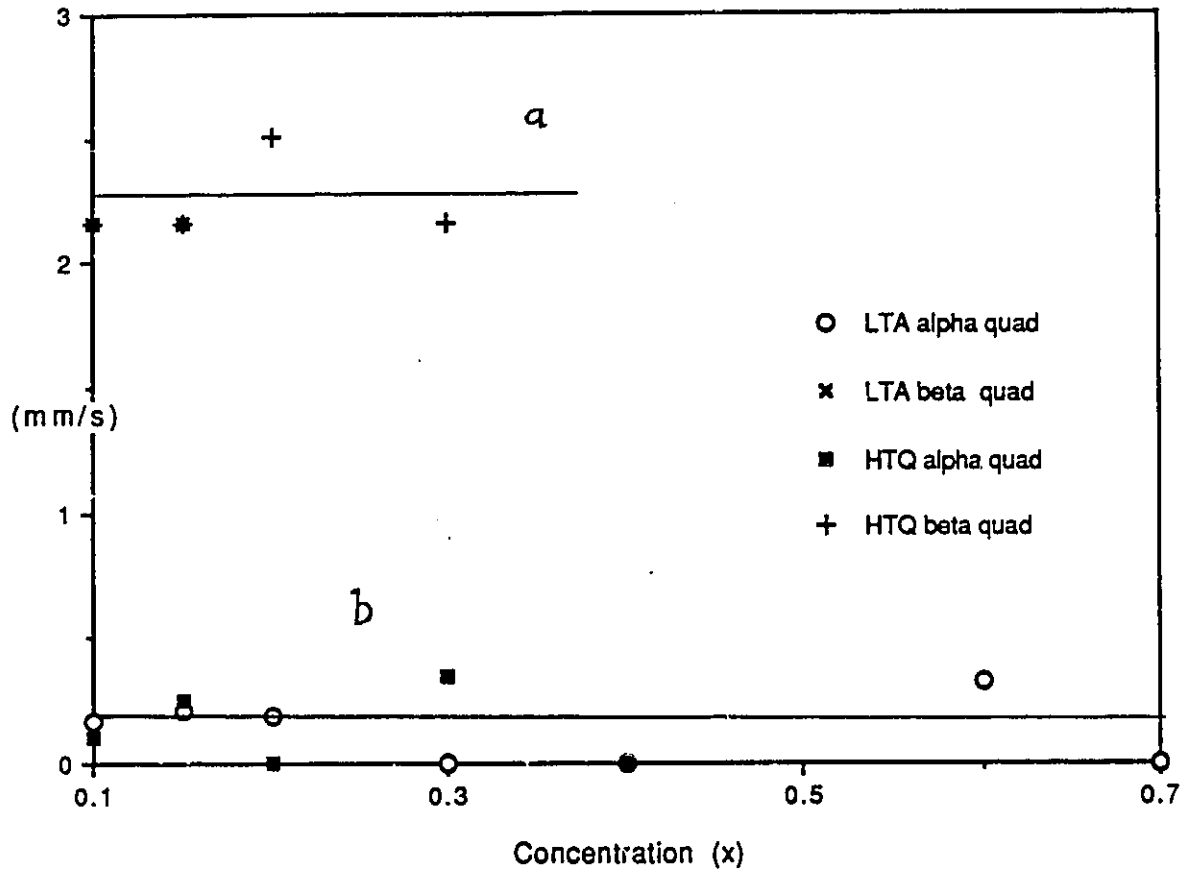

Fig.3.3.8 Mossbauer quadrupole splitting parameters are graphed for both the LTA and HTQ samples, and for both the α and β doublets. The values given for the α doublet are estimates.

unlikely that Fe^{3+} could obtain such a large quadrupole splitting[3]. This splitting is of the magnitude expected for Fe^{2+} in tetrahedral or octahedral stereochemistry.

Because the α-doublet is due to Fe^{3+}, the quadrupole splitting would normally be associated with electric field gradients resulting exclusively from low symmetry ligand fields. This is due to the expected high symmetry of the ion which results in a small ionic contribution to the electric field gradient (EFG). However it is possible that some contribution to the Fe^{3+} splitting is from the ion itself. As will be indicated in the following section, it is possible that crossover conditions are being approximated in these materials. In this case usually far-removed excited states can approach the ground state and mix with it, altering the net electron distribution hence ionic electric field gradient. In this particular instance, a lowering of the $^4T_1$ state would modify the spherical symmetry of the high-spin ($^6A_1$) ground state, and result in an increase in the electric field gradient. This would lead to a relatively large temperature dependent quadrupole splitting as the thermal populations of the levels (therefore the net ionic asymmetry) changed. The mixing would also lead to a decrease in the magnetic moment of the Fe sites as will be seen in the following section.

In summary, the Mössbauer analysis is particularly useful in providing information on the ionization state of the

[3]The largest Fe^{3+} quadrupole splitting quoted in ref [55] for high-spin Fe^{3+} occurs in a highly asymmetrical environment and is 1.66 mm/s. Such values do not seem attainable in the cubic-based chalcopyrite environment.

Fe ions. It seems fortunate that the technique is applicable in the case of Fe-containing semiconductors in which the question of the Fe ionization state is important. In contradistinction, the question hardly arises in cases concerning Mn which has a uniquely stable (Mn^{2+}) d^5 configuration. The assignment of Fe^{3+} in the equilibrium condition of these materials seems quite meaningful and is consistent with that previously reported in related materials[4], but the Mössbauer technique cannot distinguish important details such as the spin states of these 3+ ions.

It is interesting that although the Fe^{3+} state seems the preferred one, it is not difficult to produce Fe^{2+} within the adamantine structure (ex. HTQ materials). For Fe^{2+}, a stronger chemical similarity with Mn in alloy semiconductors would seem to be expected, however the possibility exists that neighbouring Fe ions participate in rapid charge-transfer transitions, a behaviour without counterpart in the case of Mn.

[4]This is not consistent with some new results obtained for doped samples [84].

3.4) Magnetic Measurements

Low-field susceptibility measurements of the type described in chapter 2, were carried out on a variety of samples with various heat treatments. Large sample masses (≈50 mg.) were generally required to obtain good signals. The Curie-Weiss temperatures θ, and the magnetic transition temperatures T_c of the samples which showed Curie-Weiss behaviour over the range of the measurements are summarized in table 3.4.1. Some typical susceptibility curves are graphed in figs.3.4.1. The important qualitative feature of the magnetism of the $z \leq 0.2$ LTA samples is exemplified by their smooth susceptibility curves which decrease monotonically with increasing temperature (figs. 3.4.1a-e). In contrast, the susceptibility for a polyphase sample with nominal concentration x=0.1 is shown in fig.3.4.1f. The complex susceptibility exhibited by this sample is due to the presence of impurity phases and inhomogeneity.

The χ^{-1} plots for the homogenous materials (figs. 3.4.2a-g) clearly indicate Curie-Weiss behaviour over the highest temperature range of the measurements (130^0-210^0K) while non-Curie-Weiss behaviour occurs below this. The qualitative form of the deviation from Curie-Weiss law is that seen for known spin-glass transitions in other alloys [85], and will be discussed in the following. Most of the graphs 3.4.2c-f do not show data points at low temperature due to the fact that the high temperature susceptibility measurements from which the Curie-Weiss parameters were extracted are

Figs.3.4.1 susceptibility vs. temperature for $CuIn_{1-x}Fe_xS_2$.

Fig.3.4.1a $CuIn_{1-x}Fe_xS_2$ x=0.04 LTA
susceptibility vs. temperature

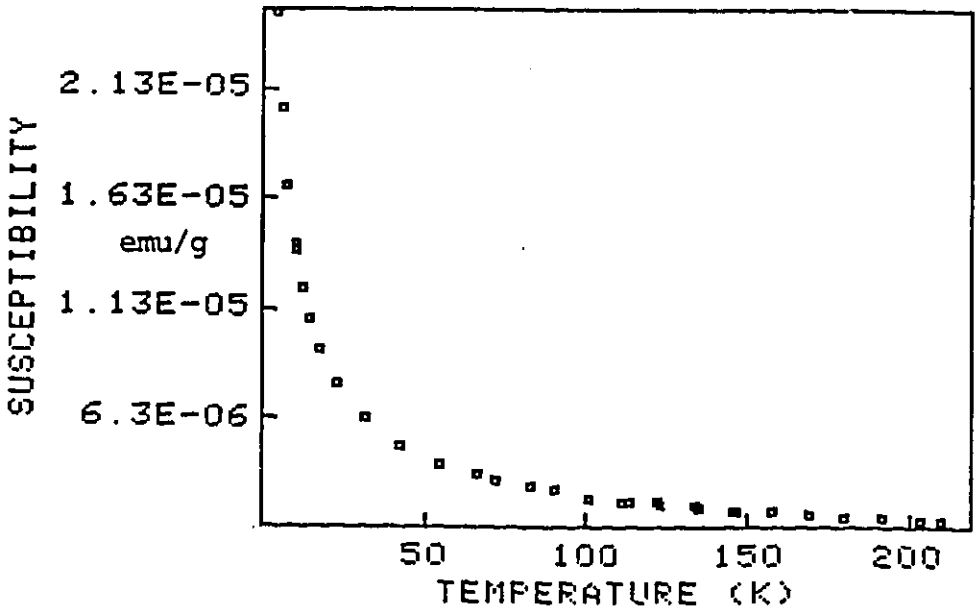

Fig.3.4.1a illustrates the low-field susceptibility of the x=0.04 LTA sample.
The susceptibility curves for the LTA samples with x=0.06, x=0.1, x=0.15, and for the HTQ sample with x=0.3 are shown on the following two pages. The crossed data points on Fig.3.4.1d (x=0.15) are field-cooled data and illlustrate the absence of temperature induced hysteresis. The qualitative similarity in the curves a to e is contrasted with Fig. 3.4.1f, in which the susceptibility of a polyphase sample with nominal concentration x=0.1 is shown.

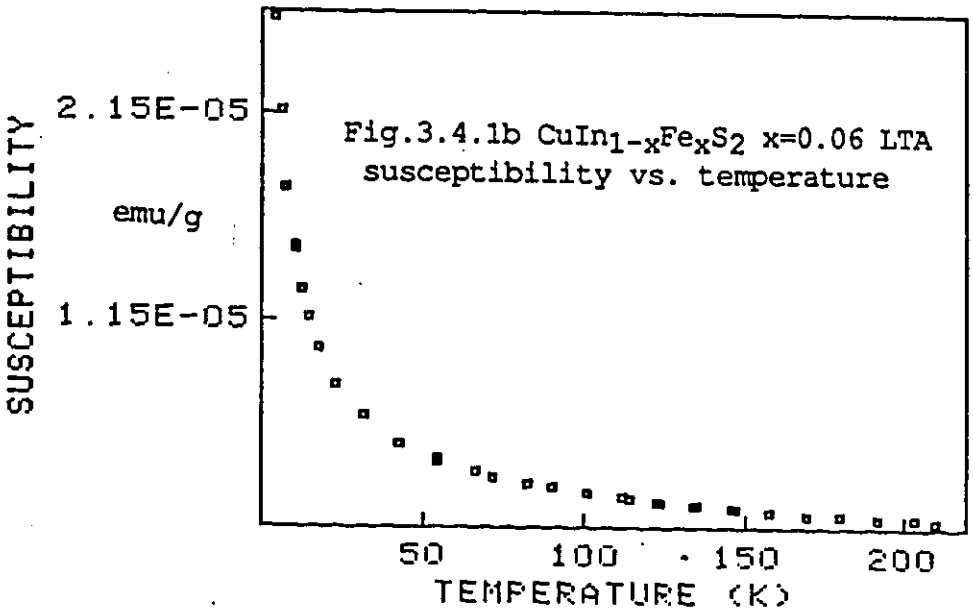

Fig.3.4.1b $CuIn_{1-x}Fe_xS_2$ x=0.06 LTA susceptibility vs. temperature

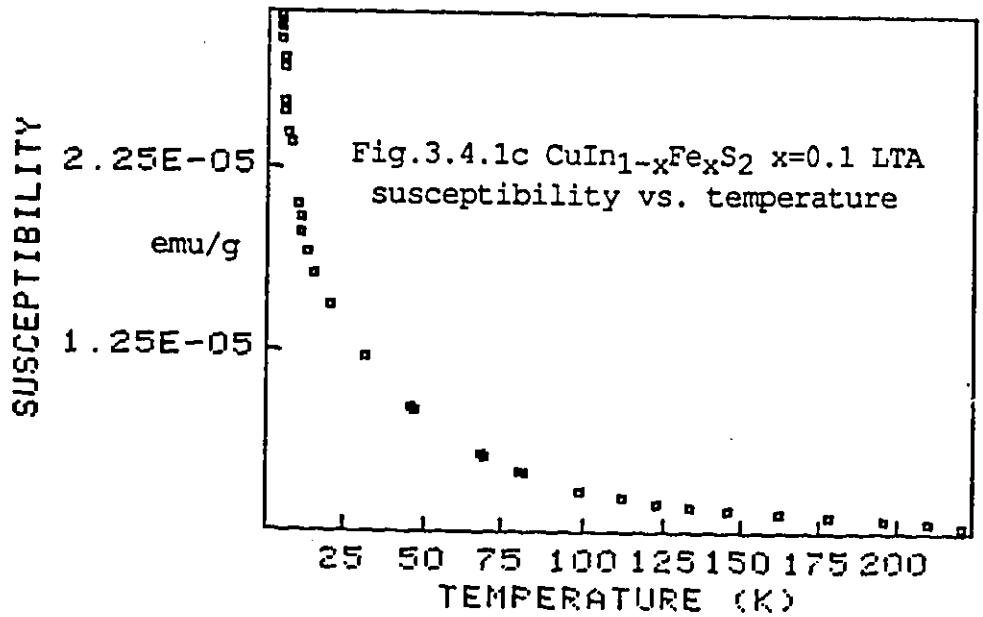

Fig.3.4.1c $CuIn_{1-x}Fe_xS_2$ x=0.1 LTA susceptibility vs. temperature

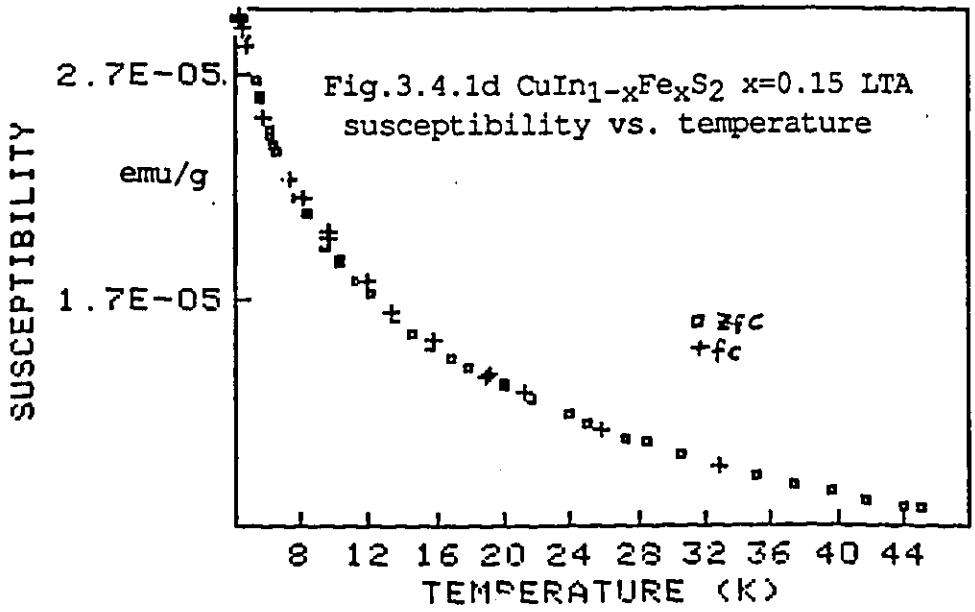

Fig.3.4.1d $CuIn_{1-x}Fe_xS_2$ x=0.15 LTA susceptibility vs. temperature

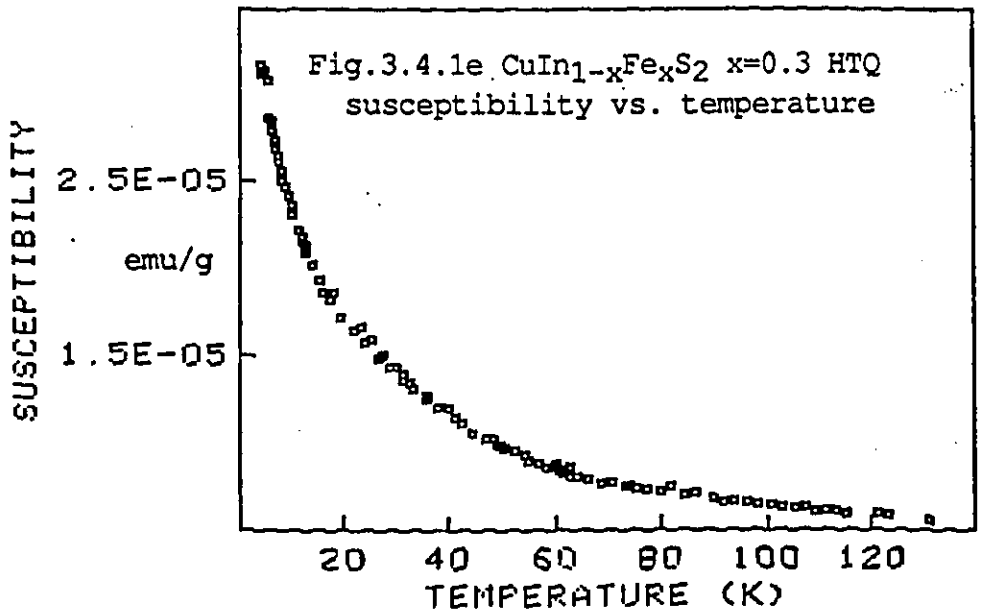

Fig.3.4.1e $CuIn_{1-x}Fe_xS_2$ x=0.3 HTQ susceptibility vs. temperature

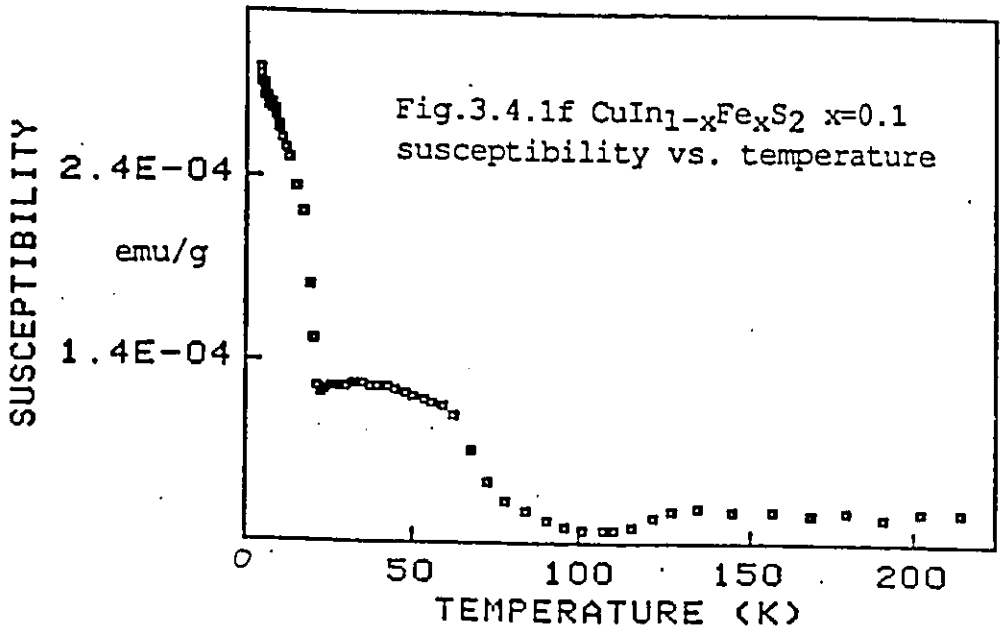

Fig.3.4.1f illustrates the magnetic behaviour of a poly-phase sample. x-ray analysis of this sample indicated the presence of unidentified phase(s). This sample did not display Curie-Weiss behaviour over the temperatures attainable in the susceptometer.

Figs.3.4.2 inverse susceptibility vs. temperature for $CuIn_{1-x}Fe_xS_2$.

Fig.3.4.2a $CuIn_{1-x}Fe_xS_2$ x=0.04 LTA
inverse susceptibility vs. temperature

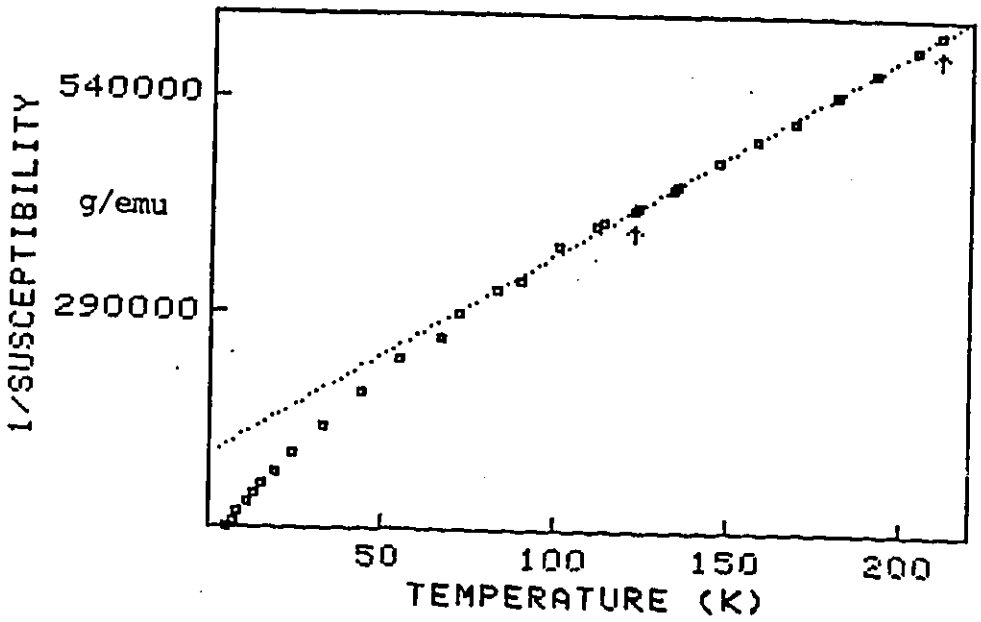

Fig.3.4.2a illustrates the inverse susceptibility vs. temperature for the x=0.04 LTA sample. Curie-Weiss behaviour is seen over the high temperature region of the diagram. The inverse susceptibility curves for the LTA samples with x=0.06, 0.1, 0.15, and for the HTQ samples with x=0.3, and x=0.6 are shown on the following three pages. Also shown is an example of the broadened cusp-like behaviour in the inverse susceptibility of the x=0.4 LTA material.

Fig.3.4.2b $CuIn_{1-x}Fe_xS_2$ x=0.06 LTA
inverse susceptibility vs. temperature

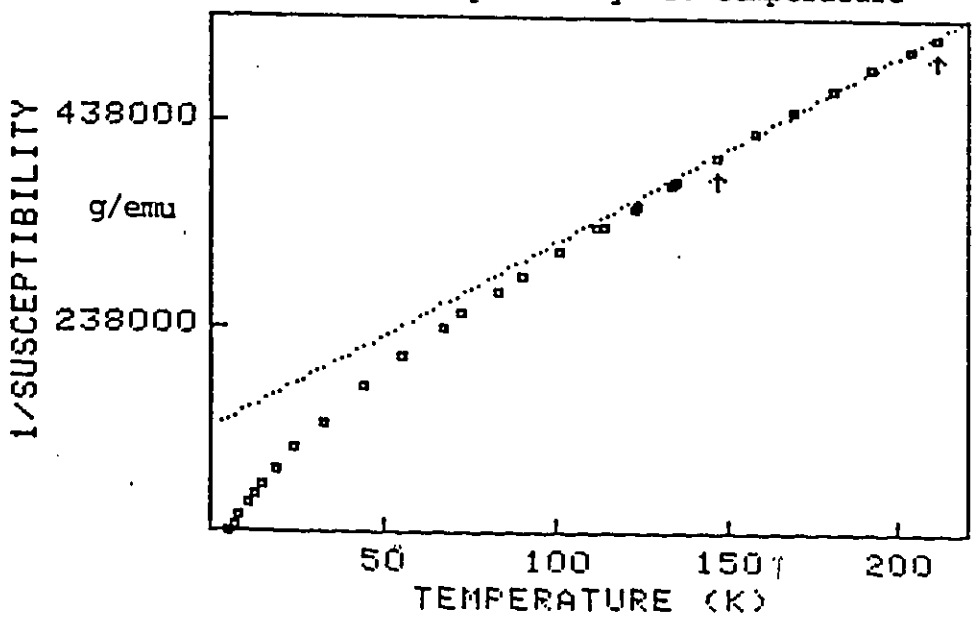

Fig.3.4.2c $CuIn_{1-x}Fe_xS_2$ x=0.1 LTA
inverse susceptibility vs. temperature

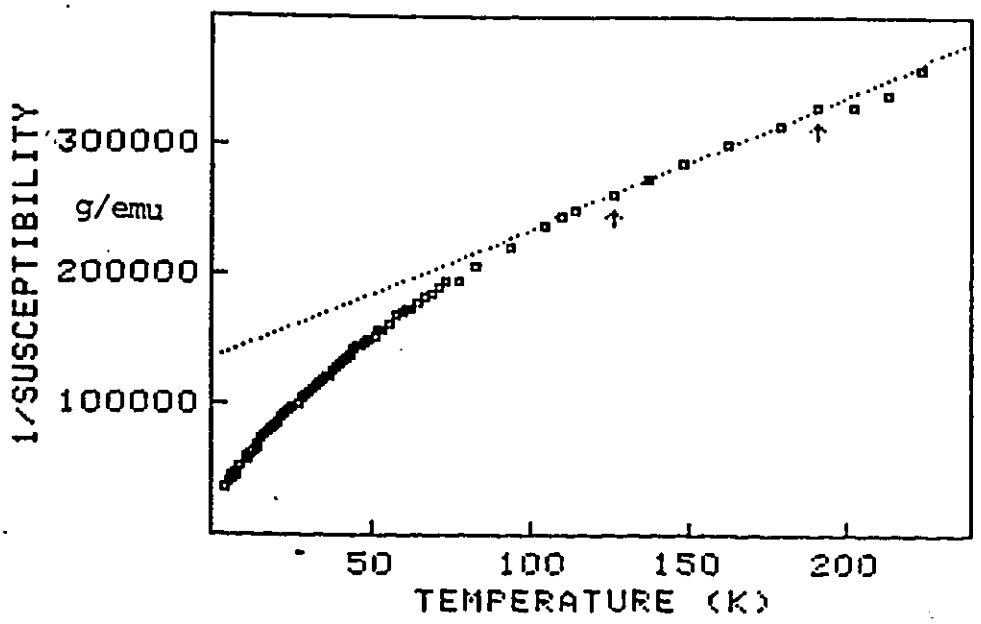

Fig.3.4.2d $CuIn_{1-x}Fe_xS_2$ x=0.15 LTA
inverse susceptibility vs. temperature

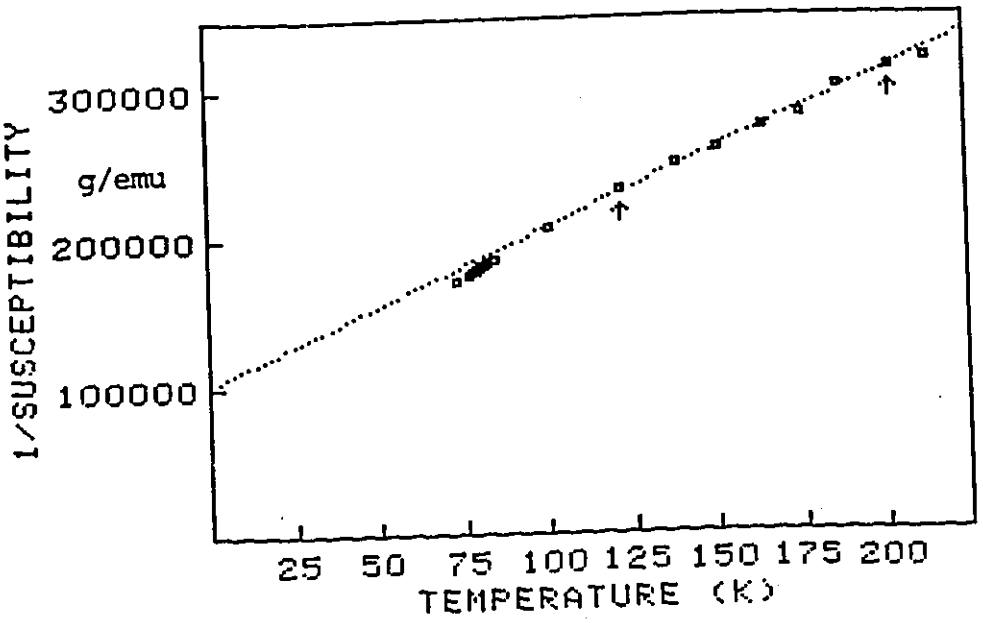

Fig.3.4.2e $CuIn_{1-x}Fe_xS_2$ x=0.3 HTQ
inverse susceptibility vs. temperature

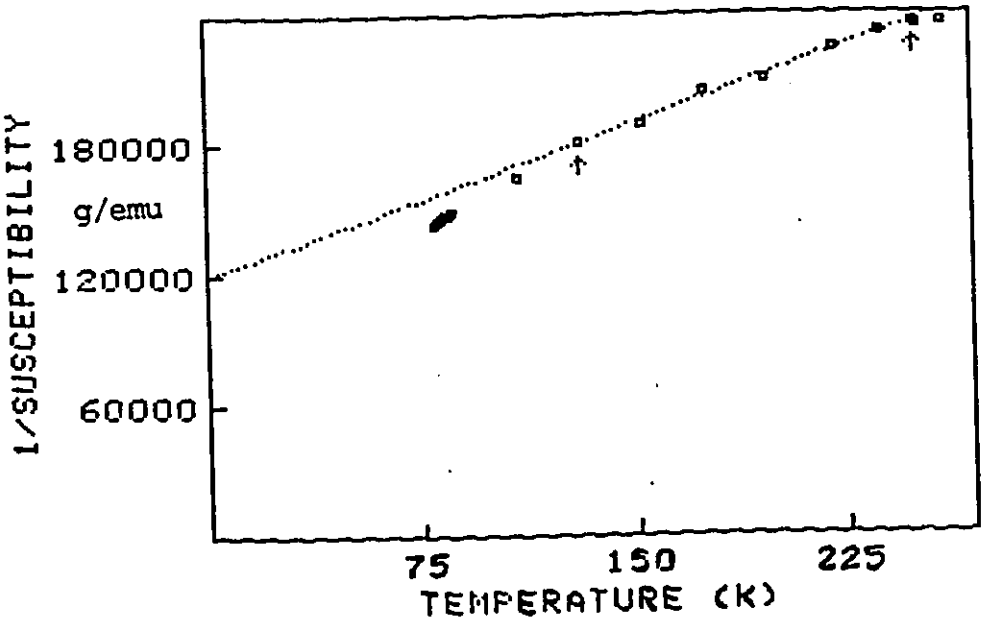

Fig.3.4.2f $CuIn_{1-x}Fe_xS_2$ x=0.6 HTQ
inverse susceptibility vs. temperature

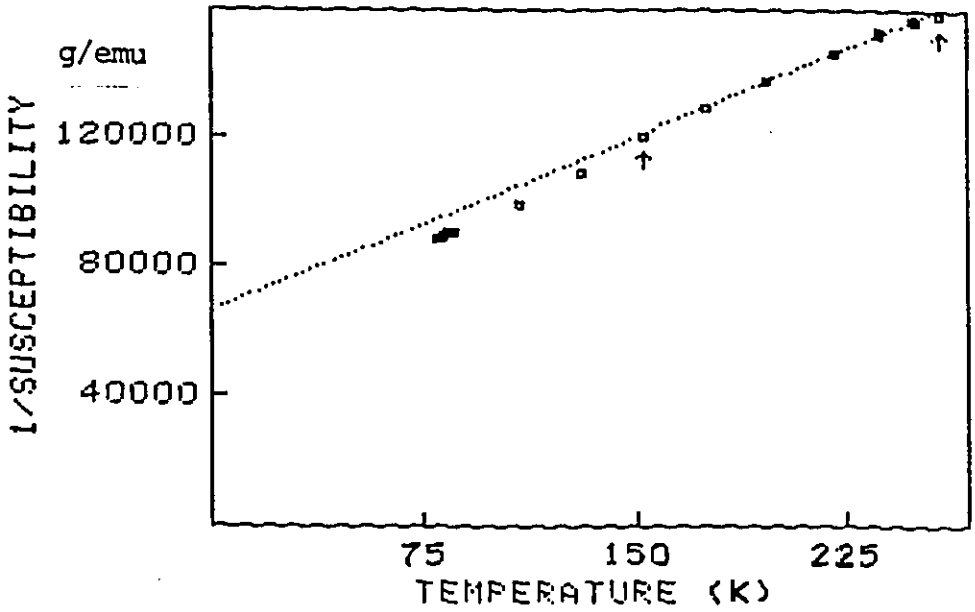

Fig.3.4.2g $CuIn_{1-x}Fe_xS_2$ x=0.4 HTQ
inverse susceptibility vs. temperature

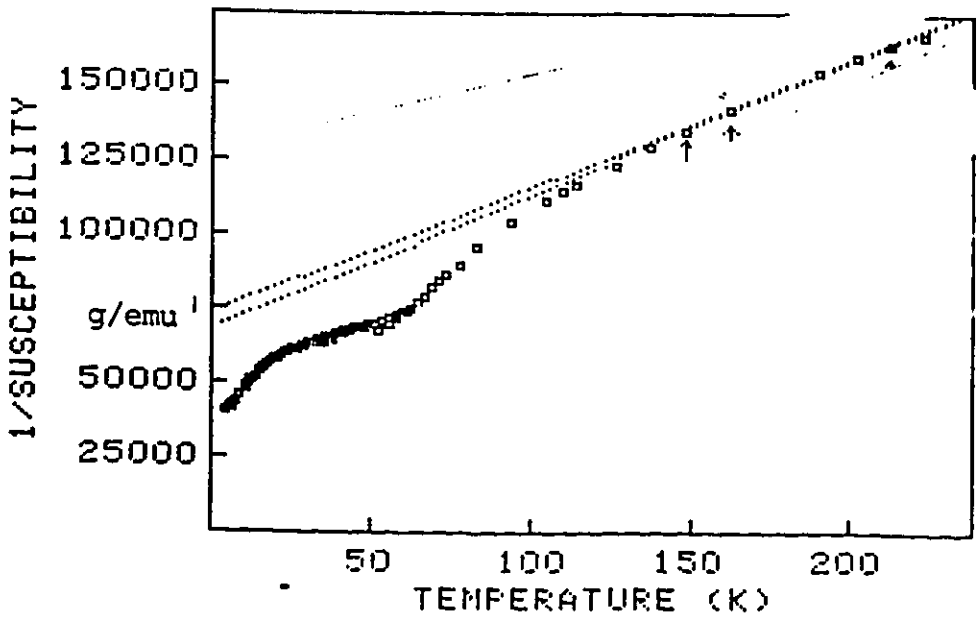

shown. The measurements over the high temperature regime of the apparatus are very helium intensive thus two sets of data were taken for these samples, one set at low temperature (4-100 K), and one set which covered the range as high above 100 K as the apparatus allowed.

As indicated in the introductory section 2.6 (see eq. 2.6.3), the effect of the net temperature independent susceptibility depends om the relative magnitudes of D and C, and between the magnitude of θ compared to the measuring temperature. From the magnitudes of the atomic diamagnetic susceptibilities and the effective diamagnetism of the sample chambers, the magnitude of D for the typical Fe-containing sample is estimated to be $1x10^{-8}$ emu/g. This is a negligeable effect, and can be ignored in this case. Thus the linearity of χ^{-1} indicates that it is not necessary to apply further corrections due to diamagnetism and that the accuracy of the C and θ values can be estimated directly from the error in the slopes of the χ^{-1} curves.

The Curie-Weiss temperatures of the LTA and HTQ samples are graphed in fig. 3.4.3. As can be seen from that plot, all the θ values lie (within error), on a positively sloped line. Since the magnitude of θ is an indication of the strength of the cumulative interactions between spins, an increase in θ with increased Fe concentration is expected. The fact that

(next page)

Fig.3.4.3 Curie-Weiss temperature (θ) vs. composition (x)

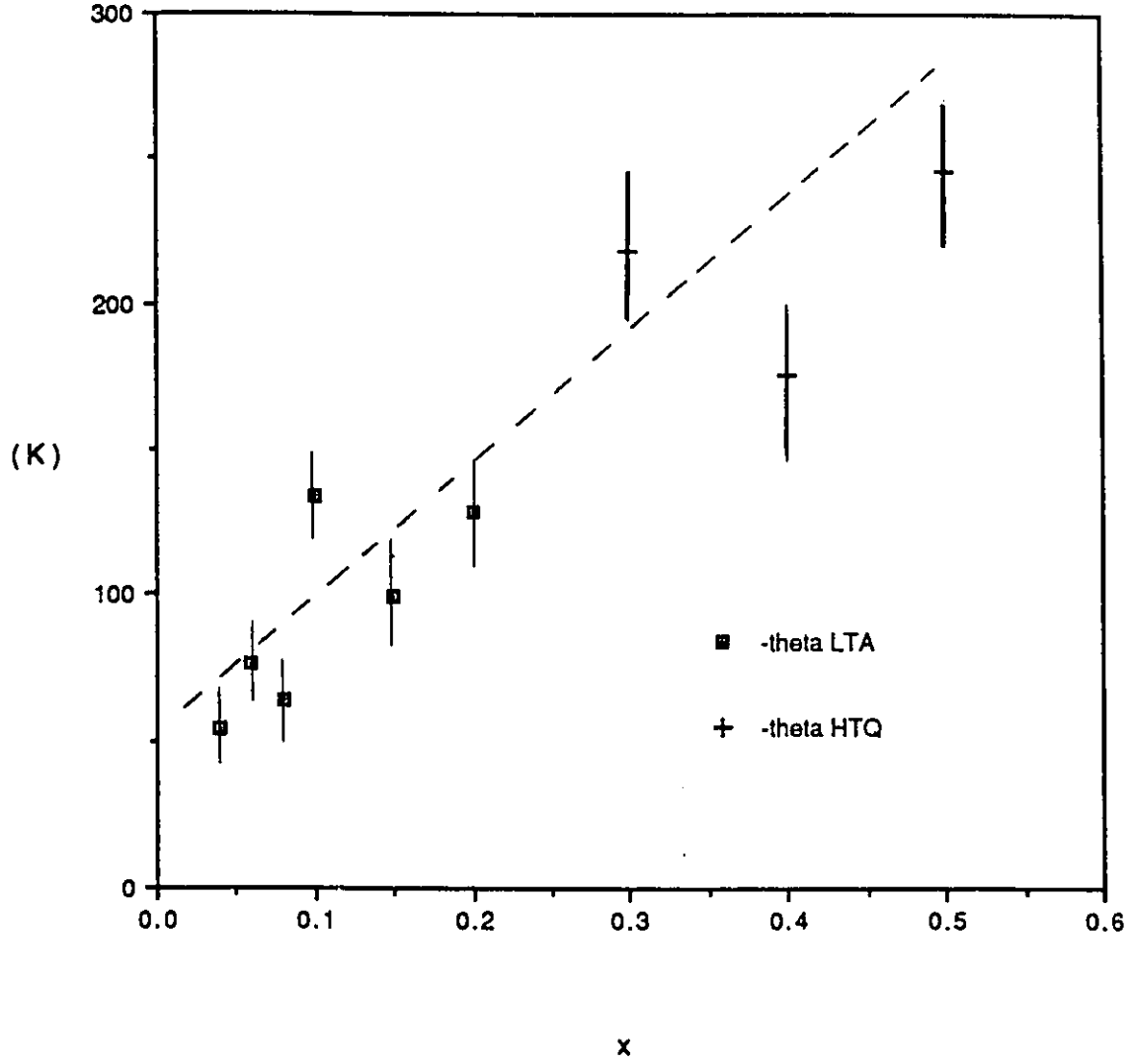

Fig.3.4.3 graphs the variation of the apparent Curie-Weiss temperature as a function of concentration (x) in $CuIn_{1-x}Fe_xS_2$. The experimental Curie-Weiss temperature is indicative of antiferromagnetic interactions. The data from both LTA and HTQ samples is shown, with errors estimated directly from the inverse susceptibility curves.

the HTQ samples yield θ values consistent with the extrapolation from the LTA materials, once again illustrates the close relationship of the equilibrium and quenched substances as well as indicates the small effect of the presence of Fe^{2+} in the HTQ samples. Not all the samples can be represented on this graph due to the limited temperature range of measurement (from 4^0-250^0 K) which does not extend into the paramagnetic behaviour of the high x materials.

The simplest possible interpretation for the magnetic response of the single-phase alloy samples consists of a magnetic phase change model. The component which dominates over the high temperature range of measurements is characterized by the negative Curie-Weiss temperatures and is related to the cusp-like behaviour in the system. The magnetc transition region itself is characterized by the departure from paramagnetic behaviour. The second contribution which dominates at low temperature is the non-Curie-Weiss regime which could have contributions from unpaired or non-interacting moments resulting from small antiferromagnetic clusters or isolated spins respectively [83]. In the following, the possibility that the $^6A_1$ level ceases to be the ground state for certain compositions of the single phase field will arise. In this case the above interpretation of the magnetic response would not apply, however for the sake of having a model on which to base an interpretation, it will be assumed in the following that the behaviour described above does occur.

The susceptibility curves do not indicate clear cusp-like features normally expected for spin glasses, however they do indicate broad peaks and non-reversible (i.e. field-cooled vs. zero-field-cooled) behaviour. This may be associated with the blurred x-ray reflections, and caused by slight variations in composition. A good example of this is the (non-equilibrium) sample HTQ x=0.6 whose susceptibility peak, x-ray diffraction and Mössbauer spectra are all highly broadened.

The susceptibility peaks can often be better distinguished from the plots of κ^{-1} than from the plots of κ themselves. On the inverse susceptibility curves, regions of high susceptibility appear as downward excursions relative to the extrapolated higher temperature values. This is indicated on sample x=0.4 of fig. 3.4.2f. Note that although non-Curie-Weiss behaviour at low temperature is possible even for an 'ideal' paramagnet, it usually occurs in the form of a weakening of the susceptibility [59]. In the case of random alloys, a further complication arises at low temperature due to the onset of spin correlations in near-neighbour complexes interacting via J_1.

Even though the susceptibility peaks are broad, a characteristic transition temperature can still be estimated. These estimates yield the graph of T_c vs. x shown in fig. 3.4.4. On this graph is also seen the Neel temperatures of the high concentration samples taken from the DTA data obtained from the Venezuelan group. Similar behaviour in alloy

Fig.3.4.4 Magnetic transition temperatures
(T) vs. composition (x)

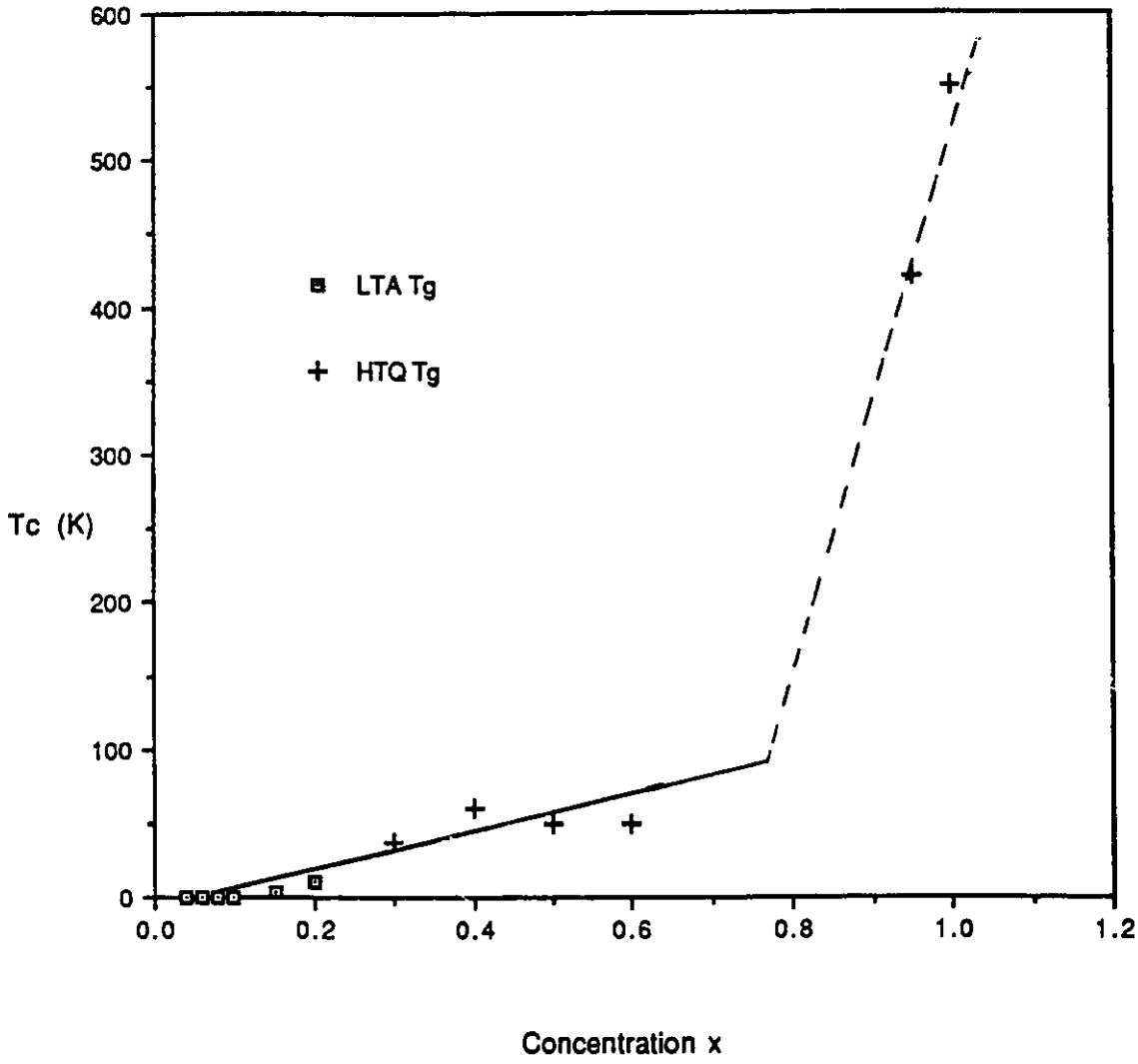

Fig.3.4.4 illustrates the variation of the estimated transition temperatures with concentration (x) in $CuIn_{1-x}Fe_xS_2$. The transition temperatures are taken to be the temperatures at which the observed enhancement of the susceptibility occured.

systems which exhibit both spin-glass and antiferromagnetic transitions has been reported [86]. The rapid changeover from spin-glass to antiferromagnetic behaviour is characteristic of these systems and can be understood as follows. Similarly to θ, T_g is expected to increase with concentration. In the case of T_c however, there is a critical concentration beyond which further random substitution of Fe on Indium sites, leads to sufficient crystallographic order to support an antiferromagnetic phase. Indeed Monte-Carlo calculations of nearest-neighbour percolation on an FCC lattice suggest that spin-glass behaviour only occurs in the range of concentrations x-0.18 to x=0.4 [87], however this would be modified by the presence of next-neighbour interactions.

As indicated in the preceeding, the plots of χ^{-1} in figs. 3.4.2a to 3.4.2f illustrate Curie-Weiss behaviour over the high temperature range of measurement. From these, the p_{eff} value can be extracted (see 2.6), where p_{eff} is the average number of Bohr magnetons per ion contributing to the paramagnetic response and is given by:

$$p_{eff} = g \sqrt{J(J+1)}$$

In the calculation of this quantity from the Curie-Weiss behaviour of the susceptibility, the assumptions that g=2 and J=S were made. The validity of using the free-electron g value in these calculations stems from the ESR results and will be discussed later along with the implications of the J=S assumption. A value for p_{eff} of the high-x samples is not available due to the presence of their non-Curie-Weiss

behaviour in the middle of the available range of measurement.

The graph of p_{eff} as a function of concentration is shown in fig.3.4.5 both LTA and HTQ samples were used in this plot. Also shown are the p_{eff} values corresponding to S=5/2 and S=3/2. The p_{eff} value can be seen to change with an increase in concentration, from the value expected for the atomic d^5 ground state, to the observed value of the Fe moment in $CuFeS_2$ (which coincides with S=3/2) [82] at high x. The changeover seems to occur over a narrow range of concentrations between x=0.1 and 0.2. This change in p_{eff} must be associated with a change in the spin state of the majority Fe^{3+} ions that are observed in the Mössbauer spectra of these materials.

Similar behaviour in the Fe moment in chalcopyrites has been reported in the case of $CuAl_{1-x}Fe_xS_2$ [72] and can be inferred from the measurements on $CuGa_{1-x}Fe_xS_2$ [73]. The data taken from the latter case is shown in fig. 3.4.5b, along with the previously reported result from [72]. This change-over from the free-ion p_{eff} to the $CuFeS_2$ value has been attributed to d-delocalization. The question of how the reduction of our Fe moment occurs, will be considered in 3.4.2.

3.4.2) ESR

ESR investigations were based on the single broad line at g=2 which was observed and attributed to the -1/2 to 1/2 transition of Fe^{3+}. As seen in 2.4, this is the most robust ESR transition, due to the fact that the energy difference

Fig. 3.4.5a peff vs. concentration (x)
for Cu(InFe)S

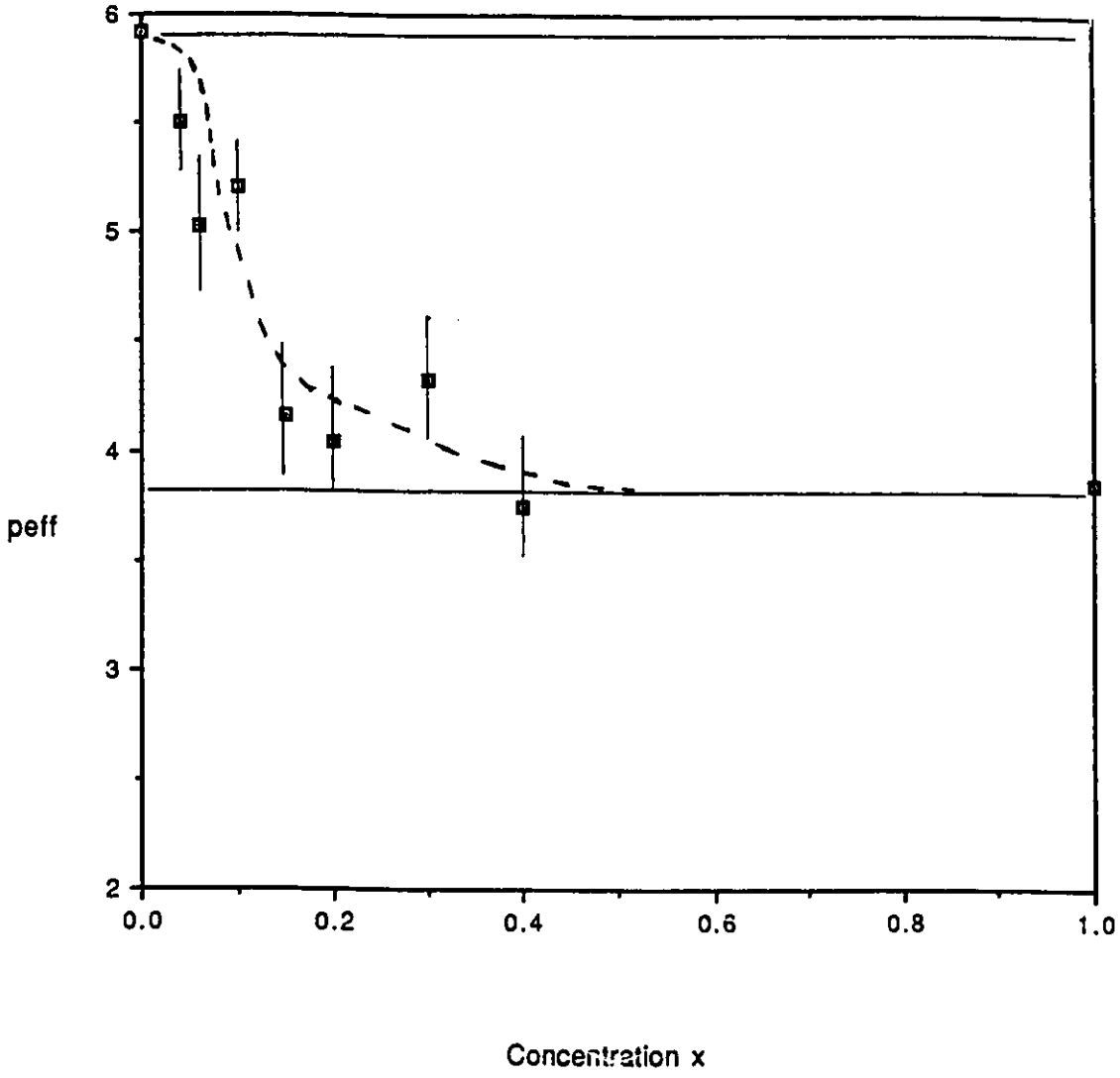

Fig.3.4.5a gives the variation of the magnetic moment as a function of concentration (x) in $CuIn_{1-x}Fe_xS_2$. The p_{eff} data represent the average magnitude (in units of μ_B) for the magnetic moments within the materials. The two horizontal lines indicate the values appropriate for S=5/2 and S=3/2. The line drawn through the data points is a guide for the eye.

Fig. 3.4.5b peff vs. Concentration
(including data from [72], [73])

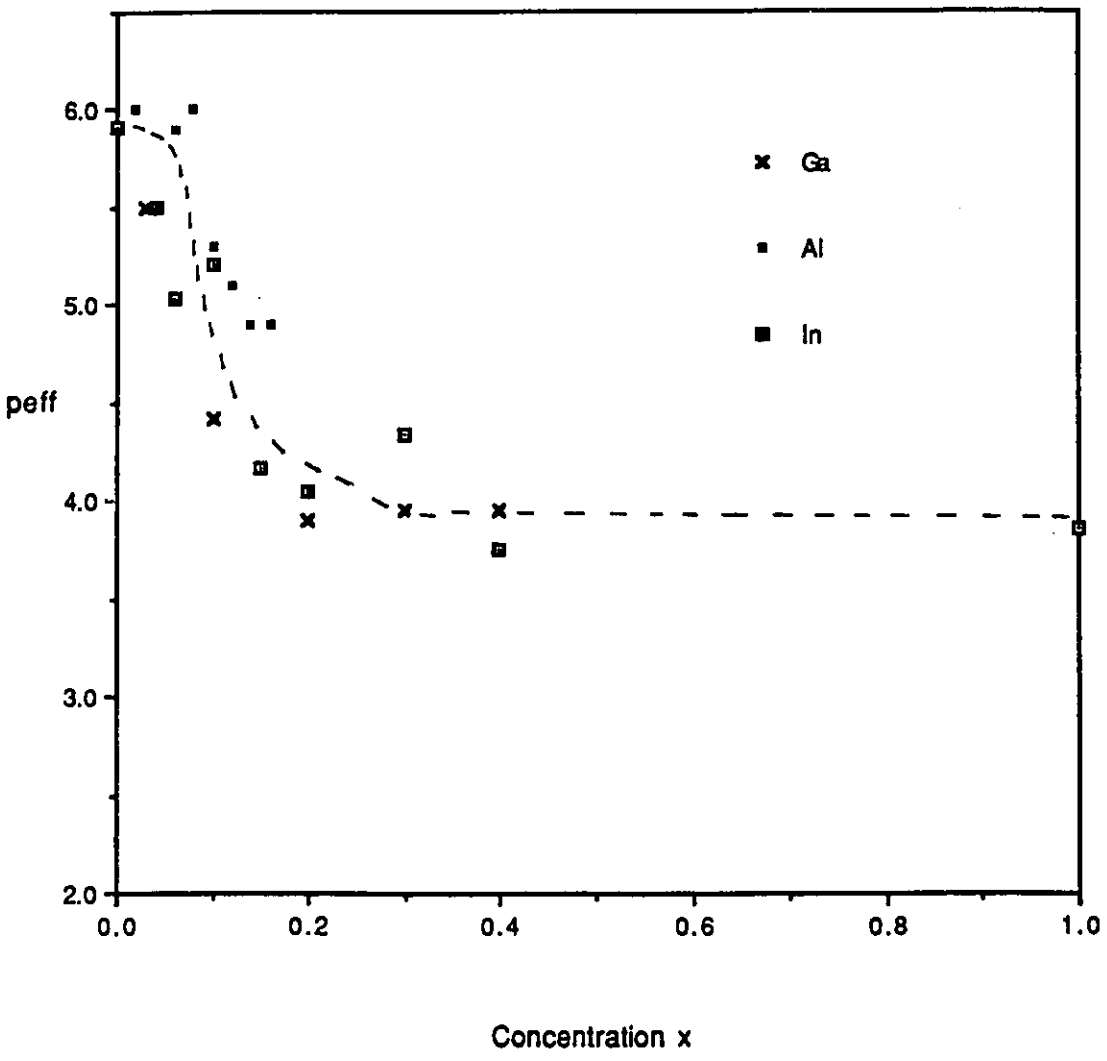

Fig.3.4.5b includes the data pertaining to other chalcopyrite structure Fe-sulfides. The data pertaining to $CuAl_{1-x}Fe_xS_2$ has previously been shown in [72]. The data pertaining to $CuGa_{1-x}Fe_xS_2$ was obtained from the susceptibility measurements reported in [73]. The present $CuIn_{1-x}Fe_xS_2$ system is included for comparison purposes.

between the -1/2 and +1/2 levels is totally independant of the random crystal fields and hence depends solely on the magnetic field at the location of the ion.

Various anomalous features of the ESR were observed. As can be seen in table 3.4.1, the linewidth was not found to increase monotonically with concentration as is the usual case in DMS [49]. This anomaly occured over the concentration range which coincides with the reduction of p_{eff}, and is perhaps associated with a change in the relaxation mechanisms during the p_{eff} change.

The x=0.1 and 0.2 samples gave similar results during a low temperature ESR study. This is exemplified by the data from the x=0.2 sample seen in figs.3.4.6. The region of low temperatures over which the linewidth increase occurs coincides with non-Curie-Weiss behaviour in the inverse susceptibility. Unfortunately, the approximations made in equating the ESR intensity with the susceptibility (see 2.4) were not valid for this material, so that a comparison of these two quantities could not be carried out.

The g values obtained from the ESR of the powder specimens are averages of the tensor components. All the g-values were very close to 2 over the non-critical regimes of the ESR, except for the low g value of 1.93 observed for the HTQ x=0.4 sample. This low g value is attributed to demagnetisation in the high-x material. The shift in the g-value with a lowering of temperature is seen as the shift in the centroid of the ESR line in fig 3.4.6a. this suggests

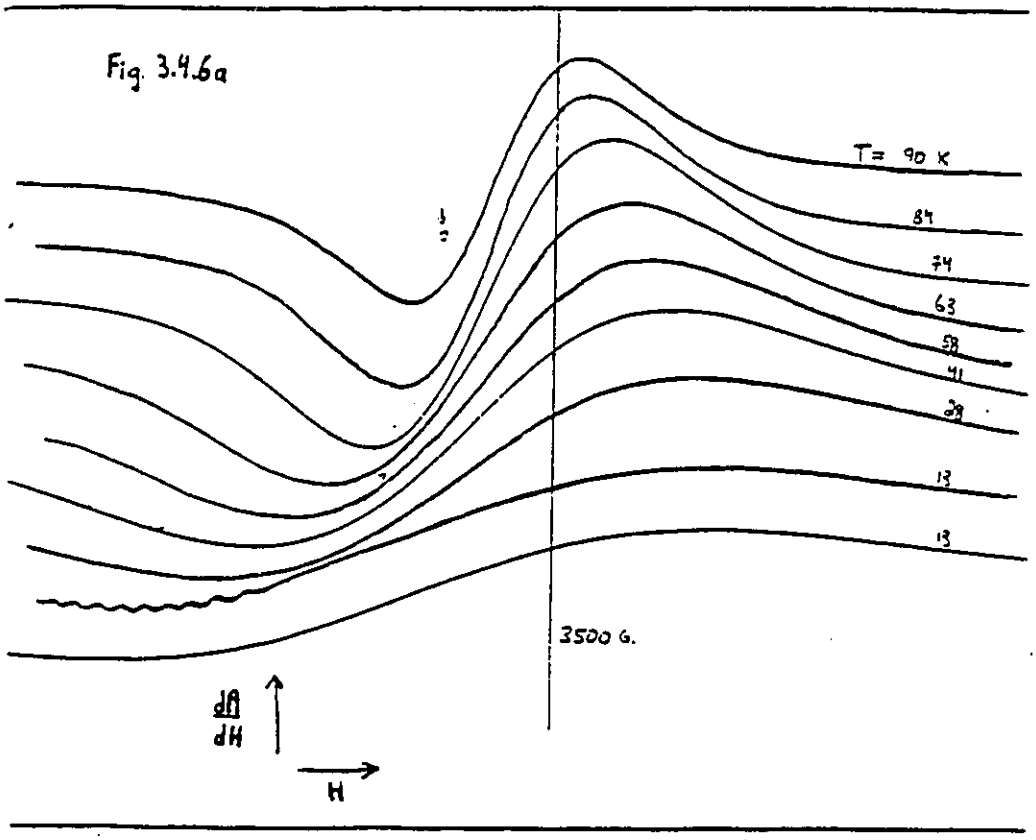

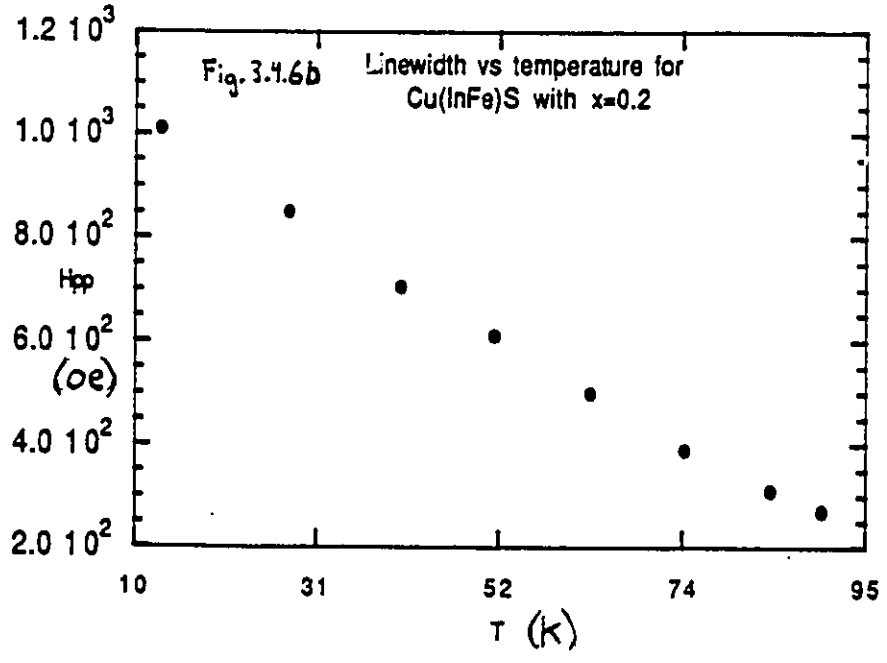

Fig.3.4.6a. Reproduction of low temp. ESR traces for x=0.2 $CuIn_{1-x}Fe_xS_2$. Fig.3.4.6b. Estimated ESR linewidth vs. temp. for the same sample.

that there is a critical behaviour occurring, however the linewidth increase does not follow the expected form of $(T-T_c)^{-p}$ (see 2.4) over this range.

As mentioned in the introduction to ESR (2.4), the technique can be sensitive to impurities in the samples. Indeed samples which showed polyphase x-ray patterns all showed complicated lineshape, or base-line behaviour. For example, the x=0.04 sample was remeasured 6 months after the initial measurement and yielded a considerably different signal relative to its initial state, probably due to the assimilation of water or oxygen during that time.

ESR, like Mössbauer spectroscopy, gives information on the chemical state of the magnetic ions. The presence of a -1/2 to 1/2 transition indicates the presence of Fe^{3+}, however as in the Mössbauer measurement, cannot be used to characterize the spin-state of the Fe^{3+}. This is due to the fact that any S=1/2 Kramers doublet would contribute to this transition. Unlike the Mössbauer measurements of these materials, the ESR is expected to be insensitive to the presence of Fe^{2+}. In fact the Fe^{2+} ion in an octahedral field at low temperatures, can produce the double quantum signature mentioned in section 4.3 [60, p327], however in the case of tetrahedral fields a singlet ground state arises. This has been shown in the case of Fe^{2+} in II-VI DMS where good agreement between experiment and ligand-field theory has been found [88], [89], [90], [91], [92], [93].

The behaviour of Fe^{2+} in the II-VI environment is

expected to be qualitatively similar to that of the present I-III-VI_2 case, which includes a tetragonal distortion induced by the non-cubic symmetry, and weaker low symmetry fields due to the next near neighbour atoms in the alloy. The g-values of the low- lying Fe^{2+} spin-orbit split states are expected to be large hence in principle distinguishable from the Fe^{3+} -1/2 to 1/2 transition however the Fe^{2+} lines are expected to be highly broadened. This is due to the fact that Fe^{2+} is known to couple strongly to its environment whereby small departures from cubic symmetry in the crystal field can cause large zero-field splittings [94], a condition for enhanced inhomogenous broadening. Also, the spin-orbit coupled Fe^{2+} states lead to very short spin-lattice relaxation times [60] which increases the homogenous broadening. Both these effects render the Fe^{2+} transistions invisible over the available temperature range in much the same way that the higher Fe^{3+} (5/2 to 3/2, and 3/2 to 1/2) transitions are not seen.

Thus the ESR and Mössbauer data indicate the presence of a majority of Fe^{3+} within the α phase $CuIn_{1-x}Fe_xS_2$, however the susceptibility measurements show that the magnetic moment of the Fe ions decreases as a function of concentration. In the following section an interpretation for these results will be given.

3.4.3) Crystal (Ligand) Field Approach

The obvious explanation for the p_{eff} drop is that of the occurence of low-spin Fe^{2+} in the matrix. The amount of Fe^{2+}

actually seen by the Mössbauer measurements however falls far short of accounting for the the behavior in fig.3.4.5a and can thus can be ruled out .

It is clear that the p_{eff} change must then be associated with a change in the state of the Fe^{3+} ions in the crystal. Thus the next obvious interpretation for such a change is that it is due to the delocalization of the Fe d electrons. Indeed this is the explanation put forth by Kambara [77]. Although not discussed in that reference, the delocalization must be associated with hybridzation. Indeed the mixing of noble metal d-levels in the valence bands of the pure I-III-VI_2 materials is well documented [4], [17]. In the case of $CuInS_2$ over 30% d character in the uppermost valence states has been reported [17]. There is good evidence to support the fact that the Mn d-levels in DMS also mix into the valence band. In fact approximately 26% Mn d-character has been found in the upper valence band of $Cd_{1-z}Mn_zSe$ at z=0.2 [95]. The injection of d characetr in the valence band implies an opposing p-like contribution to the 'localized' d levels. More precisely, it would seem that the narrow d-band associated with the magnetic ions should broaden and receive higher amounts of p-character as the magnetic concentration increases. The hybridization could then alter the electronic energy levels in a way that could favour spin-pairing. In this case the behaviour of p_{eff} would be understood as due to the hybridization and delocalization of the magnetic levels.

It is interesting to note that the low spin value seen

in the high x alloys, and in $CuFeS_2$ closely approximates that of an S=3/2 state. This suggests that a crossover description of the type seen in crystal field theory may be usefull.

Although it is a rare occurence, several cases of $^6A_1$-$^2T_{2g}$ crossover, giving a transition from a high-spin (5/2) ground state to a low-spin (1/2) ground state, have been documented in inorganic molecules by Mössbauer spectroscopy [55]. In our case of tetrahedral fields it is possible that another crossover occurs. Indeed the fact that the high concentration value of p_{eff} coincides with the spin-only value of the $^4T_1$ (S=3/2) state seems to suggest the presence of a $^6A_1$-$^4T_1$ crossover.

The correlation diagram for a d^5 state in a tetrahedral field is given in fig. 3.4.7. The terms $^6A_1$, $^4T_1$, $^2T_2$, are all candidates to become the ground state in arbitrary crystal fields. The exact way that the levels cross in the intermediate crystal field regime depends on the precise values of the atomic parameters for example the Racah parameters (see appendix 1) as well as on the details of the bonding with the neighbouring ions which create the crystal field. Such considerations signal the transition from 'crystal' fields to 'ligand' fields however the correlation diagram is generally thought to apply in both cases. 'Crossover' refers to the crossing of levels and can result in a change of the ground state spin configuration as can be seen from comparing the high and low-field ends of fig. 3.4.7. If the value of the crystal field is such that the crossing level

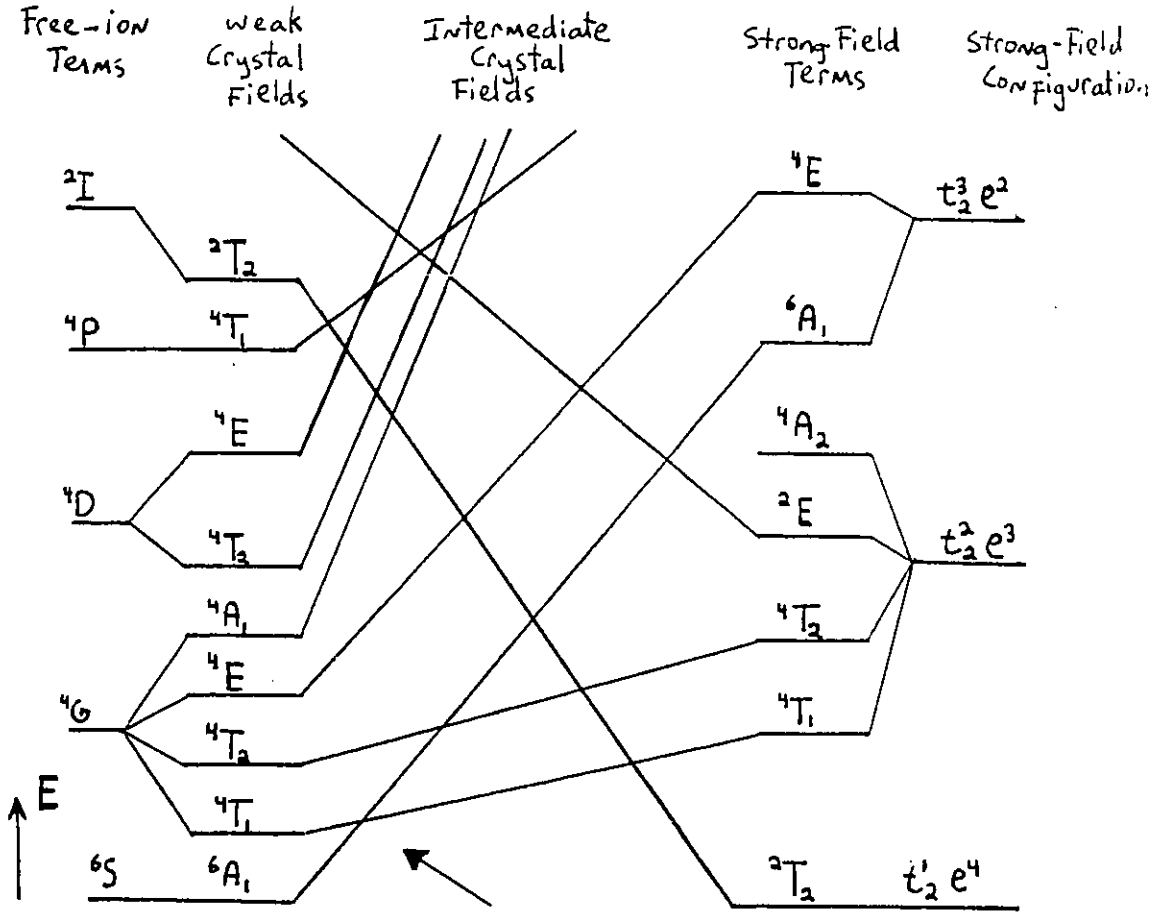

Fig.3.4.7 Correlation diagram for d^5 in T_d symmetry.
The correlation diagram connects the free ion terms (on the left) to the strong-field configurations (on the right) according to their symmetry. Only the lower portion of the whole correlation diagram is shown. Lines from weak-field terms which do not end on a configuration on the right hand side of the diagram continue off the scale shown here. The energy scale increases in the direction shown. The crossover from the $^6A_1$ to a $^4T_1$ ground state is marked with an arrow. The diagram is not to scale.

energies are sufficiently close, crossover can result in the simultaneous population of more than one level. The latter case will be referred to as a mixing of levels.

Indeed, abnormally small energies of the $^4T_1$-$^6A_1$ transitions have been observed in infrared luminescence measurements on Fe^{3+} doped $CuGaS_2$ and $CuAlS_2$ [96], and have been attributed to an "anomalous lowering" of the $^4T_1$ crystal field state. As specified in [96], the observed transitions occur at approximately half the energy (5000 cm^{-1}as compared to 10000 cm^{-1}) at which they occur in many octahedrally coordinated ferric oxides. These authors also verify (by Zeeman effect measurements) the integrity of the $^6A_1$ ground state which verifies the validity the crystal field description at low x. The anomaly may be qualitatively explained by the hybridization discussed above.

As mentioned above, the change in p_{eff} associated with crossover-type behaviour occurs over the restricted concentration range which seems to coincide with the range of d-delocalization and moment reduction reported for $CuAl_{1-x}Fe_xS_2$ [72]. If delocalization and hybridization result in having a spin 3/2 level become the ground state, any possible use of crystal field theory is excluded since that theory strictly applies only for the case of well localized charged neighbours exerting electric fields of a given symmetry on well localized central ion states. Rather it would seem that an effective, concentration dependant ligand field occurs which increases in strength proportionaly to x.

This description seems plausible in so far as the $^6A_1$ state at low x can be confidently identified, and the magnetic moment of the high x state corresponds to spin-only moment of the $^4T_1$ state. The fact that the measurements in the high x regime show p_{eff} values very close to the spin-only value of the $^4T_1$ state and thus that g=2, indicates that the orbital momentum of the state is for all practical purposes, fully quenched. Indeed the problem of determining theoretically the magnetic moment of a crystalline state in the presence of spin-orbit coupling, low-symmetry ligand fields and d delocalization is difficult. For these reasons it is known that the magnetic properties of T ground terms are sensitive to the presence of low-symmetry ligand field components and to d-t_2 delocalization [94]. Both of these effects result in a quenching of the orbital momentum and a tendency to decrease any temperature dependance of the moment, and to bring it closer to the spin-only value. This fortifies the ligand-field description, however the complete lack of temperature dependence of the magnetic moments must be considered. This can best be seen by considering the ideal case of crossover as shown directly on fig.3.4.7.

The temperature independence of the moments over the range of the measurement is evidenced from the Curie-Weiss behaviour of the samples. This would be expected for samples removed from the narrow ligand-field transition region however not so for those samples displaying an intermediate p_{eff}, in particular for the $z \leq 0.1$ on fig. 3.4.5. In general a

temperature-dependant Boltzmannian distribution over the two states is expected;

$$\frac{N_2}{N_1} \propto \exp-\beta(E_2-E_1)$$

where N_2 signifies the population of the higher energy state. This leads to a temperature-dependant moment when $kT \cong \Delta E$, otherwise only the lower level is populated. Since $kT \cong 0.017$ eV (136 cm^{-1}) at 200°K whereas the term splittings on fig. 3.4.7 are nearly two orders of magnitude larger (5,000 cm^{-1}), there is only a narrow range of concentration over which one would expect any thermal variation of the magnetic moment over our measuring temperatures. This range of concentration should necessarily coincide with the range over which the moment reduction occurs and the absence of such variation could only be consistent with the crossover scenario if it were due to slight variations in the composition of the samples. Even in a hypothetical exact crossover scenario, any small variation in sample composition would give the apparent temperature independance of the observed average moments due to the averaging that occurs in the bulk measurement.

The temperature independance of the moments raises doubts concerning the prediction (see section 3.3) that the Mössbauer α-doublet splitting should also be temperature dependent, since exactly the same mechanism is assumed to operate there. The ligand-field description thus seems to give a qualitative description of the p_{eff} change, however it can be seen that this approach is only approximate.

Other explanations for the reduction of the Fe moment from the $^6A_1$ value in $CuFeS_2$ have been studied. Obviously the moment reduction could be accomplished by adding 'down' spins to the Fe, and this is the approach taken by various authors [97] [98]. clusters of atoms in that lattice [97], [98]. The result of the molecular (cluster) orbital calculations of Kambara et. al [97] is that the Fe moment is caused by an average occupation of 5.8 electrons per Fe, although there is a discrepancy between Fe at the center and the corners of the cluster used to approximate the crystal. It is also significant that these calculations predict very similar results for dopant Fe concentrations, hence are not complete representations since it is now known (see fig. 3.4.5) that the J=5/2 value is approached at low x (the J=5/2 value has since also been reported [99] for Fe doped into $CuGaS_2$). particular material. Also, it is not clear how the addition of electrons to the Fe could be made consistent with the observed Fe^{3+} ionization state.

In fact this is an example of how alloy systems can give information about end member compounds. Notably we now know that only a low concentration of Fe is required to yield the chalcopyrite ($CuFeS_2$) p_{eff}, but that at very low concentrations, the free-ion value exists. This indicates that the Fe ions 'interact' strongly and suggests why molecular orbital treatments are not satisfactory. Rather invoking something like d-delocalization may be essential in achieving an accurate explanation. This makes all the more

impressive the possibility that the simple ligand-field description might apply at all.

As an example of the kind of considerations involved, it is well known [74 pr-21] [94], that π-bonding in some octahedrally coordinated transition metal sulfides induces a splitting of the e_g and t_{2g} Fe orbitals. This splitting is similar to the 10Dq splitting of ligand-field theory, and results in the t_{2g} set having lower energy. This has been used to explain the presence of low-spin states of the metal in these materials. Indeed such molecular orbital considerations demarcate the limit of applicability of ligand-field theory, and are discussed in detail in ref [94, p189]. π bonding can also occur in tetrahedral complexes along with p-d(t_2) hybridization which together can also greatly effect the ordering of the energy levels. The Fe alloy system could thus provide an experimental testing ground for the transition from a crystal-field (low x), to a ligand-field to a delocalized band description of the Fe states.

To summmarize, the techniques brought to bear on the system of study in this chapter have been very useful together. The magnetization data correlated well to the previous results since single-phase paramagnetic behaviour occured, as expected on the basis of x-ray and Mössbauer data for both the low- concentration LTA materials as well as for the HTQ samples.

4.1.0) Ordering In The Mn-Containing Chalcopyrites

The number of different types of crystallographic order that a material can support generally increases with the number of elements that make it up. A good example of this is the cationic ordering which occurs in the case of the chalcopyrites. This type of ordering is only possible when two distinct types of cations are present in the crystal. The substitution of a third cation (Mn) in the chalcopyrite alloy systems we are concerned with, leads to the possibility of other types of order not possible in the parent compound.

In this section, we will survey the early work from the Ottawa group which suggested that crystallographic ordering of Mn could be occurring in the $(I\ III)_{1-z}Mn_{2z}VI_2$ chalcopyrites. Although some recently obtained information will also be presented with this review, most of the results obtained in the course of the present research project will be presented in the later sections of this chapter.

4.1.1) Magnetic Susceptibility

The most obvious evidence for ordering comes in the form of magnetic susceptibility data, in particular the dependence of the susceptibility cusp temperatures (T_c) on heat treatment.

The susceptibility cusps are in general interpreted as indicating the presence of magnetic critical temperatures. Indeed, as shown in the introductory chapter, DMSare a class of materials in which spin glass and antiferromagnetic phases are ubiquitous [6].

As indicated in section 1.2, a prerequisite to spin glass behaviour in these materials is some degree of randomness (disorder) of the magnetic ions on the cationic sublattice(s). For this reason, any tendency to order is expected to reflect itself on the magnetic behaviour. In particular, fully ordered systems are not expected to sustain spin glass behaviour, and partially ordered systems could display different spin glass temperatures from fully disordered ones.

The latter effect has been reported in the cases of $(AgIn)_{1-z}Mn_{2z}Te_2$ and $(CuIn)_{1-z}Mn_{2z}Te_2$ [100], and $(AgGa)_{1-z}Mn_{2z}Te_2$ [101]. In these materials, different cusp temperatures have been reported (see fig.4.1.1.) for samples of identical composition, which however display apparently identical powder x-ray patterns. The magnetic behaviour, as characterized by the cusp positions, has been shown to be different for quickly cooled samples than for slowly cooled ones, and the behaviour under various annealing conditions has been investigated. Distinct sets of T_c's have been associated with both the zincblende and chalcopyrite phases of these materials, indicating that the inter-Mn correlations (ordering) occur in both of these phases.

The key observation reported in [100] is that the resulting samples have apparently identical powder x-ray patterns and lattice parameters but different magnetic behaviour. This indicates a change in the inter-Mn interactions within the same basic crystal type, and thus suggests the crystallographic ordering of the magnetic ions.

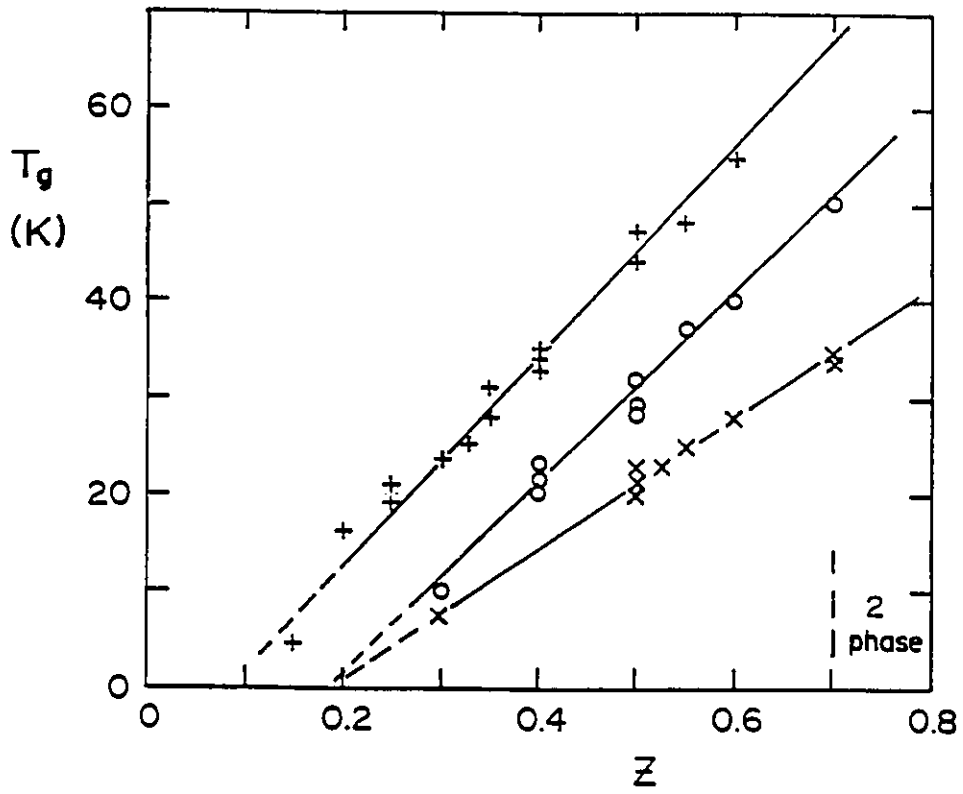

Fig.4.1.1 Susceptibility cusp temperatures (T_g) vs. composition (z) for $(AgIn)_{1-z}Mn_{2z}Te_2$.
Illustrated is the concentration dependence of the various susceptibility cusp temperatures seen in the $(AgIn)_{1-z}Mn_{2z}Te_2$ alloys as reported in reference (100). The various groupings evident in the graph have been attributed to disordered zincblende, X ordered zincblende, o and + ordered chalcopyrite forms of the materials. These were obtained by appropriate heat treatment as described in (100). Such behaviour in the materials indicates the presence of inter-Mn correlations.

The susceptibility cusps in these cases can be separately enhanced or diminished according to the detailed heat treatment, a fact which is made all the more significant by the observation of the concurrent linear variation of each type of T_c with Mn concentration (see fig.4.1.1). The lines connecting data points in the figure define the sets of transition temperatures which are correlated to the heat treatment, and phase diagram data in this way. The labels seen in fig. 4.1.1 refer to the Mn-ordering only. This is order to avoid confusion with other types of cationic ordering such as that of the cationic ordering which occurs in the transition from zincblende to chalcopyrite structure. Samples rapidly quenched from high temperature are associated with the highest disorder i.e. Mn-disordered zincblende phase, whereas slowly cooled samples are attributed with the highest forms of order, culminating in the Mn-ordered chalcopyrite phase. The wide range of behaviour seen is attributed to the complicated nature of the phase diagram and the possibility of many types, and degrees of Mn-ordering. Indeed the ordering is highly sensitive to sample preparation[1].

Together with the observed constancy of the crystal structure, the above constitutes strong evidence for the interpretation that the cusps are directly related to a configurational effect relating to the magnetic (Mn) ions within a homogenous environment.

Another signature for ordering is the occurrence of

1 Some ordered structures are suspected to form relatively rapidly, even upon cooling in certain cases.

non-linearity in the Curie-Weiss θ vs. z (concentration). θ is one of the parameters that characterize the high temperature paramagnetic regime of the magnetism. The mean-field expression for θ [66] is:

$$\theta = 2/3k\ S(S+1)\ \sum n_i J_i \qquad (4.1.1)$$

where n_i is the number of ith magnetic nearest neighbours and J_i is the corresponding exchange constant. This expression can be seen, for the case of a random substitution of Mn on the cation sites, to scale with z:

$$\theta = 2/3k\ S(S+1)\ z\ \sum n_{oi} J_i \qquad (4.1.2)$$

here n_{oi} is the number of ith nearest cation neighbours. Thus any significant[2] deviation from linearity in θ vs. z can be an indication of a configurational correlation between magnetic ions. Similarly, the occurrence of more than one θ in homogenous materials of identical stoichiometry also illustrates the phenomenon. In other words, if materials with identical stoichiometry can be prepared with different θ's, one would conclude that most probably, the materials support some form of ordering.

This is shown to be the case in figs. 4.1.2a and 4.1.2b. These plots illustrate the range of θ values as a function of concentration in the chalcopyrite materials previously discussed. The exact heat treatments of the samples is given in the figure. The onset of non-linearity is not associated with a visible (x-ray) change in crystal structure.

[2]An example of 'non-significant' change in θ is one due to a change in J caused by a concentration dependent change in lattice parameter [91].

Fig. 4.1.2a $(AgIn)_{1-z}Mn_{2z}Te_2$ Θ vs. z

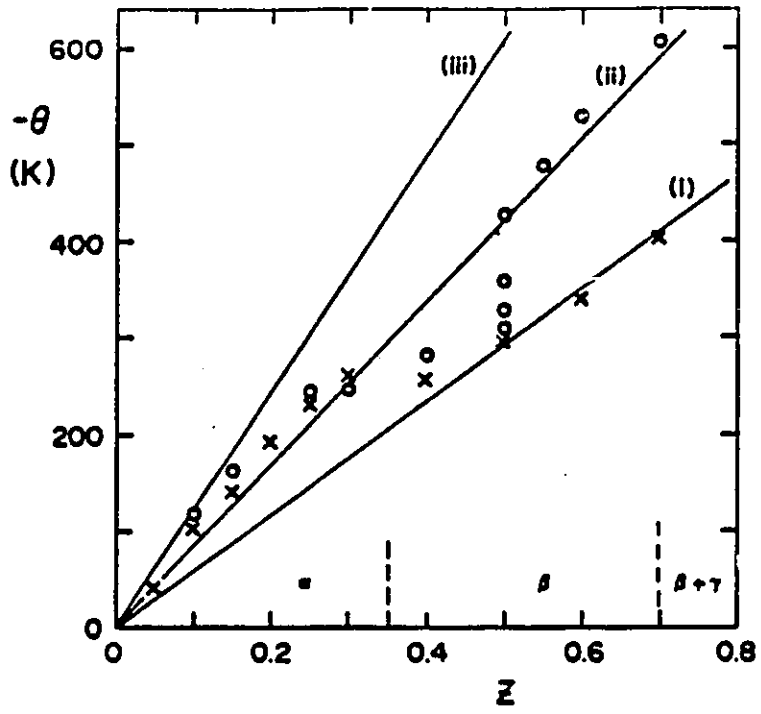

Fig. 4.1.2b $(CuIn)_{1-z}Mn_{2z}Te_2$ Θ vs. z

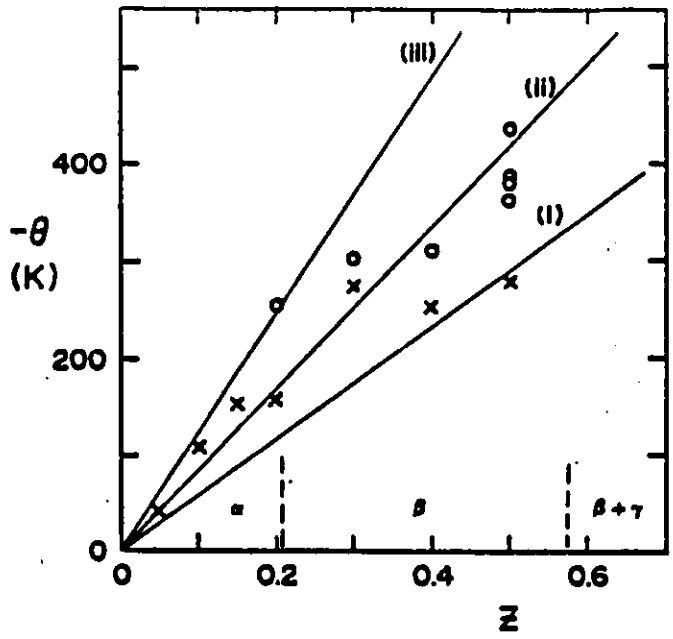

Figs. 4.1.2a and 4.1.2b (from ref. (100)). Curie-Weiss temperatures (Θ) vs composition (z) for $(AgIn)_{1-z}Mn_{2z}Te_2$ (4.1.2a), and $(CuIn)_{1-z}Mn_{2z}Te_2$ (4.1.2b) illustrating the non-scaling and heat-treatment dependency characteristic of ordering. The points marked X represent water-quenched samples, and those marked O represent slowly cooled samples.

Fig.4.1.3, taken from [102], shows for comparison the scaling behaviour observed in the zincblende alloy $Cd_xZn_yMn_zTe$, in which Mn ions always randomly occupy the cation sites.

The non-scaling behaviour illustrated in figs.4.1.2 occurs due to the effective averaging of θ values corresponding to the ordered and disordered fractions present in the samples. Since the crystallographically ordered phase fields exist at low temperatures, the slowly cooled samples display the largest amount of order. The lines illustrated in the figures correspond to the expected θ vs. concentration curves for the various fully ordered and fully disordered samples as indicated.

The non-scaling of θ with concentration in sulfide chalcopyrites has also been observed by another independant SMSC research group [103], and will be discussed further in the next sections.

It may be remarked from equation (4.1.1) that a concentration dependent change in the effective ionic spin value (S) could also lead to an apparent nonlinearity in θ. This could be caused from a failure to properly account for the exact quantity of Mn ions in the samples, or through a real change in the Mn spin state. The former effect would result for example in the event that some elemental (antiferromagnetic) Mn remained in the sample, this would effectively reduce the net number of Mn ions contributing to the paramagnetic signal from which θ is derived. The latter effect would presumably be due to changes in the crystal-field operating on the Mn as a function of composition similarly to

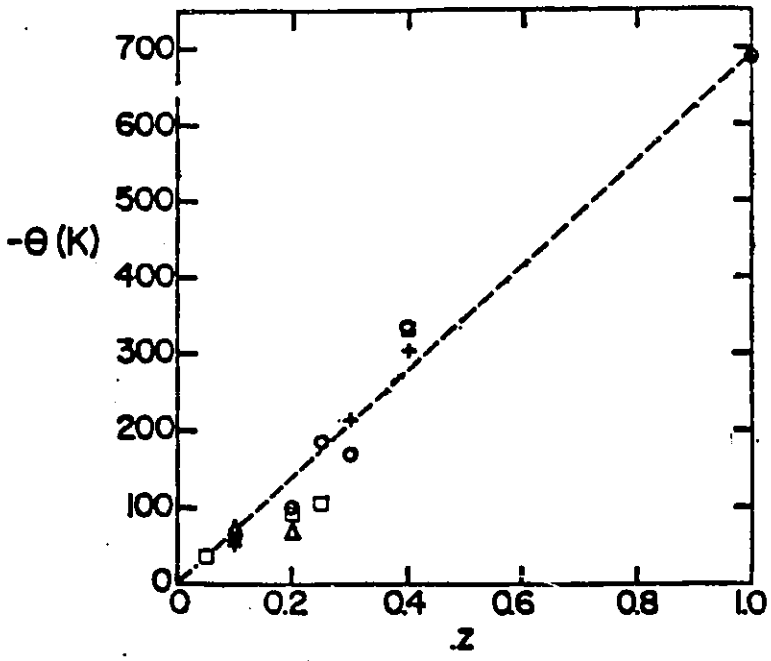

Fig. 4.1.3 (From ref. [102]). Curie-Weiss temperature (θ) vs. Mn composition (z) for various samples of the system $Cd_xZn_yMn_zTe$. The scaling behaviour seen over the full range of solid solution suggests the random nature of the Mn substitution.

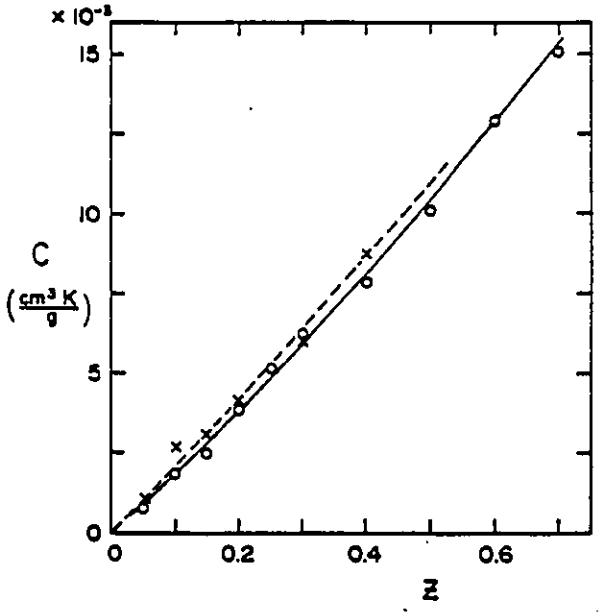

Fig. 4.1.4, Curie constants (C) vs composition.
The measured and expected Curie constants for both the $(AgIn)_{1-z}Mn_{2z}Te_2$ (measured, O and predicted ———) and the $(CuIn)_{1-z}Mn_{2z}Te_2$ (measured, X and predicted ------) samples as reported in ref. [100] are shown. The agreement between the measured and expected values indicates that Curie-Weiss behaviour does describe the magnetic susceptibility of these materials.

the iron case reported in the previous chapter.

The above considerations can be seen not to be the case from fig.4.1.4 which illustrates by virtue of the agreement between the experimental and theoretical Curie constants, both the constancy of the the S=5/2 spin assignement, and the fact that all the Mn ions do indeed contribute to the paramagnetic signal from which θ was extracted. This will also be discussed further in the following sections.

4.1.2) Optical Energy Gap

The energy gaps of the alloy systems can also be used as indicators for the occurrence of ordering. This was first documented in 1985 for the cases of $(CuIn)_{1-z}Mn_{2z}Te_2$ and $(AgIn)_{1-z}Mn_{2z}Te_2$ in the context of the related systems $Cd_x(CuIn)_yMn_zTe_2$ [104] and $Cd_x(AgIn)_yMn_zTe_2$ [105], [106]. The energy gaps of these materials can be measured by optical absorption (see chpt.2) and have been found to be direct in each case. Mn-ordering is expected to affect the band structure and hence the energy gaps of the materials.

Unlike in magnetic measurements whereby all magnetic phases present in a sample give their characteristic signature, on measuring the energy gaps by optical absorption, usually only a single (lowest energy) gap can be extracted from the material. Only in exceptional cases [107] can both ordered and disordered energy gaps can be seen in the same sample, due to the difficulty of applying the absorption technique to such cases, specifically the difficulty in producing thin enough samples for measurement (see section

2.).

The main aspect of the optical behaviour is the fact that the energy gap values, as a function of composition, extrapolate to one of a limited number of distinct 'aiming points' at z=1.0, shown on fig. 4.1.5. In this figure, the various groupings of alloys into sets according to their extrapolated E_o vs. z curves can be seen. The insensitivity with respect to concentrations x and y of the members of the largest family of lines (marked with an 'A' in the figure) suggests that these are strictly due to changes in the Mn (z) arrangement. Similar behaviour has since been found in $(AgGa)_{1-z}Mn_{2z}Te_2$ [108].

The extrapolated points can be used to categorize the samples into 'similarity' groups, for example the value of 2.83 eV (fig. 4.1.5) can be associated with Mn-disordered zincblende structure because it derives from the samples of zincblende structure, and is identical to that previously found in the strictly disordered zincblende system $Cd_xZn_yMn_{(1-x-y)}Te$.

In this analysis, generalities can be drawn from the specific systems simply by extrapolating into the regime all the systems have in common; i.e. to z=1.0. Other aiming points are similarly taken to be related to an underlying structure or general trend, and can be associated with Mn ordering in the various chalcopyrite systems.

Some optical measurments were performed in the course of this research and found to yield single absorption steps characteristic of a direct bandgap. The gap energies were

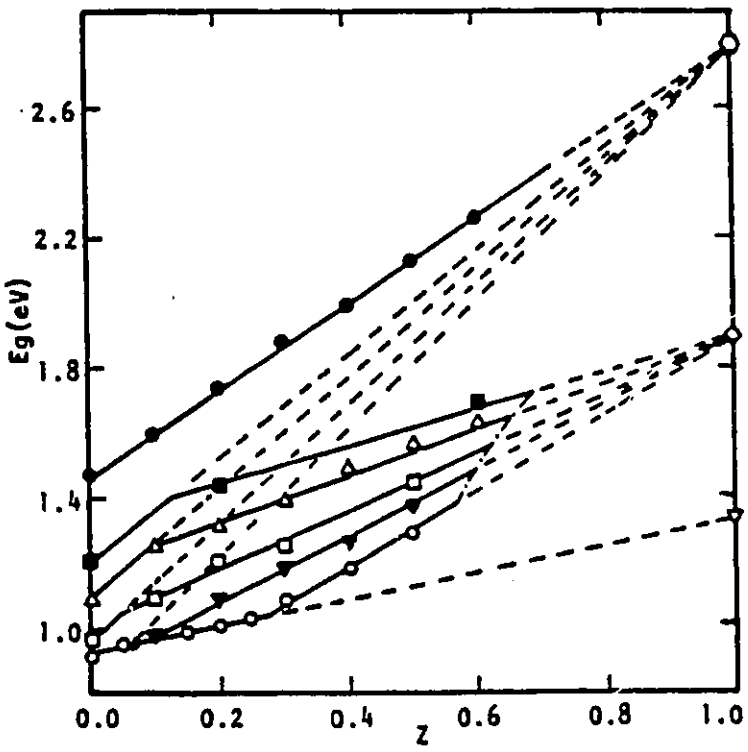

Fig. 4.1.5 Optical 'aiming points' in $Cd_{2x}(CuIn)_yMn_{2z}Te_2$. This graph, taken from ref.[105], illustrates the groupings which occur on the basis of room temperature optical energy gap, in the system $Cd_{2x}(CuIn)_yMn_{2z}Te_2$. The optical energy gap in eV is graphed on the vertical axis, against the Mn-concentration (z) on the horizontal axis. The various plot symbols indicate fixed x:y ratios in the chemical formula. (○) x=0, (▼) y=3x, (□) y=x, (△) x=3y, (▩) x=7y, (●) y=0. The lowest two groupings have been attributed to ordered cubic and ordered chalcopyrite phases (in order of decreasing energy) in [105]. The highest aiming point at 2.83 eV, corresponds to the energy gap of the hypothetical zincblende MnTe. The behaviour illustrated here shows the cation-content dependency of the Mn-ordering.

found to be concentration dependant and had values consistent with thcse previously found in these slowly cooled alloys. Since the measurments were limited by the signal strength as discussed in section 2.3.1 (see also section 4.3), these proved to have little value in identifying the behaviour of the ordered structure.

4.1.3) Electron Spin Resonance

A previously unexplained feature of the ESR of many materials closely related to the chalcopyrites under investigation was studied as a possible signature of Mn-ordering. The feature was an extra narrow (ΔH=120 Gauss) resonance line distinguishable from the expected broadened resonance of the random alloy (see fig.4.1.6a).

ESR studies have been performed in various alloy systems related to the chalcopyrites [109]] [110]. In particular, the zincblende $Cd_xZn_yMn_{1-x-y}Te$ [111] system is of interest because, in many ways it is expected to be analogous to the zincblende phases of the chalcopyrites. In these systems, the prominant feature of the ESR is a single broad ($\Delta H \simeq 600$ Gauss) line of approximately Gaussian shape, which is centered at $g \simeq 2$. The linewidth is strongly temperature dependant.

In contrast, multiple or superimposed ESR lines like the one described above, could occur in a composite system containing two distinct magnetic environments. This could be realized in a partially ordered material in which the ordered inter-Mn interactions are significantly different from those in the disordered fraction.

The 120 Gauss (narrow) line has, in the course of this investigation, been correlated with the occurrence of additional x-ray reflections in the corresponding samples indicating the non-equilibrium or poly-phase nature of the samples, and thus will not be studied further.

The possibility remains of attributing other observed non-simple (i.e. non-Lorentzian or Gaussian) lineshapes to Mn-ordering in certain samples. In particular, since the alloys being studied have rather high Mn concentrations, alloy broadening could be expected to play a role in both the Mn-ordered and disordered fractions, hence multiple broad ESR lines may be the expected signature for partially ordered samples.

This will be discussed further in the section 4.3. In the meantime, we simply note that multiple broad lines are hard to distinguish from each other, especially at moderate and high Mn concentration where the ordering is expected to be most significant, hence the ESR is expected to be an insensitive indicator for such signatures of the ordering.

As an interesting example of the type of difficulty that can arise in these investigations, it is true that a qualitatively identical double-line spectrum to that in fig.4.1.6a can occur due to double quantum transitions [60, p.292, 327] [112] [113, (pages.437, 482)] see fig.4.1.6b. Such transitions are observable at moderate to high microwave power. It can be seen, however that the fine structure of Mn in these and related materials does not support the double quantum phenomenon (see section on ESR). This fact was

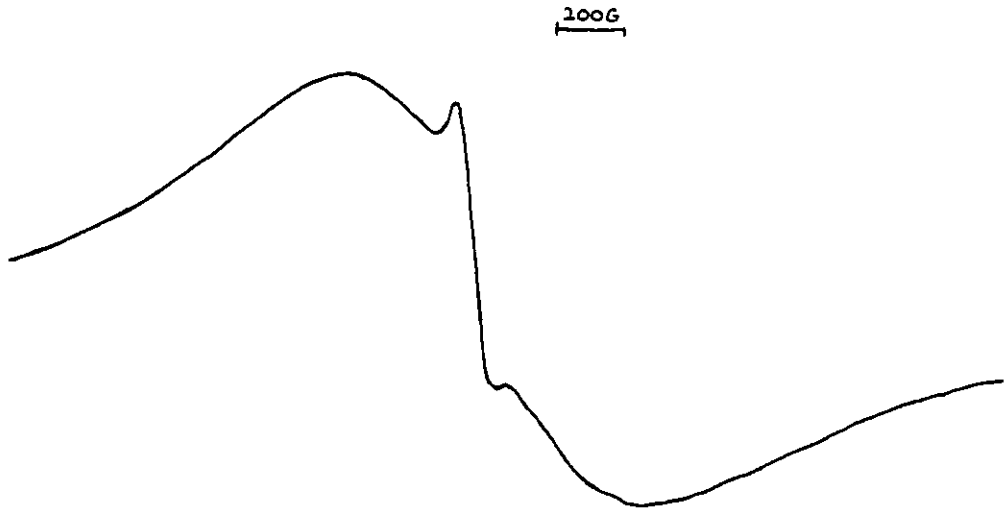

Fig. 4.1.6a, Experimental ESR trace of polyphase $Cd_{2x}(CuIn)_yMn_{2z}Te_2$ sample. Illustrated is an accurate reproduction of the double-line ESR signal due to a sample of $Cd_{2x}(CuIn)_yMn_{2z}Te_2$ with nominal composition x=0.40, y=0.40, z=0.20. The double line feature was investigated as a possible signature of Mn-ordering, however was determined to be due to the presence of a second phase in the sample.

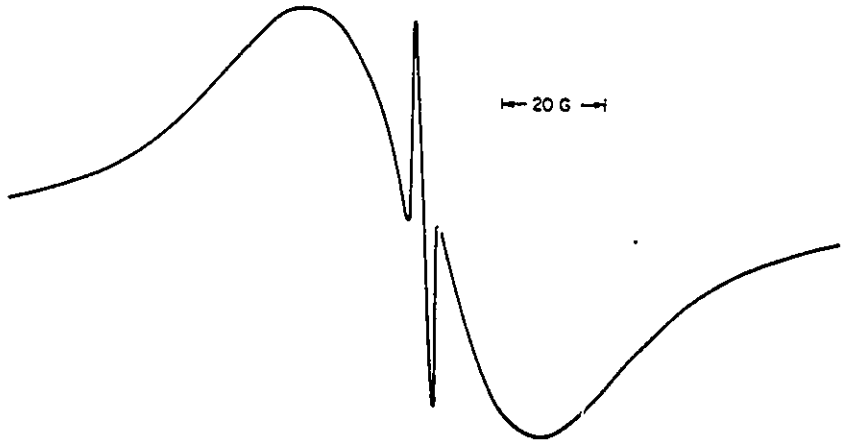

Fig. 4.1.6b, Double quantum ESR transition.
Illustrated is the qualitatively identical ESR spectrum to that given in 4.1.6a, which is due to the superposition of single, and double quantum ESR absorptions. The example given in this figure is due to Ni^{++} in MgO, and is given in reference [60] as an example of the double quantum phenomenon.

corroborated experimentally during the course of this research, by the observed invariance of the narrow line with respect to microwave power.

4.1.4) X-ray Diffraction

Although faint x-ray reflections possibly attributable to ordering have been reported for the case $(CuIn)_{1-z}Mn_{2z}Te_2$ [105], these have not yet been explained. In fact there is no reported conclusive x-ray analysis of Mn ordering in these materials.

As indicated above, samples with apparently identical powder x-ray photographs can have very different magnetic and optical behaviour. Since the magnetic and optical properties are so intimately connected to the crystal structure, this constitutes strong evidence to suggest that some crystallographic ordering can occur without a corresponding powder x-ray signature. This is probably due to the weakness of the ordering lines associated with the ordered structure. This also leads us into the uncommon situation of using the magnetic susceptibility data as a means of characterizing the materials.

It will be shown that some plausible ordered structures can be very hard, or impossible to distinguish from their disordered counterparts by use of Debye-Scherrer photographs alone. One good example of this phenomenon already mentioned is the case of chalcopyrite $(CuIn)_{0.5}MnTe_2$ whose combination of c/a=2 and weak ordering lines make it virtually indistinguishable (by this technique) from the corresponding

zincblende phase.

Detailed measurement of single crystals of these materials would greatly facilitate solving the ordering problem, however the phase diagrams of these systems do not admit easy production of mono-crystals. In particular the ubiquity of multi-phase fields below the liquidus precludes all simple high temperature growth techniques. Low temperature growth techniques such as chemical vapour phase deposition introduce other complications regarding sample purity and stoichiometry, but represent another possible research project. An unsuccesfull attempt was made to obtain diffractometer data on what appeared to be a single crystal of material which was cleaved from one of the ingots.

The absence of a clear powder-x-ray signature for Mn-ordering does rule out any possible changes in crystal structure which would require drastic changes in the crystal structure and so still does provide guidance toward solving the ordering problem.

4.2.0) Proposed Ordered Structure

The information summarized in the previous sections indicates that some kind of correlationn between Mn ions occurs within these materials. In order to proceed with an experimental investigation of this Mn ordering, it is useful to explore firstly the types of Mn-structures which might be expected to exist. In this way, an ordered structure can be postulated and then its existence (or not) correlated with experiment. In this sub-section some physical arguments which

provide a basis for postulating an ordered structure will be reviewed.

The 'charge-balancing' which occurs in the adamantine structure semiconductors was discussed briefly in 1.1. There it was noted that the chalcopyrite structure is made up of charge-balanced tetrahedra just as the binary compounds are. In the chalcopyrites this balanced condition is achieved by having two of each cation in each tetrahedron which has an anion at its center. This observation suggests that even in the zincblende phases of the I III VI_2 compounds (in which the cations are randomly arranged), there could still be a majority of such tetrahedra. The disorder would then be achieved largely by randomizing the orientation of these tetrahedra, however some unbalanced tetrahedra are still required in such an arrangement. This may also be a mechanism for the persistance of short range order above the crystallographic transition temperature.

It has been postulated by Garbato et. al. [26] that since tetrahedra which contain exactly two Mn atoms and one atom each of the group I and III elements are electrically balanced to the same extent that tetrahedra in the parent compound are, such structures represent the lowest energy configuration. By contrast, tetrahedra with an excess of group I atoms must become 'acceptors', and tetrahedra with an excess of group III atoms must donate electrons in order to maintain local charge balance. Given this constraint and recalling the fact that the tetrahedra are interconnected, it can be shown that the only consistent way to arrange the Mn

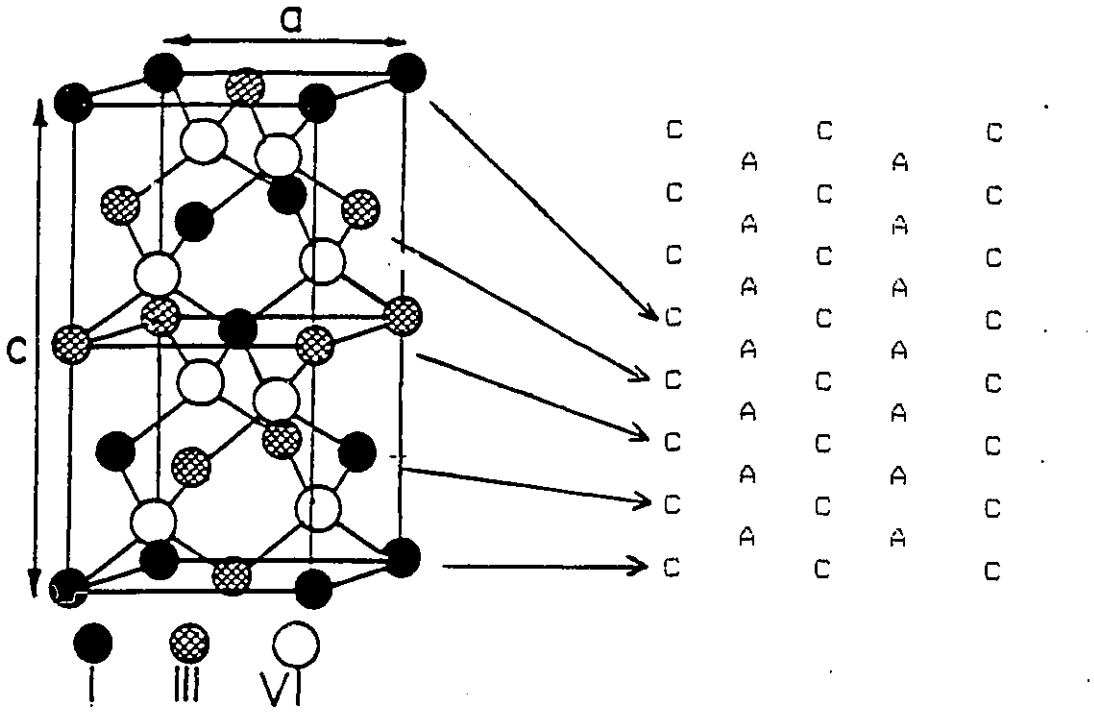

Fig.4.2.1a. Planes in the chalcopyrite structure.
Illustrated are the stacked cation and anion planes within the chalcopyrite structure. The representation at right will be utilized in fig. 4.2.2 to illustrate the possible types of Mn-ordering which may occur.

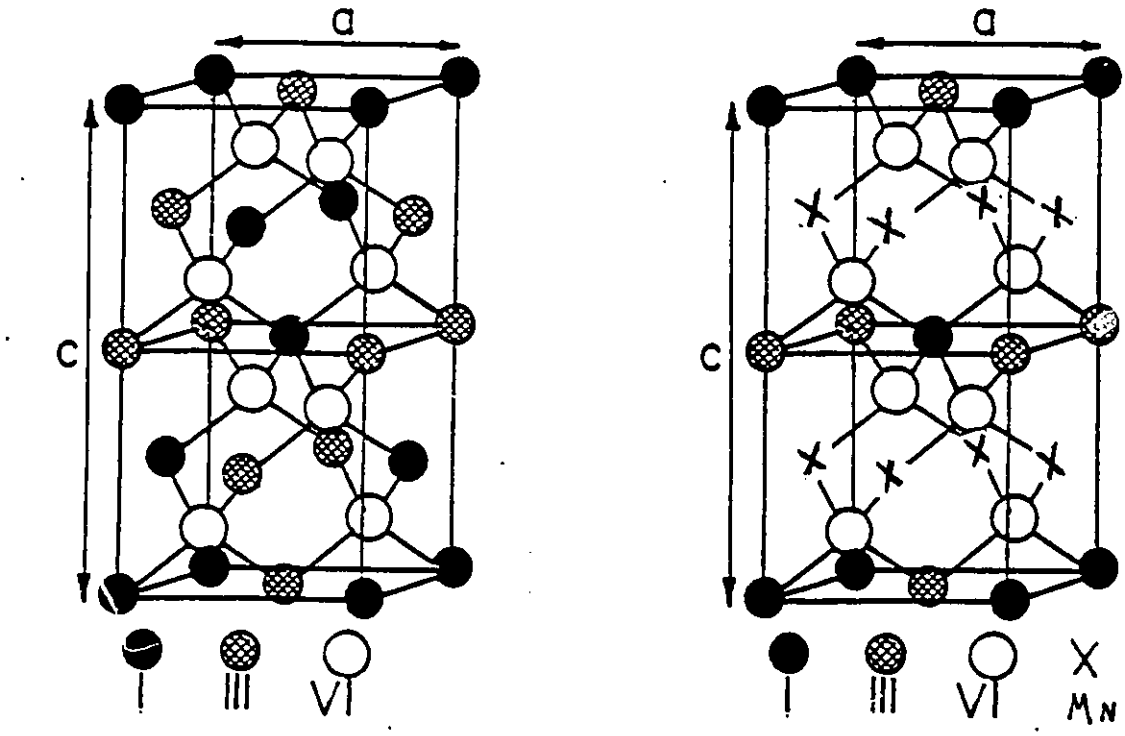

Fig.4.2.1b. The stannite structure.
The conventional unit cells of the chalcopyrite and stannite structure are shown for comparison purposes.

atoms at intermediate and high concentration, is into planes perpendicular to the c axis. The planar structure of the chalcopyrite and stannite structures is illustrated in figs.4.2.1a, and 4.2.1b. In order to facilitate the discussion of planes perpendicular to the z-axis, it can be understood that in all the following, the word 'plane' implies this particular orientation. Fig.4.2.1a illustrates the chalcopyrite unit cell in relation to an edge view which shows how both all the anions and cations fall into coplanar sets which when alternately stacked in the z-direction, recreate the whole crystal. In the following these are referred to as the anion and cation planes. In this figure can be seen how the cation planes in the chalcopyrite structure always contain equal numbers of I and III cations, and how replacing such planes with Mn yields the stannite structure shown in 4.2.1b. The stannite structure can be seen to maintain the local charge balance adjacent to the planes. The planar clustering scenario can result in various stannite-like forms of ordering which will be described in the following sub-section. Such Mn replaced c planes are in contrast to Mn strings, clusters or Mn-planes of any other orientation.

In summary, the above indicates a possible reason to expect correlations between Mn ions substituted into I-III-VI_2 chalcopyrites. More specifically, what is suggested is that a stannite-like ordering, favouring planar (2-dimensional) Mn clusters, could be the preferred configuration.

4.2.1) The Stannite-Like Ordering

The stannite structure of the mineral of the same name, Cu_2SnFeS_4 is illustrated in fig. 4.2.2a, in the shorthand introduced fig.4.2.1a. The chalcopyrite structure is included in the figure for comparison. Although the alloys under investigation are not isovalent with the mineral stannite, the chemical formula for a hypothetical stannite form of the Mn containing alloys is also illustrated in the figure. Such a stoichiometry occurs in the alloy only for z=0.5; $(AgGa)_{1-z}Mn_{2z}Te_2$ for z=0.5 is $(AgGa)_{0.5}MnTe_2$ which is equivalent to $Mn_2AgGaTe_4$ as illustrated.

Although the exact stannite configuration can be realized only for one specific concentration i.e. z=0.5, the above arguments suggest that the tendency to form planar Mn-clusters occurs in the general case. Such a tendency could then manifest itself at lower concentrations ($z \leq 0.5$) in various ways. In the first case, partially filled planes at the fixed stannite positions can be envisioned. In this case the planes become more filled as the Mn concentration increases, becoming totally filled at z=0.5 (see fig.4.2.2b). Alternatively, full stannite-like Mn-planes which are randomly spaced perpendicular to the z-direction can be envisioned. The number of such planes would depend on the exact Mn concentration (see fig.4.2.2b). In either of these scenarios some degree of disorder is required in order to satisfy the postulated tendency toward planar clustering concomitantly with the continuous range of the Mn concentration. In the first case, some randomness occurs within the planes since

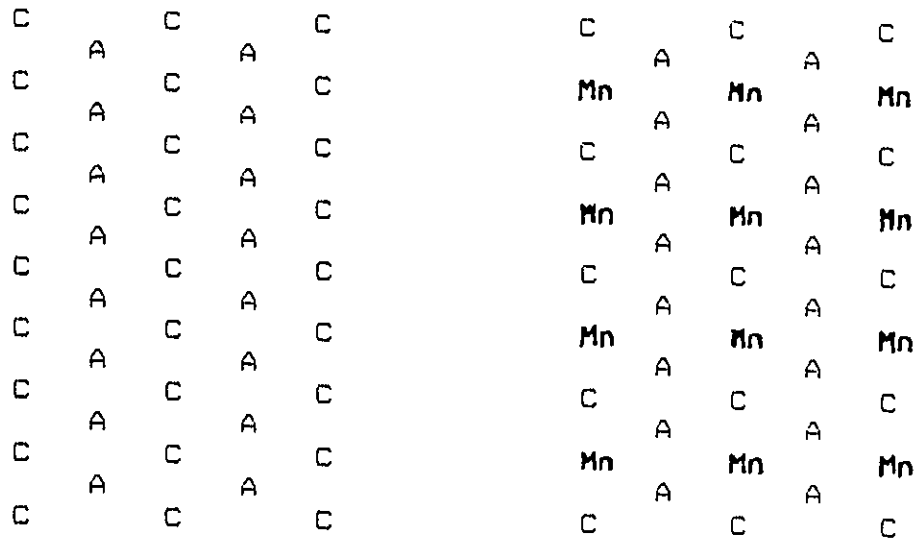

Fig. 4.2.2a, Schematic diagram of the chalcopyrite and stannite structures. The letters 'A' and 'C' stand for anion and cation respectively as illustrated in fig.4.2.1a.

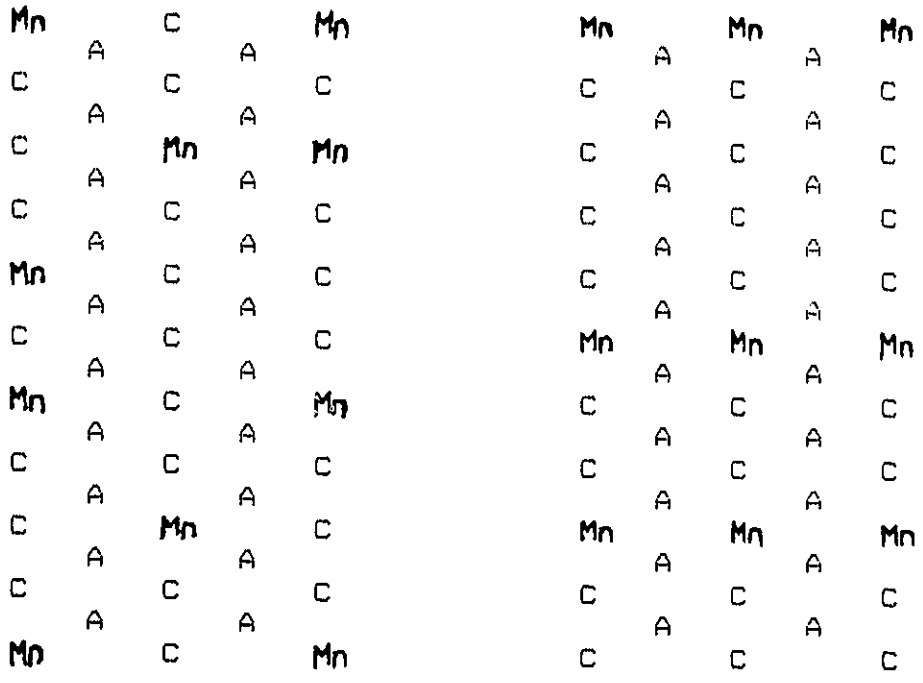

Fig.4.2.2b. Possible stannite-like ordered structures. The illustration at left illustrates the random substitution of Mn on the stannite plane positions within the zincblende matrix. At right is illustrated the postulated ordering condition in which the full stannite-like Mn planes occur which are distributed quasi-randomly in the c direction. Both lattices shown represent the z=0.30 composition.

they are in general not completely occupied by Mn ions. In the second case a quasi-random spacing between full planes must occur since in general the number of planes is not commensurate with the lattice. Based on a consideration of local strain, one would not expect adjacent Mn-planes in this case.

From energy considerations, one might expect randomly spaced full planes over partially filled ones, however configurational entropy must also be considered. In fact the interplay between the energy and entropy terms of the free energy would suggest the occurance of; a) random three dimensional Mn placement, b) partially filled planes and c) full planes, as the temperature is successively lowered and this is a possible interpretation of the ordered phases seen in fig 4.1.1 This will be discussed further in the following sections.

In the remainder of this chapter, the results of experiments designed to test the planar Mn hypothesis will be presented. Since the chalcopyrites have qualitatively new features compared to more usual DMS, such an endeavour is bound to yield some insight into the actual condition in the material, regardless of whether the hypothesis is proven correct or not. In particular, this is expected to answer the question of whether or not the T_c's attributed to ordering in fig 4.1.1 can be associated with distinct stages within the planar ordering hypothesis.

4.3) Search for Signatures of Stannite Ordering

4.3.1) X-ray Signatures

As seen in the previous section, the possibility of exact stannite order occurs in the alloys for z=0.5. In these cases a search for the x-ray ordering lines seems the logical starting point. Before carrying this out, a preliminary analysis of the x-ray structure factors is useful to give an idea as to how clear the x-ray signature for the ordering would be.

The structure factor, introduced in chpt.2, is the crystallographic factor which relates the crystal structure to the coherent reflections which such a structure will induce in a beam of short wavelength radiation. The intensity of the reflections is proportional to the various terms seen in equation (2.1.6) of chapter 2. The two important ones for the present analysis are the structure factor and the multiplicity. The structure factor is given by:

$$F^2 = [\sum_s f_s \cos 2\pi(hx_s + ky_s + lz_s)]^2 + [\sum_s f_s \sin 2\pi(hx_s + ky_s + lz_s)]^2 \qquad (4.3.1)$$

The summations are taken over all the atomic positions (x_s, y_s, z_s) in the unit cell and the scattering factors (f's) are those of the corresponding atoms. The h,k,l are the Miller indices which indicate the family of crystallographic planes responsible for the reflection, and the multiplicity is the number of families of such planes.

It is well known that certain small displacements of the atoms from their ideal positions can greatly affect the values

of the scattering structure factors. This will be shown to be an important consideration in the section 4.4 in which such displacements must be considered in the neutron diffraction fitting. Since only an estimate is appropriate for the immediate analysis, the structure factor of the ideal crystal can be used.

The atomic positions in the hypothetical stannite configuration of the $(I\ III)_{0.5}Mn_{1.0}\ Te_2$ materials (see fig. 4.2.2) are:

Atomic Group	Coordinates
I	$(000)\ \ (1/2,1/2,1/2)$
III	$(00,1/2)\ \ (1/2,1/2,0)$
Mn	$(0,1/2,1/4)\ \ (1/2,0,1/4)$
	$(0,1/2,3/4)\ \ (1/2,0,3/4)$
Te	$(1_4/,1/4,1/8)\ \ (3/4,3/4,1/8)$
	$(3/4,1/4,3/8)\ \ (1/4,3/4,3/8)$
	$(1/4,1/4,5/8)\ \ (3/4,3/4,5/8)$
	$(3/4,1/4,7/8)\ \ (1/4,3/4,7/8)$

It has been shown [104] that the reflections arising from this structure are as follows (notation as in reference[116]):

Type A ▸ h and k odd, l singly even

$$\text{with } F^2_{hkl} = 16[(f_I + f_{III} + 2f_{Mn})^2 + 4f^2_{Te}] \qquad (4.3.2a)$$

Type B ▸ h and k even, l doubly even with h+k+l/2 singly even

$$\text{with } F^2_{hkl} = 16[f_I + f_{III} + 2f_{Mn} - 2f_{Te}]^2 \qquad (4.3.2b)$$

Type C ▸ h and k even, l doubly even with h+k+l/2 doubly even

$$\text{with } F^2_{hkl} = 16[f_I + f_{III} + 2f_{Mn} + 2f_{Te}]^2 \qquad (4.3.2c)$$

Type D ▸ h and k one odd one even, l odd

$$\text{with } F^2_{hkl} = 4[f_I - f_{III}]^2 \qquad (4.3.2d)$$

Type E ▸ h and k even, l singly even

$$\text{with } F^2_{hkl} = 16[f_I + f_{III} - 2f_{Mn}]^2 \qquad (4.3.2e)$$

Type F ▸ h and k odd, l doubly even

$$\text{with } F^2_{hkl} = 16[f_I + f_{III} - 2f_{Mn}]^2 \qquad (4.3.2f)$$

Type E and F reflections have the same structure factors.

Type A, B, and C reflections are derived from cubic analogs, and can be called structure reflections. These also exist for the chalcopyrite structure and have identical structure factors to that case. Type D, E, and F reflections can be called ordering reflections, since they depend on the cationic ordering, and as such do not have cubic counterparts. The Type D reflections can be called chalcopyrite ordering reflections since they are characteristic of the chalcopyrite case. The structure factor of stannite Type D lines is however reduced by a factor of 2 relative to the pure chalcopyrite case. Type E and F reflections are the stannite ordering reflections and do not appear in the case of chalcopyrite structure.

Using these expressions with x-ray atomic scattering factors, the relative intensities of the stannite ordering lines can be estimated. These results are tabulated in Table 4.3.1. In this table the structure factors of relevant line types for each of the cases involving Cu and Ag as group I elements and In and Ga as group III elements are tabulated. Some representative hkl's are given in order to illustrate that in the case of low-angle reflections, the multiplicities further decrease the

Table 4.3.1 Predicted Scattering Factors for Ordering Lines

Material	Line Type (Example)		F^2(x-ray)	m	Intensity
CuIn	A	112	238	8	1904
		312		16	3808
	B	200	25.6	4	102.4
		420		8	205
	D	103	0.8	8	6.4
		211		16	13
	E/F	110	3	4	12
		310		8	24
AgIn	A	112	258	8	2067
		312		16	4134
	B	420	15.3	8	122
	D	---	0.0	--	0.0
	E/F	110	8.4	4	34
AgGa	A	112	760	8	6080
	B	420	26	8	208
	D	103	1.0	8	8
	E/F	110	3.1	4	12.4

Table 4.3.1 summarizes the expected x-ray ordering line intensities for the z=0.50 compositions of the $(AgIn)_{1-z}Mn_{2z}Te_2$ (abbreviated AgIn), $(CuIn)_{1-z}Mn_{2z}Te_2$, (abbreviated CuIn), and $(AgGa)_{1-z}Mn_{2z}Te_2$ (abbreviated AgGa). The lines labelled D are chalcopyrite ordering reflections and theose labelled E/F are stannite ordering reflections. The intensities of some of the structure reflections (types A and B) are given in order to allow for comparison. The intensities shown are the products $I=F^2*m$ where F^2 is the structure factor, and m is the multiplicity of the lines. The angular envelope, and temperature factor is not included in the intensity calculated above. It can be seen that the ordering line intensities, (D, E, F) are orders of magnitude less intense than the structure reflections.

relative intensities of the ordering reflections with respect to the structure reflections.

In each case, all the ordering reflections are at least two orders of magnitude less intense than the strongest structure reflections (type A), and one order of magnitude less than the weakest (type B). To provide a basis for comparison, note that the type B reflections are not visible in the x-ray films of the $(AgIn)_{0.5}MnTe_2$, and barely visible in the $(CuIn)_{0.5}MnTe_2$ and $(AgGa)_{1-z}Mn_{2z}Te_2$ systems, making the cubic and chalcopyrite phases of these materials practically indistinguishable by powder x-ray diffraction. Since the ordering reflections are expected to be about 10 times less intense than these, this illustrates how both stannite and chalcopyrite ordering reflections are not expected to be visible in powder photographs of these materials. This also illustrates a basic problem associated with observing x-ray signatures of any cationic ordering which occurs for cations of similar scattering power, i.e. ordering lines tend to be weak due to the fact that they result from differences in atomic scattering factors.

Indeed no ordering reflections were found in the x-ray films of these materials and given the expected difficulty of finding direct (x-ray) evidence for ordering, a study of the susceptibility and ESR of samples with various heat treatments was undertaken.

4.3.2) Magnetic Susceptibility Signatures

The mineral Stannite (Cu_2SnFeS_4) is known to be an antiferromagnet. In this case however the magnetic atoms do not occupy distinct planar sites and so the magnetic behaviour of the mineral is expected to be very different from that of the hypothesized stannite-ordered $(I\ III)_{1-z}Mn_{2z}Te_2$, which has the magnetic atoms (Mn) on coplanar sites.

Over 20 samples (most of composition z=0.5) in the $(AgIn)_{1-z}Mn_{2z}Te_2$ and $(CuIn)_{1-z}Mn_{2z}Te_2$ systems were prepared as well as numerous samples of $(AgGa)_{1-z}Mn_{2z}Te_2$ with compositions z=0.25, z=0.33, z=0.40 and z=0.50. These were prepared as described in the following paragraphs, characterized by x-ray analysis and studied for their magnetic properties by susceptibility, and ESR measurements.

In the course of this investigation it was found, contrary to the proposed phase diagram (fig.4.3.1) of ref.[103], that the Ag-Ga z=0.5 samples were poly-phase. These samples showed x-ray lines characteristic of MnTe and $MnTe_2$. The magnetic behaviour of these polyphase samples was very different from that of the single phase samples. Most of the polyphase samples displayed complex low temperature response including a small peak or step at the $MnTe_2$ transition (90 K), however one sample had a smooth paramagnetic-like susceptibility over the range from 4-100K. All polyphase samples however displayed a very large temperature hysteresis at 90 K. The important observation from the susceptibility results of the known polyphase materials is that the identification of magnetic impurities such as $MnTe_2$ from the

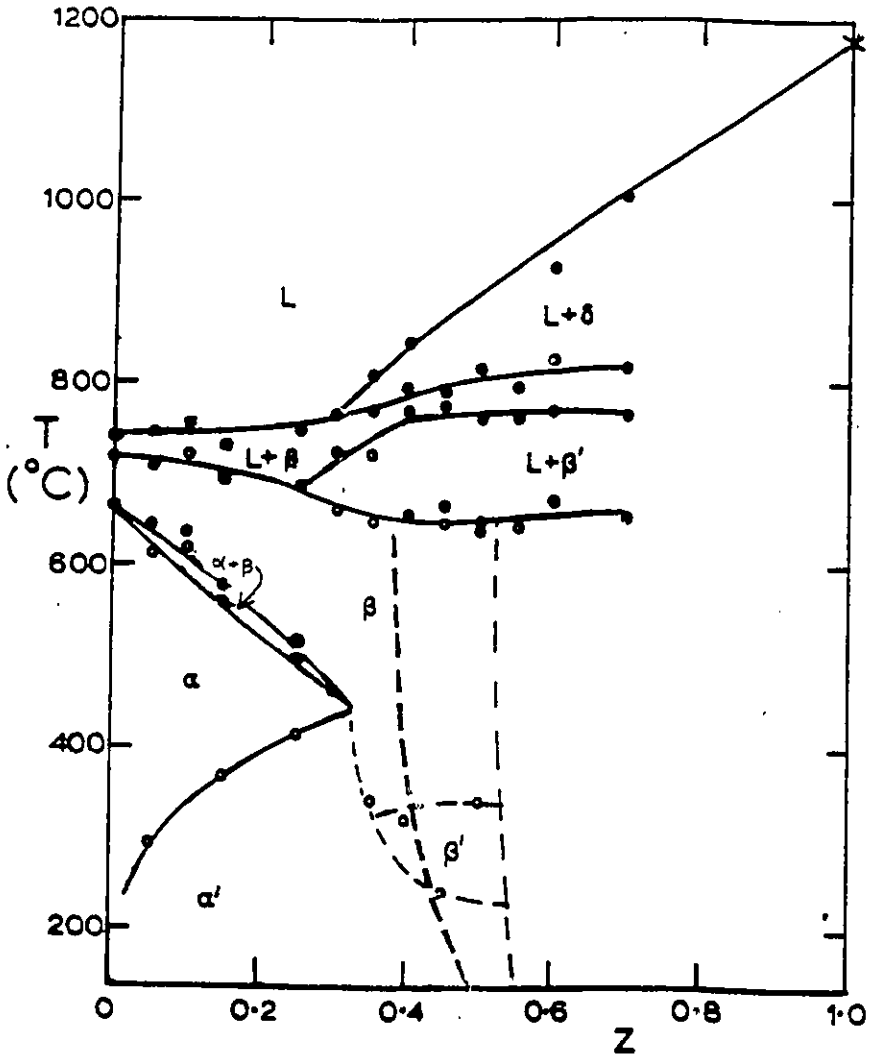

Fig. 4.3.1. Correction to the $(AgGa)_{1-z}Mn_{2z}Te_2$ proposed phase diagram (temperature (°C) vs. composition (z)).
The proposed phase diagram for the $(AgGa)_{1-z}Mn_{2z}Te_2$ system is shown as given in reference [108]. The dark dashed line intersecting the B and B' fields illustrated, is the corrected boundary as required by the observed poly-phase nature of the z=0.50 samples which were fabricated in the present research (see text). The exact position of near-vertical lines such as the one illustrated can however, only be estimated.

zfc (zero-field-cooled) susceptibility can be unreliable, however in the case of $MnTe_2$, the fc (field-cooled) signature is very clear. By making further samples it was determined that the boundary of the α field near room temperature existed closer to the concentration z=0.44 as illustrated in the diagram. Samples of this composition were found by x-ray analysis to be single phase only when very slowly cooled, indicating that probably the α phase boundary curves to lesser z at higher temperature as illustrated.

Since the above constraint on the Ag-Ga z=0.5 composition was found, this material was not studied further in connection with the ideal stannite ordering, however other concentrations of the Ag-Ga system were studied and form the bulk of the results reported in the last three sections of this chapter.

A previously unreported feature of the susceptibility of the slowly cooled and low-temperature annealed single-phase Ag-Ga materials is the prominent maximum near 8 K in the z=0.40 composition shown on fig 4.3.2. This feature was found to be reproducible and due to the large numer of samples prepared and characterized for neutron diffraction (see section 4.4), is known to be characteristic of the high concentration material. Samples of concentration z=0.37 and z=0.44 were prepared in order to find the sensitivity of this feature to concentration. One sample with z=0.44 which was polyphase exhibited a complex low-T susceptibility with no broad maximum, while the sample which was single phase had a broad maximum at 12 K. The z=0.37 sample displayed a qualitatively dissimilar maximum in the form

Fig. 4.3.2, Static susceptibility (chi) vs. temperature (K) for $(AgGa)_{1-z}Mn_{2z}Te_2$, z=0.40.

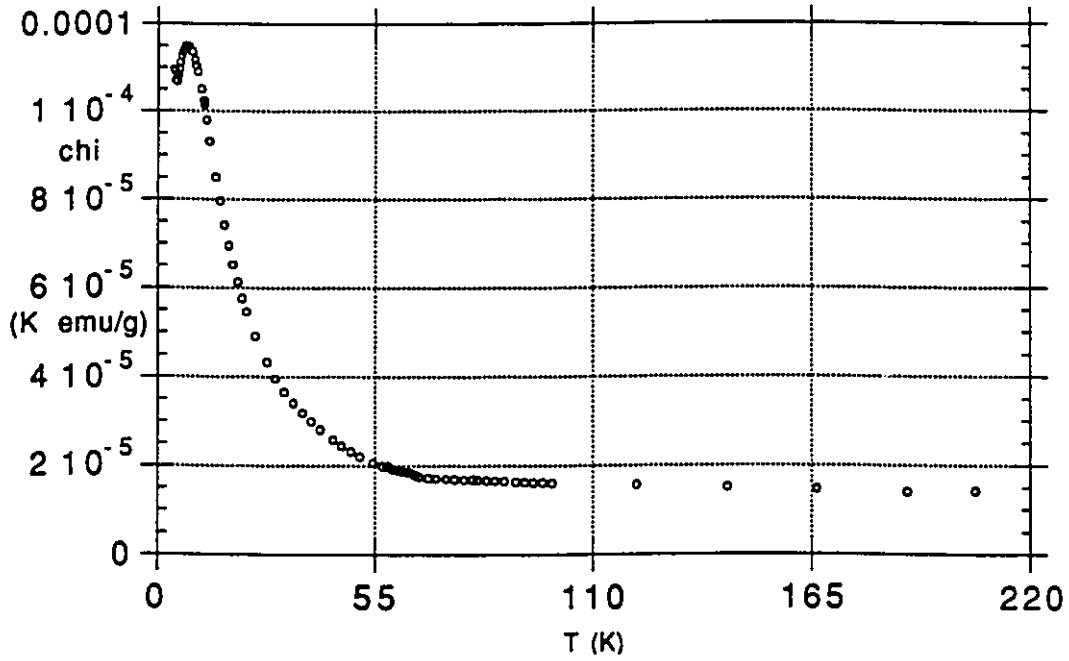

Inverse susceptibility (1/chi) vs. temperature (K) for $(AgGa)_{1-z}Mn_{2z}Te_2$, z=0.40.

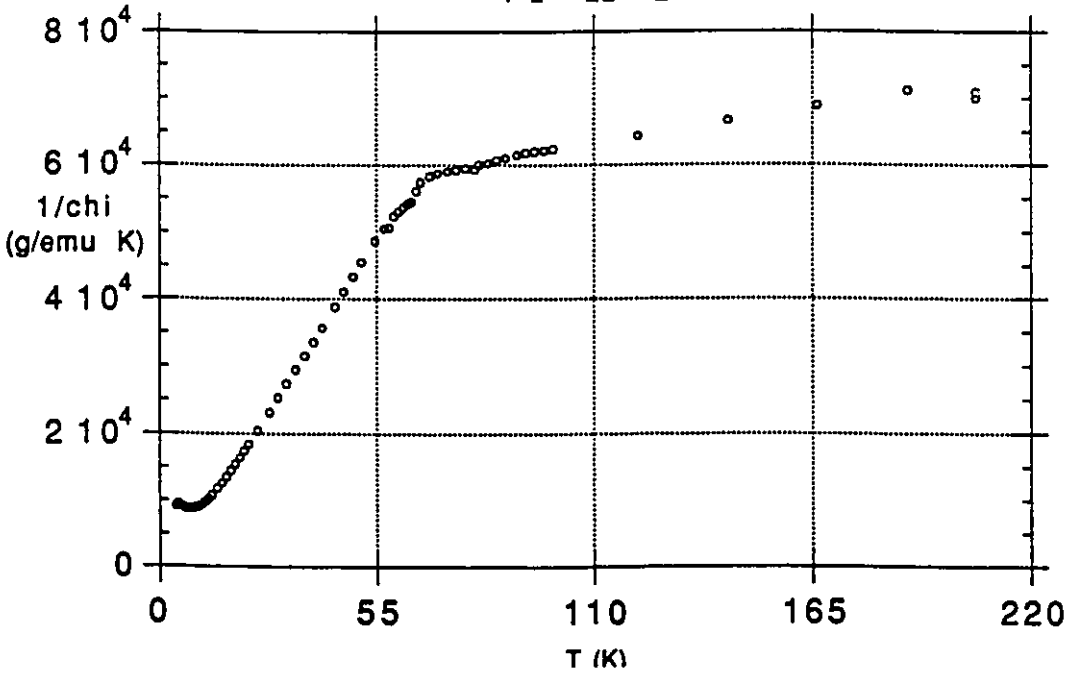

Fig. 4.3.2 Susceptibility and inverse susceptibility of $(AgGa)_{1-z}Mn_{2z}Te_2$, z=0.40. Note the prominent broad maximum at 8 K in the susceptibility, and the abrupt change of behaviour at 63 K visible in the inverse susceptibility.

of a plateu in the χ curve extending from 4-11 K. The occurance of such a low ordering temperature was, in the course of this investigation initially attributed to a two dimensional magnetic transition associated with the planar Mn, however for reasons relating to the strength of the full 3-dimensional interactions in the matrix (to be elucidated in section 4.5), this hypothesis was deemed to be untenable. The Ag-Ga system will be analyzed in detail in the following sections.

The Cu-In and Ag-In systems were studied with emphasis placed on the z=0.50 concentration. The apparent Curie constants (C) obtained from the slopes of the inverse susceptibility of these samples are given in table 4.3.1. In the case of the Cu-In system, the compositions z=0.25, 0.33 and 0.40 were prepared by the usual melt and anneal technique, the final processing being a slow cool in the annealing oven. The two lowest concentrations displayed cusp-less zfc susceptibility with a slight enhancement in the response and hysteresis around 70 K, which also coincided with the onset of C-W behaviour in their inverse susceptibility (χ^{-1}). Such susceptibility variation for these materials has not been previously reported, the expected response being clear cusps ranging from 5-20 K. The z=0.40 sample displayed a cusp at 35 K which corresponds to the previously reported series of cusps in the chalcopyrites, and associated with Mn-ordering.

Seven samples of the Cu-In system with z=0.50 were also prepared. These were annealed at 600 C for a minimum of 2 weeks, then heat treated in the following ways. Sample #1 was

TABLE 4.3.1a

Apparent Curie-Weiss constants from inverse susceptibility for $(AgIn)_{1-z}Mn_{2z}Te_2$

Composition $(AgIn)_{1-z}Mn_{2z}Te_2$	Expected C (emu K/g) x10^{-2}	Sample Name & max. T (K)		Apparent C (emu K/g)x10-
z=0.25	0.486	25SFC	130	0.99 ± 0.01
z=0.33	0.658	33SFC	200	0.70 ± 0.03
z=0.40	0.809	40SFC	200	0.95 ± 0.06
z=0.50	1.038	#2	200	1.25 ± 0.05
		#3	200	1.14 ± 0.05
		#4	270	1.09 ± 0.05
		50SC	250	1.20 ± 0.05
		50WQ	260	1.22 ± 0.05
		50VSC	240	1.19 ± 0.20
		#6	100	1.53 ± 0.05

Tables 4.3.1a and 4.3.1b (following page) show the apparent Curie constants (C) for two of the three Mn-chalcopyrite alloys studied. The Ag-Ga Mn-system data is presented in section 4.5 (table 4.5.1). The apparent C values are those obtained from the raw data with no diamagnetic correction, errors quoted are estimated self consistently from the measured errors in the slopes of the inverse susceptibility. The expected C values are those calculated according to equation (2.4.3). Also shown are the maximum temperatures achieved during the sample measurement.

TABLE 4.3.1b

Apparent Curie-Weiss constants from inverse susceptibility for $(CuIn)_{1-z}Mn_{2z}Te_2$

Composition $(CuIn)_{1-z}Mn_{2z}Te_2$	Expected C (emu K/g) x10^{-2}	Sample Name & max. T(K)		Apparent C (emu K/g)x10-
z=0.25	0.525	25SFC	180	0.59 ± 0.02
z=0.33	0.706	33FC	180	0.83 ± 0.05
z=0.40	0.862	40SFC	200	0.96 ± 0.04
z=0.50	1.100	#1	200	1.32 ± 0.05
		#2	200	1.26 ± 0.03
		#3	200	1.1 ± 0.2
		#4	200	1.18 ± .04
		#5	200	1.22 ± 0.02
		50QQ	200	1.22 ± 0.05
		50SSC	200	1.21 ± 0.02

further annealed at 300 C for 20 days then 200 C for 3 months, this sample will be referred to as LTA200 (low temperature annealed). Two samples were cooled from the 600 C anneal over a period of about 24 hours by shutting off their annealing ovens, these will be referred to as the furnace cooled samples. Sample #4 is labelled LTA150, and sample #5 is labelled LTA100, both in similarity to sample #1 above, although LTA100 was placed directly at 100 C after the initial 600 C anneal, a fact which is of some importance as will be seen in the following. Sample #6 was quenched by dropping it as quickly as possible from the 600 C annealing oven into cold brine, it is referred to as the Q600 sample, similarly sample #7 was quenched from 400 and is called the Q400 sample. The duplication in the sample treatments was carried out in order to check the reproducibility of the results.

As expected, evidence for stannite ordering in the x-ray photographs was not seen. Indeed there were no discernable differences among the x-ray photographs of the samples, all appeared to be single phase cubic structure as expected from the previously reported results on this material. Although the cubic and chalcopyrite forms of this material are practically indistinguishable by x-rays alone, the samples are expected from the phase diagram to be predominantly cubic.

From the susceptibility results it is possible to clearly segregate the samples into 3 categories; 1) those exhibiting a prominent cusp at $\sim$ 28 K (all the quenched and furnace cooled samples), 2) those without clear susceptibility cusps (the

Figs.4.3.3a, and b, Susceptibility and inverse susceptibility of $(CuIn)_{1-z}Mn_{2z}Te_2$, z=0.50 samples.

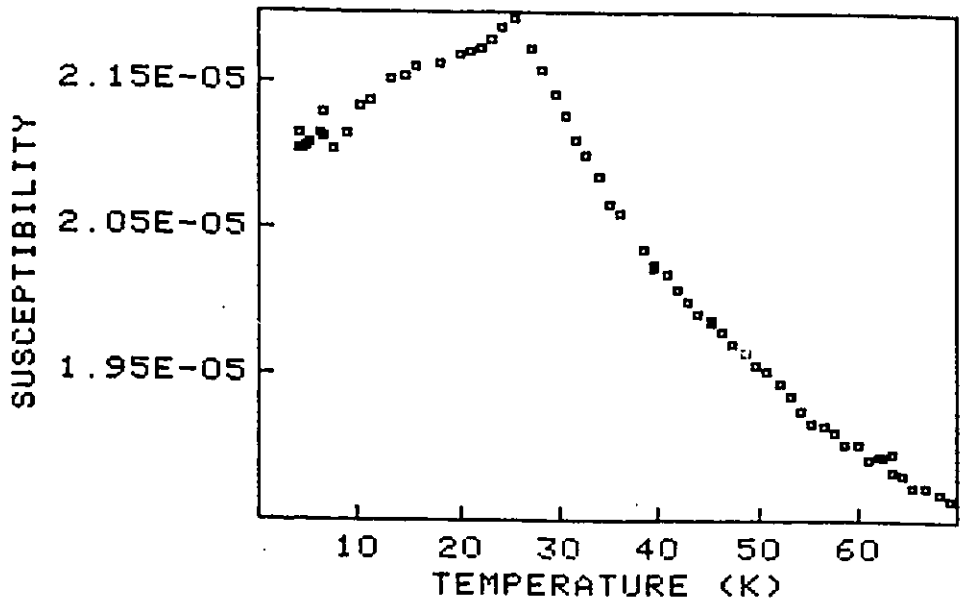

Fig.4.3.3a, The 28 K zfc susceptibility cusp of the Q400 sample.

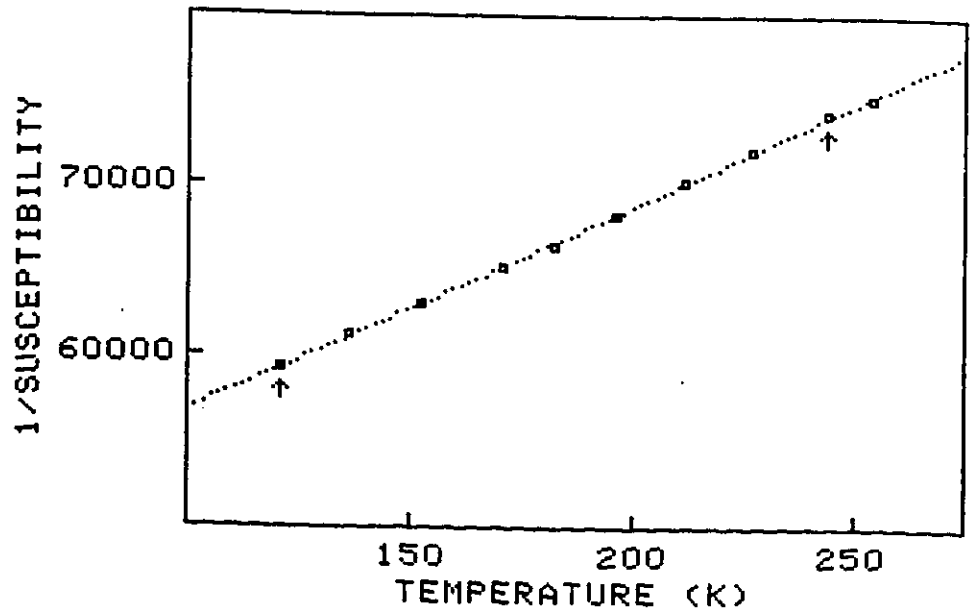

Fig.4.3.3b Inverse susceptibility of the Q400 sample illustrating Curie-Weiss behaviour above 100 K.

LTA200 and LTA150 samples) and 3) those with complex low temperature susceptibility (the LTA100 sample). These are all illustrated in figs 4.3.3a to f.

It is highly likely that the prominant cusps are due to the response of the large majority of spins because in the cases the cusps occur, the residual low temperature paramagnetic component is small (see chp.2). Also, the associated high temperature (80 to 220 K) paramagnetic behaviour, (as characterized by the Curie constant which is proportional to the number of spins present), closely approximates that expected for the number of Mn atoms in the samples. This rules out the possibility of the cusp being due to small amounts of 'magnetically active' (i.e. ferromagnetic) impurities since in this case one would still expect to see the low temperature ($\leq$ 10 K) paramagnetic signal corresponding to the high temperature paramagnetic behaviour which is consistent with full amount of Mn in the sample acting paramagnetically. The possibility of the cusps being due to large amounts of impurities or extraneous phases is ruled out by the absence of extra lines on the x-ray photograghs.

The theoretical value for the Curie constant is given by equation (2.4.3), and has the value

$$C = 4.375 \ \frac{\text{Kemu}}{\text{mole}}$$

for S=5/2 ions, which is equivalent to

$$C = 10.96 \times 10^{-3} \ \frac{\text{K emu}}{\text{gram material}}$$

for the Cu-In z=0.50 system. This value can be seen to be lower than the values measured from the susceptibility curves of table

4.3.1. This systematic deviation is possibly due to a 'multi-component' aspect of the susceptibility which is described in general terms in section 2.4, and will be considered in detail in section 4.5 in which a fitting of the susceptibility of the Ag-Ga system is undertaken.

The occurrance of a $\approx$ 29 K cusp in the Cu-In system for z=0.5 has been previously seen [100] and interpreted as characteristic of ordered zincblende material (β' phase). Susceptibility curves such as those of two of the LTA samples have not been previously reported. Also, other cusp temperatures previously reported for quenched samples of Cu-In z=0.5 were not observed in the present work, however this is not surprising in view of the fact that as stated in [100], it is difficult to quench samples fast enough to produce such peaks.

The β' nature of the Q600 sample is understood if as suggested in [100], the quenching is not rapid enough to retain the β-field characteristics to room temperature. It is made clear in that reference that it is very difficult to quench the materials rapidly enough to see the disordered peak, hence it is clear that the 29 K cusp is actually a feature of the β' phase.

The suppression of the 29 K cusp in the LTA150 and LTA200 samples is highly significant. The LTA200 sample is a particularly good example since not only is the cusp absent, but also any associated temperature hysteresis which is often a more sensitive indicator for the presence of a magnetic transition. One logical explanation for the cusp-free susceptibilities is that these represent an ordered structure which has small zfc

cusps. This follows from general priciples outlined in section 4.2 and by comparison to related DMS systems for example, the $Cd_xZn_yMn_{1-x-y}Te$ system in which susceptibility cusps (due to spin-glass transitions) occur at all values of concentration above the nearest neighbour Mn-percolation concentration on the zincblende cation sublattice [111]. This random Mn near-neighbour percolation limit corresponds to a concentration of approximately $2z=0.18$ in the chalcopyrite systems, and is very near the value at which the previously seen T_c's extrapolate to at low concentration in these chalcopyrite systems. The absence of the usual cusps at concentrations high above the random-cation near-neighbour percolation limit is strong evidence to support a new non-random configuration of Mn. This will be discussed further in section 4.5.

The LTA150 sample was annealed within the α' phase boundary, and is expected to represent conditions in the α' field. It is then significant that the LTA150 sample still shows a residual enhanced susceptibility and hysteresis at 29 K, indicating that even in this case full equilibrium is not achieved. This further supports the idea that the Q400 sample also did not achieve equilibrium in the β' field.

The LTA100 sample, which has a complicated magnetic response around 29 K was probably not fully in equilibrium. Unlike the other LTA samples, LTA100 was not annealed at progressively lower temperatures ending in the nominal low temperature, rather it was placed into the 100 C annealing oven directly after being furnace cooled from 600 C. Since the x-ray

Figs.4.3.3c, and d, Susceptibility and inverse susceptibility of $(CuIn)_{1-z}Mn_{2z}Te_2$, z=0.50 samples.

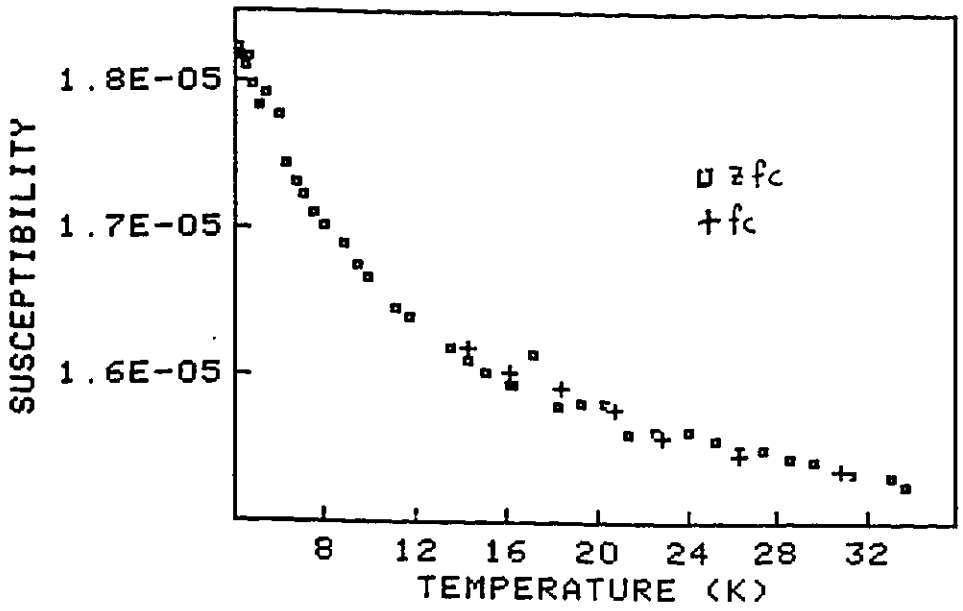

Fig.4.3.3c, The low temperature cusp-free susceptibility of the LTA150 sample. Note the lack of temperature-induced hysteresis at 28 K in the fc (field-cooled) data.

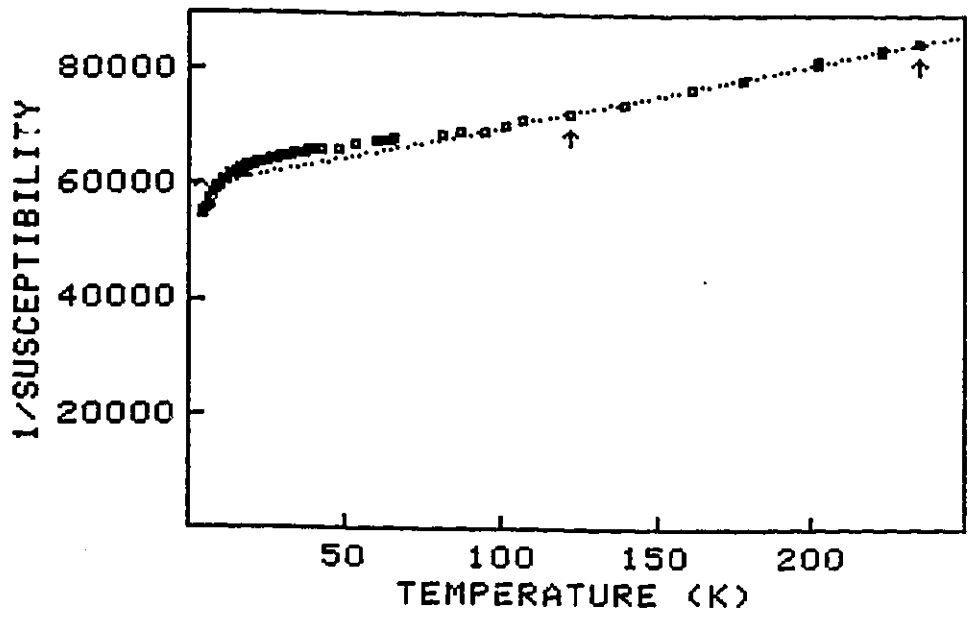

Fig.4.3.3d Inverse susceptibility of the LTA150 sample illustrating Curie-Weiss behaviour above 100 K.

Figs.4.3.3e, and f, Susceptibility and inverse susceptibility of $(CuIn)_{1-z}Mn_{2z}Te_2$, z=0.50 samples.

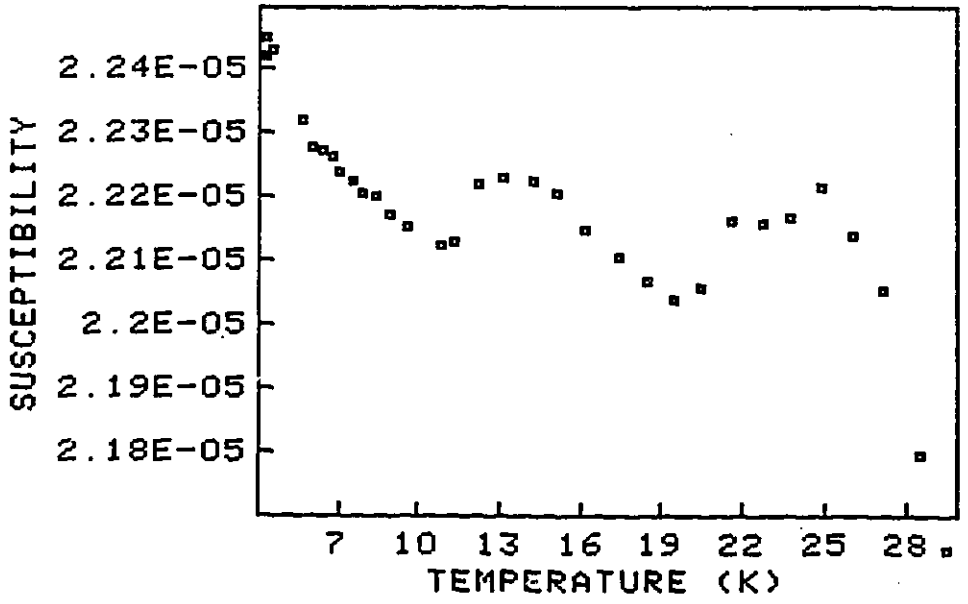

Fig.4.3.3e, The complex low temperature zfc susceptibility of the LTA100 sample.

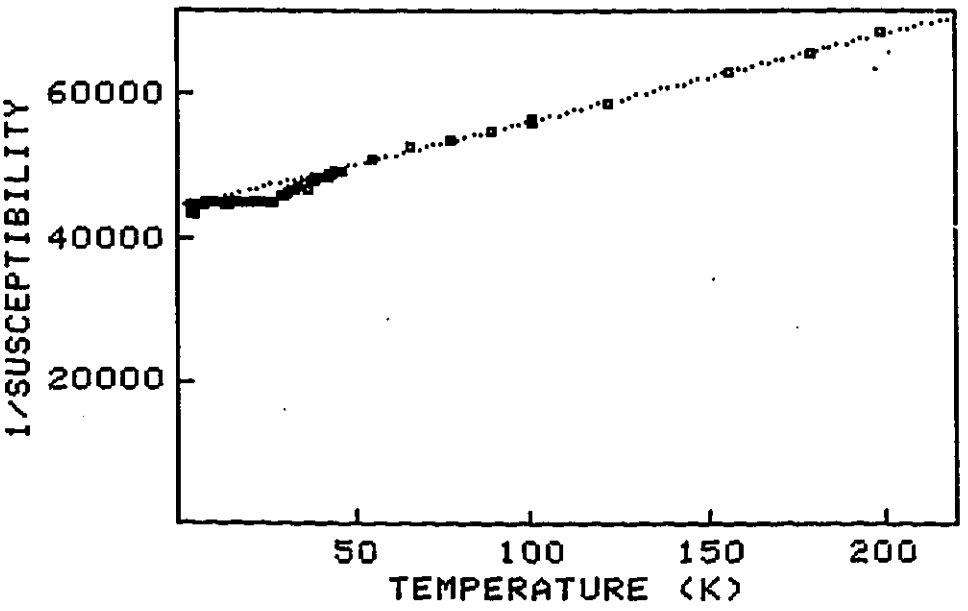

Fig.4.3.3f Inverse susceptibility of the LTA100 sample illustrating the robustness of the Curie-Weiss behaviour above 100 K.

diffraction from this sample is indistinguishable from the others and since the remaining magnetic parameters (C and θ) are equal to those of the other samples, it is probable that LTA100 was not fully in equilibrium as a result of the low annealing temperature and correspondingly long time required to achieve equilibrium.

The important characteristics of the cusp-less behaviour of the LTA200 susceptibility are the onset of C-W behaviour near 80 K and possible enhanced susceptibility near that temperature, as well as a significantly higher apparent θ value (-550) than that of the samples exhibiting cusps (-400).

To summarize the results on the Cu-In system, the observed susceptibilities are of the correct magnitude expected for the spins behaving in C-W fashion, however the detailed low temperature magnetic behaviour of the materials is quite sensitive to the heat treatment. Some of the previous results reported for the alloy have been reproduced (zfc cusp temperatures) and new behaviour has also been seen. In the z=0.50 composition, the prominant cusp at 25-29 K previously associated with ordered zincblende disappears in the low-temperature annealed condition. It seems likely that a new form of ordering may be associated with the absence of the low-temperature cusp, large θ and onset of C-W behaviour (and possible enhanced susceptibility) near 65 K.

In the case of the Ag-In system, a similar series of samples to the Cu-In case were investigated. For the z=0.25, and 0.33 slowly cooled samples, large zfc cusps at 21-23 K

consistent with those previously associated with ordered chalcopyrite were obtained [100] (see figs. 4.3.4a, b). The z=0.40 slowly cooled sample displayed χ cusps at 23 and 35 K which correspond to the previously reported ordered chalcopyrite and ordered cubic phases of the materials (figs. 4.3.4c, d). The C values of these samples were all within 10% of the theoretical values (see table 4.3.1) and the θ parameters were 250-300 K as previously reported in ref [100].

The majority of the Ag-In z=0.5 samples displayed a prominant cusp at 20-22 K previously attributed to disordered zincblende (figs.4.3.4e, f). This peak was found to be quite robust with respect to sample heat treatment. Four samples which were alternatively slowly cooled or quenched displayed this cusp and the associated θ value of 350 K. The LTA200 sample displayed complex low-T behaviour however two measurements on different pieces of the ingot gave practically identical results indicating the homogeneity of the material. Two separate measurements of the LTA150 sample were also taken and these too gave very similar results which consisted of a peak at 28 K with little or no associated hysteresis and an increasing χ toward low temperature. One sample displayed a broad maximum in the zfc χ near 5 K and had a θ=-620, however this sample also had a C value which was anomalously high (50% higher than expected).

To summarize the results of the Ag-In system, we see that once again the previously reported results on the materials can be reproduced and that the zfc behaviour is highly sensitive to

Figs.4.3.4a, and b, Susceptibility and inverse susceptibility of $(AgIn)_{1-z}Mn_{2z}Te_2$ samples.

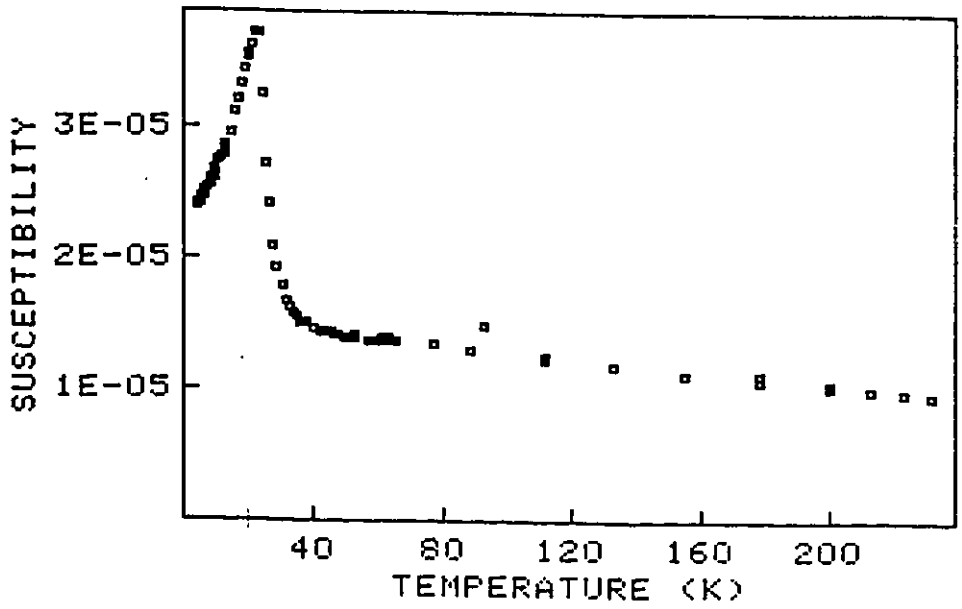

Fig.4.3.4a, The 22 K zfc susceptibility cusp of the z=0.33 slowly cooled sample. The z=0.25 sample displayed qualitatively identical behaviour.

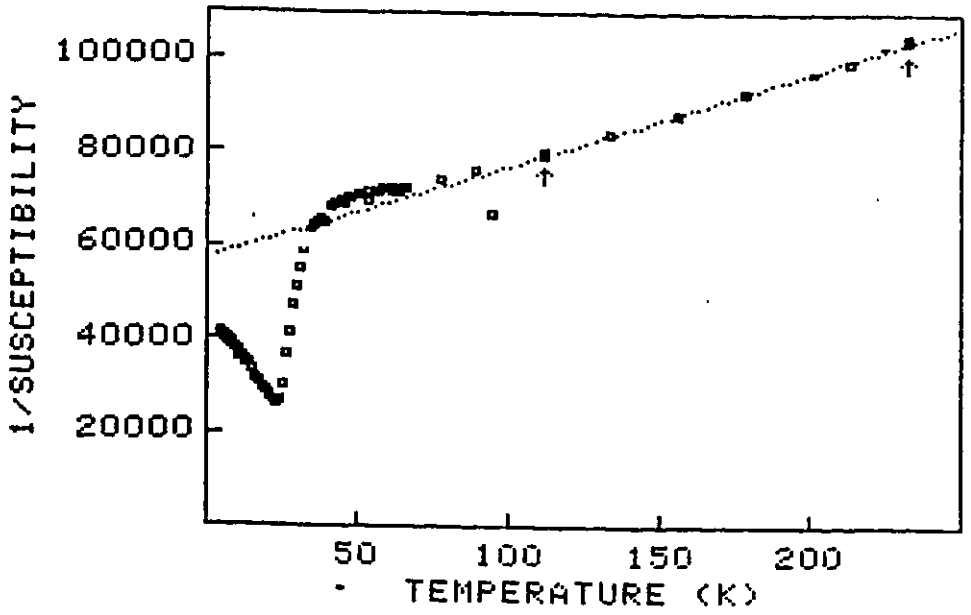

Fig.4.3.4b Inverse susceptibility of the Z=0.33 sample.

Figs.4.3.4c, and d, Susceptibility and inverse susceptibility of $(AgIn)_{1-z}Mn_{2z}Te_2$ samples.

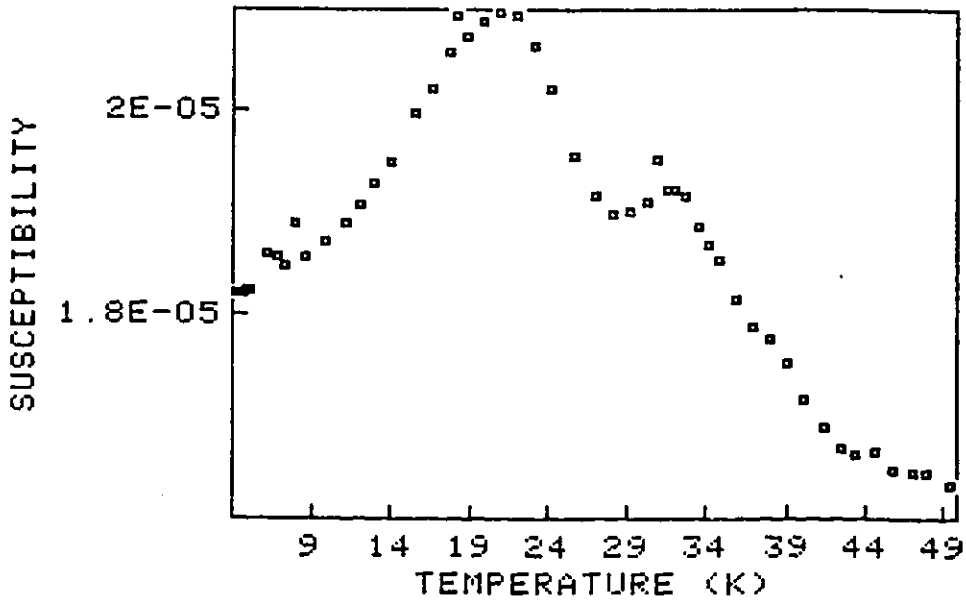

Fig.4.3.4c, The low temperature zfc susceptibility of the z=0.40 slowly cooled sample. The two peaks in the susceptibility occur at the previously reported values of 23 and 35 K.

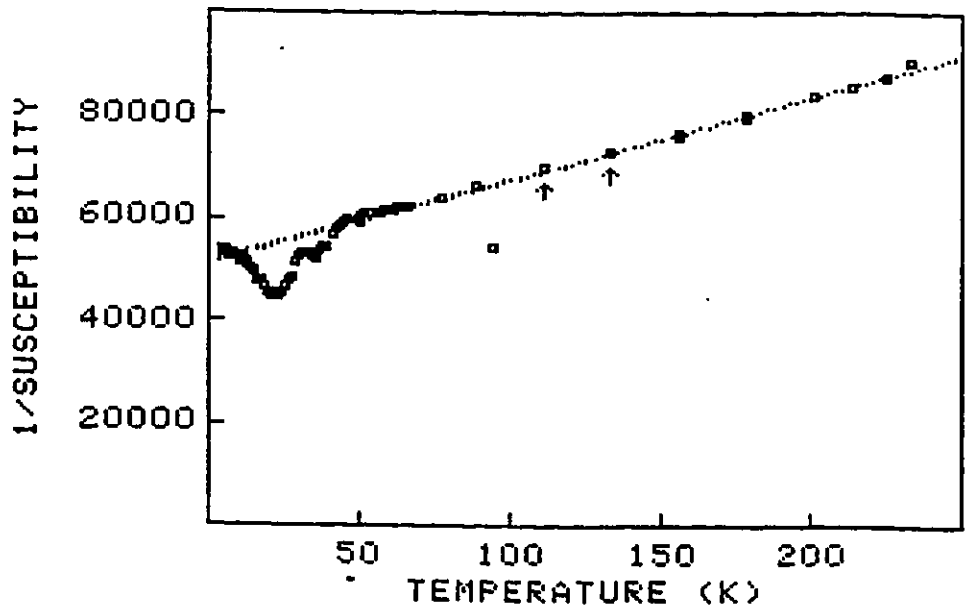

Fig.4.3.4d Inverse susceptibility of the Z=0.40 sample.

Figs.4.3.4e, and f, Susceptibility and inverse susceptibility of $(AgIn)_{1-z}Mn_{2z}Te_2$ samples.

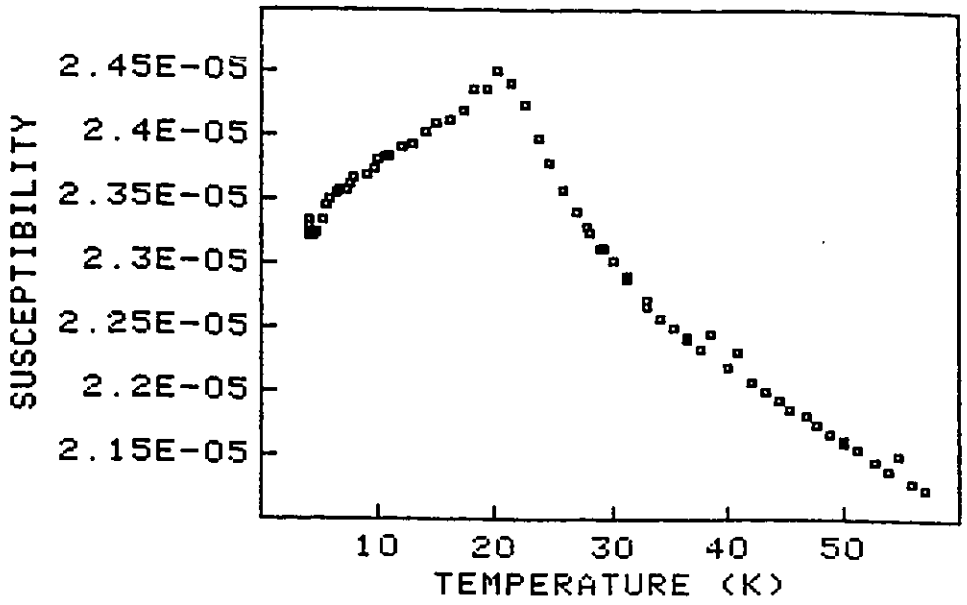

Fig.4.3.4e, The low temperature zfc susceptibility cusp of the z=0.50 samples.

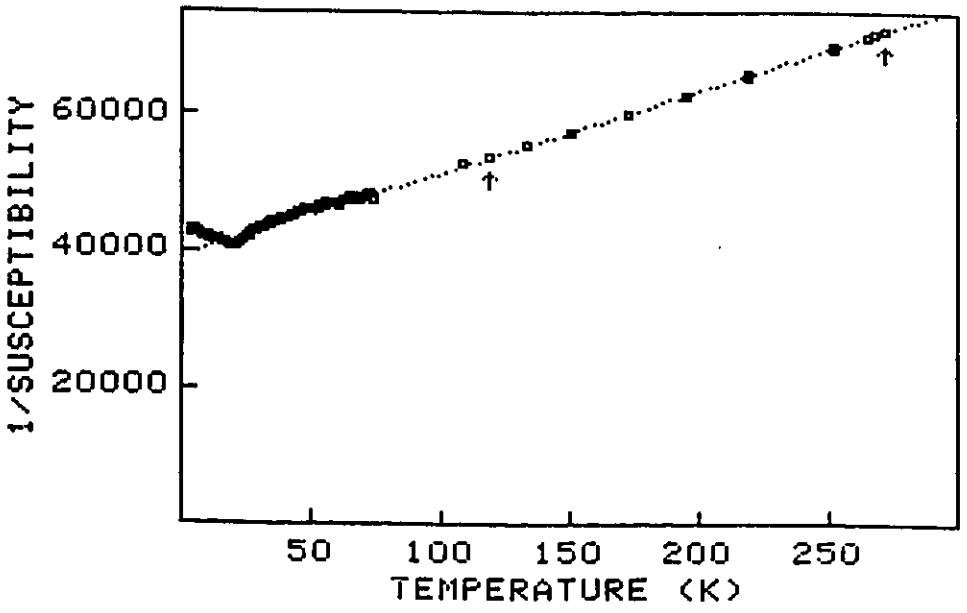

Fig.4.3.4f Inverse susceptibility of the Z=0.50 sample.

the details of the heat treatment. In general, certain aspects of all three solid-solutions were noticed. One significant feature of most of the susceptibility curves which will be of utmost importance in the following sections is the drastic change of behaviour near 65 K constituting the low-temperature boundary of the apparent C-W paramagnetism. This is especially visible on the χ^{-1} vs. T of the materials particularly those of the z=0.40 Ag-Ga stoichiometry as can be seen in fig. 4.3.2. The behaviour suggests that as the samples are heated, some freeing of spins causing a large contribution to the net paramagnetism of the sample occurs at that temperature. It is possible that this change of behaviour is the magnetic signature for the low-temperature highly ordered phase and indeed this observation is the primary motivation for the analysis in section 4.5. This interpretation would explain the near concentration independence of this feature since in principle an ordered Mn fraction could be characterized by its own magnetic signature which is largely independant of the host lattice. Some care must be taken in this interpretation since the same can be said of the magnetic signature of an impurity, and for this reason some consideration of the possible impurities will be summarized here.

The important parameters of MnTe and $MnTe_2$ are summarized in table 4.3.2. The most important parameter is the magnetic ordering temperature which can be seen to be significantly different from 65 K in both cases. In the case of MnTe, the T_n is well above the measured range of temperatures however the

Table 4.3.2 Important Parameters of MnTe and $MnTe_2$

Material	Group	Structure	Intense Diffraction Lines		
MnTe	$P6_3/mmc$	NiAs	3.17_x	2.46_x	2.08_s
$MnTe_2$	Pa3	FeS_2	3.11_x	2.84_x	1.86_s

Material	Lat. paramter a(A)	c(A)	T_n	ESR (ΔH_{pp})
MnTe	4.158	6.726	300 K	450 G
$MnTe_2$	6.950	----	86.6 K	560 G

Table 4.3.2 summarizes some of the parameters of the two most important potential impurities in the Mn-containing systems. The d values given in the first of the above tables represents the lattice plane spacings of the three most intense diffraction lines. Other aspects of the compounds are as follows: MnTe is known to have a crystallographic phase change at 200 K, and is an example of a 3-D Ising antiferromagnet. $MnTe_2$ has a Curie-Weiss temperature θ=-530 K and has a value for the nearest neighbour exchange of $-J_1/k$=6.7.

presence of significant amounts of this compound can still be ruled out due to the fact that the Curie constants of the alloys correspond to the expected number of spins in the sample acting paramagnetically below the MnTe transition.

In order to study the $MnTe_2$ case in detail, a sample of $MnTe_2$ was fabricated. Element weights corresponding to the correct stoichiometry were sealed as usual in a quartz ampule which was then quenched from the melt (1300 C) and then annealed at 400 K. This procedure was undertaken in order to inhibit tellurium segregation below the liguidus. The susceptibility of two separate parts of the resulting $MnTe_2$ ingot were measured. The zfc χ curves were found to be slightly different in detail however each had a cusp or step at about 90 K consistently with the T_n quoted above. This signature is not similar to that seen in the alloys, and as will be shown in the following pages, the ESR signature of $MnTe_2$ is also absent in the ESR of the alloys. This indicates that the observed 63 K χ cusp is not due to $MnTe_2$ and that $MnTe_2$ is not a significant impurity in the alloys.

Heusler alloys were also considered as a possible impurity within the chalcopyrite samples. A relevant example of these ferromagnetic alloys is Cu_2MnIn, the amorphous form of which has been reported to exhibit a spin-glass cusp T_g near 60 K [114]. The possibility that such alloys are significant impurities in the chalcopyrites is unlikely due to the fact that their expected magnetic signatures have not been seen in all the previous history of the fabrication of the chalcopyrite DMS. Also the 60 K spin glass behaviour is associated only with the

amorphous forms of these alloys which are difficult to produce, in ref [114] they were produced by rf sputtering. In the crystalline form, the Heusler alloys are ferromagnetic with transition temperatures of the order of 600 K. It thus seems highly unlikely that the 63 K feature observed in the chalcopyrites be due to amorphous Heusler alloy impurities.

Finally it also unlikely that the 63 K feature is caused by a structural phase transition of a magnetic impurity since this requires the coincidence of such a transition with the C-W behaviour of the chalcopyrites. Such transitions have never been reported in the previous work with the chalcopyrites making their presence here highly unlikely.

The above considerations indicate that the most plausible explanation for the concentration independant features of the susceptibility of the chalcopyrite alloys is that they be associated with ordering. These features, including an enhancement of the susceptibility at or very near the onset of Curie-Weiss behaviour in the χ^{-1} and the large θ, are especially visible in the Ag-Ga case (see fig 4.3.2). This will be discussed further in the section 4.5.

We have seen that correlating the susceptibility data with the phase diagram can be difficult due to the uncertainty in the annealing times required to achieve equilibrium, and the lack of supporting evidence from x-ray characterisation due to the indistinguishability of the cubic and chalcopyrite phases. As an example, note that the furnace cooled samples often do not represent what seems to be the equilibrium condition at low

temperature. This illustrates that the furnace cooling procedure is too fast to allow equilibrium to be achieved, however this still leaves open the question of how slow a cooling rate is required.

4.3.3) ESR Signatures

ESR was carried out on most of the above mentioned samples. In the case of the Cu-In system, the type of non-simple ESR lineshape observed is the same as that discussed previously (section 4.2), namely two superimposed broad lines with the same effective g value (see fig. 4.3.5). There is a prominant 2700 Oe room temperature line in all but the LTA200 samples, which line fits reasonably well to lorentzian profile over the measured field range. The high symmetry of this wide line is consistent with the fact that the samples are cubic and hence do not have g value anisotropy. The LTA200 sample which displays cusp-less susceptibility, is distinguished by a significantly broader ESR line of approximate width 3600 Oe. This is also illustrated on fig. 4.3.5. The weak narrow line also occurs at g=2, and never accounts for more than a few percent of the total ESR intensity.

The width of the narrow line (4.20×10^{-2}T) does not coincide with that of $MnTe_2$ ($\simeq 6.0 \times 10^{-2}$ T) and this substantiates the previous conclusions on the negligible amount (if any) of $MnTe_2$ in the samples. 4.20×10^{-2}T is close to the linewidth observed for MnTe (4.50×10^{-2}T), however the narrow line seems to persist below the MnTe antiferromagnetic ordering temperature

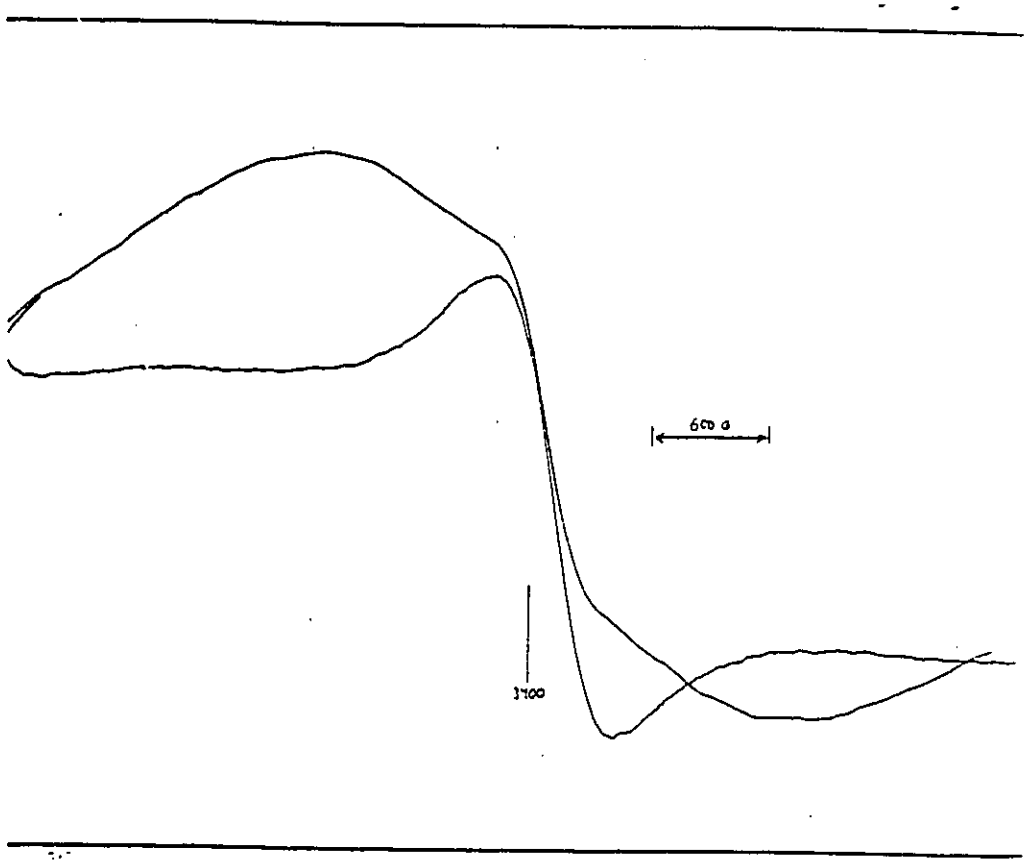

Fig. 4.3.5 ESR spectra of $(CuIn)_{1-z}Mn_{2z}Te_2$ z=0.50 samples. Illustrated are the room temperature ESR of the Q400 and the LTA200 samples. The composite aspect of both lines can be seen. The wide (>2000 G) lines vary significantly with respect to sample, while the narrow lines do not. The narrow (420 G) line probably accounts for less than a few percent of the total ESR intensity even in the LTA200 case.

(307 K). ESR can be performed on magnetically ordered systems [115], however for a given magnetic field range, high microwave frequencies are required in order to excite the collective (spin-wave) modes. The x-band ESR of antiferromagnetic materials is considerably weaker than the x-band ESR of the same materials in their paramagnetic state. Indeed in attempting to replicate the double line feature by mixing (antiferromagnetic) powdered Mn ($\Delta H \simeq 2.40 \times 10^{-2} T$) with one of the chalcopyrite ESR samples, it was found that nearly 50% by weight of Mn powder was required in order to even poorly mimic the double line feature. Also, this quantity of Mn considerably altered the tuning characteristics of the cavity.

It is likely that the narrow line is due to small amounts of impurities, and that both the ordered and disordered fractions contribute to the broad line. Indeed it is primarily due to the extreme width of the broad line that the narrow line is distinguishable at all. Also, similar narrow line features have been observed in zincblende materials not suspected to support Mn-order [111]. Such structures have been attributed to exchange narrowed absorptions due to Mn-clusters.

A series of ESR traces as a function of temperature were obtained for the furnace cooled Cu-In sample (figs. 4.3.6a, and 4.3.6b). This sample displayed a prominent 29 K susceptibility cusp. It was found that both the broad and narrow lines decreased their widths with an increase in temperature (fig.4.3.6a). This could be due to the the increase in the dynamical, temperature induced 'motional' narrowing effect

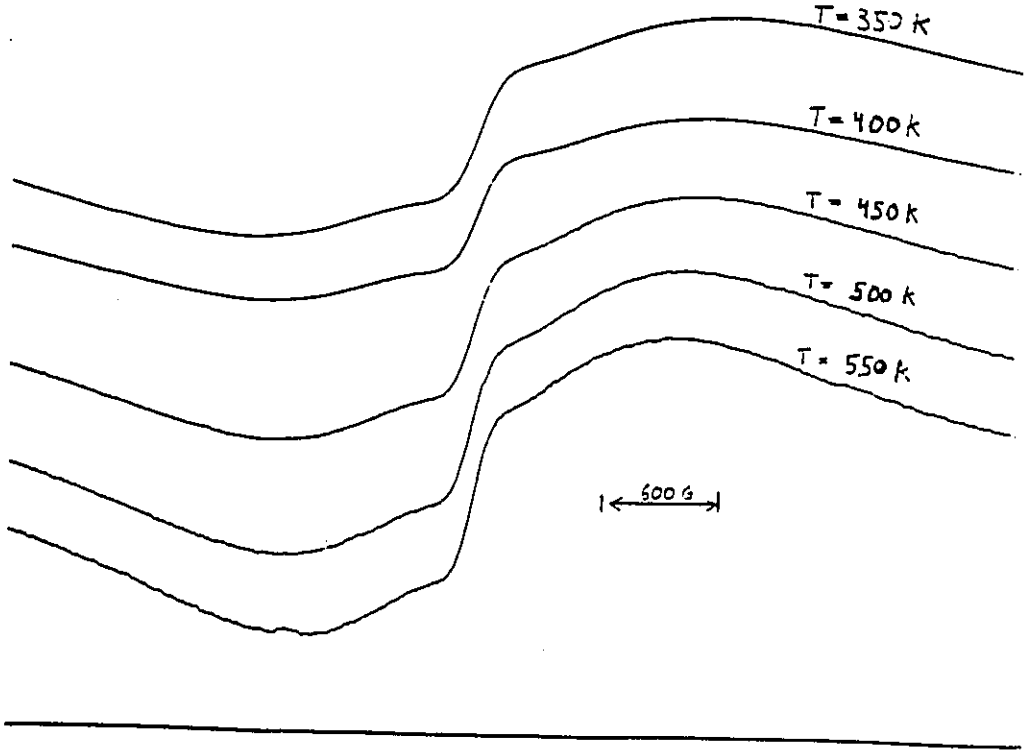

Fig. 4.3.6a High temperature ESR spectra of $(CuIn)_{1-z}Mn_{2z}Te_2$ z=0.50 furnace cooled sample.

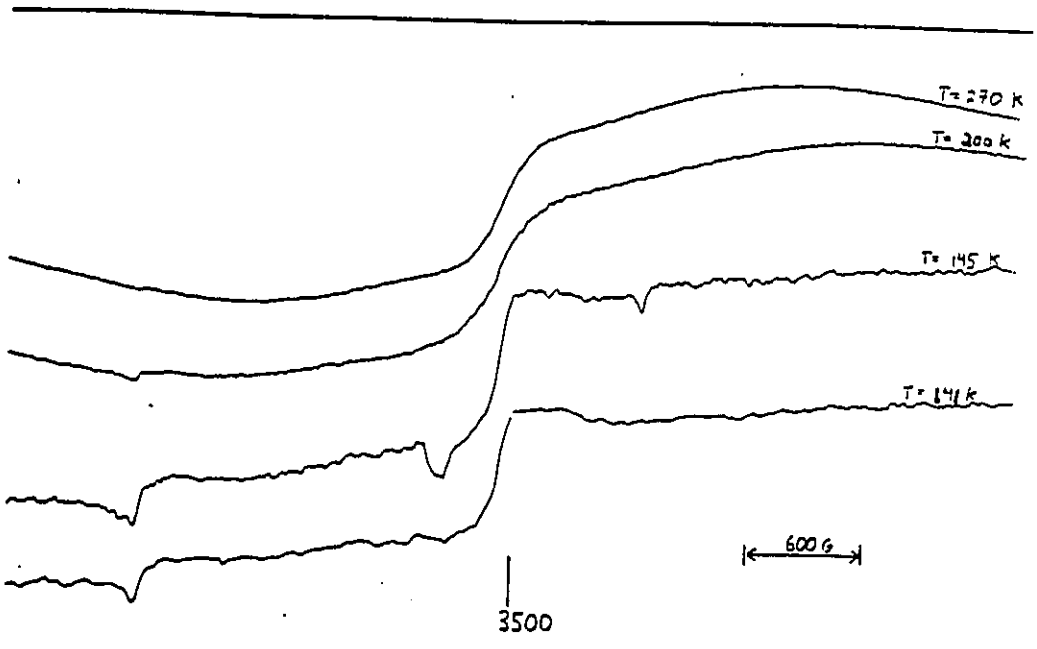

Fig. 4.3.6b Low temperature ESR spectra of $(CuIn)_{1-z}Mn_{2z}Te_2$ z=0.50 furnace cooled sample. These figures illustrate the spin-glass like linewidth increase of the broad line as a function of temperature decrease.

and/or represent the high temperature tail of the spin-glass linewidth behaviour.

At low temperature (fig 4.3.6b), it was found that the broad line's width increased with decreasing temperature effectively reaching infinite width at ≈145 K, wherease the narrow line did not change. This wide difference in behaviour indicates that the two systems responsible for the lines are not strongly coupled magnetically.

The increasing width of the broad line is consistent with the onset of a spin-glass transition at the cusp temperature. This can be seen from comparison to other known spin glass DMS alloys [110]. The fact that the narrow line does not appreciably change indicates the absence of critical broadening and thus that the impurity responsible for it remains paramagnetic over the measured temperature range.

In view of the above discussion, it is proposed that the narrow ESR line is due to a small amount of paramagnetic impurity, possibly associated with the Cu metal used in the sample fabrication. This could explain a similar double line feature which was observed in some of the Cu-sulfides which are the subject of the preceding section.

In general, non-critical line broadening in the alloy is expected to be of the inhomogenous type [53]. The broadening is attributed to the wide range of sites which result from random alloying, and so is expected to be most prominent in disordered structures. Indeed, the presence of a significant contribution to the high temperature line broadening specifically from the

inter-Mn interactions (as opposed to interactions between Mn and other cations for example) would seem to imply the existence of a magnetic phase transition in the material at some appropriately low temperature. In the present system however, it seems that the ordered structure yields room temperature ESR lines at least as wide and possibly wider than the disordered one, and that these wide lines do not imply the usual low temperature magnetic susceptibility cusps. A full discussion of this will be presented in section 4.6 however it is useful to note that the above observations lead one to postulate that the broadening due to the assumed ordered structure (as seen in the LTA200 sample) is not exclusively due to inhomogenous effects, but could be due to dynamical broadening (homogenous) associated with the onset of a higher temperature magnetic transition.

The Ag-In z=0.50 samples displayed room temperature lines of width 1700 Oe. These lines were also highly symmetrical and centered at g=2. The temperature dependance of the furnace cooled sample linewidth follows the expected behaviour for spin-glass and is seen on figs.4.3.7a, and b. A residual paramagnetic signal can also be seen in the AgIn lines, however in this case the effect is even less pronounced than in the CuIn materials.

The Ag-Ga slowly cooled samples displayed qualitatively different behaviour compared to the above cases. All concentrations studied (z=0.25, 0.33, 0.40) showed asymmetric room temperature lines with widths of approximately 360 Oe, the z=0.25 sample having a slightly wider line (see fig.4.3.8a).

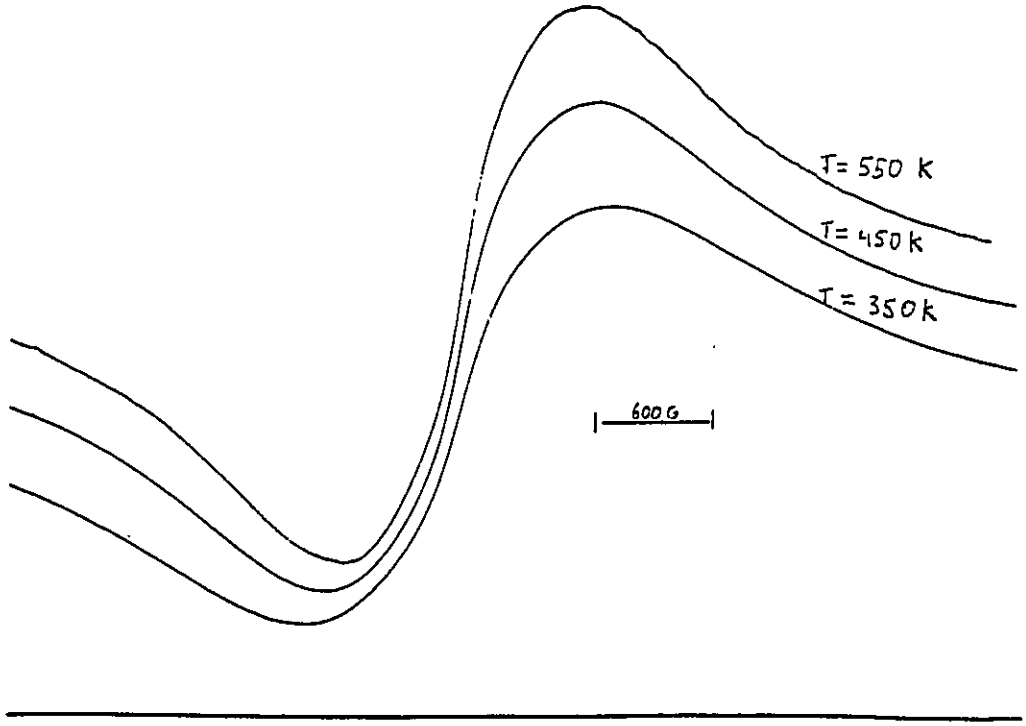

Fig. 4.3.7a High temperature ESR spectra of $(AgIn)_{1-z}Mn_{2z}Te_2$ z=0.50 furnace cooled sample.

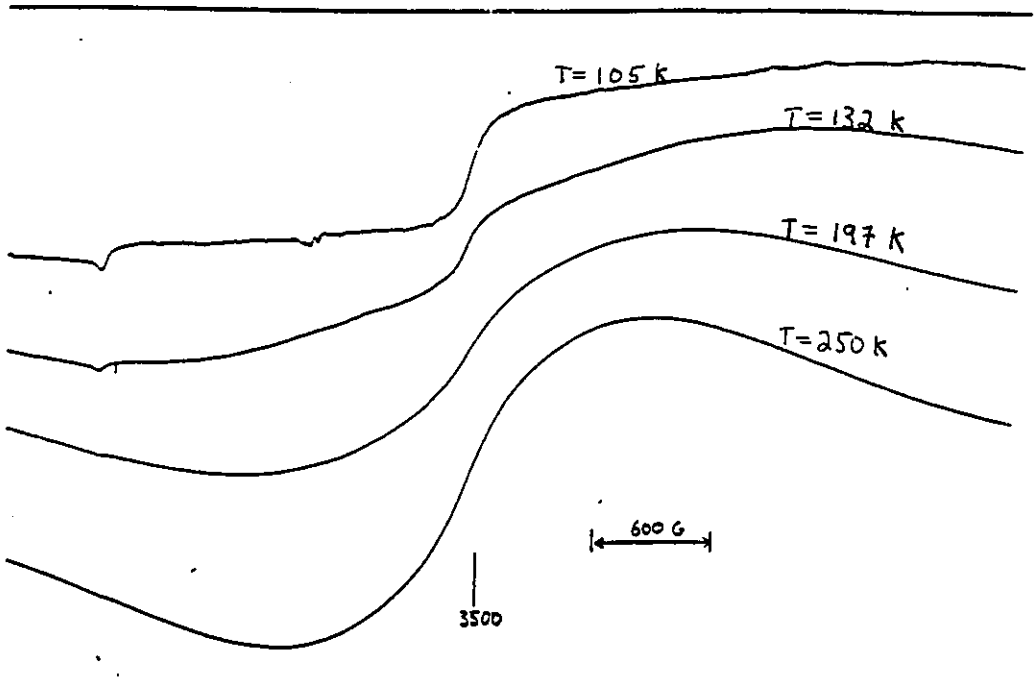

Fig. 4.3.7b Low temperature ESR spectra of $(AgIn)_{1-z}Mn_{2z}Te_2$ z=0.50 furnace cooled sample. These figures illustrate the spin-glass like linewidth increase of the broad line as a function of temperature decrease. The narrow line is less significant than in the Cu-In case (figs. 4.3.6).

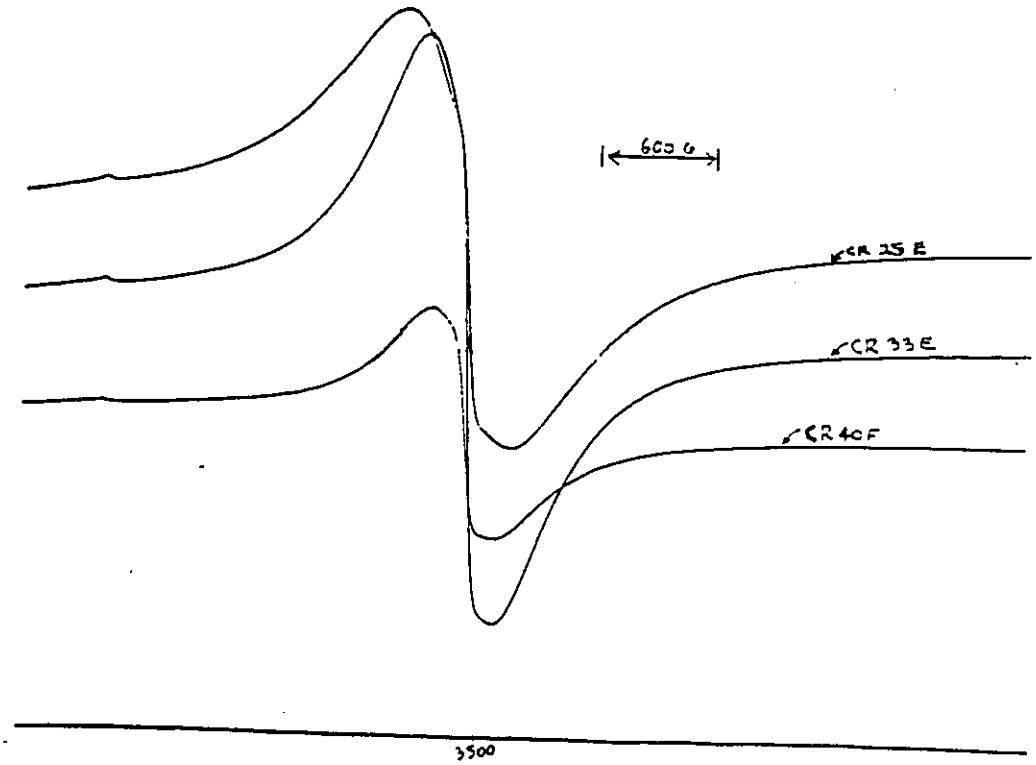

Fig. 4.3.8a Room temperature ESR spectra of $(AgGa)_{1-z}Mn_{2z}Te_2$ z=0.25 (CR25E), z=0.33 (CR33E), z=0.40 (CR40F) LTA samples.

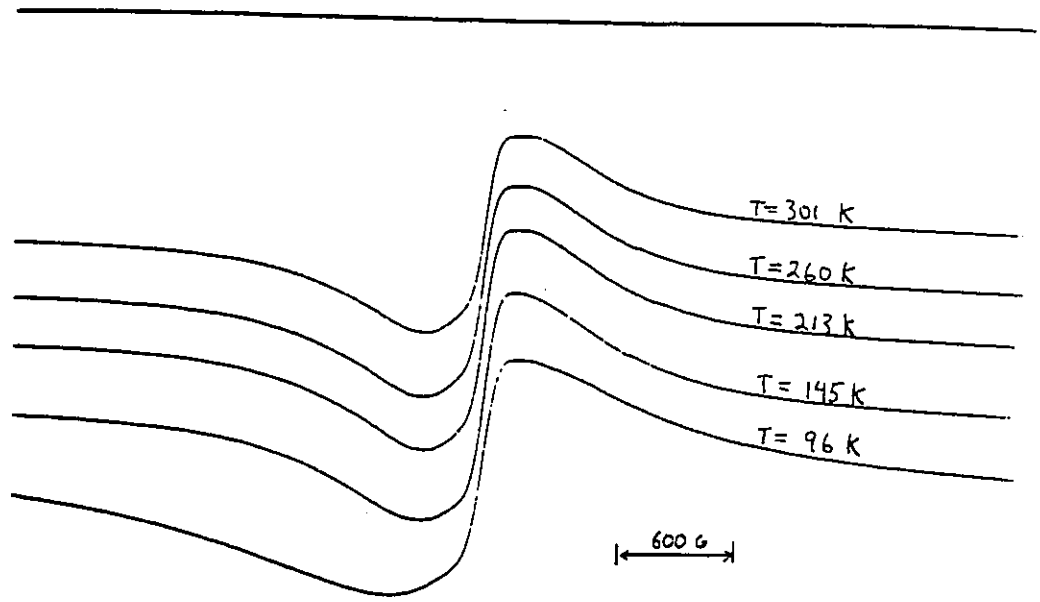

Fig. 4.3.8b Low temperature ESR spectra of $(AgGa)_{1-z}Mn_{2z}Te_2$ z=0.40 (CR40F) LTA sample. These figures illustrate the lack of significant concentration, or temperature dependence of the ESR in the Ag-Ga system. Note also the line asymmetry.

All but the z=0.25 lines showed a relatively small amount asymmetric broadening with the approach toward 60 K from above. This is exemplified by the spectra obtained for the z=0.40 sample illustrated in fig.4.3.8b. The g-value did not seem to change measurably over this temperature range, however g is difficult to estimate for asymmetric lines.

The Ag-Ga samples did not seem to follow spin glass behaviour as observable by the ESR. The line asymmetry observed suggests a non-cubic structure. The ESR also indicates that some paramagnetism is retained to low temperatures (50 K), however there is a change in behaviour of the line profile at higher temperatures.

4.3.4) Optical Energy Gap

The optical energy gap of the Ag-Ga alloys was measured in order to ascertain whether or not a double absorption edge feature as indicated in [105] for the related systems could be found. The absorption was analyzed as described in section 2.3.1 and fig. 2.3.2 illustrates a typical result. As exemplified in this figure, only one absorption edge which rendered an E_g very similar to that prevously reported for the slowly cooled material [108] was seen as summarized in the following.

$(AgGa)_{1-z}Mn_{2z}Te_2$	E_g(eV)
z=0.25	1.275±.005
z=0.33	1.284±.005

$(AgGa)_{1-z}Mn_{2z}Te_2$	E_g(eV)
z=0.40	1.252±.005

The absorption edge from which these values were obtained can be seen to extend up to the region of photon energies which coincides with the ^6S - ^4T ionic Mn transition and this prevents the observation of any further detail such as a second absorption edge.

An interesting feature of the optical absorption of these materials is the large 'tailing' of the absorption exemplified in fig. 2.3.2, and the high 'background' absorption which was subtracted from the data in the analysis. This has been observed in other multinary polycrystalline DMS samples [35] [105].

4.3.5) Summary

In the course of the preliminary observations on the Cu-In, Ag-In, and Ag-Ga solid-solutions, many of the previously reported results on the powder x-ray photographs, magnetic susceptibility, ESR and optical energy gap of these materials were reproduced. The magnetic measurements provide the clearest signatures for Mn-ordering, while the x-ray photograph, ESR and optical absorption data are relatively insensitive to the possible ordering. The ESR and magnetic susceptibility behaviour of the Ag-Ga system deviates the most from the previously reported behaviour in the chalcopyrite alloys associated with random-Mn distributions, and hence suggests that this system may be the best suited for further study.

New behaviour has been seen in the low-temperature annealed forms of all the materials which suggests possible modifications to the previous interpetations of the ordering conditions. The data obtained so far does not provide clear evidence for, or against the planar ordering hypothesis and so one system (the Ag-Ga alloy system) was chosen to be analyzed in greater detail, as described in the following sections.

4.4) Neutron Diffraction

In section 2.1, the important aspects of neutron diffraction (abbreviated as nd) which are needed for the understanding of the analysis to be presented in this section were given. As mentioned in section 2.1, the Cu-In and Ag-In alloys are less well suited to the nd technique by virtue of the relatively high neutron absorption coefficient of Indium. This is an unfortunate circumstance because these are the two alloys that exist as single-phases in the z=0.50 concentration, which is the only composition that can give exact stannite ordering. Luckily, the low-temperature annealed Ag-Ga alloys used in the present work have the advantage of providing some of the clearest 'non-standard' magnetic susceptibility signatures (section 4.3), particularly the presence of a χ cusp at 63 K in all the concentrations studied, and the broad χ maximum at 8 K in the z=0.40 samples. These features of the susceptibility can then be correlated with the nd data (see section 4.5) and in a sense, make up for the limitations imposed by the Ag-Ga solubility limit.

The single most important feature of the nd for the alloys under investigation is the negative scattering factor associated with Mn. The neutron (f_n), and x-ray (f_x), scattering factors for the elements in the alloys which were studied are as follows:

element	f_n	f_x
Ag	0.59	47.0
Ga	0.73	31.0
Mn	-0.37	25.0

element	f_n	f_x
Te	0.54	54.0

These scattering factors lead to the qualitatively dissimilar behaviour of the structure factors as a function of concentration which can be seen on fig.4.4.1.

Some work has previously been carried out on the nd of the ch alloys. D. Bissonette [116] calculated the expected nd line intensities for fully Mn disordered, Mn disordered on one cation sublattice, and for stannite ordered $(AgGa)_{1-z}Mn_{2z}Te_2$. The nd pattern of one z=0.40 sample was analyzed in terms of these scenarios, with the conclusion that none were found to apply. The stannite ordering used in ref [104] is that of random Mn substitution on the fixed stannite plane positions as discussed in section 4.3. The sample used in those investigations was however not heat treated in a way that optimized ordering and the other possible ordering schemes described in 4.2 were not considered. In particular the ordering scheme in which full Mn-planes which are randomly spaced in the z direction was not investigated. The full-Mn plane scenario will be studied extensively in this chapter.

Samples of the Ag-Ga alloys with z=0.25, z=0.33, and z=0.40 compositions were prepared. These concentrations were chosen in order to cover the single-phase, high concentration region of the phase diagram which is the most interesting from the point of view of the ordering. Relatively large samples are required for nd, and 12 grams of each alloy composition were prepared in the form of six 2g ingots. The ingots received very similar heat treatments ending with a relatively

Fig.4.4.1 X-ray and neutron structure factors for $(AgGa)_{1-z}Mn_{2x}Te_2$ as a function of concentration.

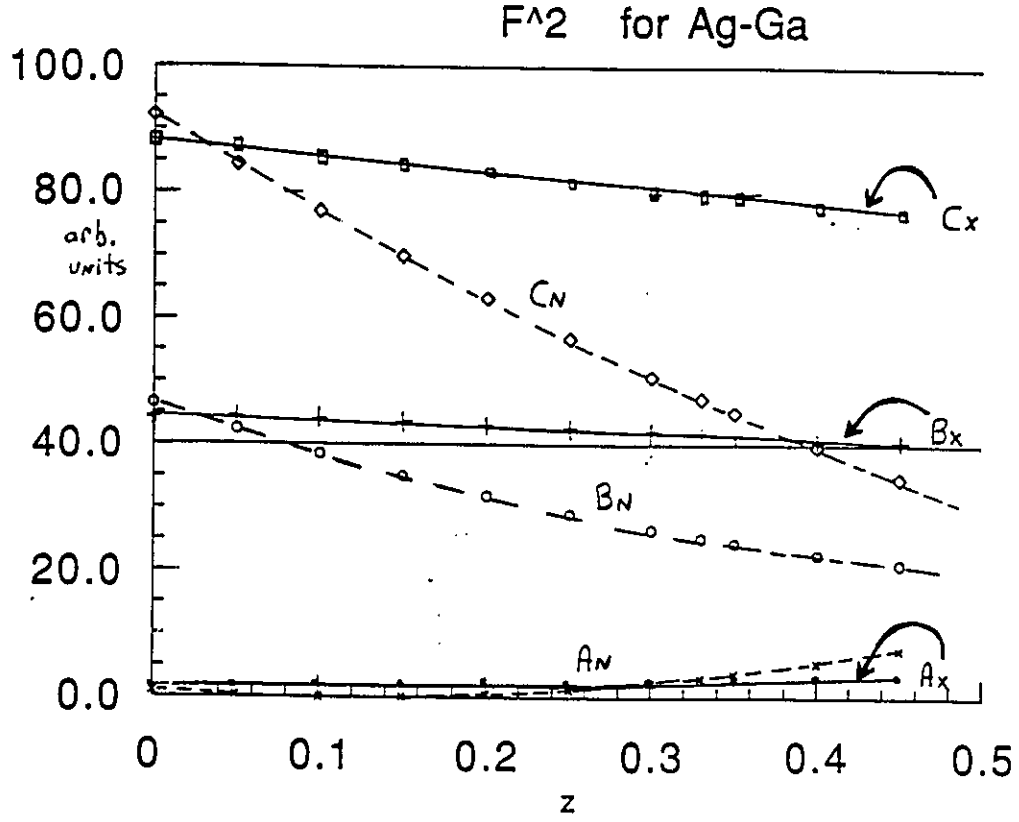

Fig.4.4.1 Structure factor variation as a function of Mn concentration for x-ray, and neutron diffraction.
Dashed lines represent z variation of the neutron structure factors, unbroken lines represent the x-ray structure factors. The labels A, B, C represent the line types as classified in the text, the subscripts indicate the lines appropriate to neutron (n), and x-ray (x) scattering. The structure factors are shown together on an arbitrary scale in order to facilitate comparison.

low-temperature anneal (≤350 C) and slow cool to room temperature. This heat treatment was chosen, in the absence of detailed phase diagram data in order to reproduce the conditions believed to result in Mn-ordering. The heat treatment was appropriate to the production of the low temperature ordered phases associated with the non-standard χ signatures described above, and not the 'Mn ordering' proposed in [100] and associated with the relatively high temperature, linearly z dependent T_c's discussed in that reference. It was hoped to obtain nd data on the linear-z T_c material by suitably re-annealing and quenching the already measured samples, but it was not possible for these measurements to be made at Chalk River in time for the present work.

Material from the majority of the ingots was characterized by x-ray (film) and magnetic susceptibility measurements. The magnetic response of the samples was of the form described in the previous section, which does not display the low-temperature (20-40 K) cusp. The close similarity of the susceptibility curves of different ingots also indicated the reproducibility of the LTA state of all the materials of equivalent composition. The x-ray photographs yielded apparently single phase patterns with lattice parameters consistent with those previously reported for the Ag-Ga alloys [108]. However line intensity anomalies were seen on the x-ray photographs which indicated the possible presence of cubic (β) phase. The materials were then finely powdered in preparation for nd, and sent to Chalk River, where Drs. T. Holden and D. Noakes carried out the data collection. Some

examples of the resulting diffraction patterns are illustrated in figs. 4.4.2 to 4.4.4. The x-ray diffractometer patterns shown in the figures were collected from pieces of the same ingots used in the nd. Dr. A. Lalonde of Ottawa U. (Geology) and Ronald Conlin of the Carleton Geology department assisted in the data collection.

4.4.1) Experimental Results

Some of the significant features of the diffractometer patterns for samples annealed in the low temperature ordered condition can be seen directly from figs 4.4.2 to 4.4.4:

1) Presence of cubic phase.

Additional contributions to the low angle sides of the x-ray and nd 112 reflections can be seen and these are attributed to the presence of compositionally identical cubic β phase. Although the c/a ratio of the tetragonal component is not equal to 2, the cubic (β) phase is practically unresolvable in the patterns due to the coincidences of the diffraction lines. The β phase adds intensity to only one member of lines in some c/a split pairs. This is illustrated in fig 4.4.4a where the arrows indicate the coincidences between the α and β reflections. The only β line which is clearly resolved occurs for the 111 in the x-ray patterns. The lattice parameters of the materials were calculated as described previously and are shown in the table below. Due to the fact that the β lattice parameter must be estimated from the single β-111 line, the lattice parameter of the β phase is not known to as high an accuracy as that of the α phase. A

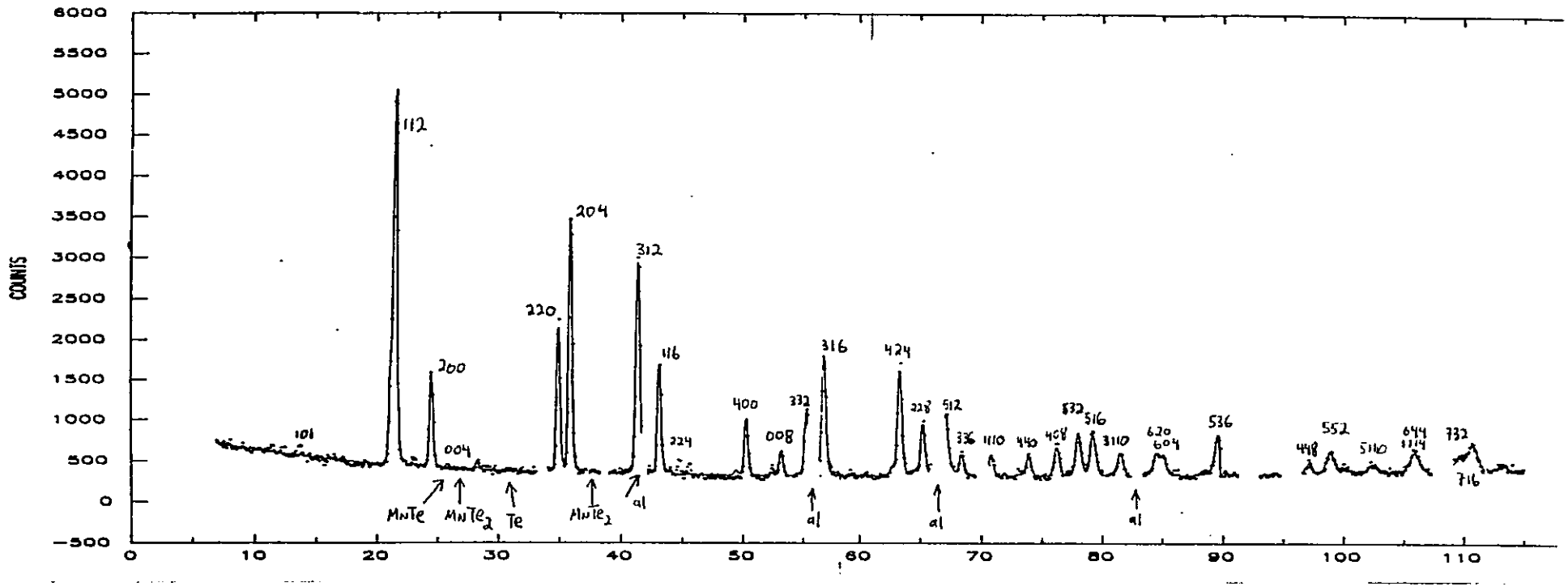

Fig. 4.4.2 Neutron Diffraction Pattern of the $(AgGa)_{1-z}Mn_{2z}Te_2$ z=0.33 material.
The diffraction histogram given above represents neutron counts vs. scattering angle (deg.). The Miller indeces of the tetragonal peaks are given. The gaps in the data due to the aluminum reflecions are shown with arrows, as are the positions illustrating the absences of certain would-be impurity peaks.

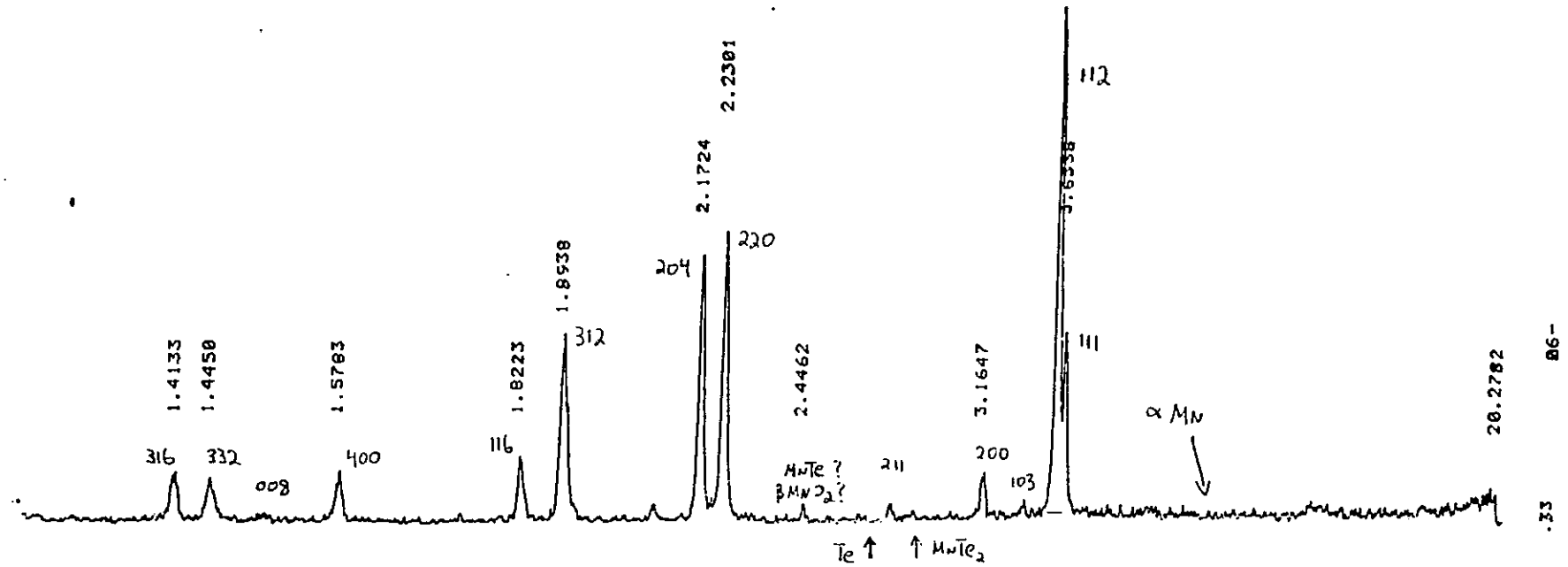

Fig. 4.4.3 X-ray Diffraction Pattern of the $(AgGa)_{1-z}Mn_{2z}Te_2$ z=0.33 material.
The diffraction pattern given above represents diffracted x-ray intensity vs. plane spacing ('d') value, which is given above the peaks. The positions illustrating the absences of certain would-be impurity peaks are given by the arrows.

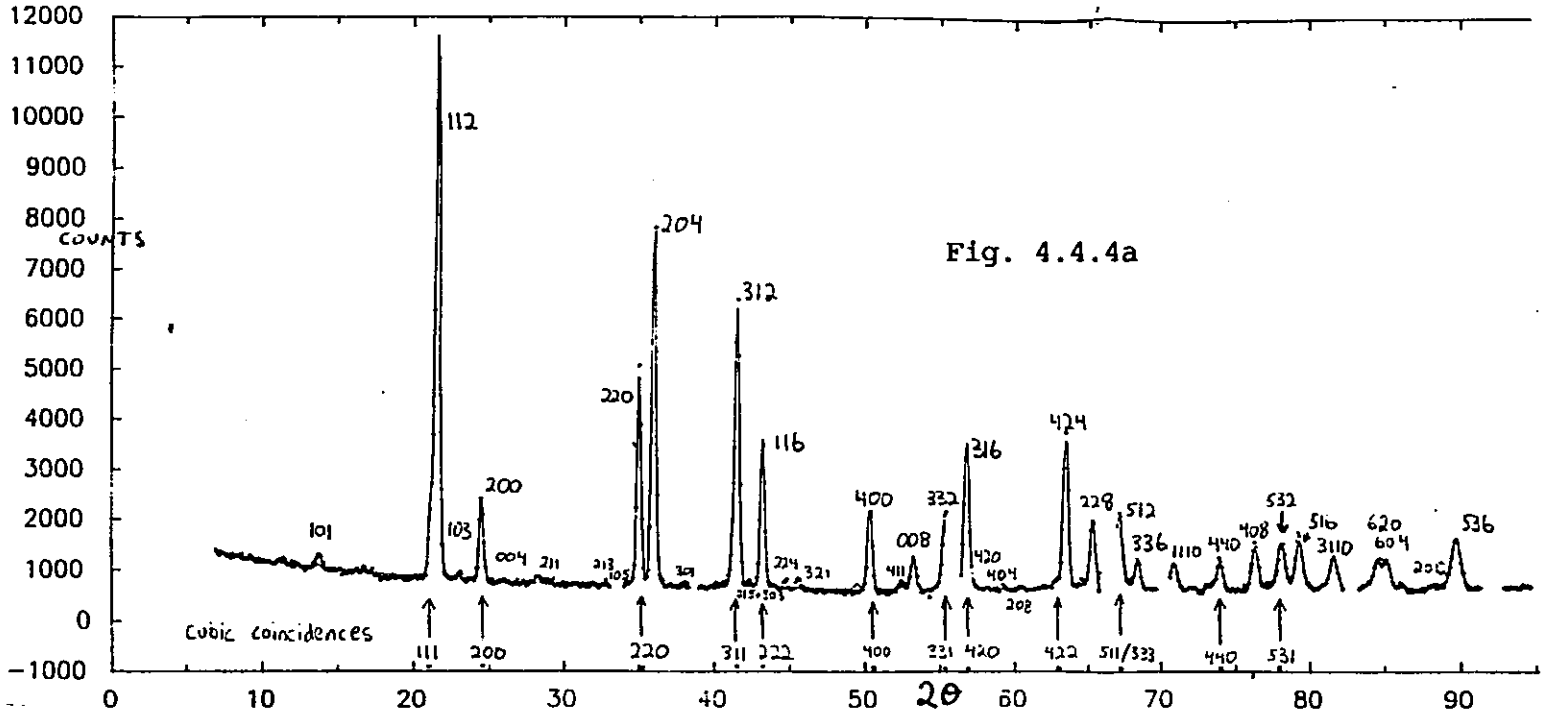

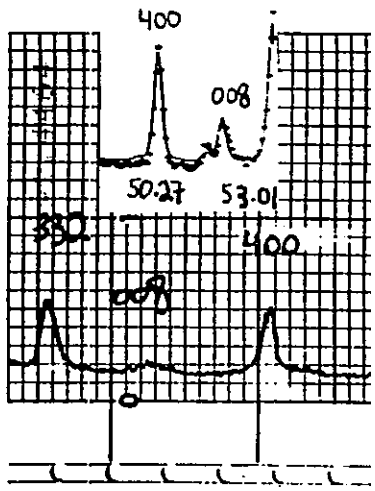

Fig. 4.4.4b

Fig. 4.4.4a Neutron Diffraction Pattern of the $(AgGa)_{1-z}Mn_{2z}Te_2$ z=0.25 material. The diffraction pattern given above illustrates the coincidences of line positions between the closely related tetragonal (α) and zincblende (β-cubic) phases present in the material. The indeces of the cubic lines are given beneath the arrows, while the teragonal indeces are given above the lines. This sample contains approximately 7% cubic phase.

Fig.4.4.4b Neutron and x-ray diffraction of $(AgGa)_{1-z}Mn_{2z}Te_2$ z=0.40, 400 and 008 reflections. The relative difference in the behaviour of the 400-008 reflection pair are seen by comparing the x-ray and nd result. Broadening of the x-ray 008 is evident.

small, systematic variation of lattice parameter as a function of concentration can be seen.

Table 4.4.1. Lattice parameters as a function of concentration for the nd samples. α, β refer to the tetragonal and cubic phases respectively

parameter	z=0.25	z=0.33	z=0.40
α(a)	6.297	6.313	6.322
α(c)	11.974	11.991	12.036
β(a)	6.28	6.29	6.29

This has not been previously reported for the solid-solution. The values for the tetragonal lattice parameter 'a' vary outside the expected range between the value for $AgGaTe_2$ [4] (0.6326 nm) and the value of 'a' obtained from extrapolating the lattice parameters of the Cu-In and Ag-In systems to z=1.0 (0.6333 nm) [105]. Similar deviations of the lattice in Ag-In and Cu-In LTA(100^{o}C) samples has been seen and attributed to Mn-ordering [107].

The presence of β phase can be understood in terms of the nature of the α-β boundary seen in the phase diagram (fig 4.3.3). The increasing amount of β phase with bulk concentration is consistent with the curvature of the α-β boundary to lower temperatures at higher z. Indeed previous measurements do suggest that long annealing times at low temperature are required to convert β to α phase [107].

2)Absence of impurities.

The absence of any extra lines not attributable to the chalcopyrite (or zincblende) structure in either the x-ray or nd patterns sets a low upper limit to the amount of possible impurity phases present in the samples. Indeed plausible

impurities that can be ruled out[1] to the limit of resolution of the diffraction experiments are; (a) the elements Ag, Mn, Te, (b) five oxides of Mn (c-Mn_2O_3, orth-MnO_2, c-MnO, orth-Mn_2O_3, Mn_3O_4), (c) the compound $MnTe_3O_8$, (d) seven distict tellurides of Ag ($AgTe_2$, $AgTe_3$, Ag_2Te (2 forms), AgTe (2 forms), Ag_5Te_3), (e) the telluride of Ga (Ga_2Te_3) and (f) manganese telluride. MnTe can be ruled out to the limit of resolution of the x-ray diffractometer patterns, however $MnTe_2$ is possibly present at the limit of resolution in the z=0.33 and z=0.40 samples.

Compounds whose presence cannot be ruled out due to the coincidental positions of their strong diffraction peaks with the lines already present, are β-MnO_2, and elemental Ga. Elemental Ga cannot be present however, as implied by the absence of other pure element diffraction lines, and the amount of the oxides is known to be small from the purity of the starting materials. It can thus be concluded that the integrity of the material under investigation is good. Indeed the only unexpected line present on either the x-ray or nd patterns is the weak d=2.447 line visible only on the x-ray patterns of the z=0.25 and z=0.33 materials. This line coincides well with the strong [117] reflection of β-MnO_2 however since this line does not appear in the neutron diffraction patterns, it is possible that the MnO_2 is concentrated on the surface portions of the ingots which were used for the x-ray analysis.

3) Presence of chalcopyrite ordering lines;

[1]Referenced in JCPDS [1$\bar{1}$7] manuals.

The observation of most of the ch ordering (type D) lines 101, 103, 211, 213, 105, 301, 303, 215, 321, 107, 323, 305, 411 and 217, (see fig 4.4.4) in both the x-ray and nd, substantiates the presence of cationic ordering as expected from the phase diagram and sample heat treatment. It is an interesting observation that whereas 101 is visible in the nd, it is absent in the x-ray pattern.

4) Absence of stannite ordering reflections;

The absence of the type E and F reflections, particularly in the nd in which they are expected to be visible [116], indicates the absence of a stannite phase in the samples investigated here. This rules out the possibility that the samples segregate into Mn-rich stannite, and Mn-poor ch phases.

5) Intensity Anomalies;

By considering only the ratios of intensities of closely spaced lines, one can neglect the influence of the angular intensity envelope (see 2.4), and facilitate the qualitative analysis of the intensities. Also, certain intensity ratios are simply related to the multiplicity ratio and hence are identical for both the x-ray and nd. In this way intensity anomalies can be made apparent directly from the diffraction patterns or the integrated intensity data obtained from the diffractometer. For example, the expected intensity ratio 200/004=2 whereas the estimated experimental (x-ray and nd) 200/004 ratios are of the order 10^2-10^3. The expected 220/204 ratio is 1/2, and in the nd, ratios of 0.55, 0.6, and 0.4 are seen, however in the x-ray patterns, these ratios are all

larger than 1. In the above examples the intensity anomalies are qualitatively consistent with the presence of β phase which adds intensity only to the tetragonal 200 and 220 lines. However other anomalies can be seen not to be related to the presence of β phase. For example, the expected 400/008 ratio is 2, and the presence of β phase would be expected to increase the apparent 400/008 ratio due to the coincidence of the β 400 with the tetragonal (α) 400. In the z=0.25 nd pattern however, a 400/008 ratio less than 2 (1.8) is seen. Indeed the amount of β phase in the z=0.25 is small and thus this anomaly must be associated with the tetragonal (α) phase.

6) Line-shape anomaly;

There appears to be a broadening of the x-ray 00l lines (004, 008) which is particularly visible on the z=0.40 composition (see fig.4.4.4b). As is well known, a selective broadening of only certain diffraction line profiles indicates the occurence of distortion -related effects as opposed to simple finite crystallite-size broadening [32]. Note that although the x-ray 008 seems broadened, the nd 008 seems normal, this suggests that the effect is enhanced in the x-ray case due to cleavage/orientation in the x-ray experiment geometry.

It can thus be concluded that the materials are mixed cubic and tetragonal phases of the same composition, and that the purity of the samples (with the possible exception of trace amounts of MnO_2 and\or $MnTe_2$) is higher than that resolvable by the diffraction measurements.

Although there is high confidence in the interpretation

that the materials are mixtures of compositionally identical α and β phases, it is important to note that different composition cubic and ch phases were also studied as possible models. Any such model could only be consistent with the phase diagram data under the assumption that fractional crystallization occurs upon cooling from the high temperature liquid + solid field. This could in principle result in inhomogeneities in the material, which however would be hard to justify in view of the previously reported DTA, x-ray, magnetic and optical energy gap measurements of these alloys, and would also be inconsistent with the observed systematic variation of the lattice parameter with concentration.

One such analysis was carried out at Chalk River by Dr. D. Noakes and there it was found that the Mn-concentrations of the two phases needed to be very different in order to explain the data. This can be understood by observing that high Mn concentrations in the adamantine lattice are required in order to produce high 200 intensities (see fig.4.4.1). A simple lever rule analysis illustrates however that no such model can work within the bounds of concentrations allowed for in the phase diagram. This can be seen as follows, considering the diffraction intensity function (2.4.4) to be of the form $I = pF^2 * f(\theta)$, with $f(\theta)$ being the angular envelope function (which includes the Debye and Lorentz factors), one can readily show for a postulated mixed tetragonal (ch) and cubic (c) material of different Mn concentrations, that the apparent intensities of overlapping 112(ch) and 111(c), and 200(ch+c) lines are:

$$I_{112+111} = 8[Z_1 F^2_{112}(ch) + Z_2 F^2_{111}(c)] * 1.2 \qquad (4.4.1a)$$

$$I_{200+200} = 4[Z_1 F^2_{200}(ch) + (3/2) Z_2 F^2_{200}(c)]*1.0 \qquad (4.4.1b)$$

with the lever-rule coefficients Z_1 and Z_2 given by;

$$Z_1 = (z-z_c)/(z_{ch}-z_c), \qquad Z_2 = (z_{ch}-z)/(z_{ch}-z_c)$$

where z is the nominal composition appearing in the chemical formula $(AgGa)_{1-z}Mn_{2z}Te_2$, and z_{ch}, z_c are the actual Mn concentrations of the postulated split-off tetragonal and cubic phases respectively, i.e. of the mixture β-$(AgGa)_{1-z_c}Mn_{2z_c}Te_2$, and α-$(AgGa)_{1-z_{ch}}Mn_{2z_{ch}}Te_2$. For the z=0.25 material, the experimental nd intensity ratio 112/200 equals 6.5, and is anomalously low. Considering the extreme case of maximal Mn concentration gradient which maintains consistency with the phase diagram data, one utilizes z_{ch}=0.0 and z_c=0.44 in the relations above. With these values one finds an intensity ratio 112/200 = 17 which is not low enough to account for the data. This illustrates the deficiencies of the two phase model. Indeed it can be shown that in order to explain the experimental nd result from within the two phase scenario, one either requires a hypothetical zincblende form of $MnTe_2$ or significantly more Mn than actually exists in the material. In either case such a model would not reproduce the observed x-ray intensities. This strongly supports the assumption utilized above that any residual cubic (β) phase should have the identical composition to the ch phase, and that an ordering effect causes these intensity anomalies.

Since we will be studying the tetragonal line intensities in detail, it is important to accurately account for the β phase. Fortunately, the cubic 111 reflection is sufficiently resolved in the x-ray diffractometer pattern to give a

reasonable estimate of the amount of β phase present. The amount of β phase can be estimated directly from the 112/111 intensity ratio since these lines have identical structure factor, multiplicity and intensity envelope function. The expected intensity of all the β lines could then be calculated using 2.3.3, and subsequently subtracted from the appropriate ch lines. For the purposes of such an analysis, a MINUIT subroutine was written which utilized two free parameters in the expression 2.3.3 to accomplish the above analysis. The free parameters are the global intensity factor and the Debye factor. In the case of x-rays, the additional angular variation caused by the atomic scattering factors was absorbed into the exponential form of the Debye factor. For the purposes of providing MINUIT with a starting value for the Debye factor, an estimate of the expected magnitude of the Debye factor was arrived at from the reported θ_D for the compound $AgGaTe_2$ [118]. θ_D and the Debye factor are linked together by the relationship between the thermal mean square atomic displacement and the phonon spectrum in the Debye model [32];

$$\Delta x^2 = \frac{424}{M_a \theta}\left(\frac{T}{\theta}\right)\left[\frac{1}{4}\frac{\theta}{T} + \phi\left(\frac{\theta}{T}\right)\right] \text{ where } \phi\left(\frac{\theta}{T}\right) = \frac{T}{\theta}\int^{\theta/T} y\, dy\, [(\exp y)-1]^{-1} \qquad (4.4.2)$$

where M_a is the average atomic mass, and the units of Δx^2 are given in cm^2.

It is important to state the assumptions implied by the use of the two-crystallographic phase model. Firstly it is assumed that the intensities of the separate reflections due

to the cubic and tetragonal phases add together at the same scattering angle. Thus in the analysis of the intensities, phase relations at the scattering site are not required. In the following section, this will be distinguished from the case where scattering amplitudes must be added thus maintaining the phase relations of the scattered waves. The latter is appropriate to the case when the two crystal 'phases' (reflection sources) are intimately interconnected such as in the case of a partially Mn-ordered material.

Secondly in extrapolating the expected higher angle cubic line intensities from the 111 reflection, it is assumed that finite size effects which lead to a broading of the diffraction lines do not occur. Although this represents the usually expected or 'default' condition, the only way to verify this assumption would be through a detailed analysis of the background intensities which would be difficult to carry out with the present data, and which seems unnecessary in view of the small amounts of β phase involved especially in the low z materials.

The x-ray and nd intensities as fit to the cubic + chalcopyrite model are illustrated in figs. 4.4.5 to 4.4.7. In these figures, the experimental integrated intensities are represented in bar-graph form with the dark bars (labeled 'data') signifying the experimental data and the lightest bars (labeled 'fit ch+c') representing the fits. In the x-ray case, the fits to the data with the chalcopyrite-only condition (labeled 'fit ch') are also shown for comparison purposes. The chalcopyrite structure utilized in the fitting

Fig.4.4.5a 'Chalcopyrite'+cubic (zincblende) fit to nd intensity for $(AgGa)_{1-z}Mn_{2z}Te_2$ z=0.25

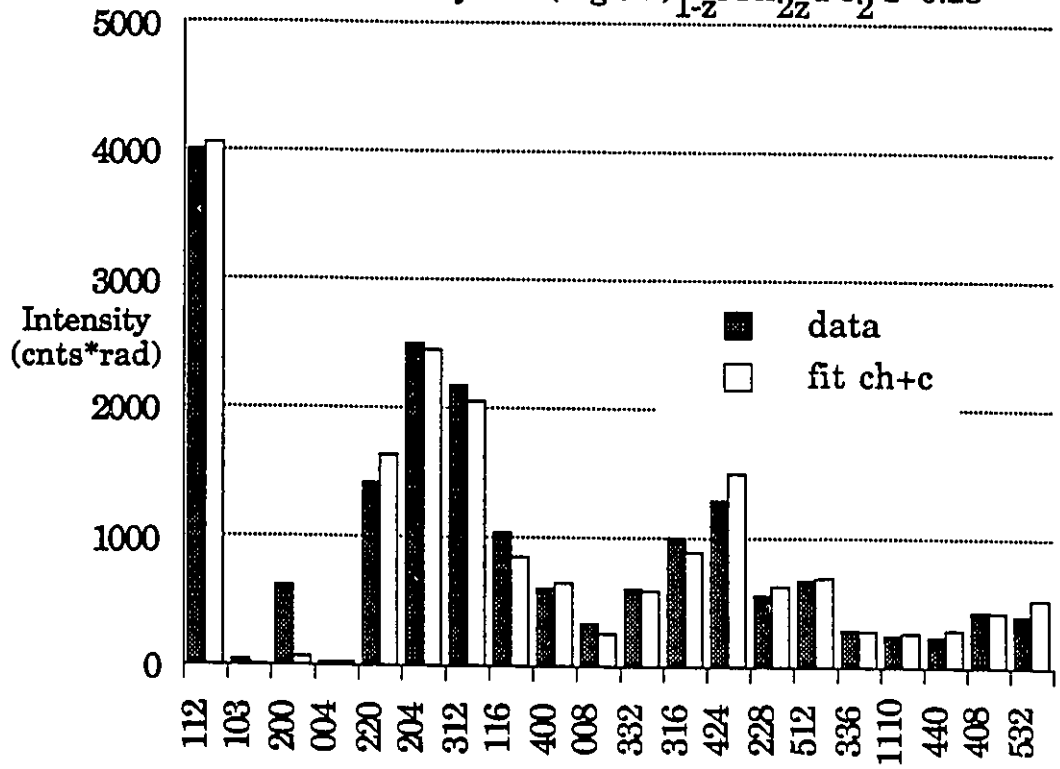

Fig.4.4.5b 'Chalcopyrite' ('fit ch'), and 'chalcopyrite'+ zincblende ('fit ch+c') fits to x-ray intensity data for $(AgGa)_{1-z}Mn_{2z}Te_2$ z=0.25

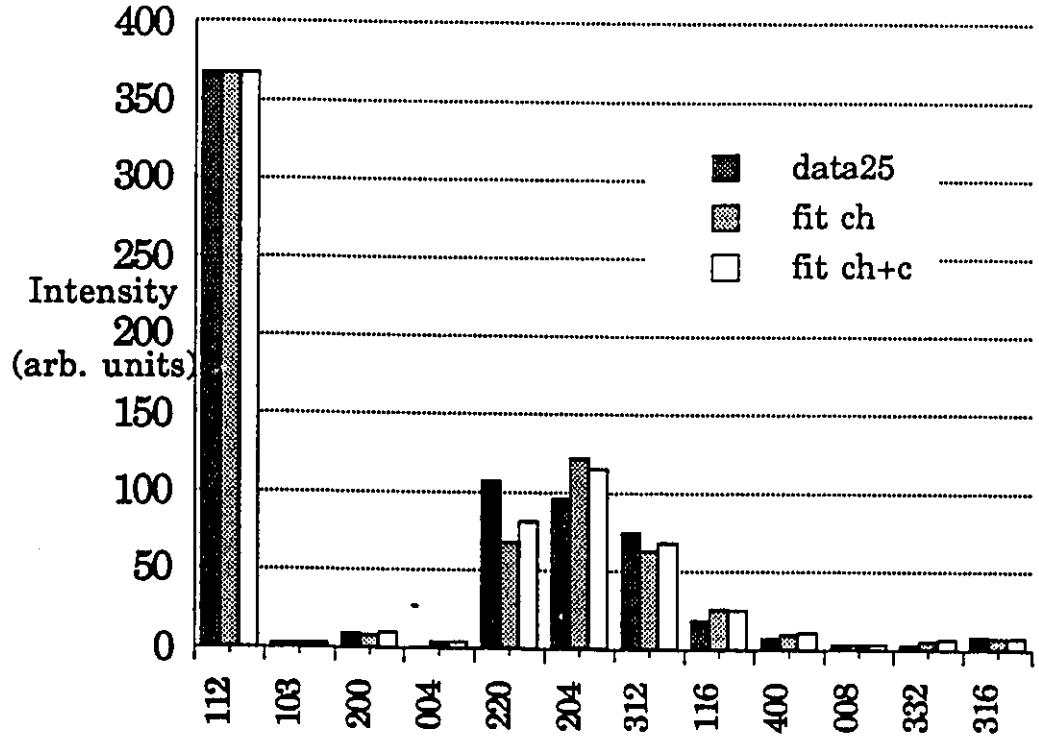

Fig.4.4.6a 'Chalcopyrite'+cubic (zincblende) fit to nd intensity for $(AgGa)_{1-z}Mn_{2z}Te_2$ z=0.33.

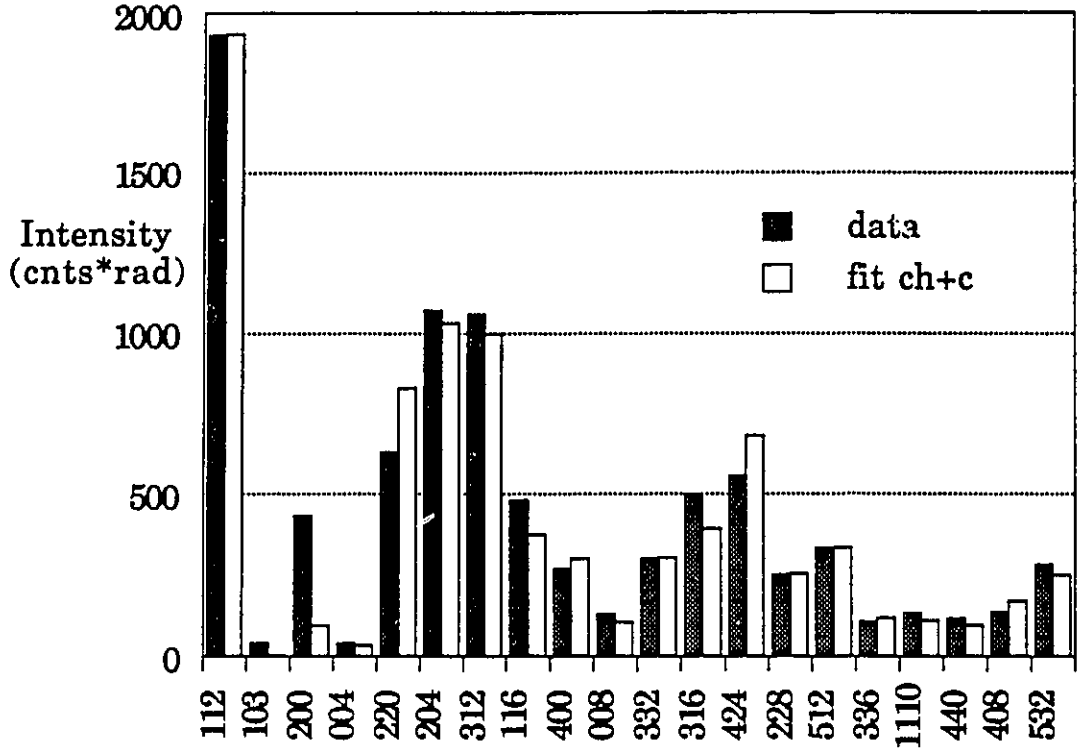

Fig.4.4.6b 'Chalcopyrite' ('fit ch'), and 'chalcopyrite'+ zincblende ('fit ch+c') fits to x-ray intensity data for $(AgGa)_{1-z}Mn_{2z}Te_2$ z=0.33

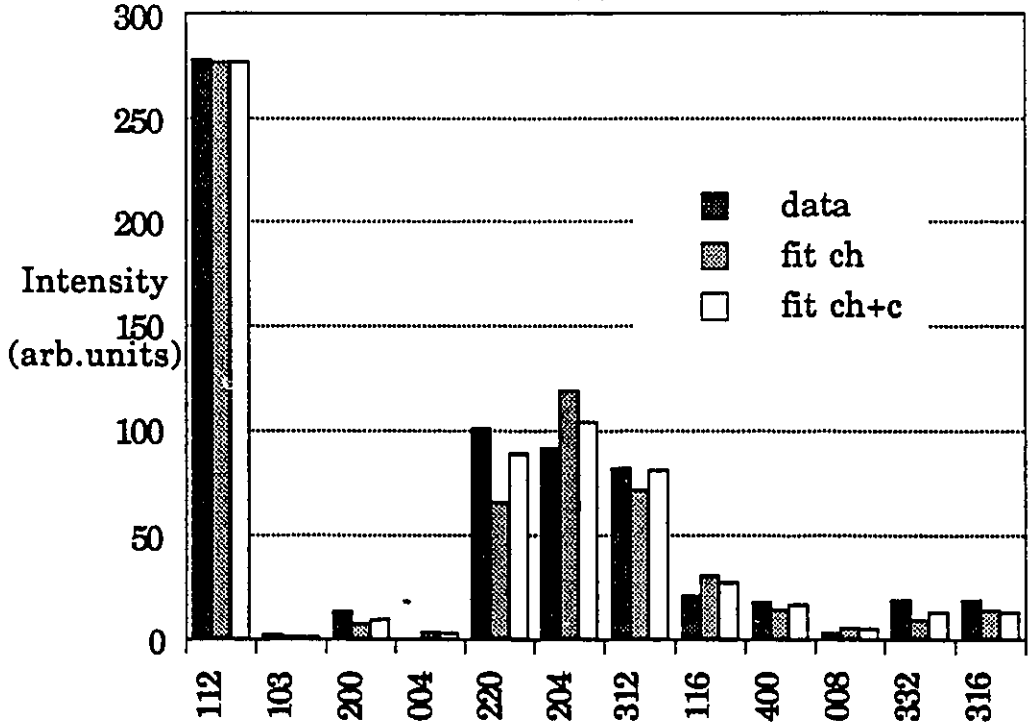

Fig.4.4.7a 'Chalcopyrite'+cubic (zincblende) fit to nd intensity data for $(AgGa)_{1-z}Mn_{2z}Te_2$ z=0.40.

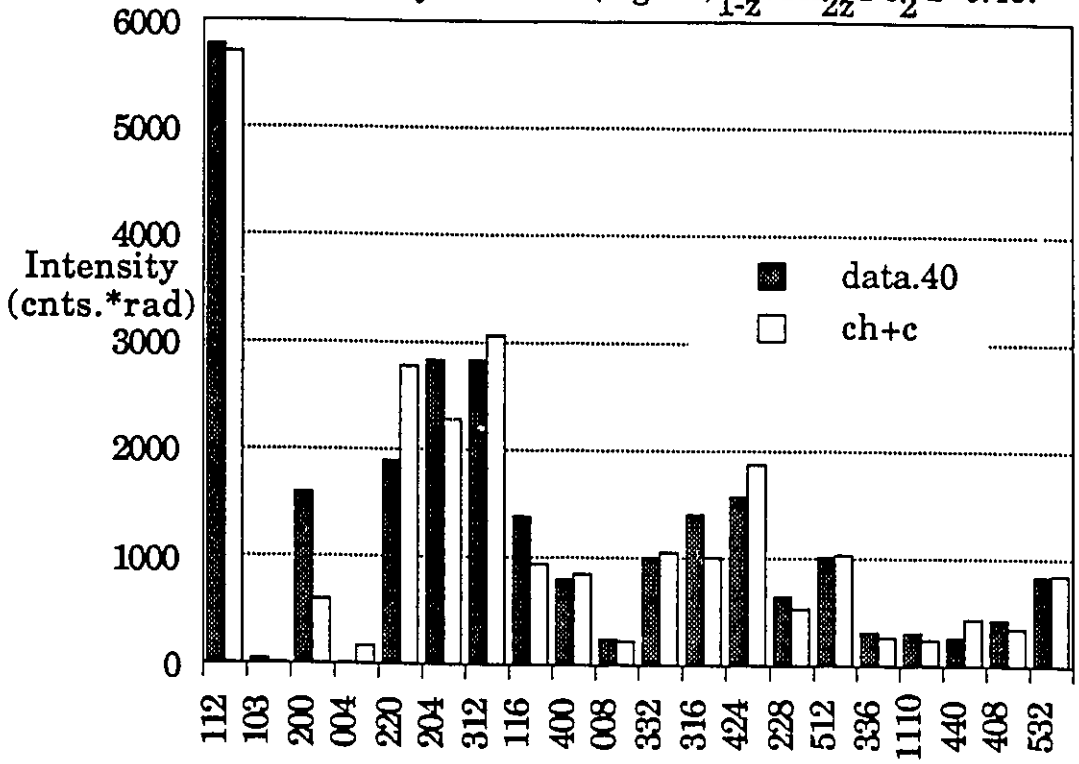

Fig.4.4.7b 'Chalcopyrite' ('fit ch'), and 'chalcopyrite'+ zincblende ('fit ch+c') fits to x-ray intensity data for $(AgGa)_{1-z}Mn_{2z}Te_2$ z=0.40

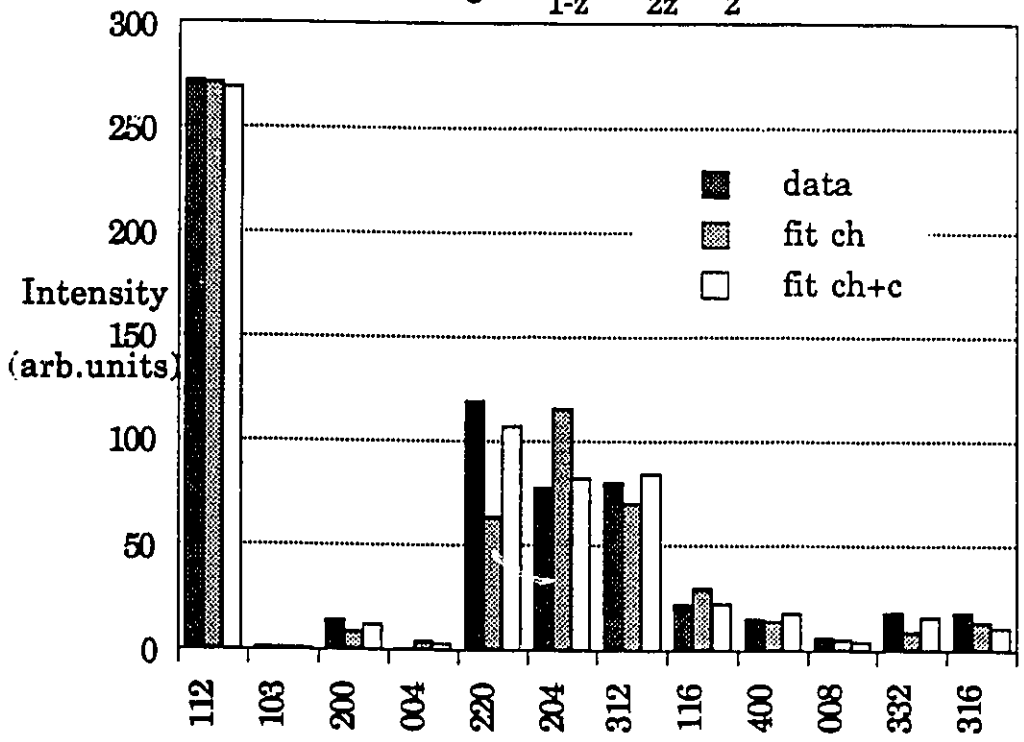

is appropriate to Mn occupying any of the ideal cation sites within the chalcopyrite cationic sublattice. However the fitting can in principle, repesent structures other than chalcopyrite so it is labeled as 'chalcopyrite' (in quotation marks) in the figure captions. This imporant detail will be elaborated upon in the following pages. The fits can be seen to have interesting properties, some of which are listed in the following:

1) Ordering line intensities

The 103 intensity was included in the fits, as an example of the ordering line intensities since this line has the most reliable intensity information of all the ordering lines. Comparing the fit intensity to the experimental data for this reflection, and noting the relative sizes of the ordering lines, it can be seen that the ordering lines are slightly more intense than expected (relative to the ch 112).

2) Anomalous type-B structure reflections;

By comparison to the 112 reflection, the results of the previous observations regarding certain line intensities can be verified. In particular it can be seen that the nd 200 intensities are anomalously large, and that the 004 reflections are generally weaker than expected, particularly those of the x-ray patterns. These observations indicate a departure from the ideal ch structure, and will be used to ascertain aspects of the Mn-ordered structures in the following pages.

3)Incorrect line intensities;

Similarly to observation 2, it can be ascertained from the

diffractometer data that the ratios of other structure reflection pairs are not equal to those expected for the ch + zincblende structures. As expected from the previous observations, the nd 400/008 ratios are incorrect, as are the ratios of the 332/316 intensities. Also, both the 332 and 316 lines are too intense compared to the 112. The nd 424 intensity is consistently low compared to the ideal ch structure. In the x-rays, the discrepancy between data and fit is highest for the low z compositions and occurs mostly in the incorrect 220/204 intensity ratio.

The reproduction of these intensities will be an important aspect of any acceptable model for the ordering, however it should be stressed that any such analysis follows the assumption regarding the β-line intensities as extrapolated from the 111. In the case under investigation the low concentration material which contains the least amount of β-phase (approx. 7% β in the z=0.25 composition) is the most insensitive to the β-subtraction and will be the sample which guides the whole analysis.

It is significant that the quality of the x-ray fit to the ch + c condition clearly improves with concentration, and the fit to the x-ray z=0.40 composition is as good as can be expected within the experimental error. The misfit in the x-ray ch+c fits at low concentration do not indicate residual cubic phase which would suggest an incorrect subtraction of the β intensity. This can be seen in Fig.4.4.8 in which although the 220 misfit suggests that not enough β phase was subtracted, the 400 misfit suggests that too much β intensity

Fig.4.4.8 Difference between data and fit to 'chalcopyrite'+cubic for the z=0.25 $(AgGa)_{1-z}Mn_{2z}Te_2$ x-ray intensity .

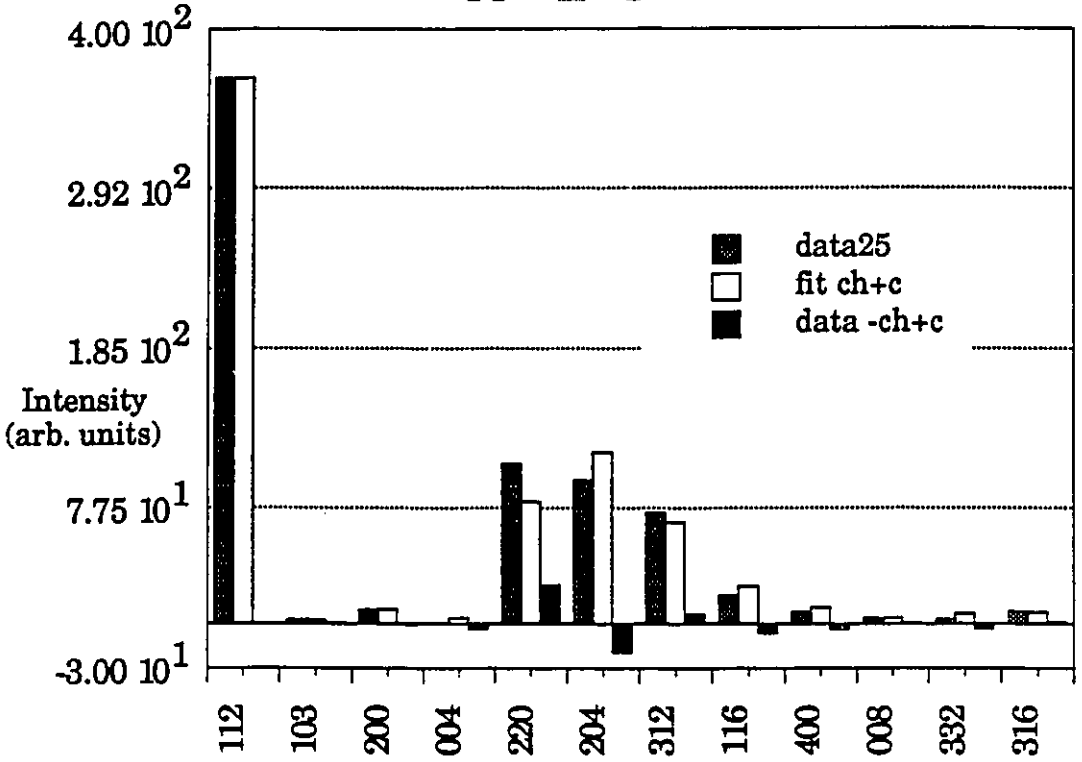

Figure 4.4.8 illustrates the 'chalcopyrite'+cubic fit to the x-ray intensity data for the z=0.25 $(AgGa)_{1-z}Mn_{2z}Te_2$ material previously seen in fig.4.4.5b. The difference (misfit) between the data and the model is also given as the black bars. The lack of systematic misfit suggests that the cubic contribution is properly taken into account.

was subtracted.

It can also be seen that the fits in the nd case are noticably poorer. This is no doubt due to the fact that the neutron scattering is more sensitive to the Mn ordering as suggested by the greater z-dependence of the nd structure factors compared to the x-ray structure factors seen in fig. 4.4.1.

4.4.2) Preliminary Analysis of Results

In order to further analyse the diffraction intensities, some important aspects of the structure factors must be considered. Firstly we note that any model of the ordering which involves a homogenous distribution of Mn on the ideal cation positions cannot affect the ch or stannite structure (type A, B,and C) reflections. This follows from the form of the structure factor (eq.4.3.1), and from the cation positions within the crystal structure. One can readily show in the case of all structure reflections (type A, B, C), that all the cation sites enter in the summations over atomic positions with positive signs. This implies that the structure factors remain identical for all structure lines independently of the details of which ideal-sites the Mn ions occupy. For example, in the case of the type B lines 200 and 004, the structure factor is equal to:

$$F^2(\text{type B}) = 16\,[\,(1-z)(f_{ag} + f_{ga}) + 2zf_{Mn} - 2f_{Te}]^2 \quad (4.4.3)$$

and can be seen not to depend on the exact Mn ion positions as long as the Mn reside on the ideal cation sublattice. The intensity ratio of these lines is then strictly related by

their multiplicity ratio, for example equal to 1/2 in the case 004/200. Considering that the measured nd 004/200 ratio is effectively zero, the above implies that some effect other than simple Mn substitution on the supposed fixed cation sites is required. This leads to the consideration of atomic Mn-dependent displacements away from the ideal crystallographic sites, which will be studied in the next subsection.

In order to see if the stannite-like forms of ordering could still form a basis for the structure of the materials, a preliminary analysis of the nd data was undertaken. In particular, the presence of ch, and absence of stannite ordering lines as well as the anomalous type B lines are the most distinguishing features of the diffraction patterns. The anomalous type B intensities, particularly the quenching of the 004 intensity is of interest because only the 004 reflection involves differences between the scattering powers of adjacent cation and anion planes which are perpendicular to the z-direction. For this reason, 004 is expected to be most sensitive to the postulated Mn-planes. Calculations of the structure factors for various cases were attempted with the aid of Prof. Woolley and R. Johnston, a summer student who wrote a 'Basic' micro-computer program to be described in the following.

Through an analytical calculation of the structure factor, it was found that the randomly spaced full Mn planes do yield null intensity stannite ordering lines. Indeed adopting a cation plane numbering system whereby each successive cation

plane site above an arbitrary origin is assigned an integer index (1, 2, 3,...) in order of its distance from the origin, it can be shown that the intensity of the stannite ordering lines derived from the structure factor 4.3.2 in the random-plane condition is proportional to $(n_e-n_o)^2$ where n_e is the number of Mn-planes on even-numbered cation plane sites and n_o is the number of Mn-planes residing on odd-numbered sites. This follows intuitively from the fact that in the ideal stannite configuration, the Mn planes would be either all odd or all even, and it can be seen that opposite parity Mn-planes contribute out of phase scattered waves to the type D (ordering) reflections.

The randomly spaced full Mn planes are expected to have little affect on the chalcopyrite ordering lines due to the fact that the Mn ions are effectively randomly distributed on the planes which give rise to the ordering reflections.

These conclusions were verified with the micro-computer program which calculated the structure factors of a superlattice cell composed of 10 conventional ch unit cells stacked in the c-direction. The calculated intensities were normalized to the observed 112 line intensity. The planar Mn ordering was assumed to be of the type discussed above (and in section 4.2) whereby full Mn-planes with random interplane spacings occur. Adjacent Mn-planes were not allowed in accordance with the discussion in 4.2. The ability to account for the presence of the ch, and absence of the stannite ordering lines is an important feature of the planar Mn ordering scheme.

In order to explain the anomalous type B intensities, deviations of the atomic positions from the ideal ch lattice sites are required. It is known that in the structure of actual stannite materials, displacements of the anions perpendicular to the single-element cation planes occur [119]. In the chalcopyrite case, it is also known that the cations remain very close to the ideal lattice sites whereas the anions are generally displaced from theirs [120]. Indeed these displacements can be accurately measured by x-ray diffraction and other techniques, and are known for many of the chalcopyrite compounds. In order to assess the importance of the anion displacement on the type B intensity in the proposed random Mn plane configuration, z-axis displacements of the Te planes adjacent to the Mn-filled planes were postulated. Displacements were introduced into the program and these were postulated to be chalcopyrite-like displacements which were also coupled to the Mn-planes, as described in the following subsection.

It can be shown from the behaviour of the type B neutron structure factor as a function of concentration that for concentrations greater than z=0.11, the anionic displacements can only decrease the type B intensities. For example it is easy to show that in the z=0.25 composition, the 004 intensity is reduced to zero by displacing only two of the four anion planes in the unit cell by 0.6 A in the z direction. Of course such z-displacements leave the 200 intensity unaffected. This could describe the mechanism behind the enhancement of the 200/004 ratio.

4.4.3) Diffraction Data Fitting

The full Mn plane with random inter (Mn) plane spacing model discussed in the previous section, was incorporated into a fitting of experimental nd and x-ray line intensities. Given the importance of the anionic displacements from their ideal tetrahedral sites, three displacement parameters were introduced as free fitting parameters. In accordance with the above discussion, it is assumed that only the anion (Te) displacements are required to reproduce the real crystal structure, thus the parameters represent the displacement from the ideal of the Te atoms along the three principal (cartesian) crystal axes. The bond lengths in $AgGaTe_2$ have been calculated [121] to be; R_{Ag-Te}= 2.72 A, R_{Ga-Te}= 2.65 A, and show the tendency of the Te atoms to move away from the Ag, and toward the Ga atoms.

Fig. 4.4.9 indicates the displacements of a Te atom adjacent to a Mn plane under the assumption that the Te is displaced toward the Mn. For reasons outlined in section 4.2, near-neighbour Mn planes were not allowed in the plane distribution and this together with the assumption that the Mn-planes are completely filled (no interplanar Mn) severely restricts the combinations of displacements utilized. Fig. 4.4.9 and the accompanying table indicate the three sets of displacements which are possible. The displacements δ_0 occur in the case when the Te atom has no near-neighbour Mn atoms and correspond to the known displacements δ_0=0.015 (in units of the lattice parameter) in $AgGaTe_2$. The remaining two cases

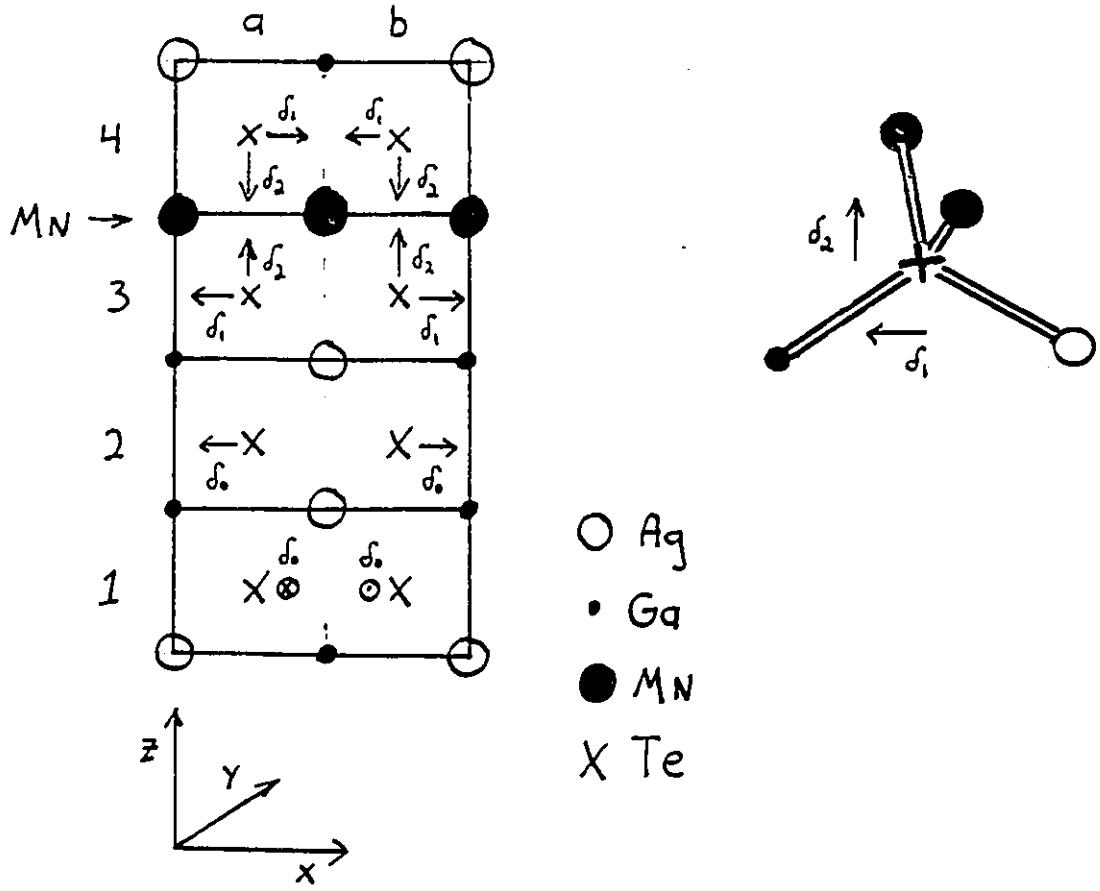

	No Mn adjacent			Mn Above			Mn Below		
	x	y	z	x	y	z	x	y	z
1a	$-d_o$	0	0	$-d_1$	$-d_1$	$+d_2$	$-d_1$	$+d_1$	$-d_2$
1b	$+d_o$	0	0	$+d_1$	$+d_1$	$+d_2$	$+d_1$	$-d_1$	$-d_2$
2a	0	$+d_o$	0	$+d_1$	$+d_1$	$+d_2$	$-d_1$	$+d_1$	$-d_2$
2b	0	$-d_o$	0	$-d_1$	$-d_1$	$+d_2$	$+d_1$	$-d_1$	$-d_2$
3a	$+d_o$	0	0	$+d_1$	$+d_1$	$+d_2$	$+d_1$	$-d_1$	$-d_2$
3b	$-d_o$	0	0	$-d_1$	$-d_1$	$+d_2$	$-d_1$	$+d_1$	$-d_2$
4a	0	$-d_o$	0	$-d_1$	$-d_1$	$+d_2$	$+d_1$	$-d_1$	$-d_2$
4b	0	$+d_o$	0	$+d_1$	$+d_1$	$+d_2$	$-d_1$	d_1	$-d_2$

Fig. 4.4.9 Anionic displacements utilized for diffraction data analysis. The crystallographic cell displayed at upper left represents part of a planar Mn-ordered chalcopyrite lattice. Illustrated are the various displacements of the anions (X) which were postulated in the diffraction data fitting. The figure at upper right illustrates the displacements in relation to the orientation of a tetrahedron. The table above lists all the possible displacements of the anions in the model. Positive d parameters signify displacements in the positive directions as defined by the axes shown.

relate to the conditions in which there is one Mn plane either directly above or below the Te plane, these correspond to stannite-like displacements. In each case the atomic displacements δ_1 are in the x-y plane and can be seen to be along the diagonal direction as expected from the orientation of the tetrahedra (see fig.4.4.9) The displacement δ_2 in the z-direction applies to the whole anion plane and occurs only in the presence of a neighbouring Mn plane. The x-y displacements (δ_1) which occur concomitantly with δ_2 are different from those of the pure compound.

The calculation of the structure factors was done similarly to that described in the previous section, however in this case MINUIT [122] was used to determine the best displacement parameters δ_0, δ_1 and δ_2, (along with the scaling and Debye factors) which rendered the best fits. Prof. R. Hodgson assisted in the analysis by writing the MINUIT minimization subroutine. A least squares criterion was utilized to accomplish the fitting.

For the x-ray data, it was found that this model could provide dramatically improved fits, the value of the least squares function being of an order of magnitude less than that of the (undisplaced) ch+c fit. In the nd data, the resulting fits were very similar to those seen previously, the least squares function being reduced by only a few percent compared to that of the undisplaced ch+c fit. Representative fits with displacements are illustrated in figs. 4.4.10. The previously seen fit to the chalcopyrite + cubic model is shown as 'fit ch+c' on fig.4.4.10b (x-ray data) in order to illustrate the

Fig.4.4.10a Planar Mn-ordered chalcopyrite with displacements ('dis.fit') and cubic contribution, as fit to nd intensity data for $(AgGa)_{1-z}Mn_{2z}Te_2$ z=0.25

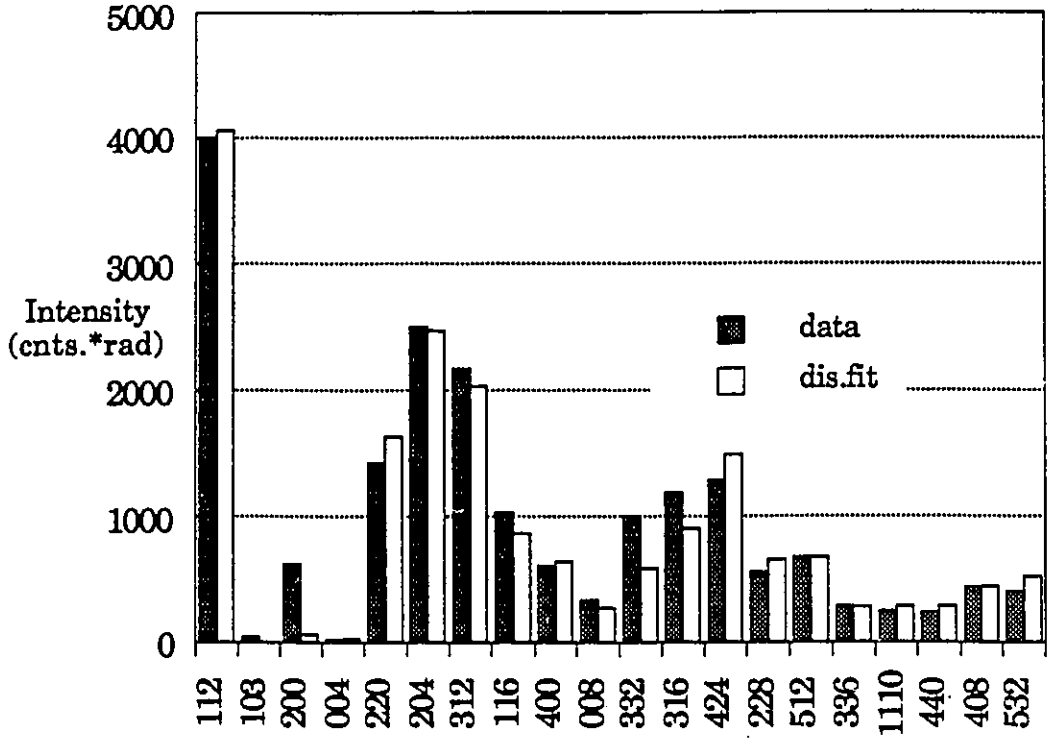

Fig.4.4.10b Planar Mn-ordered chalcopyrite with displacements ('dis.fit') and cubic contribution, as fit to x-ray intensity data for $(AgGa)_{1-z}Mn_{2z}Te_2$ z=0.25

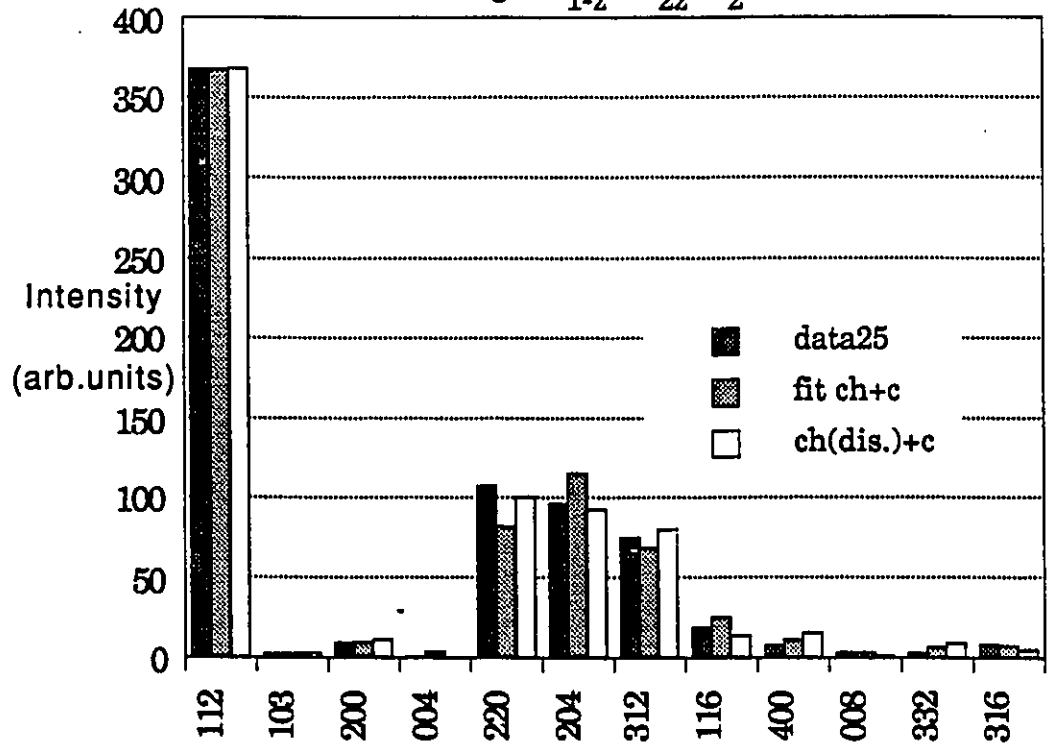

obvious improvement in the case of the displacement model.

As seen on fig.4.4.10a, the nd 200 intensity remained anomalously high. Also, the fit displacement parameters from the neutron and x-ray data do not correspond to each other. This indicates that the planar stannite-like ordering with small anionic displacements cannot reproduce the correct intensities. In particular, it is clear that a relative enhancement of the 200 occurs in the nd data, as opposed to a relative suppression of all the other lines. Discrimination between the fits with and without the δ parameters is complicated by the fact that the Debye factor shows a high degree of correlation with the δ parameters. Since the effect of fixed displacements increases with scattering angle in the same way that the effect of the Debye factor does, the quenching of intensity accomplished by the Debye factor envelope can be mimicked by various combinations of anion displacement parameters. This leads to difficulty in the interpretation of the final output parameters.

Although the use of the concept of full Mn planes gives a fair fit to the experimental data, it is seen that small anionic displacements from the ideal chalcopyrite sites cannot completely reproduce the data. This is evident from the observation that although anionic displacements can reproduce the anomalous experimental 200/004 intensity ratio, they cannot reproduce the correct absolute intensities of those lines in a way that is consistent with the rest of the diffraction intensity data. Of course, a consideration of only the anion displacements does not cover the full range of

possible displacement models based on the chalcopyrite structure. Another possibility under the assumption that small atomic displacements from the ideal sites occur, is that the cations themselves are displaced, and this leads to other diffraction effects not achievable by anion-only diplacements.

In order to assess the importance of possible cationic displacements, some analytical calculations were carried out. It was found that by displacing the Ag and Ga atoms in the xy plane, the 200 intensity could be enhanced, however with a displacement of magnitude equal to 4% of the lattice parameter, the 200 was enhanced by only a factor 1.8 while the 112 was quenched by a factor 0.92 yielding a relative enhancement of the 200 of approximately 2. This falls short of the observed 200 enhancement of approximately 7 times the expected ch intensity in the case z=0.25. It must then be concluded that small displacements from the ideal ch sites cannot completely explain the nd 200 intensity. One possibility to be considered is that in the ordered case, some cation sites are changed giving a structure closeley related to, but different in detail from chalcopyrite. Such a condition is distinct from the displacement cases considered above in which the deviation of the atom from the ideal sites was less than 10% of the lattice parameter. In the present case, qualitatively different sites within the anion sublattice are occupied.

One related crystal structure investigated as a possible basis for the Mn-ordering was that of a planar-Mn configuration within the eskebornite ($CuFeSe_2$) structure. In

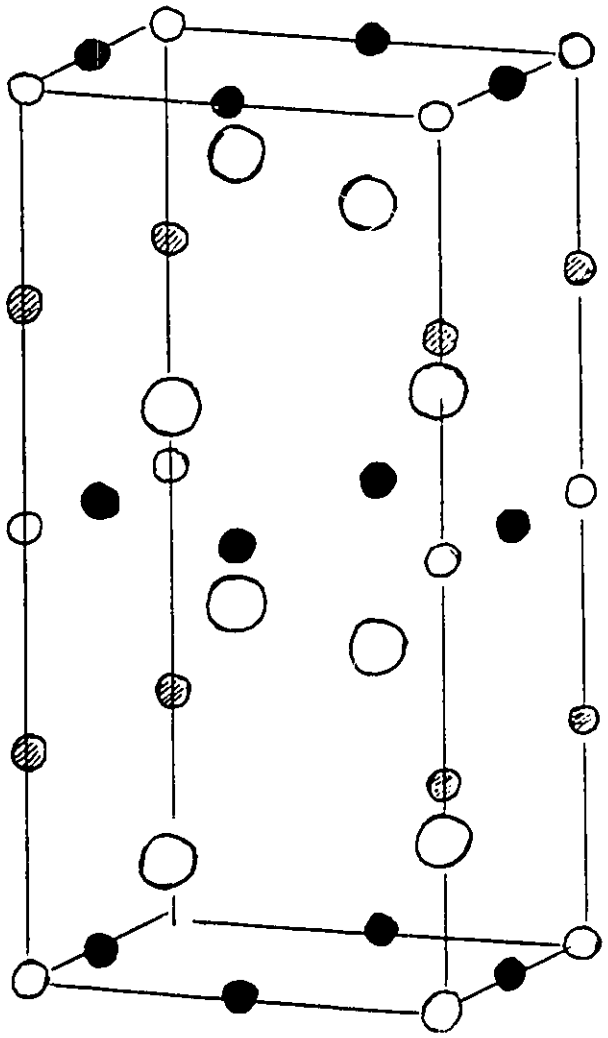

Fig. 4.4.11 Eskebornite structure.
Illustrated is the eskebornite ($CuFeSe_2$) structure. This structure is similar to that of chalcopyrite ($CuFeS_2$), however involves the occupation of different tetrahedrally bonded sites within the fcc anion sublattice than those of the chalcopyrite (zincblende) case.

this structure, illustrated in fig.4.4.11, one in four cations occupy different tetrahedrally coordinated sites from those in the ch structure. This structure however does not seem to produce significantly enhanced 200 reflections.

In addition to the tetrahedrally anion-coordinated sites, a further possibility is that cations occupy octahedrally anion-coordinated sites, i.e. sites equivalent to those occupied by the cations in the NaCl structure. Indeed the exclusive occupation of octahedral sites in the NaCl structure yields a 200/112 intensity ratio greater than unity. In order to ascertain whether the presence of Mn planes could lead to a ch-like structure containing cation sites which are octahedrally coordinated by anions, various simple structures were attempted with the MINUIT program. It was found that the predicted nd behaviour is very sensitive to whether Mn or other cations occupy the octahedral sites, whereas the predicted x-ray behaviour is much less sensitive to which species is octahedrally coordinated. In the cases with octahedrally coordinated Mn planes, it was found that the nd 200 was not appreciably enhanced, while in the cases where Ag-Ga planes occupied octahedral sites, the 200 was greatly enhanced. In the cases where the 200 was enhanced however, a greater misfit was obtained in the higher angle lines, particularly for the 332, 316 pair. One such condition is shown in fig 4.4.12, in which the fit 200 is clearly enhanced relative to that seen in the ch cases (figs.4.4.5-4.4.7). A few fits were attempted with equal amounts of octahedrally coordinated Mn- and Ag-Ga planes and these did indeed provide

Fig.4.4.12 Tetragonal+zincblende nd intensity fit to $(AgGa)_{1-z}Mn_{2z}Te_2$ z=0.25.

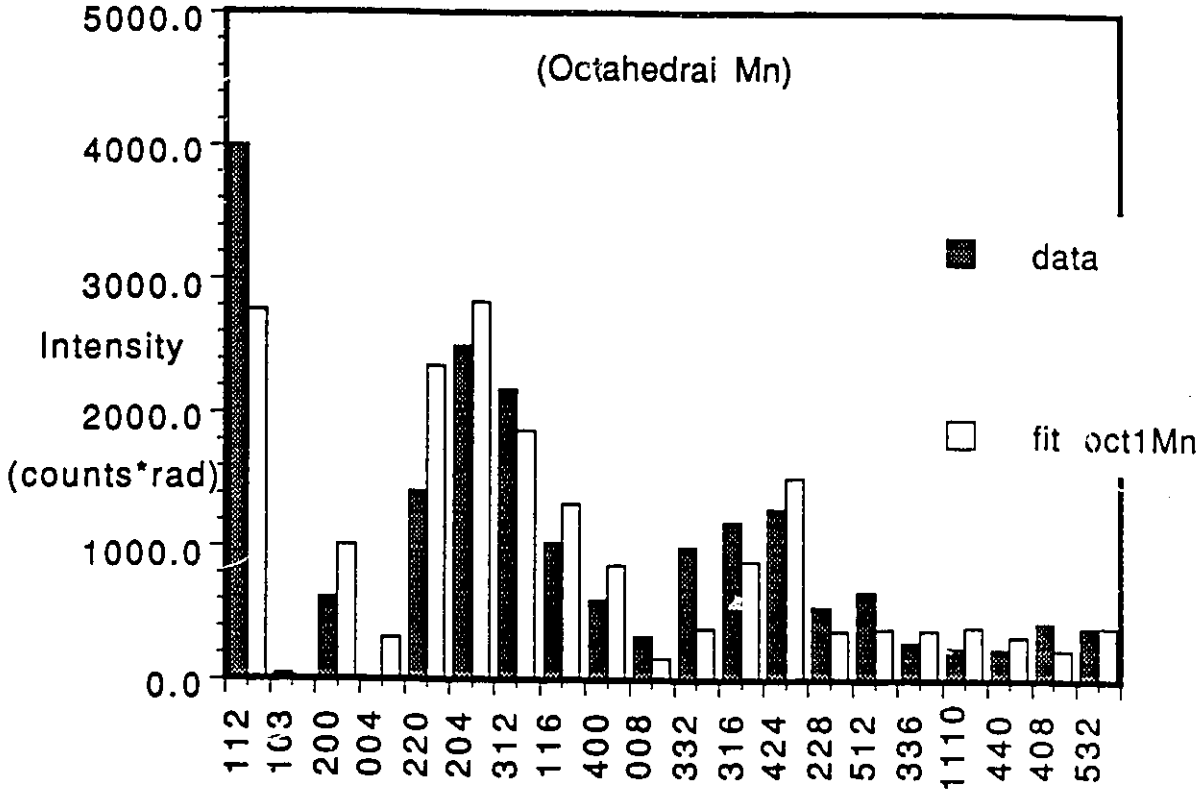

Fig.4.4.12 illustrates the effect on the neutron diffraction intensity fitting, of introducing octahedrally-anion-coordinated cation sites within the lattice. In this example, one Ag-Ga cation plane in the conventional chalcopyrite unit cell (fig.4.2.1) has been moved into a position where the cations become octahedrally coordinated by anions. The remaining lattice is otherwise identical to the Mn-containing 'chalcopyrite' lattice utilized in the previous fits. The important effect referred to in the text is the relative enhancement of the 200 intensity by the presence of octahedral cations.

good fits to the 200, however little improvement was obtained for the high angle lines. In the x-ray case, the presence of octahedrally coordinated cations was found to have the effect of increasing the 200 intensity in all cases, particularly for the non-Mn (Ag, Ga) occupying the octahedral sites.

On the basis of the nd 200 intensity, it thus seems that a mixture of octahedral and tetrahedral Mn would be required to explain the data within a crystal structure based on the fcc close-packed anion sublattice. It is possible that together with the correct displacement parameters such a model could completely explain the data, however the resolution of this problem would either require detailed single crystal measurements, or possibly a joint refinement of x-ray and neutron powder data, and cannot be expected to be resolved from the powder diffractometer data obtained in this research.

It is thus concluded on the basis of the diffraction intensities that the $(AgGa)_{1-z}Mn_{2z}Te_2$ alloys are not simple chalcopyrite structure. Rather it seems that their crystal structure is closely related to that of chalcopyrite yet possibly involves the occupation of octahedrally anion-coordinated cation sites. This implies a breakdown in the simple interpretation of the tetrahedral bonding in these materials, and must be expected to have important implications in their ESR and magnetic behaviour.

The possibility of such changes in the structure and hence modification of the the simple tetrahedral bonding picture is shown by the series $CuFeS_2$, $CuFeSe_2$, and $CuFeTe_2$. $CuFeS_2$ is chalcopyrite structure while $CuFeSe_2$ (eskebornite) has one in

four cations transferred to different tetrahedral sites, thus upsetting the simple tetrahedral bonding picture. In the case of $CuFeTe_2$, 2 of each 4 cations in the conventional unit cell are transfered to other tetrahedral sites and the structure shows a much more obvious planar form [70b].

It is of interest to note that the ionicity of the bonds and the ionic sizes are important factors in determining the characteristics of the bonding. A series of binary structures which illustrate the range of behaviour are NaCl (octahedral coordination, 6 near-neighbours), CsCl (cubic coordination, 8 near-neighbours) and ZnS (tetrahedral, 4 near-neighbours). Another relevant example is found in the case of the ferrites, which are covalently bonded materials with mixed octahedral and tetrahedral stereochemistry. Also, the DMS system $Cd_{1-z}Mn_zSe$ exhibits both tetrahedral (ch) and octahedrally coordinated (NaCl) structures [123].

4.4.4) Summary

It is clear that some form of Mn-ordering is required by the absence of the random-Mn magnetic susceptibility signature T_c(disordered). The obvious model to be tried was the chalcopyrite-stannite based random planar Mn-ordered model, however the analysis is complicated by the presence of cubic phase in the samples. In the present analysis, the inclusion of displacements of anions and cations from their ideal sites, as would be expected from the values for chalcopyrite and stannite structures, causes relatively small changes in the overall fit to the experimental data. These experimental

values, particularly for the 200 reflection, indicate that the actual structure may be closely related to the chalcopyrite case, but with some cations occupying octahedrally coordinated rather than tetrahedrally coordinated sites. However from the considerations indicated above, it would be still be expected that randomly spaced Mn planes occur in this structure.

For the reasons summarized in section 4.3, the occurence of some type of planar Mn-ordered structure remains a strong probability. One of the most attractive features of a planar Mn-ordering scheme which incorporates randomness in the planar distribution, is that it provides for the absence of new (non-ch) ordering lines on the x-ray and neutron diffraction patterns. In particular, the absence of stannite-like ordering lines is achieved by a random plane distribution despite the similarity such a configuration has with the stannite structure. The second attractive feature of the planar Mn-ordering, is the expected concentration independance of the resulting magnetic signature. This is particularly true given that the newly observed dominant magnetic susceptibility (63 K) feature of these LTA samples is concentration independent, and that the presence of significant amounts of magnetic impurities can be ruled out by the diffraction patterns themselves.

It is thus of interest to inquire as to how the magnetic measurements can be utilized to investigate the possible presence of Mn-planes within the actual crystal structure of the materials. This will be discussed further in section 4.6.

4.5) Magnetic susceptibility data analysis

4.5.1) Analysis of Susceptibility Data on LTA $(AgGa)_{1-z}Mn_{2z}Te_2$ Samples.

The fitting of the magnetic susceptibility data to a simple model based on Curie-Weiss behaviour was attempted for the representative LTA and slowly cooled $(AgGa)_{1-z}Mn_{2z}Te_2$ z=0.25 and z=0.33 materials whose experimental χ data will be shown in the following (figs.4.5.5), and for the z=0.40 susceptibility seen previously in fig.4.3.2. Some analysis was carried out also for the $(AgIn)_{1-z}Mn_{2z}Te_2$ sample 50SC shown in fig. 4.5.1. The basic properties of magnetic materials which motivate this study are summarized in section 2.4. The fitting is limited by a lack of knowledge about the detailed magnetic behaviour below the transition temperatures.

A two magnetic phase model was chosen because there are two distinct features in the susceptibility and ESR of these materials, and because various models and experimental results discussed previously could in principle provide such two-magnetic phase behaviour. In particular it is of interest to determine if the magnetic behaviour can be correlated with either the presence of the hypothesized planar-ordered Mn, or with the experimentally observed presence of cubic β phase.

Equation (4.5.1) represents two distinct magnetic contributions of the C-W form added to the temperature independent diamagnetism, and represents the model used in the fitting.

$$\chi = \frac{C_1}{T-\theta_1} + \frac{C_2}{T-\theta_2} + D \qquad (4.5.1)$$

Fig.4.5.1a Static susceptibilty vs. temperature for the slowly cooled $(AgIn)_{1-z}Mn_{2z}Te_2$ z=0.50.

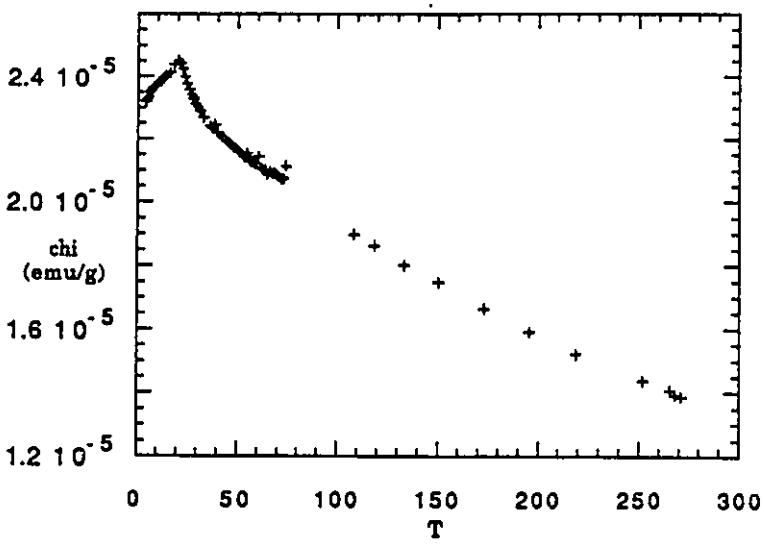

Fig.4.5.1b Inverse susceptibilty (1/chi) vs. temperature (T) for the slowly cooled $(AgIn)_{1-z}Mn_{2z}Te_2$ z=0.50.

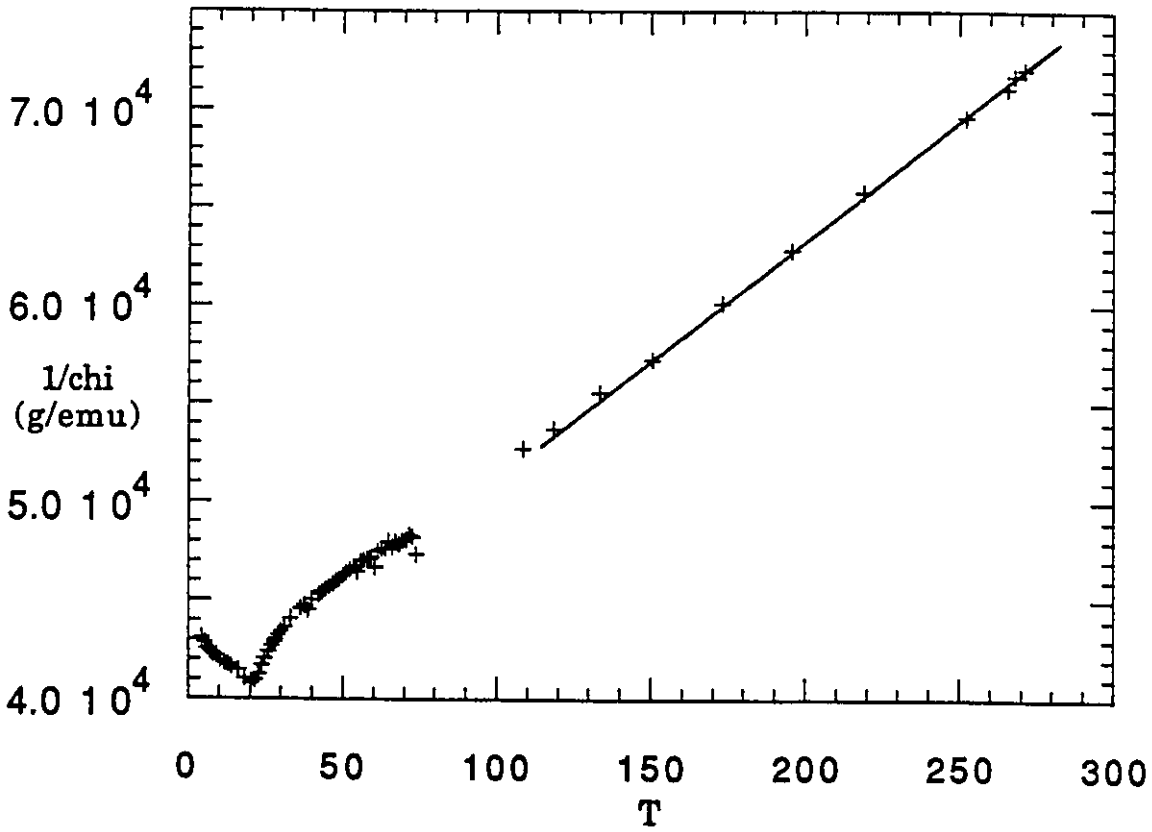

Figs. 4.5.1a, and b, illustrate the experimental susceptibility behaviour of the slowly cooled Ag-In z=0.50 material. The prominent susceptibility cusp is evident on both plots. On the inverse plot (4.5.1b), approximate Curie-Weiss behaviour can be seen. The theoretical C value for this material is 0.0104 K emu/g, while the apparent C taken from the slope of the linear portion of the inverse susceptibility renders C=0.0118 K emu/g.

The fitting was attempted only over the paramagnetic regime of the susceptibility since only over this range of temperatures is the form of the response known precisely.

The model involves the assumption of the independence of the two magnetic subsystems which is implied by the existence of the two distinct Curie Weiss θ values postulated in eq.4.5.1 above. This will be referred to in the future as the distinct θ assumption. Other cases in which a single homogenous material behaves as two distinct magnetic systems have been documented and this will be discussed later in this section.

As seen in equation (4.5.1), the fitting incorporates 3 independent parameters; θ_1, θ_2, and one of the C values. The other C value is constrained by the relation $C_1+C_2=C_t$ where C_t is derived from the total number of spins present in the sample.

One paramagnetic term represents spins which have a transition at low temperature. In the cases of the Ag-Ga samples with z=0.25 and z=0.33, the transition to which the spins of this subset belong, is below the lowest temperature measured (4 K), and in the case of the Ag-Ga z=0.40, the transition appears as the broad maximum at 7.5 K.

The second term corresponds to the spins which cause the drastic change in the behaviour of the susceptibility at 65 K seen in many of the LTA or slowly cooled chalcopyrites under investigation and mentioned in section 4.3[1].

D represents the effective temperature independent

[1]In the LTA Ag-Ga samples actual susceptibility cusps occur at 63 K.

contributions to the susceptibility. The diamagnetic contribution is due to both the sample chamber and the sample, and can be either positive or negative depending on the sample mass (see section 2.4). For the susceptibility results concerned in the fitting, the estimated value for D was $D=+(5\pm2)\times10^{-8}$emu/g. This value takes into account the positive diamagnetic effect ($3\pm1 \times10^{-7}$ emu/g) of the measuring chamber. Another effect which can lead to temperature independent paramagnetism known an Van-Vleck paramagnetism can also be incorporated in the factor D.

The fitting was accomplished using MINUIT with the fitting criterion being a minimum of the 'weighted least squares' (wls) function which is of the form:

$$wls=\sum_{data}\left[\frac{(\chi_e-\chi_t)}{w_e}\right]^2 \qquad (4.5.2)$$

where χ reprents the susceptibility, w the weighting factor, and the subscripts refer to experiment (e) and theory (t). The weighting factors factors w were alternatively chosen to be $w_e=\chi_e$ or pure numbers which related to the density of experimental points in the data. These factors could be used in order to ensure that the high temperature portions of the susceptibility were properly represented in the fitting.

Fitting was carried out using data from the highest temperature range of measurements above the 63 K cusp starting at 80 ± 10 K. Thus in the fitting is incorporated the assumption that the C-W behaviour corresponding to the highest transition sets in within 20 K above the 63 K peak. This assumption as well as the assumption that the two paramagnetic contributions to the susceptibility are distinct will be

considered critically in the following subsection.

The main questions which the susceptibility analysis is designed to answer are:

1) Is it possible, through the behaviour of the Curie-constants (C) to unambiguously assign the relative number of spins contributing to each feature in the susceptibility, and does this correspond to the relative amounts of cubic and tetragonal phases?.

2) What are the magnetic parameters associated with the various components of the susceptibility, and how can we account for the large θ/T_n ratio seen from the raw data?

3) What is the cause of the 8 K broad maximum seen in the z=0.40 AgGa materials, and similar features seen in the low-temperature phases of the other materials?

4) How much can be said about the crystal structure of the material based on the magnetic behaviour?

The fitting of the susceptibility to Curie-Weiss (C-W) behaviour over the high temperature (above all T_c's) range of the susceptibility curves is justified by the fact that the observed values of the Curie constants are close to the expected values for these materials. The expected values are easily calculated according to equation (4.5.3):

$$C = g^2\mu_B^2\frac{J(J+1)}{3k_B} \text{ emu K per spin} \qquad (4.5.3)$$

The theoretical and experimental C values for the Ag-Ga alloys are tabulated in table 4.5.1, the C-values for the other alloys of interest have been shown previously in table 4.3.1. The experimental values are the apparent C values taken directly from the slopes of the χ^{-1} data. The estimated

TABLE 4.5.1

Apparent Curie-Weiss constants from inverse susceptibility for $(AgGa)_{1-z}Mn_{2z}Te_2$

Composition $(AgGa)_{1-z}Mn_{2z}Te_2$	Expected C (emu K/g) x10^{-3}	Sample Name & max. T (K)	Apparent C (emu K/g)x10^{-3}
z=0.25	5.26	CR25B 120	4.3 ± 2.0
		CR25A 200	6.3 ± 0.1
		CR25D 120	5.6 ± 0.4
		CR25F 120	5.4 ± 0.5
		CR25C 200	5.2 ± 0.4
z=0.33	7.06	CR33D 120	8.5 ± 0.4
		CR33E 125	11.4 ±1.0
		CR33F 125	7.7 ± 0.5
		CR33A 200	7.7 ± 0.5
		CR33G 150	9.5 ± 0.1
		CR33C 200	7.99 ± 0.05
z=0.40	8.61	CR40G 170	7.1 ± 0.2
		CR40E 150	8.8 ± 0.7
		CR40C 200	9.8 ± 0.2
		CR40D 200	9.5 ± 0.1
		CR40A 250	8.82 ± 0.05

Table 4.5.1 shows the apparent Curie constants (C) for the Ag-Ga samples studied. The data for the Ag-In and Cu-In systems was presented in section 4.3 (table 4.3.1a, 4.3.1b). The apparent C values are those obtained from the raw data with no diamagnetic correction. Errors quoted are estimated self consistently from the measured errors in the slopes of the inverse susceptibility. The expected C values are those calculated according to equation (2.4.3). Also shown are the maximum temperatures achieved during the sample measurement.

errors on the experimental C values are obtained from the errors in these experimental slopes, and vary widely due to the variation in the number of data points available for each sample and the quality of the measurements. The number of data points in the linear inverse susceptibility regime is roughly proportional to the highest temperature measured, a typical measurement has an interval of 10 K between data points in the temperature range from 80 K to 200 K. Discrepancies between the theoretical Curie constants and the experimental ones could be caused by any combination of the 5 effects discussed in section 2.4, which also apply to the θ parameter.

4.5.2) Assumptions

In this subsection, the assumptions under which the fitting are carried out will be considered, this elucidates the possible shortcomings of the procedure.

In order to further assess the importance of possible non-C-W behaviour, it should first be stated that the occurence of C-W behaviour in various DMS has been documented. In particular, for the previous work carried out on the Ag-Ga system, Curie-Weiss behaviour has been seen as evidenced by the presence of linear inverse susceptibility showing excellent correspondence to the expected Curie constant [101]. From the theoretical viewpoint care must be exercised because although mean field theory predicts that C-W behaviour should occur within mK of T_n in fields of the order of 1.0×10^{-2}T or

less[2] [59], it is found especially in high concentration DMS materials, that a measurable range of temperatures exists above T_n over which non C-W behaviour occurs. This is seen in both spin-glass, and antiferromagnetic materials. Of most significance for the present, is the behaviour seen in the other chalcopyrite DMS (Ag-In and Cu-In systems) also under investigation in this thesis. In the z=0.50 compositions of both of these systems, the range of non C-W behaviour seems to extend approximately 20 K to 30 K above T_n. In these cases, the non C-W regime is manifested by a curvature in the $1/\chi$ plots, while the C-W regime occurs as linear behaviour of the inverse susceptibility which exhibits correspondance to the expected Curie constant. Fig 4.5.1 shows a plot of the LTA $(AgIn)_{1-z}Mn_{2z}Te_2$ which has this feature. These data have been reproduced many times by measurements on different ingots of the same composition and are characteristic of the behaviour of the other (LTA) compositions as well.

Not all systems are this well-behaved however and other zincblende and chalcopyrite DMS, particularly spin- glasses, have strongly concentration-dependent non C-W regimes, extending from 10 K to 150 K above T_n [85] [124]. Considering that spin-glass materials are known to have large ranges of non C-W behaviour as compared to antiferromagnets, it seems a safe practice to carry out the assumption that C-W behaviour sets in about 20 K above the transition temperature as long as

[2]This is due to the fact that the C-W behaviour occurs as an asymptotic (small argument) expansion of the Brillouin function, which expansion is valid as soon as the large effective molecular field (order 10^2T) collapses at T_n.

the criterion of linear inverse suceptibility with good corresponding C values is satisfied. Stated differently, as long as the discrepancy in the measured and theoretical C values can be explained by the other effects listed in section 2.4, the occurrence of C-W behaviour in the temperature region above the highest transition remains a viable possibility. It is difficult to assess the validity of this assumption for the paramagnetic components of the susceptibility below the highest transition temperature, however this does not concern the present fitting procedure.

In order to consider the question of the independence of the separate magnetic sub-systems, note that the Curie-Weiss θ is, roughly speaking, a measure of the strength of the interactions between the member spins of a given magnetic system. In mean-field theory, θ is exactly proportional to the sum of the interaction strengths between the members of the magnetic system, thus distinct θ values would normally be taken to imply negligible interactions between the magnetic systems concerned. In view of this, it must be said that the possibility of independent θ within purported single phase materials seems unlikely. Such behaviour has however been documented [67], and in the particular case of Mn-formate dihydrate ($Mn(HCO_3)_2$ $2H_2O$) an antiferromagnetic layer structure occurs which has layers of paramagnetic ions between the antiferromagnetic ones [125]. In this case too, a two magnetic-phase model identical (less the diamagnetic term) to that in eq.4.5.1 was utilized in order to explain the magnetic behaviour of that material [126] [127].

In a mixed-magnet such as might be expected to occur in either the ch + cubic or in the planar Mn-ordered (order-disorder fraction) scenarios of present interest, it is possible that apparent θ values could represent the combined effect of the intra subsystem spin interactions and the inter subsystem spin interactions. This idea is motivated from the mft expression for θ which as indicated above, consists of a sum over all the interactions acting on an ion. Considering the crystallographically disordered fraction of magnetic ions within partially ordered structure as one system of interacting ions, it seems possible that the interactions between the disordered and ordered fractions could be considered (from the point of view of the disordered system) to simply enter into the summation leading to a θ for the disordered system which is different from that for the case in which there are no interactions between the ordered and disordered fractions. For example, concerning a hypothesized Mn-plane configuration, it is conceivable that a small fraction of disordered ions could behave paramagnetically even if they were not well isolated from other spins by virtue of the high frustration (small resultant interaction) acting upon them. Presumably these disordered spins would have an apparent θ larger than that expected from considering them in isolation. In such an environment, an applied external field would have a lesser effect on their average orientation and thus their susceptibility would be decreased as reflected in

the larger apparent[3] θ. The distinct θ assumption will be discussed further along these lines in the following section.

4.5.3) Results

Given that 3 free parameters are required in the fitting and that the data varies slowly as a function of temperature, it must be expected from the outset that a unique solution to the fitting is unlikely. Stated differently, the possibility that the wls function has several local minima must be taken into account. Luckily there exist some criteria which can be used to distinguish physically acceptable solutions from unrealistic solutions. For example, solutions with large θ values can be excluded if the magnitudes of the corresponding θ/T_n are unphysical (see section 2.4). Solutions with $\theta_1=\theta_2$, are also considered unphysical by virtue of the common[4] θ.

Some of the behaviour of the fitting parameters can be derived analyticaly and facilitates the interpretation of the fits. Recall that of all the possible combinations of parameters, we are concerned only with those that lead to linear χ^{-1}vs. T plots. Carrying out a polynomial division of the function (4.5.1) leads to a term linear in T^{-1} which is itself a function only of the C's and the products Dxθ. This suggests how even a small D can make a measurable effect on

[3]This suggests a possible signature for the distinct θ mechanism in the presence of non-negligible inter-subsystem interactions to be apparent θ values which depend on the external field.

[4]A coincidence of the θ values is still surprising even in view of the distinct θ assumption because as will be shown, the equality of the θ values implies that two summations with unrelated terms have the same outcome.

the apparent C and θ values when θ is large, as illustrated previously on fig 2.4.2. Also note from the relation (4.5.1) that each solution has a counterpart solution with C_1 and θ_1 interchanged for C_2 and θ_2. This symmetry of the solutions in the paramagnetic regime indicates that it is impossible to unambiguously assign a given C and θ to any particular T_n unless the resulting θ values are such that the criterion of θ/T_n could become the distinguishing factor.

Another class of minima in the wls can result if the two θ values are different but large enough to lead to approximately straight line behaviour over the limited range of measuring temperatures. Clearly, D could again affect these types of fits through the nonlinear terms involving D$\times\theta$'s mentioned above (see also section 2.4).

The case in which the diamagnetism is neglected in the fitting (D=0) is instructive due in part to the drastically different behaviour with respect to small changes in the total C (C_t). In the case $C_t=C_T$ where C_T is the theoretical C value (bounded by the expected range due to error in mass measurement), only fits with equal θ were found. For the case D=0 and $C_t=C_{app}$ where C_{app} is the apparent C taken from the table 4.2, any ratio of C values could be fit equally well without equal θ. This is due to the large value of the apparent θ which allows for fits with large but different θ's over the small range of temperature corresponding to the experiments, and the absence of any non-linearity due to D. This indicates how paradoxically, it is the presence of the small diamagnetic 'correction' which allows us to distinguish

between the fits at all.

It was found that using the expected value of the diamagnetic correction D = $\chi_{D(eff)}$ = $-5x10^{-8}$ emu/g, fits with significant ratios of C values (both non-negligible) did not exist as minima in the wls. The best fits were found to occur with D positive and an order of magnitude higher than that expected in the experimental setup. These fits also admit both C values to be non-negligible which is consistent with the low temperature susceptibility. All the best fits can be grouped into two classes; those with relatively high C_2 and those with low C_2. All the fits with high C_2 find similar θ_2 values of approx. -600 K and θ_1 of the order -2 K. These fits allow for one of the θ's to be relatively small and thus to be associated with the T_{n1} low-temperature transition. For this reason the high C_2 solutions are taken as the most likely scenarios. The ratios of the C values in these fits are not precise enough to be definitively associated with the ratios of cubic to tetragonal phases in the samples. Interpreting the cubic phase as the origin of the C_1 term in the magnetic response would be difficult to understand due to the absence of T_c's which are characteristic of such phases. It is possible that the situation is one in which the magnetic correlation length is larger than the crystallographic one i.e. in which the inter Mn-relationships responsible for the C_2 part of the magnetic response are maintained within the cubic-tetragonal crystal mixture. In this case, the parameters C_2 and θ_2 must be considered as representative of the ordered (planar) Mn fraction whereas $C_1$and θ_1 would be

associated with the disordered, (inter-planar) Mn. From the phase diagram data and the previous results reported for the Ag-Ga system, one would not expect significant amounts of planar ordering in the β phase, however pseudo-stannite behaviour (partially filled planes) may be expected to occur.

Two suggested explanations for the large D are; 1) the presence of residual non-C-W behaviour, and 2) presence of second order (Van-Vleck) paramagnetism in one of the components of the susceptibility. Indeed the equation $\chi=C/T + \alpha$, with α being a temperature independant term, is known as the Langevin Debye equation for the case when α represents the Van-Vleck paramagnetism. The possibility of octahedral Mn discussed in the diffraction fitting, introduces the possibility of large O_h crystal field splittings which could lower the otherwise far removed excited states enough to increase the importance of the Van-Vleck term, however the measured D value appears considerably larger than expected.

Other possibile explanations for the large apparent D are also worth mentioning. A small amount of ferromagnetic impurity could have a susceptibility which would mimic the observed temperature independant D value. Only 100 micrograms of ferromagnetic spin 5/2 Mn or Fe impurity oriented in the measuring field would contribute $+10^{-6}$emu. As indicated in chpt. 2, the purity of the commercially available Mn is rather low and indeed Fe is one of the impurities listed in the Mn assay. The possibility of amorphous Heusler alloy impurity phases was excluded in section 4.3 as a cause for the 63 K peak, however small amounts of the ferromagnetic crystalline

forms of these alloys could contribute to the effective D.

In summary, the magnetic analysis suggests that the high temperature transition is associated with the majority (C_2, ordered) Mn for two reasons; 1) the resulting minority (C_1, disordered) Mn concentrations then lead to the low T_{n1} transition temperatures which are consistent with the random 3-dimensional alloys, and 2) the most reasonable values of θ/T_n are achieved in this case, especially the value of θ_1/T_{n1}. The fitting seems to indicate a large positive (effective D) contribution which cannot be accounted for in the apparatus. Using this value of D, the most reasonable θ values are obtained as are two non-negligible C values consistent with the low temperature magnetic behaviour. Without the large positive effective D, the fitting procedure leads to no useful distinctions regarding the questions stated at the beginning of this chapter and therefore need not be considered further. Indeed the necessity of treating D as a variable parameter greatly complicates the fitting procedure and the reliability of the results so obtained.

Plots of fits representative of the large D condition are given in figs 4.5.2a to 4.5.2d. Both the χ and χ^{-1} plots are shown. Note that it is easier to see discrepancies in the fits on the inverse susceptibility plots. This is because of the wide range in the magnitude of the measurements and small magnitude of the susceptibility at high temperature.

4.5.4) Simulations

The preceding analysis was called a fitting because real

Fig. 4.5.2a Fit to susceptibility (chi) vs. temperature (T) for $(AgGa)_{1-z}Mn_{2z}Te_2$ z=0.25

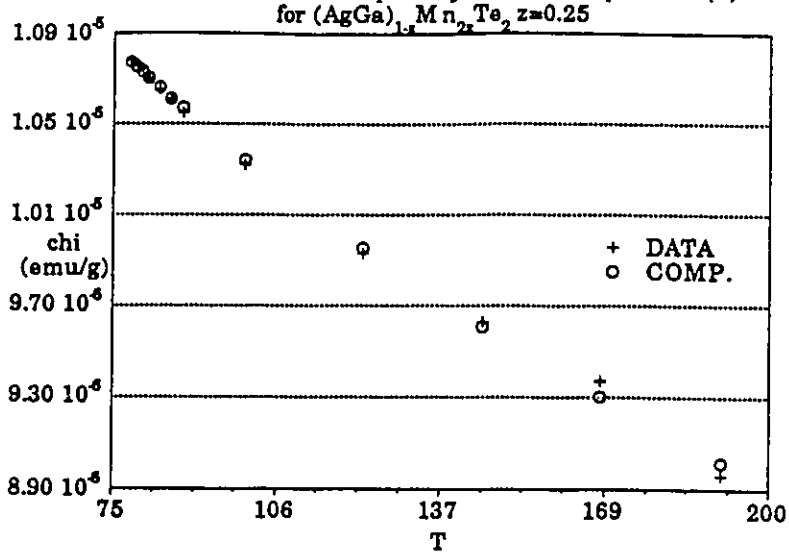

Fig. 4.5.2b Inverse susceptibility (1/chi) vs. temperature (T) (data and fit) for $(AgGa)_{1-z}Mn_{2z}Te_2$ z=0.25

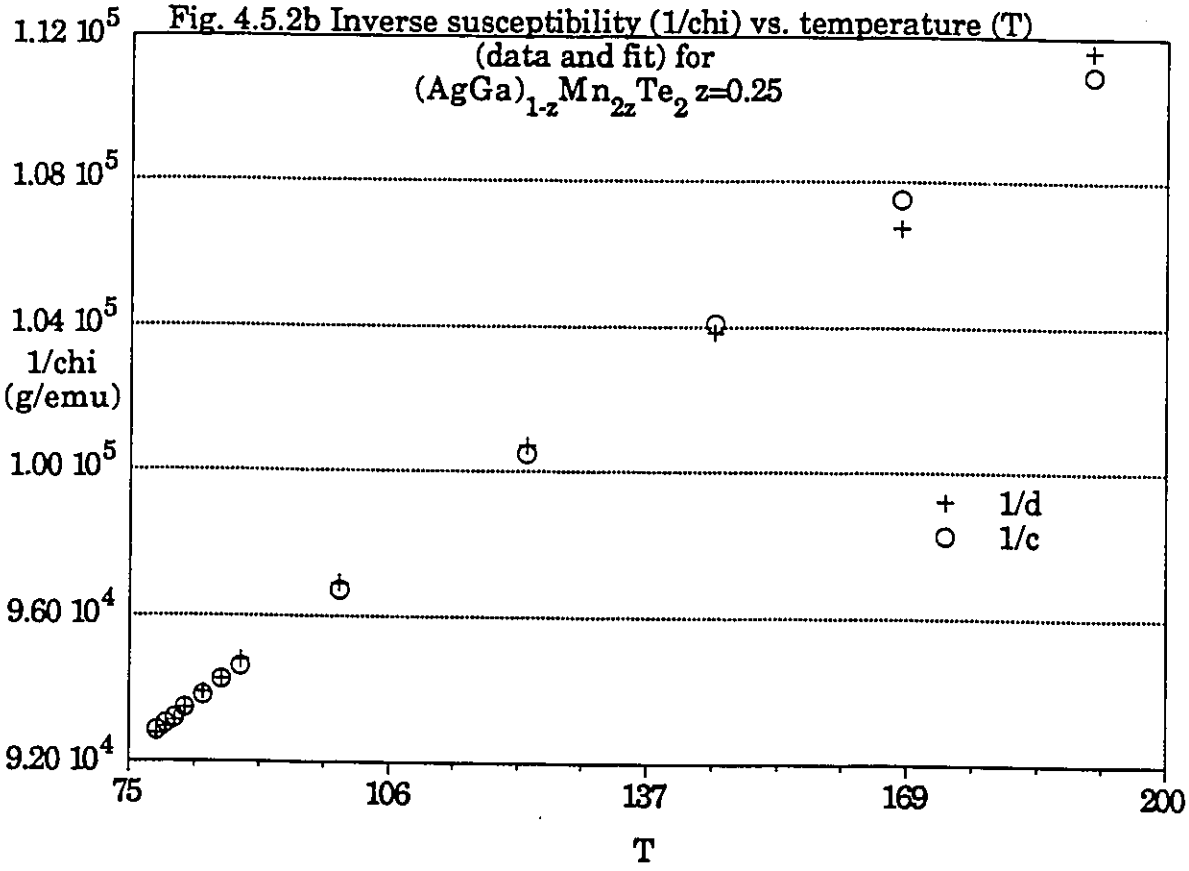

Figs. 4.5.2a, and b, give the fits to the $(AgGa)_{1-z}Mn_{2z}Te_2$ z=0.25 susceptibility data as described in the text. Since it is easier to see discrepancies between the data and the fit in the inverse susceptibility plots, only inverse plots are given in the cases of the z=0.33 (fig. 4.5.2c) and z=0.40 (fig. 4.5.2d). The parameters obtained from the fits are given in the summary section (4.5.7) in the text.

Fig.4.5.2c Fit to inverse susceptibility (1/chi) vs. temperature (T) for $(AgGa)_{1-z}Mn_{2z}Te_2$ z=0.33

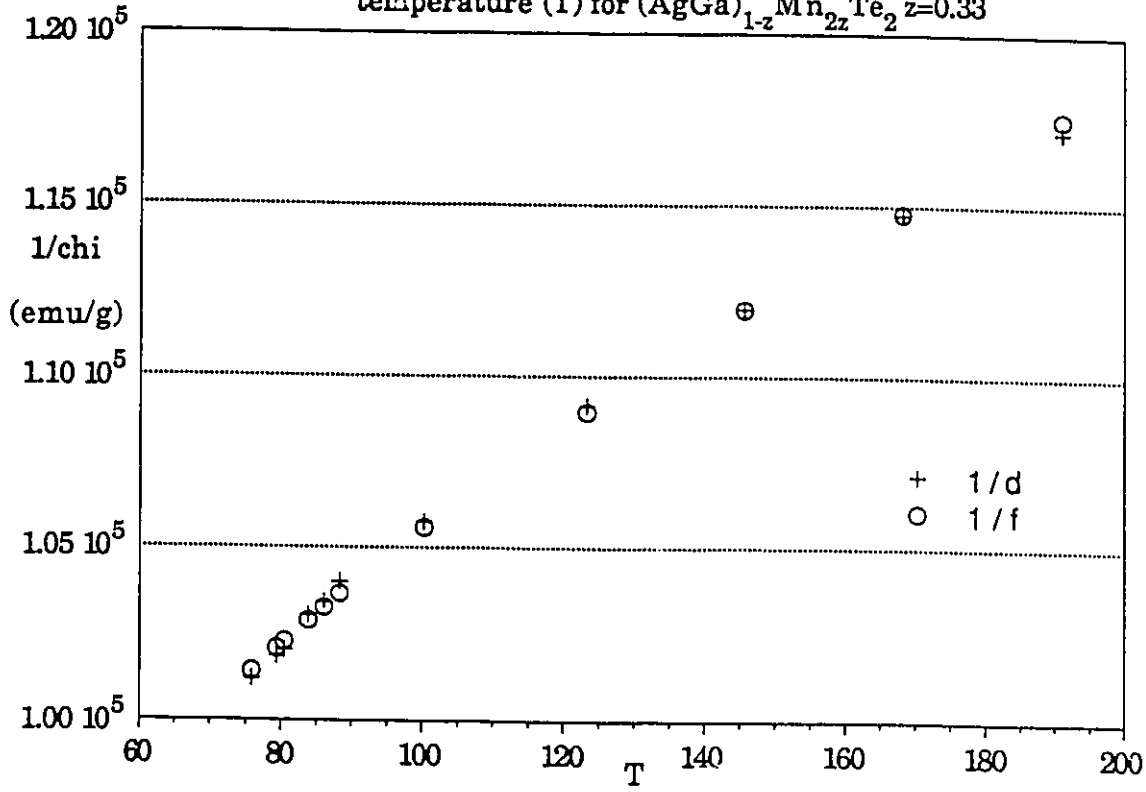

Fig. 4.5.2c illustrates the fit to the $(AgGa)_{1-z}Mn_{2z}Te_2$ z=0.33 susceptibility data as described in the text. The data points are represented as crosses (1/d), and the fit points as circles (1/f). The slight concave-down bowing of the inverse susceptibility is predominantly due to the effect of the large temperature independant susceptibility (D).

Fig.4.5.2d Fit to inverse susceptibility (1/chi) vs. temperature (T) for $(AgGa)_{1-z}Mn_{2z}Te_2$ z=0.40

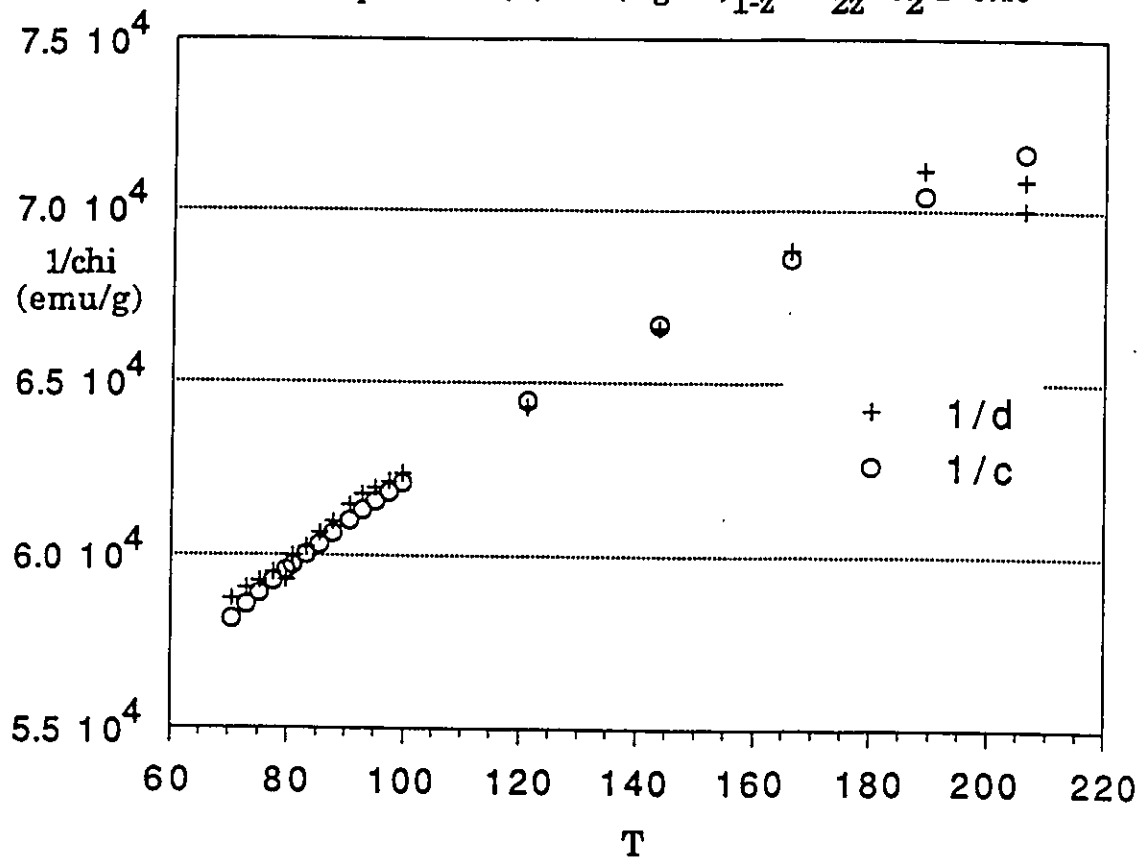

Fig. 4.5.2d illustrates the fit to the $(AgGa)_{1-z}Mn_{2z}Te_2$ z=0.40 susceptibility data as described in the text. The data points are represented as crosses (1/d), and the fit points as circles (1/f). The slight concave-down bowing of the inverse susceptibility is predominantly due to the effect of the large temperature independant susceptibility (D).

parameters C, D and θ were the expected outcome. The following simulations instead yield only the qualitative features of the susceptibility curves and are not expected to lead to real output parameters. One can thus ask if the qualitative features of the whole susceptibility curve can be simulated within the scenarios obtained from the fits. To this end, a simple model for the susceptibility consisting of the following function was employed.

$$\chi = \frac{1}{3}\left(\frac{C}{T_n-\theta}\right)X\left(2 + \frac{T}{T_n}\right) \quad \text{for T less than } T_n \qquad (4.5.5)$$

$$\chi = \frac{C}{T-\theta} \quad \text{for T greater than } T_n$$

The function is graphed in fig. 4.5.3. In the region of temperatures below the peak, the function is intended to mimic the response of an anisotropic powdered antiferromagnetic. Indeed peaks qualitatively of this type have been seen in various DMS including in the high temperature phases of the CuIn and AgIn materials under investigation.

In order to proceed with the simulations, the importance of the equilibrium nature of the susceptibility measurements must be mentioned. Field-cooled (fc) measurements are closer to equilibrium than zero field cooled (zfc) measurements since zfc magnetic response is expected to be strongly dependent on 'frozen-in' domain structure. Figs.4.5.4 show representative susceptibility measurements of both these types of measurements. In these figures can be seen the qualitative effect of the field-cooling which is to hide or smooth-out the 63 K peak. Also it can be seen from the smallness of the difference in the value of the two measurements that the zfc

Fig.4.5.3 Magnetic response function illustrated for various theta values.

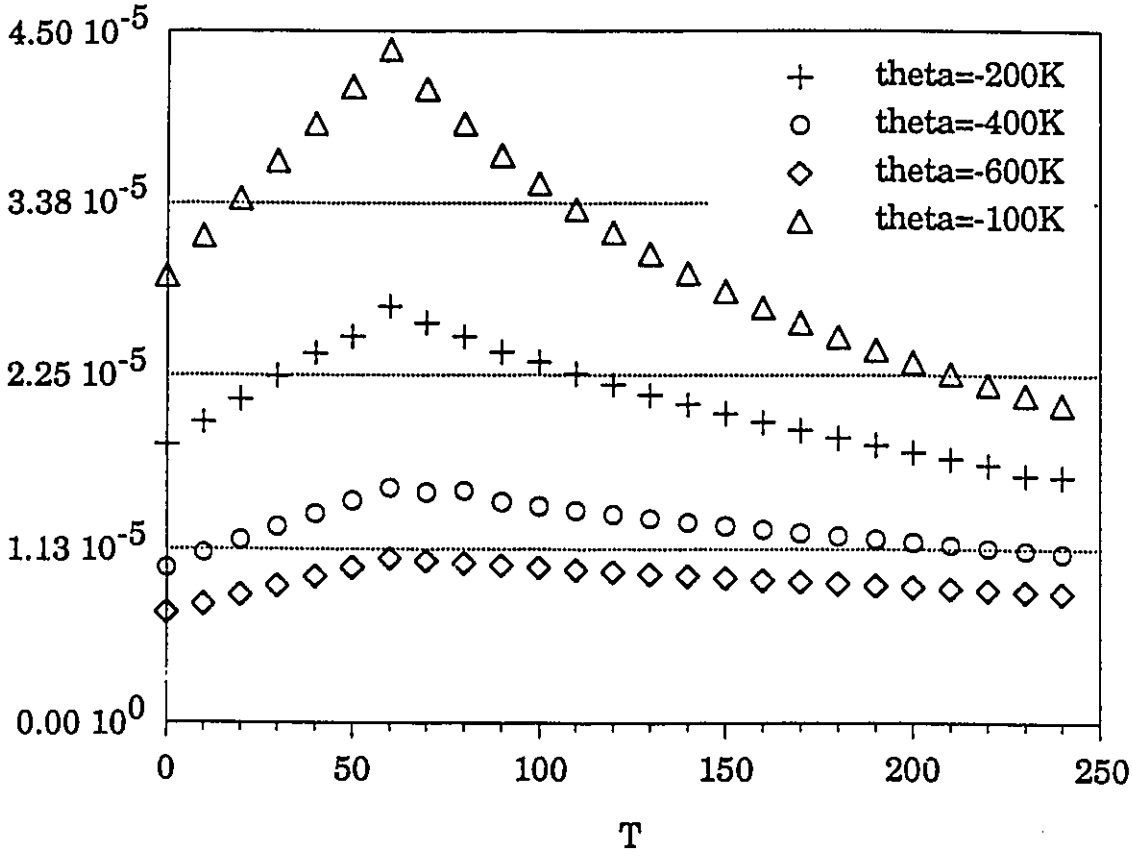

Fig. 4.5.3 illustrates the form of the susceptibility function utilized in the simulations of the magnetic data over the full range of temperatures measured. The effect of the larger theta values can be seen to lead to an overall flatening of the response. All the curves shown, utilize representative values of $C=7.0\times10^{-3}$ and $T_c=60$ K. The similarity of this response with the experimental susceptibility curve for the $(AgIn)_{1-z}Mn_{2z}Te_2$ (fig. 4.5.1) can be seen.

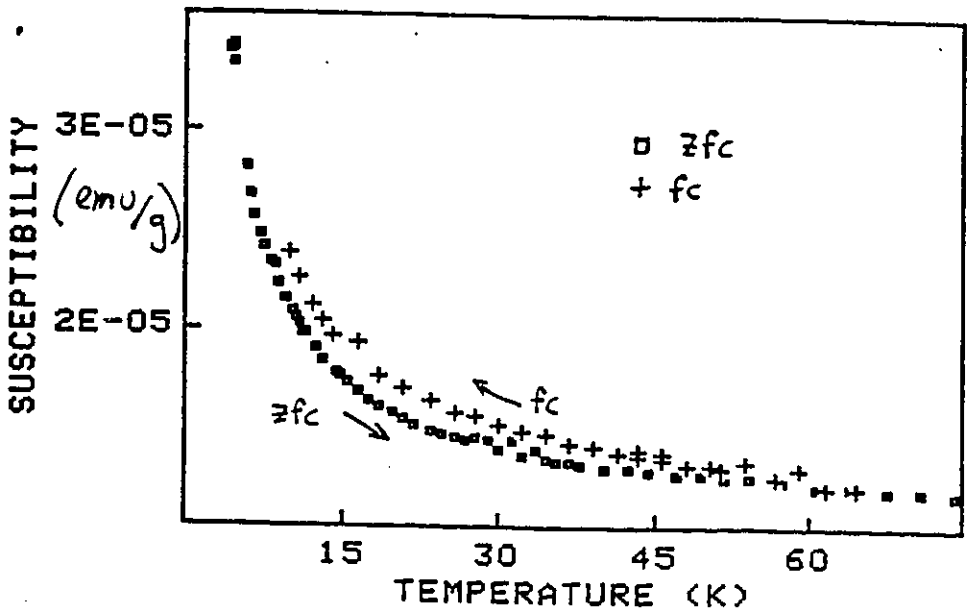

Fig. 4.5.4 Field-cooled (fc) and zero-field-cooled (zfc) susceptibility. This figure illustrates the experimental static susceptibility curve for the $(AgGa)_{1-z}Mn_{2z}Te_2$ z=0.33 material, showing both the fc and zfc curves. The lack of significant temperature-induced hysteresis suggests that the measurements represent close to equilibrium conditions.

measurements are in fact close to equilibrium. This means that the simulations originally intended to qualitatively reproduce the zfc (non equilibrium) data might reproduce the qualitative features of the equilibrium (fc) susceptibility as well. It is important to note that because the measurements are reproducible, the triangular susceptibility function does not necessarily have to represent equilibrium conditions. The function is intended simply to provide an empirical representation for the magnetic response as recorded by the experimental settup. Indeed the shapes of cusps corresponding to low dimensional transitions (for example the 2-D Ising model) tend to be sharper than the function in eq.4.2, as can be seen from the magnitude of their critical exponents [128].

The simulations were performed as if they were fits. However the intention in this case was only to qualitatively reproduce the data since the exact shape of the susceptibility is only expected to approximate the actual susceptibility in the region from low temperature up to the region immediately surrounding the highest temperature cusp.

Some resulting simulations are shown in figs.4.5.5a to 4.5.5f. Except for the small region surrounding the 63 K cusp, the simulations can be seen to be consistent with the data. Figs.4.5.5g and h illustrate a typical example of an attempt to simulate the curves under the assumption that the 63 K peak harbours very few spins. The poor quality of the simimulation is particularly evident in the inverse susceptibility plot (4.5.5f).

The simulations thus illustrate that indeed the

Fig.4.5.5a Simulation of susceptibility (chi) vs. temperature (T) for $(AgGa)_{1-z}Mn_{2z}Te_2$ z=0.25

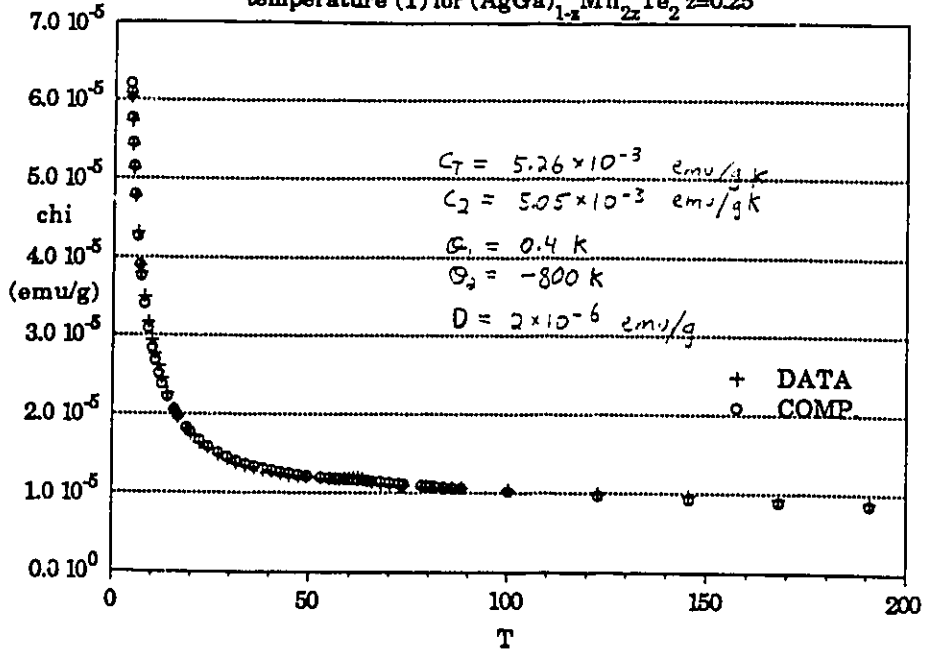

Fig.4.5.5b Inverse susceptibility (1/chi) vs. temperature (T) for $(AgGa)_{1-z}Mn_{2z}Te_2$ z=0.25 showing data (1/d), and simulation (1/c).

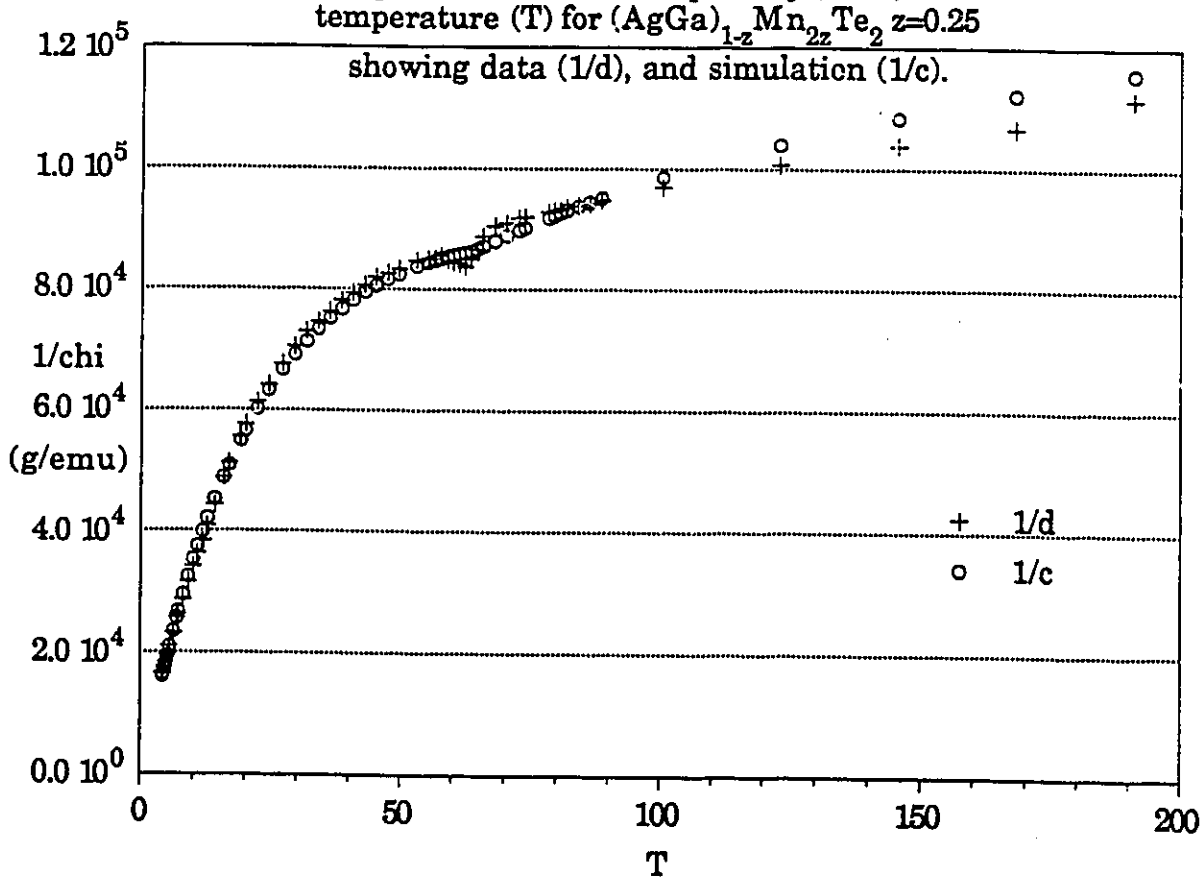

Figs. 4.5.5a, and b, illustrate the simulation of the experimental susceptibility data for the $(AgGa)_{1-z}Mn_{2z}Te_2$ z=0.25 sample over the full range of temperatures measured. The parameters obtained from these simulations are consistent with those of the fits shown previously.

Fig. 4.5.5c Simulation of susceptibility vs.temperature (T) for $(AgGa)_{1-z}Mn_{2z}Te_2$ z=0.33

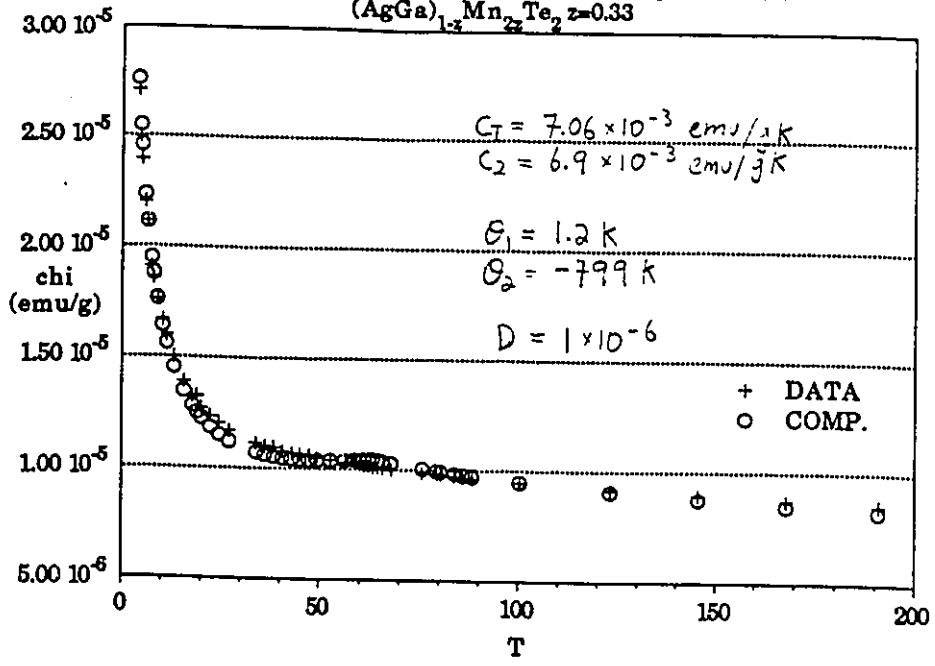

Fig.4.5.5d Inverse susceptibility simulation for $(AgGa)_{1-z}Mn_{2z}Te_2$ z=0.33

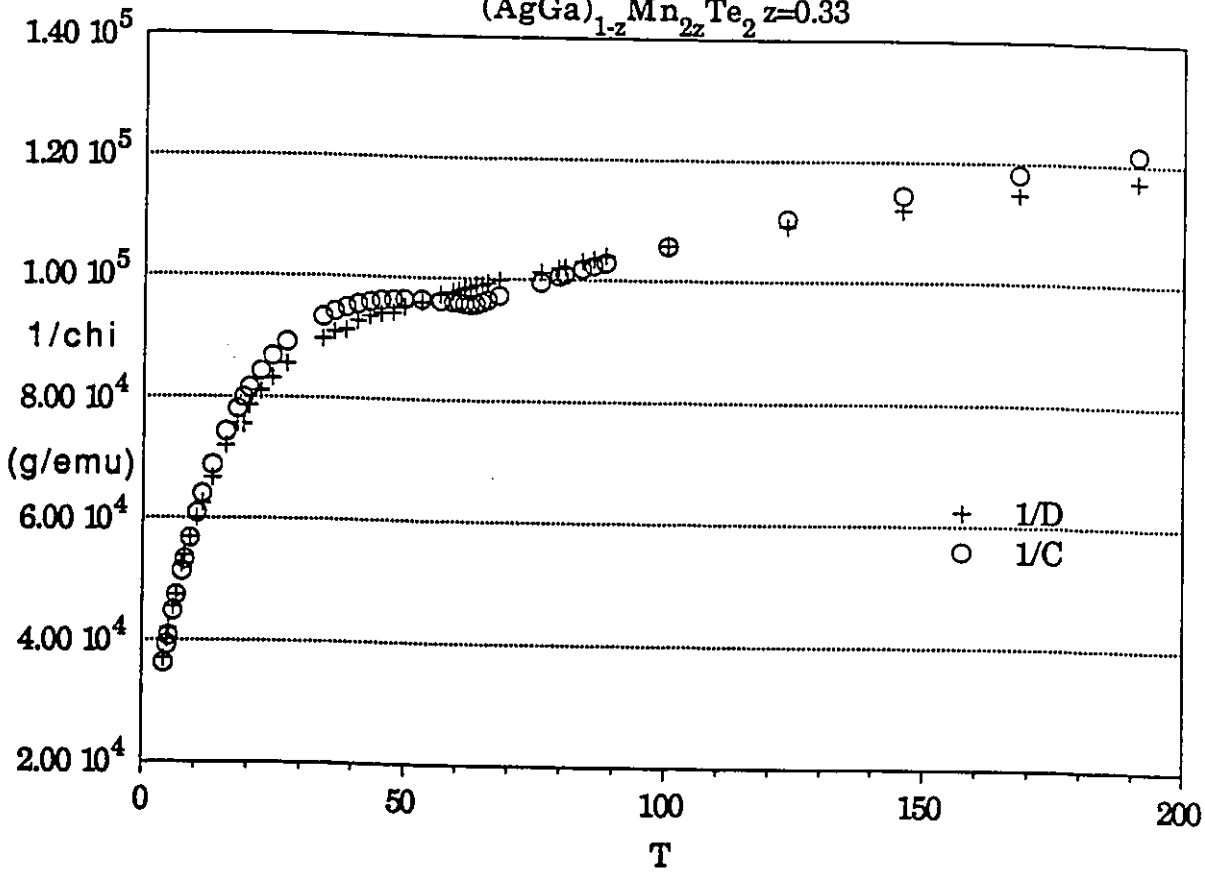

Figs. 4.5.5c, and d, illustrate the simulation of the experimental susceptibility data for the $(AgGa)_{1-z}Mn_{2z}Te_2$ z=0.33 sample over the full range of temperatures measured. The parameters obtained from these simulations are consistent with those of the fits shown previously.

Fig.4.5.5e Simulation of susceptibility (chi) vs. temperature (T) for $(AgGa)_{1-z}Mn_{2z}Te_2$ z=0.40

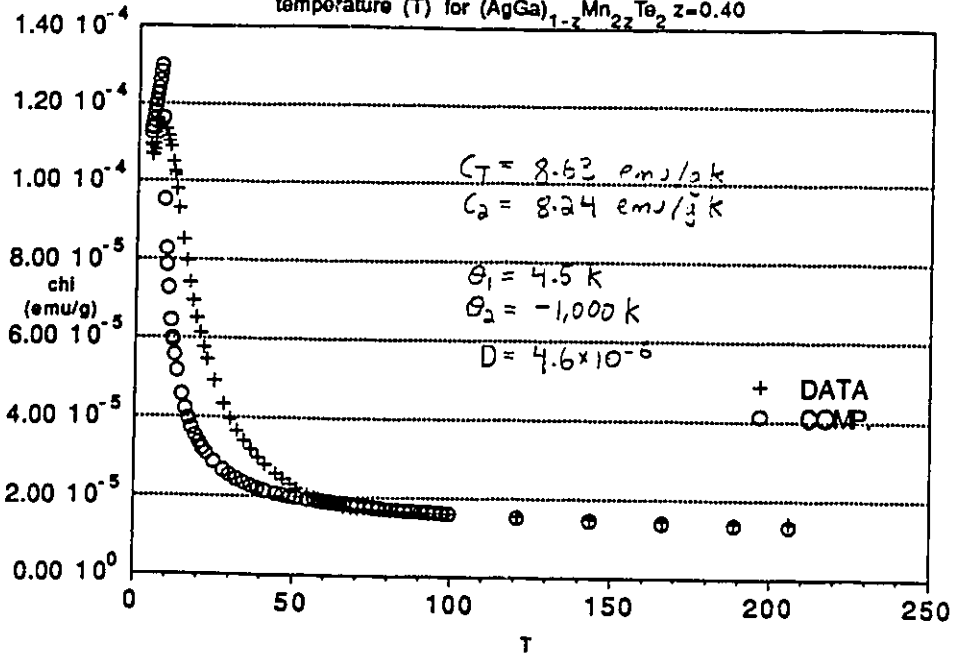

Fig.4.5.5f Simulation showing inverse susceptibility (1/chi) vs. temperature (T) for $(AgGa)_{1-z}Mn_{2z}Te_2$ z=0.40

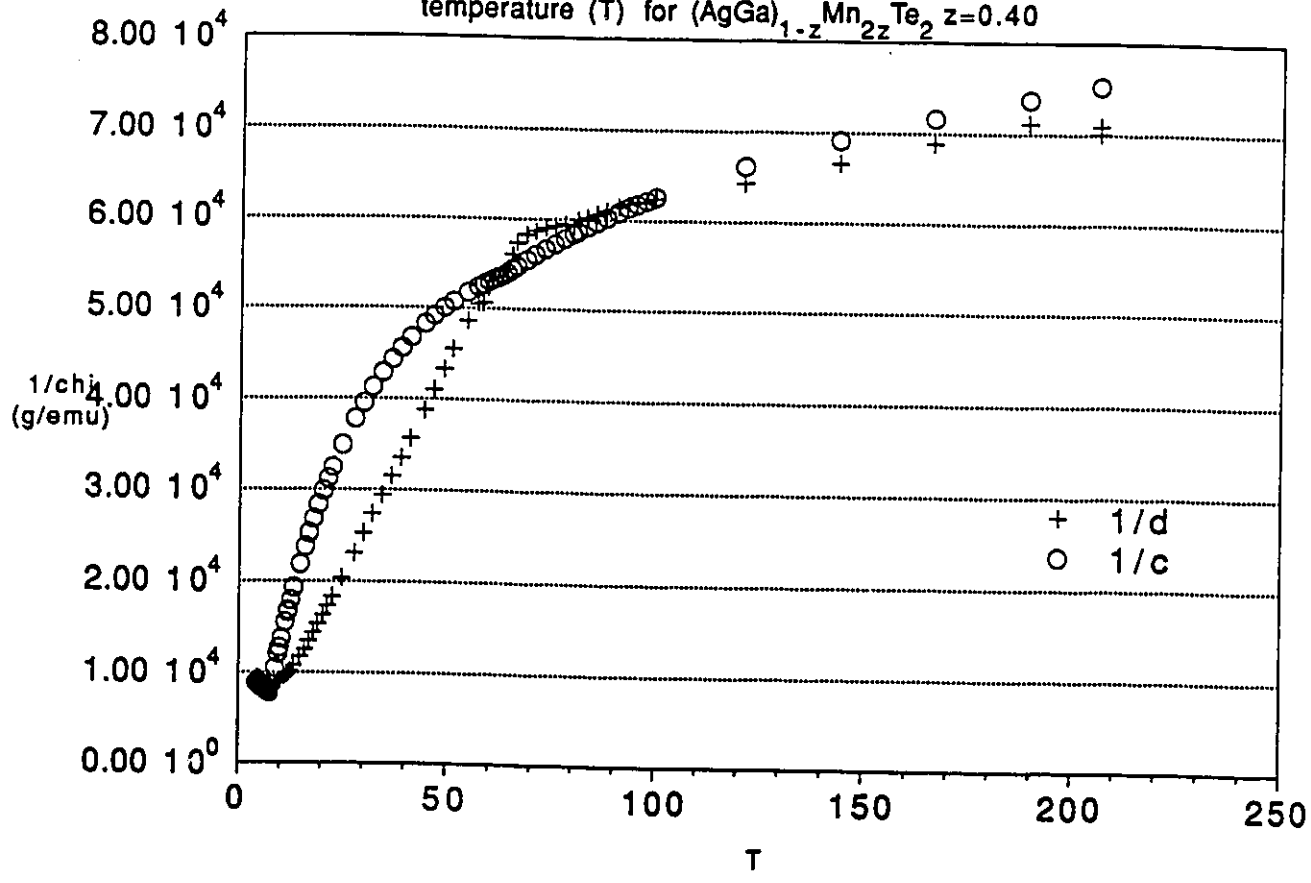

Figs. 4.5.5e, and f, illustrate the simulation of the experimental susceptibility data for the $(AgGa)_{1-z}Mn_{2z}Te_2$ z=0.40 sample over the full range of temperatures measured. The z=0.40 data does not lend itself to the simulation as easily as the data from the lower concentration materials.

Fig.4.5.5g Illustration of a poor simulation of $(AgGa)_{1-z}Mn_{2z}Te_2$ z=0.40 suceptibility (chi) vs temperature (T)

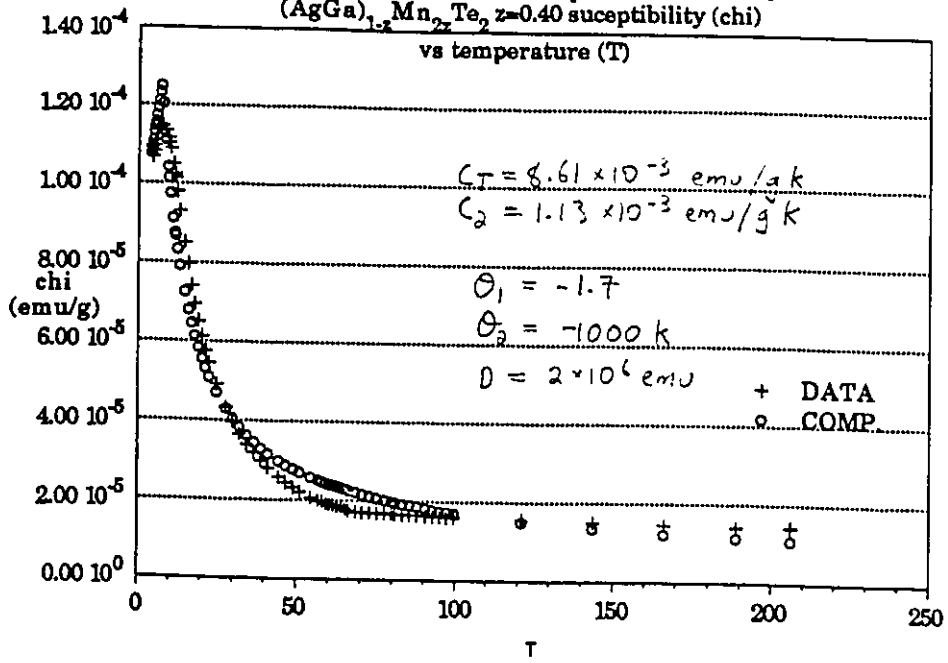

Fig.4.5.5h Illustration of a poor simulation of $(AgGa)_{1-z}Mn_{2z}Te_2$ z=0.40 inverse suceptibility (1/chi) vs temperature (T)

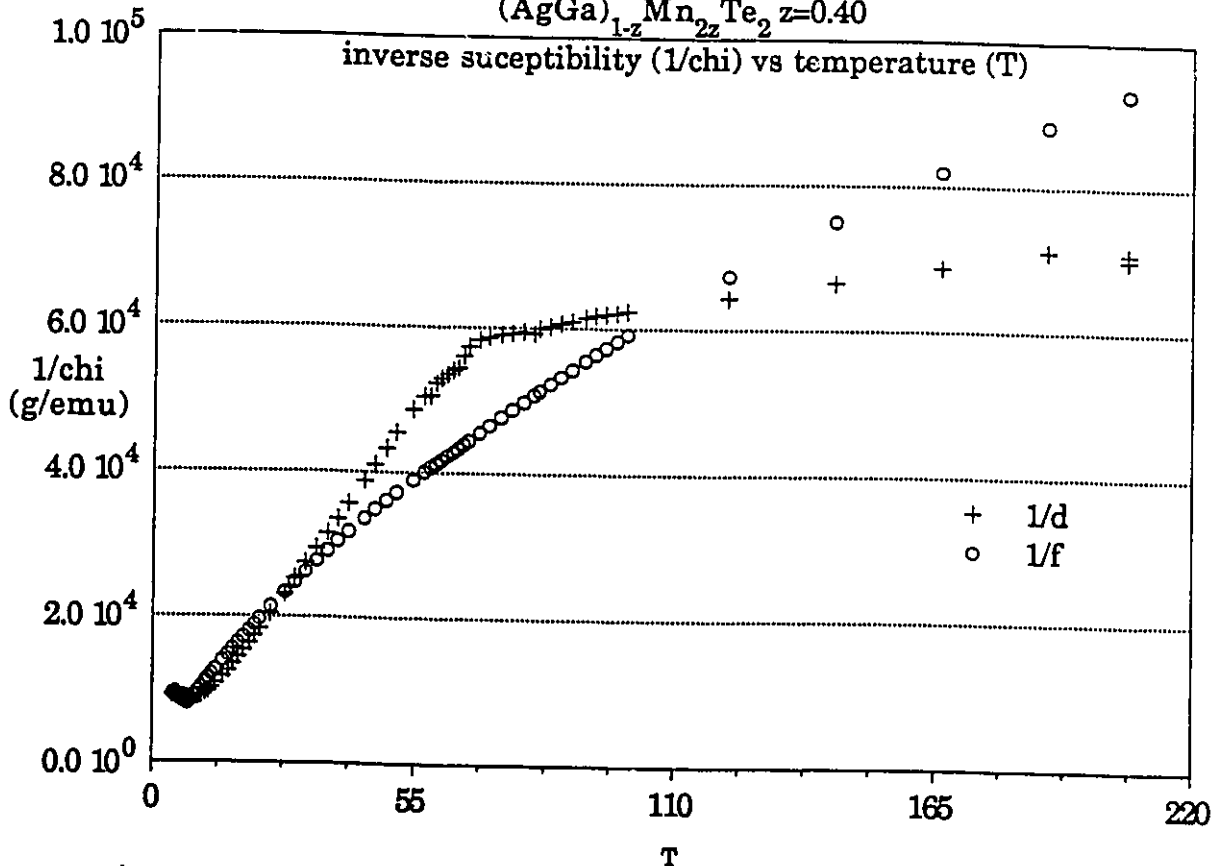

Figs. 4.5.5g, and h, illustrate a relatively poor simulation of the experimental susceptibility data for the $(AgGa)_{1-z}Mn_{2z}Te_2$ z=0.40 sample. This simulation incorporates the same response function utilized previously, however in this case, the majority of spins participate in the 8 K transition.

qualitative features of the susceptibility curves can be understood within the framework of majority C_2 (planar) spins and distinct θ, especially for the two lowest concentration materials, the poorest simulation being the z=0.40 sample. It would be misleading to believe that these simulations prove the correctness of the model since it is also conceivable that the poor quality of the low C_2 simulations could be due to non C-W behaviour in the temperature region above the low temperature (3 to 7.5 K) transitions. The simulations do seem to show that the simple model is applicable and this throws into the question the necessity of considering more complicated models.

A fit with the full susceptibility function (4.5.5) was also attempted with the available field-cooled data taken from a z=0.33 sample. The fit is illustrated in fig.4.5.6. This fit can be seen to be roughly consistent with the previous parameters found in the high temperature fits.

The discrepancy between the fit, and the simulated θ_1 values can be understood to be due to an inexact modelling of the susceptibility below the transition temperatures and close to the cusps. It is important to note that no similar simulations could be found for the z=0.40 sample in which, the assumption of isolated spin-systems may break down. At higher bulk, hence higher plane concentrations, the interplane Mn have less available sites to occupy and so lead to greater inter-plane Mn effective concentrations. In this case there would be expected to exist a critical value of the plane concentration at which the isolated systems assumption would

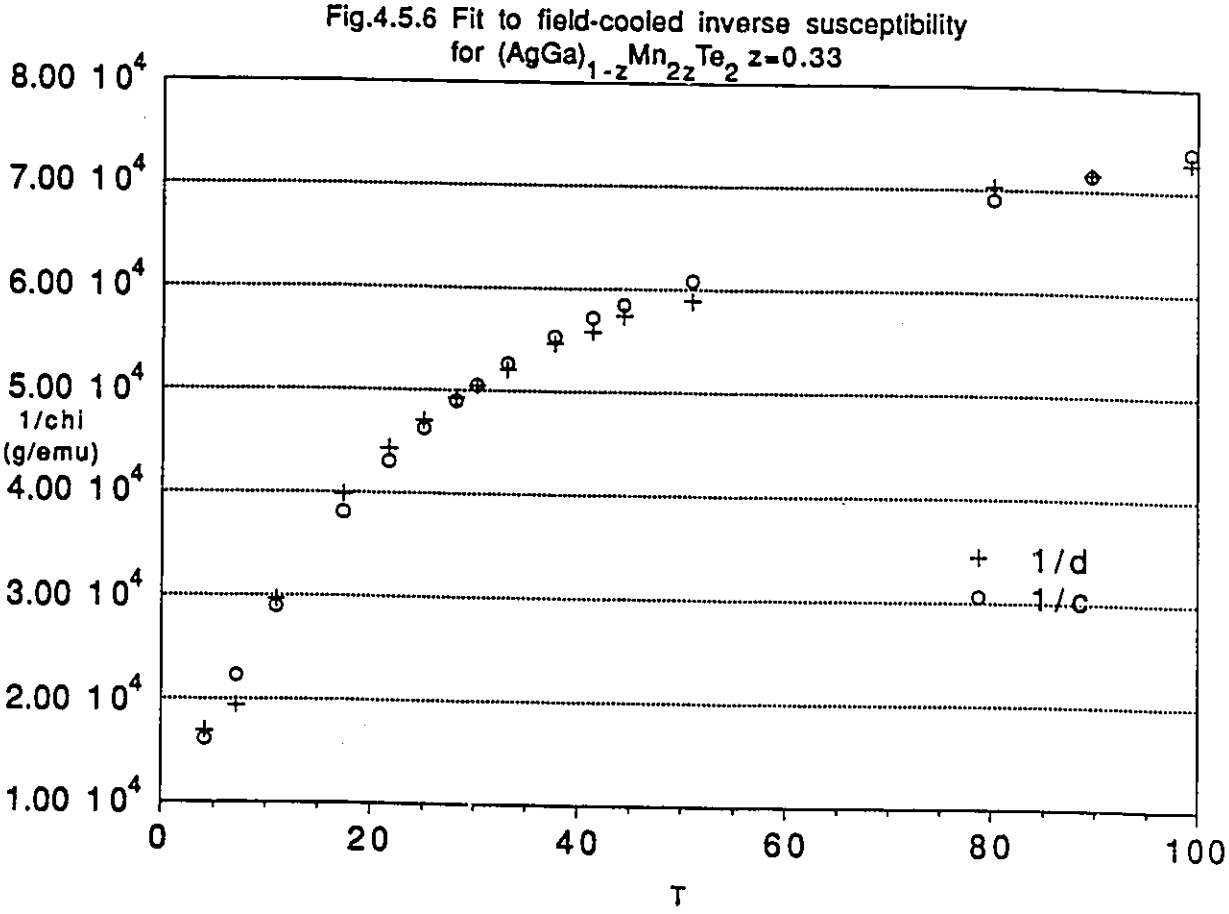

Fig. 4.5.6 illustrates the simulation of the field-cooled susceptibility of the $(AgGa)_{1-z}Mn_{2z}Te_2$ z=0.33 sample. Only the inverse susceptibility is shown. As previously, the data is represented by crosses (1/d), and the computation by circles (1/c). The parameters utilized in this simulation were C_2/C_t=0.95, θ_1=-2.2 K, θ_2=-855 K, and D=3x10^{-6} emu/g. This, and the previous results indicate that the magnetic response of these alloys can be explained by the simple model given in the text, provided that the majority of spins participate in the 63 K transition, and that their associated theta value be large.

break down. This may occur in the z=0.40 samples and explain the poor susceptibility simulations in that case.

4.5.7) Summary

The results of the fitting and the simulations can be summarized in the context of the questions posed at the beginning of section 4.4. 1) The magnetic data supports the postulate that two distinct contributions to the magnetic response occur. It is most probable that the two magnetic contributions are due to the ordered and disordered Mn-fractions, although contributions associated seperately with cubic and tetragonal phases of the materials have not been completely ruled out. 2) The magnetic parameters obtained from the fitting are as follows, (in the following C_2/C_t represents the ratio of spins with a transition at T_{c2}=63 K (C_2) to the total number (C_t) expected in the material).

Composition (z)	0.25	0.33	0.40
C_2/C_t	0.9	0.9	0.8
θ_1(K)	-2.0	-3.0	-13.0
θ_2(K)	-587	-780	-708
D(emu/g)	$1x10^{-6}$	$3x10^{-6}$	$2x10^{-6}$

The large θ_2/T_{c2} seems to be a characteristic of the ordered material and is one of the factors which strongly suggests that the high θ, and hence high C_2, must be associated with the high (63 K) transition temperature.

3) The features of the whole susceptibility above and below the transitions can be simulated with a simple model for

the magnetic response which incorporates the assumptions utilized in the fitting. The difficulty of simulating the z=0.40 result in the framework of distinct θ values can be argued to be consistent with this and suggests the cause of the 7.5 K peak in that material to be due to the interactions between the magnetic subsystems. This will be further discussed in the following section. 4) The magnetic analysis, in conjunction with the previously reported results on these materials, suggests that the Mn-ordering occurs predominantly in the tetragonal phases of these materials. In this case, the C_2 spins which are responsible for the 63 K transition are associated with the ordered (planar) Mn fraction, and the C_1 system is associated with the remaining disordered Mn.

4.6.1) Mean-Field Analysis of Mn-planes

As indicated in the previous section, a planar configuration for the Mn within the actual crystal structure is most probable since the susceptibility signature of the materials does not seem to correspond to any known bulk Mn-distributed responses in these DMS. Also the planar Mn could have properties independent of the bulk composition and thus correspond to the observed high temperature (63 K) cusp in the materials of different concentration. The Curie-Weiss θ proposed for the T_n= 63 K (T_{n2}) spin system is θ_2 =-600 ±100K and for the remaining Mn with $T_n \cong 1$ K to 4 K (T_{n1} is a function of the concentration), a $\theta_1 \cong$ -2K is proposed for the z=0.25 and 0.33 material wherease a slightly larger (more negative) θ_1 is seen for z=0.40. From the simulations of the previous section, it appears that the two lowest concentration samples can be interpreted under the assumption of distinct magnetic response described in 4.5.

One may now ask how these parameters and assumptions fit with what is known about Mn-interactions in DMS. In order to attempt to answer the question of whether Mn planar ordering could yield these results, a Mean Field Theory[1] (mft) model for the planes was studied. This model is based on the 'Generalized Molecular Field Theory' given in [66] in which the generalization refers to the applicability of the model to any number of spin sublattices. The spin sublattices are defined by their common spin orientation, number of like-neighbours and mutual interaction.

[1]Equivalently Molecular Field Theory.

The mean-field expressions for θ and T_n are;

$$T_n = \frac{2S(S+1)}{3} \frac{I_o}{k} \sum n_i \eta_i J_i \qquad (4.6.1)$$

$$\theta = \frac{2S(S+1)}{3} \frac{I_o}{k} \sum n_i J_i \qquad (4.6.2)$$

where n_i are the number of i^{th} near neighbours. and η_i are ± 1 according to the spin direction of the i^{th} neighbours in the ordered state.

From within the expectations of MFT, it is easily shown that the experimental Curie-Weiss parameters indicated above are extraordinary in some important ways. Firstly note that the typical numbers of magnetic nearest (n_1), and next nearest (n_2) neighbours corresponding to a random 3 dimensional Mn arrangment on the cation sublattice, is roughly equivalent to that expected for the postulated Mn-planar ordered structure ($n_1=n_2=4$). Using the conventional values of the exchange constants found for low concentration Mn-zincblende DMS which are typically J_1=10 K and $J_2 \cong$ 1 K, together with these n_1 and n_2 values, and limiting the summations to the first two terms in eqs. 4.5.6, we find $\theta \cong$-250 K and $T_n \cong$ 210 K. Considering the θ value as the most accurate mft parameter, it is clear that a longer range of interaction is required in order to achieve the large θ_2/T_{n2} seen in the material.

As indicated above, the observed θ_2/T_{n2} is large, yet it should be noted that it is within the range of already observed antiferromagnetic materials[2]. On the other hand, the θ_1 magnitude seems to be of the same order as the T_{n1} [2]It is significant to note that one of the highest θ/T_n ($\cong$10) occurs in a Mn compound; MnS_2 [66].

temperature.

Behaviour similar to that seen in the present Ag-Ga materials has been seen in the system $Cd_xZn_yMn_zTe$ [124]. In this material single, monotonically z-dependant magnetic transitions similar to the T_{c2} transitions have been associated with each composition. These spin-glass transitions have high values of θ/T_c and are accompanied at higher temperature with what has been referred to as 'enhanced paramagnetism' which may actually be due to a $T_{n1} < 4K$ paramagnetic type behaviour such as that modeled for the present system.

Anomalously large values of θ/T_n can actually be taken as indicative of spin-glass or low-dimensional behaviour [67], and the CdZnMnTe system is indeed known to be spin-glass. It is also possible that large apparent θ/T_n could be due to a situation leading to a 'distinct θ' scenario in which the apparent θ is caused by interactions from outside the magnetic subsystem. Whichever the case, it seems clear that long-range interactions are required in a proper analysis of the experimental results.

As indicated in section 2.3, there is good evidence from both experiment and theory that long range exchange occurs in moderate and high concentration DMS. This is understood in the context of band theory as opposed to the usual localized-cluster type analysis which leads to highly localized exchange.

The inter-Mn exchange interaction for the mft analysis was taken to be of a form used by various authors in different

circumstances (see chpt 2);

$$J_i = I_o \frac{\exp(-\alpha r_i)}{r_i^p} \quad (p=0,\ 1,\ 2) \qquad (4.6.3)$$

This form of exchange was shown to be appropriate to other high concentration DMS with p=1 or 2 [129], and found in some circumstances to yield the commonly accepted J_1 and J_2 for the same materials [124]. The exchange (4.6.3) has been used to represent interband transition mediated exchange as well as superexchange which involves virtual transitions to unoccupied Mn-d levels [130]. The precise nature of the exchange path is reflected in the parameter α, which is related to the energy differences between the excited and the ground states. Note also that by appropriate choice of parameters, this form of exchange can reproduce the usual localized exchange strengths.

As an example of the theoretical need for long-range exchange, Geertsma et. al. [131] derived an exchange interaction for DMS, valid for large r, of the type;

$$J(r) = A\frac{\exp(-\alpha r_i)}{r_i^2} + B\frac{\exp(-\alpha r_i)}{r_i^1} \qquad (4.6.4)$$

These authors considered the effect of d hybridization into the valence band. In this case, α is directly related to the difference in energy between the unoccupied states and the valence band maximum.

Given that various known materials have magnetic parameters similar to those associated with the C_2 magnetic system, ($MnTe_2$ has T_n= 90 and θ=-500K), it is clear that one could design an Mn structure which has the desired magnetic parameters. Nevertheless this would leave open the question of how such a material yields the dominant magnetic signature

of the alloy samples without giving a characteristic x-ray, neutron and ESR signature. This is why the planar hypothesis is attractive, since planar Mn clusters could easily have a magnetic response of their own and thus would explain the concentration-independance of the magnetic reponse of the solid solution.

In order to simplify the analysis, the present MFT model applies the exchange of the simple form given in (4.6.3). The system consists of a planar square spin distribution as found on either tetrahedral or octahedrally coordinated cation planes. The spin configuration in the ordered state is assumed to be of the antiferromagnetic type illustrated in fig 4.6.1. In this figure, a view of an Mn-plane from looking down the c axis is given, dotted sites refer to up spins and crossed sites refer to down spins. Note that the precise spin orientation (i.e. whether it is in or out of the planes) is not specified.

The MFT expressions for the T_n and θ with the exchange interaction (4.6.3) are as follows:

$$T_n = \frac{2S(S+1)}{3} \frac{I_o}{k} \sum n_i \eta_i \frac{\exp(-\alpha r_i)}{r_i^p} \qquad (4.6.5)$$

$$\theta = \frac{2S(S+1)}{3} \frac{I_o}{k} \sum n_i \frac{\exp(-\alpha r_i)}{r_i^p} \qquad (4.6.6)$$

n_i are the number of i^{th} near neighbours. and η_i are ± 1 according to the spin direction of the i^{th} neighbours in the ordered state.

A MINUIT subroutine was written which used a minimum least squares criterion to find values of the exchange parameters I_o and α which yielded given input T_n and θ values.

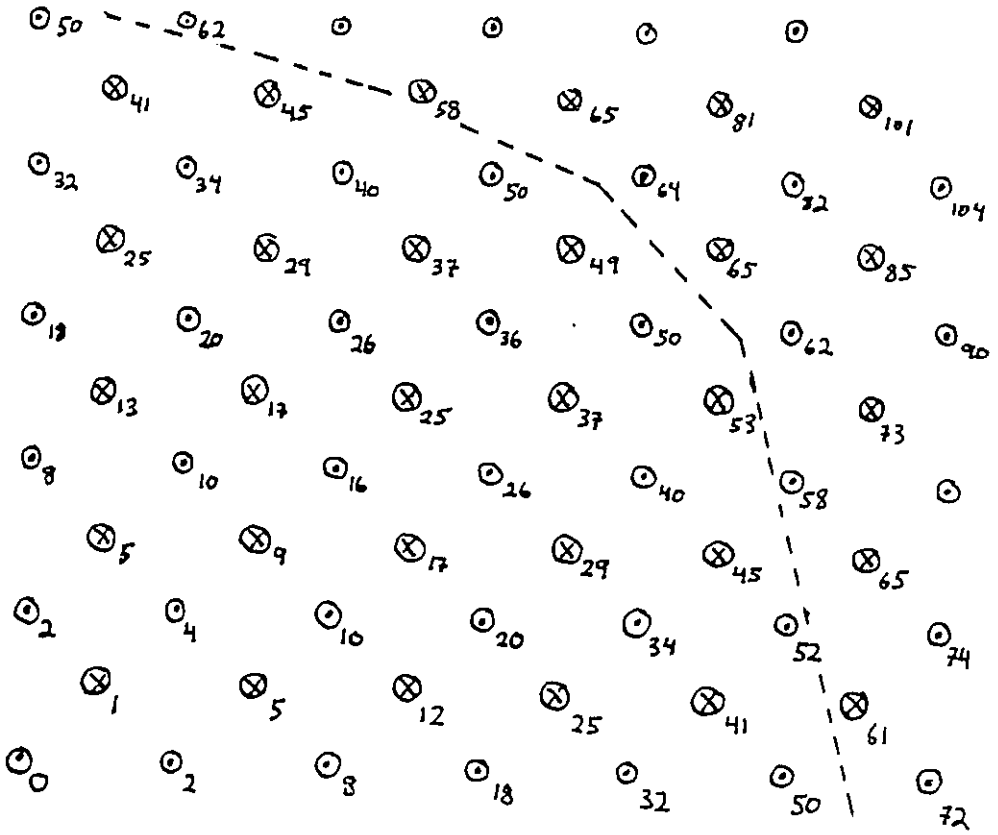

i	1	2	3	4	5	6	7	8	9	10	12	13	14	15	16	17	18
n_i	4	4	4	8	4	4	8	8	4	8	4	4	8	12	8	8	4
d_i	1	2	4	5	8	9	10	13	16	17	18	20	25	26	29	32	34
s	-	+	+	-	+	-	+	-	+	-	+	+	-	+	-	+	+

i	19	20	21	22	23	24	25	26
d_i	36	37	40	41	45	49	50	52
n_i	4	8	8	8	8	4	12	8
s	+	-	+	-	-	-	+	+

Fig. 4.6.1 The Mn-planes utilized in the MFT calculations. Illustrated are the Mn-positions on a plane in the proposed ordered structure. Also given are the number of ith near neighbours (n_i), the square of their distance from the origin (d_i) in units of $a/\sqrt{2}$ where 'a' is the lattice parameter, and the sign of the spin orientation in the ordered (antiferromagnetic) state. The distances from the origin are equivalent to the ith near-neighbour distances r_i and are given by the formula $r_i=\sqrt{d_i}* a/\sqrt{2}$. These are the only sets of parameters which enter into the MFT calculations.

Due to the potentially long-range nature of the exchange, terms in the summations (4.6.5) and (4.6.6) relating up to the 26^{th} nearest-neighbour were taken into account. The results of this analysis are shown in table 4.6.1. In this table is a survey of the possible solutions for the model, both with p=1 and p=2 where p is the power of the denominator in the expression (4.3). This survey is limited to the extent that the truncation of the series leads to error, however the qualitative features such as the approximate combinations of parameters which do not have solutions in the required range (T_n=63 K, θ=-600 K) can be identified by the behaviour of the parameters, particularly by the tendency of α to approach 0 with increasing θ/T_n in the case of p=2. The last term (26th) of each series is also given in the table as a percentage of the first term, in order to illustrate the quality of the convergence.

The tendency toward relatively long-range interactions is seen in the tendency of α to be smaller for the case p=2 than it is for p=1. No solutions exist for p=2 with $T_n \simeq$ 63 K and magnitude of θ >500 K (θ negative) as was also verified by graphical analysis, while in the case p=1 such solutions do exist. In particular, in the p=1 condition, solutions with $T_n \simeq$ 63 K and theta near θ=-600 K, yield typical values of α=1.5 nm^{-1} and I_o=-8.5 K. In this analysis, it is wise to consider the MFT solutions in the region above the expected T_n since MFT is known to generally overestimate T_n by as much as a factor of 2 especially in cases of low coordination (i.e. low-dimensionality) such as in the present model.

Table 4.6.1 Mean-Field Analysis of Mn Planes for p=1, a=0.63 nm.

theta K	T_n K	alpha nm^{-1}	I_o/k K	J_1/k K	1st term nm^{-1}	Last term nm^{-1}
-2000	63	0.23	-5.4	-11	2.03	0.26
-1500	63	0.36	-5.0	-9.5	1.91	0.20
-700	63	0.84	-4.47	-6.9	1.55	0.06
-600	63	1.0	-4.5	-6.5	1.45	0.05
-500	63	1.1	-4.6	-6.1	1.37	0.04
-700	120	1.56	-9.5	-10.5	1.12	0.01
-600	120	1.8	-10.1	-10.0	1.00	.007
-500	120	2.2	-11.2	-9.5	0.85	.003

Mean-Field Analysis of Planes for p=2, a=0.63 nm.

theta K	T_n K	alpha nm^{-2}	I_o/k K	J_1/k K	1st term nm^{-2}	Last term nm^{-2}
(no solutions for T_n=63, with theta between -500 and -700)						
-700	100	0.09	-1.8	-8.5	2.26	.003
-600	120	0.48	-2.3	-9.4	1.81	.001
-500	120	0.77	-2.5	-8.9	1.66	6E-04

Table 4.6.1 summarizes the solutions of interest found from the mft model of the planar Mn in the $AgGaTe_2$ matrix. p refers to the power of r (distance) in the denominator of expression (4.6.3). Theta refers to the Curie-Weiss temperature, alpha refers to the prefactor in the exponential form for the exchange, and I_o is the overall scale factor. The 'first' and 'last term' collumns on the far right of the table indicate the terms in the truncated series summation of the near neighbour exchange interactions. The last term represents the effect of the 26th nearest neighbour Mn within the plane. The other parameters were determined from the input theta and T_n values. These results illustrate how in mean field theory, long-range interactions are required to produce the magnetic parameters associated with the planes from experiment.

Using these representative values of α and I_o, a value of the near neighbour exchange of J_1=9.8 K is found. This is of the same magnitude as expected for Mn-DMS (see section 2.2). Utilizing, the 3-dimensional next near neighbour distance in the expression for the exchange energy yields the 2^{nd} neighbour exchange strength to be J_2=4.4 K. This is larger than the usually utilized values of J_2 in Mn-DMS. The model thus illustrates that it is possible for the Mn-planes to have an antiferromagnetic ordering temperature T_n=63^{o}K and θ=-600^{o}K with the long-range exchange interaction of the form (4.6.3) with p=1. A more realistic model might employ an exchange interaction of the form given in (4.6.4), or include exchange anisotropies due to band structure anisotropies, however since this would introduce additional free parameters, it is more useful to proceed with an inquiry regarding the properties of the present simple model.

Without a detailed knowledge of the crystal structure, one is left merely to speculate on the form of the magnetic interactions within the lattice. It never-the-less seems probable that the z=0.40 concentration could be distinct in its behaviour. Assuming that the number of atoms per plane remains identical to the chalcopyrite case, it can be seen that the z=0.40 concentration has Mn-plane spacings incommensurate with the lattice, and is equivalent to a mixture of 10/17 of z=0.33 with 7/17 of z=0.5 composition. The z=0.5 component of the lattice is necessarily stannite like, in which case it does not seem possible that the Mn planes could act independantly of each other. This is due to

the strength of the interplane interaction and the fact that the planes have no x (or equivalently y) displacement relative to each other, and thus have a simple fixed interplane configuration which could lead to more usual types of ordering. Also, interplanar (disordered) ions have a greater chance of occupying sites adjacent to the planes in the higher concentrations.

The z=0.40 composition is different from the lower concentration sampes due to its broad peak at $8^{o}K$, the loss of a clear zfc peak at $63^{o}K$, and in the fact that it yields consistently poorer simulations and fits under the conditions specified in the previous section. It is probable that these qualitatively different aspects of the z=0.40 composition (compared to the z=0.33 and z=0.25) are due to the manifestation of the inter-subsystem interactions and that the broad peak at $8^{o}K$ may represent the full 3-dimensional freezing temperature which involves a freezing of the disordered fraction with the ordered (planar) one.

In summary, it seems possible that Mn planes could be effectively isolated or independent in the z=0.25 and z=0.33 concentrations but not in z=0.40 sample. In this case the planes interact much more strongly, as do the planar and interplanar Mn. This is consistent with the breakdown of the distinct θ assumption in the case z=0.40. The distinct θ result has been considered in the context of the fully isotropic exchange interaction presented. The possibility of anisotropic exchange which weakens the interaction along the z direction would give an even better model.

The present simple model has been inspired by the striking features of the sample susceptibilities, particularly the absence of the previously reported spin-glass or antiferromagnetic cusp in such high Mn-concentration materials, the otherwise coincidental onset of apparent Curie-Weiss behaviour immeadiately above the $63^{o}K$ peak, and the high θ/T_n value corresponding to it. The qualitatively different behaviour of the z=0.40 sample seem plausible under the assumption of distinct θ. These results suggest that a similar distinct θ effect could occur in other materials not normally considered ordered. Specifically the 'enhanced paramagnetism' seen in the $Cd_xZn_yMn_{1-x-y}Te$ system and attributed to the superparamagnetism of Mn clusters.

4.7) Summary and Conclusions

This chapter has been concerned with the ordering behaviour of Mn within the chalcopyrite I-III-VI_2 materials. Because some of the experimental results, for example the occurence of a concentration-independent magnetic cusp, would normally be assumed to imply more usual phenomena such as the presence of impurities etc. these possibilities were also investigated. One such possibility investigated to explain the nd and magnetic data of the Ag-Ga system, was that the materials consist of cubic and tetragonal phases with different stoichiometry. The problems with this interpretation are that it either requires the existence of more Mn in the sample than was used in its preparation, or that the Mn-rich phase have very high Mn concentrations in order to reproduce the nd 200 intensities. The implications of the latter can be seen directly from the z=0.25 x-ray diffractometer result where the zincblende component forms roughly 7% of the sample mass. This is approximately equivalent to the total mass of the Mn in the sample, and indicates that the postulated zincblende phase would practically have to be a new form of Mn, and further requires this new phase to have the same structure and lattice parameters as the tetragonal (α) $(AgGa)_{1-z}Mn_{2z}Te_2$ phase. In view of this, and the previous knowledge obtained on the Ag-Ga system, it is clear that Mn-ordering occurs.

The identification of the exact nature of the ordering has however proved difficult. The inquiry into the nature of

the ordering has become complicated by the fact that, contrary to what was previously believed, the x-ray and nd data indicate that the crystal structure of the alloys, although tetragonal with $c/a \propto 2$ and lattice parameters very similar to those of the corresponding zincblende phases, does not correspond exactly to chalcopyrite. Instead of having a situation in which the Mn substitution could be imagined to occur within the fixed framework of the chalcopyrite structure, it seems that the Mn -containing alloys order into another crystal structure distinct from that of chalcopyrite. Since single crystals of the materials were not available, this necessitated a search for more indirect signatures of the ordering such as those that might be found in magnetic, ESR and optical measurements. This was done in the framework of an Mn-ordering scheme in which planar Mn-clustering occurred. The results of this analysis are that it seems very probable that random planar Mn-ordering occurs, but that the available data does not conclusively prove this.

One interesting possibility arrived at during these investigations is that the structure of the alloys involves both octahedral and tetrahedrally coordinated Mn. The implications of this will be discussed in the following chapter.

5.0) Summary and Synopsis

In studying a selected few DMS systems, one can gain access to some general features of the whole class of DMS materials. This chapter summarizes, and illustrates the interelations between the various results found on the specific DMS systems studied in this report. Of particular interest are those results which relate to the crystallographic ordering of the magnetic ions.

As discussed in chapter 4, the number of possible types of ordered structures increases with the number of elements making up a material. However the formation of ordered superstructures is never guaranteed solely by the addition of new elements into the matrix. For example, although the I-III-VI_2 derived material $CuZn_2InS_4$ could in principle support various crystal structures (including chalcopyrite and/or stannite stucture), it has only been reported to exhibit either zincblende or wurtzite structure [133].

In the Mn- and Fe-based I-III-VI_2 systems studied in this work however it is clear that magnetic-ion ordering plays an important role, and that these systems provide a complimentary picture of the possible types of ordering in these materials. In the case of the $CuIn_{1-x}Fe_xS_2$ ($x<0.2$) system, the Mössbauer, x-ray and ESR results of chp.3 clearly indicate that the 3+ state is the preferred state of the iron, and hence that the Fe ions prefer the In^{3+} sites as implied by the chemical formula. As such, the Fe order in the I-III-VI_2 lattice in such a way as to minimize the number of Fe nearest

neighbours. It is also true that high concentrations of Fe^{2+} states can be produced in that material, (for example by quenching) a feature which seems to be characteristic of the Cu-Fe-S system in general.

As expected from the discussion in section 1.2, Mn ions in the I-III-VI_2 environment do not seem to prefer any specific cation sublattice. Indeed the types of Mn-substitutions and ordering scenarios that can be ruled out in the LTA Mn alloys are; random Mn-substitution[1], Mn-substitution on either one of the cation sublattices, and any of the chalcopyrite based planar types of ordering discussed in chapter 4. As was seen in the final sections of chapter 4 however, the Mn-case is complicated by the fact that the exact crystal structure of the $(AgGa)_{1-z}Mn_{2z}Te_2$ appears not to be chalcopyrite. The departure from the chalcopyrite structure in the Ag-Ga alloys is small in the sense that only diffraction line intensities (not positions) are affected and that it is particularly obvious in the neutron diffraction 200 intensity. The possibility that some of the Mn reside in sites which are octahedrally coordinated by anions indicates however a significant departure from the considerations of section 1.2 including the Garbato hypothesis and other expectations drawn on the basis of the sp^3 adamantine bonding. This seems to be one of the most important implications of the non-isoelectronic substitution which occurs in the Mn-based I-III-VI_2 materials, and stands in contrast to the Fe-based

[1]Such a configuration occurs at high temperature [100].

system studied.

Perhaps the simplest observation which describes the differences in the crystallographic behaviour of the Fe- and Mn-based systems studied, is that the end-members of the respective phase diagrams have different interelations. In the case of the $CuInS_2$-$CuFeS_2$ system whose phase diagram has first been proposed in the course of this research, both end members have the same room temperature chalcopyrite crystal structure. On the other hand, in the $AgGaTe_2$-MnTe diagram, $AgGaTe_2$ is chalcopyrite while the MnTe is NiAs stucture. This added 'stress' in the Ag-Ga system perhaps anticipates the reason for the departure of the $(AgGa)_{1-z}Mn_{2z}Te_2$ solid solution from the chalcopyrite structure of the $AgGaTe_2$ end member. In this case, the distinguishing features of the diffraction line intensities, for example the nd 200 intensity, which paradoxically seem to have their largest deviation from chalcopyrite structure in the low Mn-concentration samples is probably due to the increasing presence of β phase in higher z samples.

The magnetic behaviour of the two alloy systems also illustrates a wide range of the possibilities available in DMS. The Mn-alloys show a stable, concentration independent S=5\2 spin state which gives rise to clear magnetic transition temperatures in the bulk materials. Indeed classical spin glass effects have been seen in the Mn-alloys prepared for this research (see fig.4.4.4). In contrast, the Fe S=5/2 magnetic state is not stable in the I-III-VI_2 environment.

This seems to be due to the greater importance of the d-levels in the bonding of the Fe-system, and may be due in part to the host lattice itself. In the case of the Cu-containing I-III-VI_2 system, Cu d-levels (which are especially shallow) mix significantly with the valence band. The result of this and other considerations, as regards the magnetic ordering behaviour of the bulk Fe-system, is that the magnetic moment of the Fe ions is concentration dependent.

Both the Mn- and Fe-systems studied show the g=2 ESR transition which is expected for the $3d^5$ (Mn^{2+} and Fe^{3+}) levels responsible for the local moments in the alloys. This is significant particularly for the Fe system which shows a concentration dependent reduction of the moment which mimics the $^6A_1$-$^4T_1$ crossover as discussed in section 3.4. Mössbauer analysis proved to be instrumental in assigning the chemical state of the Fe in this case. The amenability of the Fe system to Mössbauer analysis is serendipitous in view of the fact that if the question of the moment and ionization state of the Mn had arisen, the Mössbauer technique could not have been brought to bear in its resolution. As discussed in 1.2, Mn^{2+} is known to have unusually favourable small spin-orbit coupling to the excited states which are far removed from the ground state. Thus even in the case of octahedral environments, there is little question of the validity of the Mn^{2+}- $^6A_1$ ground state assignment. A lowering of the $^2T_2$ state in the case of octahedral Mn would however provide an explanation for the slight sub-band enhancement in the optical

absorption indicated in section 4.3, and provide an interpretation for the large 'positive diamagnetism' (Van-Vleck paramagnetism) seen in the magnetic fits of section 4.5.

It is useful to contrast the above 'chemical' description of the magnetism of these materials with a band-theory approach. Indeed the fact that in the Fe system studied, the Fe seems to take on characteristics more usually expected of a metal, namely the lower than free ion magnetic moment and the breakdown of certain aspects of the molecular orbital description [94 p.307], suggest that band theory considerations apply.

The existence of a delocalized (metallic) d sub-band has indeed been used to explain some of the properties of Fe-sulfides [74, pr-22]. The critical component of the band picture as regards the magnetism is the exact position of the d sub-band relative to the top of the valence band. With the sulfides in particular, this depends strongly on the character of the bonding between the Fe and its sulfur neighbours. As indicated in the introduction to this chapter, the appropriate metal 3d(Cu), 4s, 4p, 5s, 5p, and the t_2 group of Fe 3d orbitals are the likely candidates to overlap with the sulfur 3s and 3p orbitals. All these orbitals constitute both the valence band (in their bonding states), and conduction band (in their antibonding states), however it is generally true that bonding orbitals have characteristics more like the anion, and antibonding orbitals have characteristics more like

the cation. Hence the valence band is mainly due to the 3p and 3s of sulfur the more so with greater ionicity of the bonds. The width, position, and magnetic moment of the d sub-band is then critically related to the amount of covalency (mixing) and also to the amount of direct overlap between metal orbitals.

In the case of Mn the d-band is narrow enough and deep enough to act independently of the valence states, and the corresponding electronic d wavefunctions are somewhat localized at the Mn sites. This is not true of the Fe, whose d band is broadened due to inter-Fe ion interaction and contains considerable p-admixture leading to a decrease in the Fe moment [94 p.59]. This suggests that the inter-ion exchange should be larger in the case of Fe, as compared to Mn-DMS as is generally the case observed. Before significant amounts of Fe can be incorporated into the chalcopyrite-based lattice however, the moment reduction occurs and yields magnetic parameters similar to those observed in the Mn systems.

Some of the possibilities afforded by an ordered DMS in which no near-neighbour magnetic ions occur were discussed in chapter 3. One of the possibilities mentioned was that of the occurance of high temperature magnetic polarons. Although the Fe-based sulfide DMS seem to satisfy the ordering criterion for such behaviour, it seems that other features of the sulfides make them undesirable for high-T polaron formation. Most significantly, the magnetic properties of the material

are weakened by the Fe magnetic moment decrease as a function of Fe concentration. The moment-reduction mechanism may significantly alter the nature of the inter-moment exchange. In particular, the hybridization and delocalization of the Fe-d levels suggests that simple superexchange may not be a good basis for the description of the exchange interaction. The possibility of charge-transfer transitions between majority Fe^{3+} and minority Fe^{2+} states would also affect the nature of the exchange, and in this case the nature and possible occurence of magnetic polarons becomes unclear.

5.1) Suggestions for Further Work

The $CuIn_{1-x}Fe_xS_2$ and related systems offer the intriguing possibility of being single systems which, at increasing iron concentration, display a transition from magnetic ion crystal-field to ligand-field, to delocalized band states. The usefulness of the alloy system in providing insight into the end-member compounds is especially clear in imagining for example the evolution of infrared absorption bands as a function of concentration. Given the results in chp.3, it seems logical to assume that the infrared absorptions associated with the crystal-field states at low concentration become broader and of lower energy as x increases, possibly to the point of coalescing together into a nearly metallic absorption band as the corresponding electronic states become fully delocalized. It would be interesting to see at which point the ligand-field description

applies and thus to assess the nature of the intermediate spin state above x=0.17. Having done this one could provide further insight into the Fe states in $CuFeS_2$.

The most urgently needed work on the Mn-based system seems to be measurement for detailed, accurate crystallographic analysis. Two possibilities are 1) the measurement of single crystals, and 2) the joint refinement of powder x-ray and neutron diffraction patterns. The former possibility has been attempted by carefully cutting a small, cleavable segment of one of the ingots, however as described previously, the mono-crystallinity of the resulting material was not high enough for measurement. In view of the expected difficulty with the fabrication of single crystals, the second possibility seems perhaps more appealing. This is particularly true in view of the recent arrival to Canada of the GSAS (Generalized Structure Analysis System) Reitveld refinement package which has already succesfully been used to analyze multi-phase materials. In order to bring such an analysis to bear on the materials at hand however, it would probably be necessary to obtain high quality x-ray data which could be refined simultaneously to the neutron data already obtained.

The diffraction data and magnetic behaviour of the Mn-based systems has provided some clues regarding the crystal structure. The analysis of sections 4.5 and 4.6 strongly suggests that the low-field magnetic susceptibility can be understood in the context of a two-component model. One of

the components posesses a large negative Curie-Weiss $\theta \propto -600$ K, and transition temperature of approximately 63 K. It is very likely that this component contains the vast majority of the Mn ions (C_2) in each case considered, and must correspond to the material responsible for the observed x-ray and nd patterns. This information, along with the previously established features of the Ag-Ga system strongly suggests the presence of Mn-ordering. The Mn-ordering itself probably causes the deviation from the chalcopyrite crystal structure, and leads to the characteristic 63 K magnetic signature. This can be understood in the context of a planar Mn-ordering.

It is not immediately clear if such planar ordered Mn would manifest two-dimensional behaviour. In a truly 2-D system, all interaction pathways are also confined to the plane, a condition which is not satisfied for the superexchange and Bloembergen-Rowland (virtual transition) inter ion interactions in the DMS matrix.

The planar ordering scenario which formed the basis for the analysis of the magnetic results has not been fully substantiated. A simple mean-field analysis indicates as expected, that long range exchange interactions are required in order to produce the large θ/T_C ratio seen in the materials, and previous evidence mentioned in 4.6 suggests that this is indeed generally the case in the high concentration DMS materials.

Appendix 1

The differences in the electronic environments of the Fe and Mn ions can be summarized via the Racah parameters. These parameters relate to the electron repulsion, and correlation effects (including exchange) which occur in the ions.

Fe	$3d^6 4s^2$	Mn	$3d^5 4s^2$
Fe^{2+}	$3d^6$	Mn^{2+}	$3d^5$
Fe^{3+}	$3d^5$	Mn^{3+}	$3d^4$

Within a given free ion, the energy difference between terms of the same multiplicity is proportional to the Racah parameter 'B'. The parameter C appears in the calculation of the splittings between terms of different multiplicity. The following table gives B, and (B/C) in cm^{-1}.

Racah Parameters B (B/C) (cm^{-1}).

	2+	3+
Mn	**860** (4.8)	965 (4.6)
Fe	917 (4.4)	**1015** (4.7)

The single electron spin-orbit parameter ϑ summarizes the importance of the spin-orbit splittings within a given term. The spin-orbit splittings are generally an order of magnitude less than the term splittings.

Single electron spin-orbit splitting parameters ϑ (cm^{-1})

	0	1+	2+	3+
Mn	190	255	**300**	355
Fe	275	335	400	**460**

Some important differences between the Mn and Fe ions can be seen directly in the above tables. The parameters given indicate that one would expect larger spin-orbit splittings, and larger separations between terms of the same multiplicity in Fe^{3+} as compared to Mn^{2+}. This suggests that one could expect different level mixing properties for these ions under the influence of ligand fields. The effects of hybridization are also important, however these are not directly related to the above parameters.

Appendix 2)

The compound FeS whose mineralogical name is troilite is stable below 140°C. Above that temperature, it becomes what is known as hexagonal pyrrhotite. The name pyrrhotite applies to 10 distinct systems (including their polymorphs) with compositions; $Fe_{1-x}S$, Fe_9S_{10}, $Fe_{10}S_{11}$, $Fe_{11}S_{12}$, $Fe_{7+x}S_8$. Generally speaking this family of materials are distinguished by their varying amounts of Fe-vacancy ordering on a NiAs structure and are antiferromagnetic, the exception is $Fe_{7+x}S_8$ which is a monoclinic ferromagnet. It is relevant to note that for many years, the Neel temperature in FeS (at 320°C) was mistaken for a composition-independant structural transition. This misinterpretation was fostered by the formation of low temperature phases upon quenching [74 cs26]. A similar feature in $CuIn_{1-x}Fe_xS_2$ phase diagram was seen in chapter 3.

FeS_2 seems to exist in two forms although the exact relationship between them is not well known [74 cs22]. The well understood cubic form (pyrite) undergoes a peritectic breakdown into hexagonal pyrrhotite and elemental sulfur at 743°C. The less well understood orthorhombic form (marcasite) is possibly sulfur deficient and metastable.

The iss field has been characterized by its quenching properties [74 cs29] with sub-fields yielding either cubic, or cubic + chalcopyrite or mooihoekite, or chalcopyrite + iss upon quenching. In general, little is known about the low

temperature phases, however it is known that three chalcopyrite-like phases do appear; $Cu_9Fe_8S_{16}$ (talnakhite), $Cu_9Fe_9S_{16}$ (mooihoekite), and $Cu_4Fe_5S_8$ (haycockite).

It is of interest to note that two of the potential magnetic impurity compounds of interest in both the Fe and Mn-based systems studied are closely analogous in crystal structure. FeS and MnTe both exhibit the hexagonal NiAs ($P6_3/mmc$) structure, and FeS_2 and $MnTe_2$ are both pyrite (Pa3) structure.

List of References

Chapter 1

[1] 'Liquid Semiconductors', Melvin Cutler, (Academic Press, New York, 1977).

[2] C.H.L. Goodman, R.W. Douglas, Physica 20, 1107-1109 (1954).

[3] 'Ternary Compounds 1977', Conf. Ser. 35, Inst. Phys. London (1977).

[4] J.L. Shay, J.H. Wernick, 'Ternary Chalcopyrite Semiconductors: Growth, Electrical Properties and Applications' (Pergammon, New York, 1975).

[5] J.S. Shah, Prog. Crystal Growth Charact. Vol 3, 333-389, (1981).

[6] G.Brandt J. Moschalkov, Adv. in Phys. Vol 33, 3, 193-256 (1984).

[7] J. Schneider, A. Rauber, G. Brandt, J. Phys. Chem. Solids, 1973, Vol 44, 443-451.

[8] J.K. Furdyna J. Appl. Phys., 53, 7637, (1982).

[9] 'Diluted Magnetic Semiconductors', vol. 25 of 'Semiconductors and Semimetals', edited by J.K. Furdyna & J. Kossut (Academic, New York, 1988).

[10] 'Diluted Magnetic (Semimagnetic) Semiconductors' edited by R.L. Aggarwal, J.K. Furdyna, S, von Molnar (Materials Research Society, Pittsburgh, 1988).

[11] L.R. Ram-Mohan, P.A. Wolff, Phys. Rev. B38, 1330, (1988).

One of the first articles on BMP is;

A. Golnik, J.A. Gaj, M. Nawrocki, R. Planel, C, Benoit a la Guillaume, Proc. 15th Conf. Phys. Semicond., Kyoto, 1980, J. Phys. Japan, 49 (1980).

[12] T. Wojtowicz, T. Dietl, M. Sawicki, W. Plesiewicz, J. Jaroszynski, Phys. Rev. Lett. 56, 2419 (1986).

[13] M.Sawicki, T. Dietl, J. Kossut, J. Igalson, T. Wojtowicz, W. Plesiewicz, Phys. Rev. Lett. 56, 508 (1986).
also
Y. Shapira, N.F. Oliviera, P.Becla, T.Q. Wu, Phys. Rev. B41, 5931 (1990).

[14] F. Pool, J. Kossut, U. Debska, R. Reinferberger, Phys. Rev. B35, 3900 (1987).

[15] T. Suski, P. Wisniewski, L Dmowski, G. Gabrecki, T, Dietl, J. Appl. Phys. 65, 1203 (1989).

[16] X. Liu, A. Petrou, J. Warnock, B.T. Jonker, G.A. Prinz, J.J. Krebs, Phys. Rev. Lett. 63, 2280, (1989).

[17] K. Yoodee, J.C. Woolley, V. Sa-yakanit, Phys. Rev. B 30, 5904 (1984).

[18] Y. Shapira, E.J. McNiff, N.F. Oliviera, E.D Honig, K.Dwight, A. Wold, Phys. Rev. B37, 411 (1988).

[19] P.A Wolff (to be published)

[20] E.D. Isaacs, D. Heiman, M.L.Graf, B.B. Goldberg, R. Kershaw, D. Ridgley, K. Dwight, A. Wold, J. Furdyna, J.S. Brooks, Phys. Rev. B37, 7108 (1988).
also
M. Bugajski, P. Becla, P.A. Wolff, D. Heiman, L.R. Ram-Mohan, Phys. Rev. B38, 10512 (1988).

[21] J.B. Goodenough, Phys. Rev. 100, 564 (1955)
and
J. Kanamori, Phys. Chem. Solids, 10, 87 (1959).
also
P.W. Anderson, 'Solid State Physics' Vol.14, editors F. Seitz, D. Turnbull (Academic, New York, 1963, p.99)

[22] A. Twardowski, M. von Ortenberg, M. Demianiuk, J.Cryst. Growth 72, 401 (1985).

[23] N.V. Joshi, L. Mogollen, Prog. Cryst. Growth Charact. 10, 65 (1985).

[24] M. Taniguchi, Y. Ueda, I. Morisada, Y. Murashita, T. Ohta, I. Souma, Y. Oka, Phys. Rev. B41, 3069 (1990).

[25] E.G.M. Taniguchi, L. Ley, R.L. Johnson, M. Cardonna, Phys. Rev. B33, 1206 (1986).

[26] A. Aresti, L. Garbato, A. Geddo Lehmann, P. Manca, Proc. 7th Inter. Conf. Tern. and Mult. Comp., Mat. Res. Soc. (Pittsburgh, 1987), p.497.

Chapter 2

[27] A. Benoit a la Guillaume (private communication).

[28] Gerald Goodchild, Ph.D. Thesis, University of Ottawa (1984).

[29] R. Triboulet, Lecture Notes, 21st course of the Int. Sch. of Mat. Sci. and Tech. Erice, Sicily (1990).

[30] B.D. Cullity, 'Elements of X-ray Diffraction' (Addison Wesley, 1956).

also

N.F.M Henry, H. Lipson W.A. Wooster, 'The Interpretation of X-ray Diffraction Photographs' (Macmillan, 1951).

[31] J.B. Nelson, D.P. Riley, Proc. Phys. Soc. 57, 160 (1945).

[32] A. Guinier 'X-ray Diffraction in Crystals, Imperfect Crystals and Amorphous Bodies', translated by P. Lorrain, D.S. Lorrain, editors H.M. Foley, M.A. Ruderman, (W.H. Freeman & Co. 1963).

[33] S.M. Lovesey, 'Theory of Neutron Scattering from Condensed Matter', (Oxford University Press, 1986)

also

'Methods of Experimental Physics: Neutron Scattering', Vol23 A, B, and C, Ed. Price and Skold (Academic Press, 1987).

also

M.A. Krivoglaz, 'Theory of X-ray and Thermal Neutron Scattering by Real Crystals', (PLenum Press, New York, 1969).

[34] W. Smykatz-Kloss, 'Differential Thermal Analysis', editor P.J. Willey (Springer Verlag, Heidelberg, 1974).

[35] G. Goodchild, O.H. Hughes, S.A. Lopez-Riviera, J.C. Woolley, Can. J. Phys. 60, 1069 (1982).

[36] B. Pamplin, T. Kiyosawa, K. Masumoto, Prog. Cryst. Growth and Charact. 1, 331 (1979).

[37] C. Rincon, J. Gonzalez, G. Sanchez Perez, C. Bellabarba, Nuov. Cim.2D, 1895 (1983).

also

M. Quintero, A.Willsher, J.C. Woolley, Jour. of Magnetism and Mag. Mat. 89, 185, (1990).

[38] M.M. Moriwaki, R.Y. Tao, R.R. Galazka, .M. Becker, J.W. Richardson, Physica B & C, 117, 467 (1983).

[39] M. Quintero, J.C. Woolley, Jour. Magnetism and Mag. Mat. (in print).

[40] E.A. Anderson 'Modern Physics and Quantum Mechanics', W.B. Saunders Company, Philadelphia (1971).

[41] S. Oseroff, R Calvo, W. Giriat, J. Appl. Phys. 50(11), (1979).

also;

J. Kreissl, W. Gehloff, Phys. Stat. Sol.(a) 81, 701 (1984).

[42] S.E. Barnes, Phys. Rev. B30, 7, 3974 (1984).

[43] C.P. Poole, 'Electron Spin Resonance' (John Wiley & Sons, 1967).

[44] A.M. Stoneham, Rev. Mod. Phys. 41, 1, 82 (1969).

[45] M. Farle, K. Babershke, Phys. Rev. Lett. 58, 511 (1987).

[46] R.M. White, 'Quantum Theory of Magnetism', (Springer Verlag, Heidelberg, 1983).

[47] 'Magnetic Resonance of Phase Transitions', editors, F.J. Owens, C.P. Poole, Jr., H.A Farach, (Academic, New York, 1979)

[48] D.L. Huber, Phys. Rev. B6, 9, 3180 (1972).

[49] D.J. Webb, S.M. Bhagat, J. Furdyna, J. Appl. Phys. 55, 6, (1984).

[50] F. Keffer, C. Kittel, Phys. Rev. 85, 2, 329 (1952)

[51] T. Taylor, A. Coles, J. Phys. F5, 121.

[52] H. Yokozawa, J. Phys. Soc, Japan, 31, 1590 (1971).
also
I. Morimoto, S. Data, J. Phys. Soc. Japan, 29, 1093 (1970).

[53] R.E. Kremer, J.K. Furdyna, J. of Magnetism and Mag. Mat. 40, 185-189 (1983).

[54] D.G. Rancourt, Nuclear Instr. & Methods in Phys. Research, (North-Holland), B44, 199-210 (1989).

[55] N.N. Greenwood, T.C. Gibb, 'Mössbauer Spectroscopy' (Chapman and Hall ltd., 1971)

[56] F. Dyson, Phys. Rev. 98, 349 (1955)

[57] Y. Shapira, S. Foner, D. Heiman, P.A. Wolff, C.R. Mcyintyre, Solid State Commun. 71, 355 (1989).
also
S. Foner, Y. Shapira, D. Heiman, P. Becla, R. Kershaw, . Dwight, A. Wold, Phys. Rev. B 39, 1173, (1989).

[58] G. Lamarche, Rev. Sci. Instrum. 60 (5), May 1989.

[59] A.H. Morrish, 'The Physical Principles of Magnetism', (John Wiley & Sons, New York, 1966).

[60] J.E. Wertz, J.B. Bolton, 'Electron Spin Resonance' (McGraw-Hill, 1972).

[61] P. Morgan, G.S. Rushbrooke, Mol. Phys. 4, 291 (1961).

[62] G.S. Rushbrooke, R.P. Muse, R.L. Stephenson, K. Pirnie, J. Phys. C5, 3371, (1972).

[63] Y. Shapira, S. Foner, P. Becla, D.N. Domingues, M.J. Naughton, J.S. Brooks, Phys. Rev. B33, 356 (1986).

[64] Handbook of Chemistry and Physics, 70 edition, editor C. Weast (CRC press inc. 1989).

[65] G. Lamarche, J.C. Woolley, R. Tovar, M. Quintero, V. Sagredo, Joun. of Magnetism, and Mag. Mat. 80, 321 (1989).

[66] J.S. Smart, 'Effective Field Theories of Magnetism', (W.B. Saunders Co., Philadelphia, 1966).

Chapter 3

[67] L.J. Dejonge, A.R. Miedema, Ad. Phys. 23, 1 (1974).

[68] V.P. Zhuse, V.M. Sergeeva, E.L. Shtrum, Sov. Phys. Tech. Phys. 3, 1925, (1958).

and

P. Manca, F. Massaza, J. Appl. Phys. 36, 647, (1965).

[69] P. Manca, F. Massaza, J. Appl. Phys. 33, 1608, (1962).

[70] S.M. Wasim, M. Ali, N. Avgerinos, I.S. Al-Saffar, R.D. Tomlinson, Nuov. Cim. D2, 1695 (1983).

[70b] A.A. Vaipolin, V.D. Pochckhan, Yu.V. Rud', V.E. Skoryukin, Proc. SSR Ac. Sci., Inorg. Mat. 20, 4, 496-499, (1984).

[71] T. Teranishi, K. Sato, J. Phys. Soc. Japan, 36, 1618.

[72] T. Teranishi, K. Sato, Y. Saito, Inst. Phys. Conf. Ser. 35 (1977).

[73] M. Digiseppe, J. Steger, A. Wold, E. Kostiner, Inorg. Chem. Vol13,8, 1828 (1974).

[74] 'Sulfide Mineralogy', Reviews in Mineralogy Vol.1, editor P.H. Ribbe, (Bookcrafters inc., 1982).

[75] R. Adams, P. Russo, R. Arnott, A. Wold, Mat. Sci. Bull. Vol.7, 93-100, (1972).

[76] J. Mycielski, Solid State Commun. 60, 165 (1986).

also

Z. Wiliamowski, K. Swiatek, T. Dietl, J. Kossut, ibid. (in press).

[77] T. Kambara, J. Phys. Soc. Japan, 36, 6, 1625 (1974)

[78] H. Robbins, R. Lambrecht, J. Sol. State Chem. 6, 402, (1973).

[79] N.N. Greenwood, H.J. Whitfield, J. Chem. Soc. (A), 1697, (1968).

[80] D. Raj, S.P. Puri, Nuov. Cim. 01. LXB, 2, 261 (1969).

[81] L. Pauling, L.O. Brockway, Zeits. Kryst. 82, 188, (1932).

[82] F. Donnay et. al., Phys. Rev. 112, 1917, (1958).

[83] A. Temperley, H. Lefevre, J.Phys. Chem. Solids 27, 85, (1966).

[84] K. Sato, (private comm. with Dr. Woolley) abstracts from; 'Eighth International Conference on Ternary and Multinary Compounds', Kishinev (1990).

[85] Ph. D. Theses, University of Ottawa, M. Quintero (1984), T. Donofrio, (1983).

[86] For the spin-glass antifferomagnetic transition in $Cd_xMn_{1-x}Te$, see R.R. Galazka, S. Nagata, P.H. Keesom, Phys. Rev. B22, 3344 (1980).
(N.B. See ref [123], for the similar result in $Cd_xZn_yMn_zTe$).

[87] G. S. Grest, E.G. Gable, Phys. Rev. Lett. 43, 16, 1182 (1979).

[88] D. Scalbert, J. Cernogora, A. Mauger, C. Benoit a la Guillaume, A. Mycielski, Solid State Commun. 68, 1069 (1989).

[89] G. A. Slack, S. Roberts, J.T. Vallin, Phys. Rev. 187, 511 (1969).

[90] M. Hausenblas, L.M. Claessen, A. Wittlin, A. Twardowski, M. von Ortenberg, W.J.M. de Jonge, P. Wyder, Solid State Commun. 72, 253 (1989).

[91] D. Scalbert, J.A. Gaj, A. Mauger, J. Cernogora, C. Benoit a la Guillaume, A. Mycielski, II-VI-89, Berlin; to be published in J. of Cryst. Growth.

[92] C. Testelin, A. Mauger, C. Rigaux, M. Guillot, A. Mycielski, Solid State Comm. 71, 923 (1989).

[93] D. Scalbert, A. Mauger, M. Guillot, J Cernogora, J.A. Gaj, C. Benoit a la Guillaume, to be published.

[94] B. N. Figgis, 'Introduction to Ligand Fields', (Interscience, 1966).

[95] S. Chehab, J.C. Woolley, Stat. Sol. b139, 213 (1987).

[96] K. Sato, T. Teranishi, J. Phys. Soc Japan, 37, 415 (1975)

[97] T. Teranishi, K. Sato, K. Kondo, J. Phys. Soc. Japan, 63, 1618 (1974).

[98] T. Kambara, K. Suzuki, K.F. Gondaira, J. Phys. Soc. Japan, 39, 764 (1975).

[99] This is discussed in ref. [73], as well as the observation that the p_{eff} deviates from the spin only value above the concentration x=0.1.

Chapter 4

[100] G. Lamarche, J.C. Woolley , R.Tovar, M. Quintero, V. Sagredo, Journ. of Magnetism and Mag. Mat. 80, 321 (1989).

[101] Munkid Al-Najjar, M.Sc. Thesis, University of Ottawa (1987).

[102] T. Donofrio, G. Lamarche, J.C. Woolley, J. Appl. Phys. 57, (6), 1937 (1985).

[103] Y. Shapira, private communication.

[104] M. Quintero, L. Dierker, J.C. Woolley, Journ. Solid State Chem. 63, 110-117 (1985).

[105] M. Quintero, J.C. Woolley, Phys. Stat. Sol.(a), 92, 449 (1985).

[106] M. Quintero, R. Tovar, M. Dhesi, J.C. Woolley, Phys. Stat. Sol.(a), 115, 157, (1989).

[107] M. Quintero, P. Grima, R. Tovar, G.SA. Perez, J.C. Woolley, Phys. Stat. Sol.(a), 107, 205, (1988).

[108] M. Quintero, R. Tovar, M. Al-Najjar, G. Lamarche, J.C. Woolley, Journ. Solid State Chem. 75, 136-140, (1988).

[109] S. Manhas, A. Manoogian, G. Lamarche, J.C. Woolley, Phys. Stat. Sol.(a), 93, 213, (1986).

[110] J.C. Woolley, S.F. Chehab, T. Donofrio, S. Manhas, A. Manoogian, G. Lamarche, Journ. of Magnetism and Mag. Mat. 66, 23-30 (1987).

[111] A. Manoogian, B.W. Chan, R. Brun del Re, T. Donofrio, J.C. Woolley, J. Appl. Phys. 53(12), 8934 (1982).

[112] J. W. Orton, P. Auzins, J.E. Wertz, Phys. Rev. Lett. 4, 128, (1960).

[113] J. Abragam, R. Bleaney, 'Electron Paramagnetic Resonance of Transition Metal Ions', (Interscience, 1962).

[114] L. Krusin-Elbaum, A.P. Malazemoff, R.C. Taylor, Phys. Rev. 27, 562, (1983).

[115] L.R. Maxwell, T.R. McGuire, Rev. Mod. Phys. 25, 279 (1953).

[116] D. Bissonette, M.Sc. Thesis, U. of Ottawa (1988).

[117] Joint Commitee on Powder Diffraction Standards, Hawalt search index, (1972).

[118] L. Grima, R. Tovar, Phys. Rev. Lett. 51, 1472 (1983).

[119] L.O. Brockway, Zeits. Kryst. 89, 434 (1934).

[120] S.C. Abrahams, J.L. Bernstein, J. Chem. Phys. 55, 796 (1971). Also J. Chem. Phys. 59, 5415 (1973).

[121] Hahn et al. J. Phys. Soc. (1953).

[122] F. James, M. Roos, Comp. Phys. Comm. 10, 343 (1975).

[123] S. Chehab, J.C. Woolley, A. Manoogian, G. Lamarche, J. Magnetism and Mag. Mat., 62, 312-324 (1986).

[124] T. Donofrio, G. Lamarche, J.C. Woolley, J. Appl. Phys. 57(6), 1937 (1985).

[125] H. Abe, K. Torii, J. Phys. Soc. Japan, 19, 10 (1964).

[126] H. Abe, K. Torii, J. Phys. Soc. Japan, 20, 183 (1965).

[127] A.F. Cohen, S.A. Friedberg, G.R. Wagner, Phys. Lett. 3, 198 (1964).

[128] H. Stanley, 'Phase Tansitions and Critical Phenomena'.

[129] D. Beckett, S. F. Chehab, G. Lamarche, J. C. Woolley, J. of Magnetism and Mag. Mat. 69, 311 (1987).
also
see L.J. DeJonge, T. Dietl in ref [10] ('DMS'; Aggarwal).

[130] W. Geertsma, C. Haas, G.A. Swatzky, G. Vertogen, Physica 86-88b, 1039 (1977).

[131] See for example, ref [4] page 15. The identification of ordered structures is often complicated by the weakness of the resulting ordering lines.